LAYER-BY-LAYER ASSEMBLY OF NANOSTRUCTURED COMPOSITES: MECHANICS AND APPLICATIONS

by

Paul Podsiadlo

A dissertation submitted in partial fulfillment
of the requirements for the degree of
Doctor of Philosophy
(Chemical Engineering)
in the University of Michigan
2008

Doctoral Committee:

Professor Nicholas Kotov, Chair
Professor John Kieffer
Associate Professor Joerg Lahann
Assistant Professor Jinsang Kim

To my beloved wife, Aneta

Acknowledgments

This dissertation would never be completed without the support, help, and advice of diverse group of people. First of all, I'm extremely grateful for having Prof. Kotov as my advisor. I appreciate the guidance, support, and encouragement he gave me in pursuing this dissertation. He was a great mentor and a true friend throughout my Ph.D. time. I also appreciate working with Prof. Ellen Arruda and Prof. Anthony M. Waas of the Mechanical Engineering and Aerospace Engineering Departments, respectively. I would also like to thank the remaining members of my committee: Prof. Joerg Lahann, Prof. Jinsang Kim, and Prof. John Kieffer, for their assistance and useful comments on my research.

Further, I thank my former and current lab mates in Prof. Kotov's research group as well as other research collaborators at the University of Michigan. Dr. Zhiyong Tang and Bong Sup Shim deserve my greatest appreciation for helpful suggestions and stimulating scientific discussions. Dr. Vladimir Sinani and Dr. Jaebeom Lee are thanked for their many contributions and advice. I also appreciate working with Lang Sui, Dr. Kevin Critchley, Dr. Sudhanshu Srivastava, Mary Carman (Woods Hole Oceanographic Institution), Prof. Philip B. Messersmith and Dr. Zhongqiang Liu (Northwestern University), Prof. A. John Hart (Mechanical Engineering, University of Michigan), and Eugene Kheng and Amit K. Kaushik (Mechanical Engineering, University of Michigan).

I would like to thank my wife, Aneta, for her love, patience, support, and encouragement which she provided me during the whole time. I could not be at this point where I am now without her. I would also like to dedicate this work to my loving parents and parents-in-law.

Finally, I would like to thank the Fannie and John Hertz Foundation for support of my research through the Hertz Foundation Fellowship. The financial support from the fellowship was an exceptional honor and provided me with freedom and encouragement to pursue the many different research avenues which I have.

Preface

In the past two decades, the development of efficient methods for preparation of nanometer-sized materials and the continually increasing ability to manipulate the nanoscale objects have brought about a technological revolution called: nanotechnology. This revolution has been especially driven by the discovery of unique nanoscale properties of the nanomaterials which are governed by their inherent size, e.g. optical, electronic, magnetic, and catalytic, to name a few. Today, the total societal impact of nanotechnology is expected to be greater than the combined influences that the silicon integrated circuit, medical imaging, computer-aided engineering, and man-made polymers have had in the last century. We are just now seeing the tip of the iceberg in terms of the benefits that nanostructuring can bring in such diverse technologies as: catalysis, energy and environment, materials engineering, medicine and biotechnology, and electronics.

Many types of nanomaterials have also been found to possess exceptional mechanical properties. This has led to tremendous interest in developing high-performance composite materials by exploiting the mechanical properties of these building blocks. In spite of a tremendous volume of work done in the field, preparation of such nanocomposites (NCs) has proven to be elusive due to inability of traditional “top-down” fabrication approaches to effectively harness the properties of the nano-scale building blocks.

This thesis focuses on the preparation of polymer/nanoparticle and polymer/polymer NCs via a bottom-up nano-manufacturing method called the layer-by-layer (LBL) assembly. In large portion of this work, two natural and inexpensive nanoscale building blocks are explored: nanosheets of Na^+-montmorillonite clay (MTM) and rod-shaped nanocrystals of cellulose (CNRs). LBL assembly is used here as a tool to study mechanical properties of polymer/nanomaterial NCs with high volume fractions of the filler. The exceptional versatility of the LBL method is also used here for preparation of novel, solely-polymeric NCs. The results described herein encompass (a) systematic study of nanoscale mechanics of MTM-based NCs with ultimate development of a transparent hybrid composite thin-film with record-high strength and stiffness, (b) development of LBL NCs from CNRs, (c) preparation of high toughness and hierarchically organized NCs by “exponential” LBL, and (d) presentation of several applications of the resulting NCs.

Table of Contents

List of Figures

List of Tables

Chapter I

Introduction

A. Nano-Scale Building Blocks: General Introduction

This thesis in great part deals with colloidal chemistry and nanoparticles (NPs) hence a brief introduction into the subject is necessary. Historically, small particles and micrometer-size colloids have been extensively studied and used for hundreds of years. However, the science and engineering of nanometer-sized particles (NPs) has been developed only in the last two decades, predominantly thanks to the development of instrumentation to probe small length scales, such as force, laser scanning fluorescence, and electron microscopes which allowed their characterization. The NPs are referred to by many different names in scientific literature, including nanoclusters, nanocrystals, or quantum dots. A definition of a NP which has been widely accepted by scientific community is any particle with at least one of its structural dimensions being less than 100 nm. This term encompasses variety of structures, such as: nanospheres, nanorods, nanowires, nanotubes, and nanoplates, and variety of compositions: organic, inorganic, metallic, magnetic, semiconducting, dendrimers, bionanoparticles, etc.. The architectural and compositional possibilities are infinite and much of the current research efforts are devoted to the synthesis of ever more complex nanostructures. The research efforts are especially driven by the discovery of variety of phenomena associated with the nanometer-dimensions of the structures.

One such phenomenon is the quantum confinement effects observed in certain types of materials. Such NPs exhibit spectroscopic features that result from an incomplete band structure caused by the limited number of atoms. Semiconducting NPs have electronic structures between that of the individual atoms and bulk materials. The effect of an incomplete band structure on exciton interactions is an object of particular interest. An exciton is an electron-hole pair that behaves as one article due to Coulombic attractions. It is characterized by Bohr exciton state. When the size of nanoparticles becomes smaller than the Bohr exciton, the spacing between energy levels increases and the band gap widens. Quantum confinement results in a blue-shift of the adsorption edge and a corresponding shift in the photo- and electroluminescence. Therefore, the optical absorption and emission characteristics of semiconducting nanoparticles can be tuned by changing its size. This makes possible to use them as light-emitting diodes, where one type of semiconductor can be used to produce a whole spectrum of visible light.[1-7]

An important nanomaterial being extensively studied is the carbon nanotubes (CNTs). CNTs have been discovered by Sumio Iijima[8] in the early 1990's, shortly after the discovery of the Nobel Prize winning allotrope of carbon, the fullerenes or buckyballs.[9] CNTs are essentially rolled graphite sheets composed of millions or more carbon atoms in which the atoms are arranged in a hexagonal pattern while the closed ends of the nanotube resemble half of a buckyball. In perspective, they are essentially stretched buckyballs and as such they are often called buckytubes. Typical diameters for single-walled carbon nanotubes (SWNTs) are on the order of 1 – 2 nm.[10,11] There are also so called multi-walled carbon nanotubes (MWNTs) which consist of concentric shells of rolled graphite sheets and as such, their diameter can be much larger. The average length of the CNTs is typically several microns however recent reports have shown preparation of centimeter-long forests of the nanotubes. As such, they represent nanowire/nanotube structures with very large aspect ratio (ratio of length to diameter).

CNTs have the simplest chemical composition and atomic bonding configuration but exhibit perhaps the most extreme diversity and richness among nanomaterials in structure and structure-property relations.[12] Depending on the chirality (the chiral angle between hexagons and the tube axis), SWNTs can be either metals or semiconductors, with band gaps that are relatively large or small, even if they have nearly identical diameters. As such, there are infinite possibilities in the type of CNT molecules and each nanotube can exhibit distinct physical properties. The unique structure and electronic properties of SWNTs impart them with variety of novel properties, e.g. ballistic transport,[13] and they have been explored for variety of applications, including logic, memory, and sensory devices,[14,15] drug delivery carriers[16] and separation membranes[17,18].

B. Nanoparticles and Nanocomposites

Nanomaterials have also been found to possess exceptional mechanical properties. The best example of these is the SWNTs which have been heralded to be the strongest known material on Earth. Different reports show that SWNTs and MWNTs have ultimate tensile strengths in the range of σ_{UTS} ~10-300 gigapascals (GPa) and Young's modulus, E ~1.1 terapascals (TPa) or 1,100 GPa (1 TPa = 1,000 GPa), with SWNTs being considerably stronger than the MWNTs. Furthermore, CNTs have relatively low density of only ~1.4 g/cm^3 which imparts them with exceptionally high specific strength (strength divided by the density).[19,20] To put this into perspective, σ_{UTS} of Kevlar fibers (the material currently used for preparation of protective body armor) can reach values of ~3.5 GPa and their modulus varies in the range of E ~ 80 - 220 GPa.[21-23] The density of Kevlar is ~1.45 g/cm^3. Another comparison can be made to steel and its alloys, which have σ_{UTS} in the range of 0.34 – 1.9 GPa and E ~210 GPa. The density of steel is ~8 g/cm^3. Overall, the attractiveness of SWNTs lays in the fact that mechanical performance of nanometer-size reinforcement is superior to its micron-size counterparts (e.g. carbon fibers, with σ_{UTS} up to 4.5 GPa and E ~100s of GPa) and NPs possess much greater surface-to-volume ratio. The strength and stiffness of the nanotubes is close to the theoretically predicted values because fewer defects are present in the molecularly precise nanotube structure.[24] Moreover, nanotubes, while stiff in the direction of the axis, they have substantial flexibility which may lead to super-tough polymer composites. Other exceptionally strong nanomaterials include graphite flakes and graphene sheets (E ~1.1 TPa),[25] cellulose nanocrystals (E ~150 GPa),[26] and clay nanosheets (E ~150-400 GPa)[27]. Given these exceptional mechanical properties coupled with the additional properties originating from nanoscale structuring, there has been tremendous interest in utilizing these nanomaterials as reinforcing fillers for developing the next-generation of high-performance and multifunctional composites.

Historically, the first clay-reinforced resin known as Bakelite was introduced in the early 1900's as one of the first mass-produced NCs and it has fundamentally transformed the nature of practical household materials.[28] Off course people were not aware of the nano-scale structure of clay at that time. Even before Bakelite, NCs were finding applications in the form of NP-toughened automobile tires prepared by blending carbon black, zinc oxide, and/or magnesium sulfate particles with vulcanized rubber.

Despite these early successes, the true NCs revolution has not begun until the early 1990's with the reports from Toyota researchers which revealed that adding mica to nylon produced substantial increase in stiffness, yield strength, and tensile strength.[29,29] The Toyota researchers showed that small volume fractions of clay additive improved the stiffness and yield strength of nylon several times and the ultimate strength by ~25% while at the same time changing the polymer's optical properties from opaque to translucent. These results coupled with the discovery of the new types of nanomaterials with controllable sizes and shapes, e.g. fullerenes and CNTs, have literally "jump started" the NCs field. The discovery of exceptional mechanical and electronic properties of CNTs has further fueled the research efforts and opened the doors to development of high-performance and multi-functional materials.[19,20,30]

Polymer NCs have been widely investigated in the past 15 years. Until today, various NCs incorporating inorganic and organic nanoparticles e.g. exfoliated clays, carbon nanotubes,[31-34] graphene nanosheets,[35] cellulose nanocrystals, or silica particles have been prepared and the resulting materials have shown some improvement of polymer's properties, e.g. strength, modulus of elasticity, hardness, or gas permeability. There are literally tens of thousands of scientific papers dealing with preparation of various polymer/nanoparticles NCs available in scientific journals, however vast majority of them show a common result: the properties of polymers are improved up to ~10 volume percent (vol.%) of the nanofiller, beyond which the material's properties usually begin degrading. This problem is largely related to the difficulty of obtaining well-dispersed large volume fractions of the reinforcing nanomaterials and a lack of structural control over the internal organization of the NCs. NPs in particular suffer from very strong tendency to phase segregate and aggregate above critical concentrations, which leads to formation of deteriorating defects. Although small improvements in properties are still beneficial in some applications, especially when they translate into overall cost reductions associated with reduced materials requirements, the potential mechanical properties of nanomaterials are largely untapped.

To give an example of this, a simple composite rule-of-mixture prediction shows that composites incorporating approx. 20 vol.% of the CNTs should achieve σ_{UTS} of at least 2 GPa and E of 200 GPa. In reality the observed properties are usually only a small fraction of these values.[36] The traditional preparation methods are simply not capable of fully exploiting the properties of individual CNTs. The most encouraging results have been obtained by using "smart" preparation approaches, instead of simple mixing. As an example, the best results with SWNTs have been reported by Baughman's research group, where they have developed a novel method for spinning polymer fibers based on poly(vinyl alcohol) (PVA) polymer. The resulting fibers consisted of ~60 wt.% of SWNTs and showed σ_{UTS} of ~1.8 GPa, and modulus, E of ~80 GPa.[37] High loading of SWNTs and alignment of the nanotubes in the direction of the fibers was critical to achieving high mechanical properties. However, while their fibers showed relatively high strength, the transfer of properties from individual SWNTs to the macroscale was far from ideal considering the properties of individual nanotubes and the fact that alignment of PVA had also substantial effect on the mechanical properties of the fibers. Another example of a smart approach entails direct synthesis of nylon from the surface of the CNTs. Using this approach, Moniruzzaman et al. have recently shown preparation of a nylon/CNT NC with yield strength of ~75 MPa, σ_{UTS} ~175 MPa, E ~2 GPa, and 140 %

improvement in toughness (properties of neat nylon used in this study are: yield strength of ~30 MPa, σ_{UTS} ~67 MPa, E ~0.88 GPa).[38] These were considerable improvements when compared to the neat polymer and previous presentations.

While CNTs have exceptionally high mechanical properties, they also have a major drawback: high price. Current cost of SWNTs can be in the hundreds of dollars per gram which makes preparation of NCs prohibitively expensive except for a few niche applications. Surely this price is bound to decrease with an increase in demand, however alternatives to CNTs already exist and are extensively investigated for preparation of NCs. These include the natural, inexpensive, and renewable NPs such as clay nanosheets and cellulose nanocrystals. In the field of clay NCs, the results presented by Toyota almost 15 years ago were the best until today in terms of strength and stiffness. The nylon/clay NC showed σ_{UTS} of ~109 MPa and E of ~1 GPa.[29,39] Other results with clay have shown interesting toughening properties, however none have shown expected properties based on the modulus of elasticity of individual platelets, E ~150-400 GPa. A novel ("smart") approach to the preparation of polymer/clay NCs was reported recently by Liff et al..[40] The authors have used a solvent exchange method to selectively reinforce hard segments in polyurethane chains which resulted in a NC with improved yield strength, E, and σ_{UTS} without loss and even improvement in the ultimate strain, thus greatly improving overall toughness. While novel and encouraging, the NC showed $\sigma_{UTS} = 60$ MPa and $E = 1$ GPa, which are still far below the properties of individual nanosheets (E ~270 GPa).

In summary, NCs offer infinite opportunities in materials design with potential to revolutionize nearly every aspect of our lives. They have potential for very broad societal impact ranging from civilian infrastructure, through energy, and on to aviation and military sectors. However, the issue of transferring the nano-scale mechanical properties to the macro-scale has to be addressed first. Achieving this will require new and "smart" fabrication methods as well as fundamental understanding of polymer behavior under extreme confinement and high loadings of NPs.

C. The Layer-by-Layer Assembly Technique

1. Introduction

The layer-by-layer (LBL) assembly technique is currently one of the most widely utilized methods for the preparation of nanostructured, multilayered thin films. It is a bottom-up assembly method (i.e. typically the films are built by layering a few nanometers of material at a time) for preparation of thin films which offers nanometer-scale precision in structuring and enables incorporation of high volume fractions on NPs. Nano-scale control over the structure alleviates the traditional phase segregation problems in NCs, hence LBL can be considered an example of a "smart" fabrication approach. It is the main focus of this thesis hence it requires adequate review of the field.

The first demonstration of LBL assembly was shown in 1966 by Iler, who presented a technique for building films of controlled uniform thickness by alternate adsorption of positively and negatively charged colloidal particles.[41] Afterwards several singular attempts have been reported but they were met with little interest in the scientific community.[42,43] It wasn't until the work by Gero Decher and coworkers in the early 1990's with oppositely polymer pairs when it was realized that LBL assembly technique is a simple and universal method of thin film preparation.[44-48]

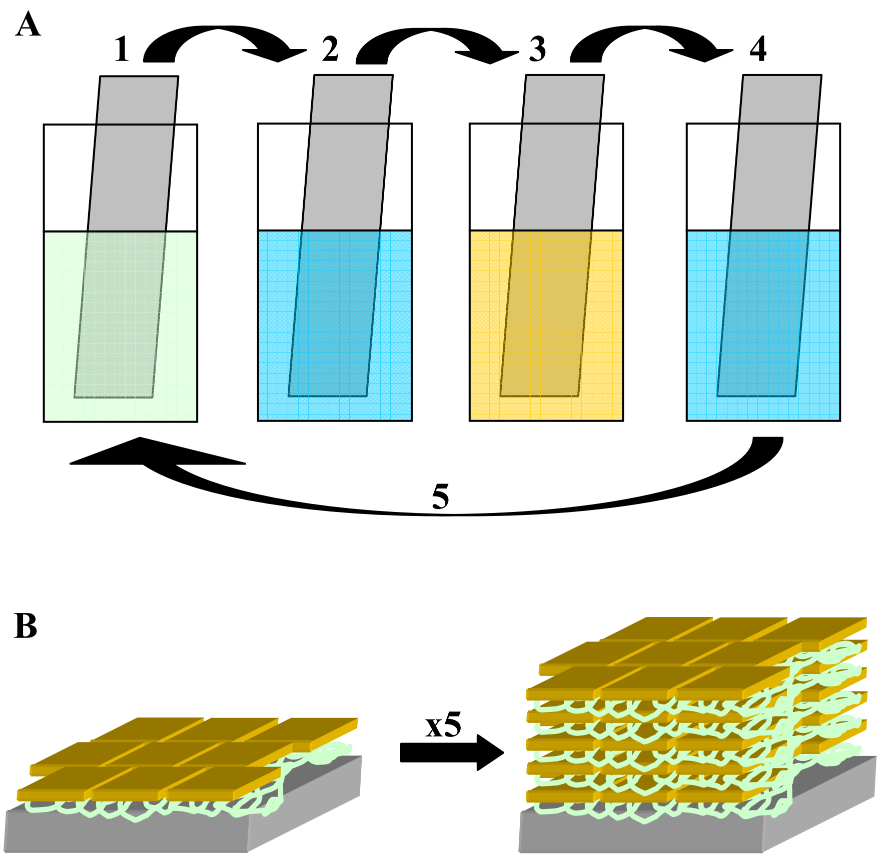

Figure 1. Layer-by-layer assembly overview. (A) Schematic representation of the LBL deposition cycle: (1) deposition of positively charged colloid, (2) rinsing with pure solvent, (3) deposition of negatively charged colloid, (4) rinsing with pure solvent, (5) return to step (1). (B) Exemplary structure of a multilayer composed of a polymer and a sheet-shaped colloid after 1 and 5 deposition cycles.

In simplest terms, LBL is based on sequential adsorption of oppositely charged layers of material onto a surface by electrostatic attraction. Given the variety of available assembly materials, it can be broken down into 3 general types of structures: (1) polymer/polymer, (2) polymer/NPs, and (3) NPs/NPs, with each being discussed in the subsequent sections. A schematic representation of a typical LBL deposition cycle is shown in Figure 1. In the initial step (Step 1, Figure 1A), a charged substrate is immersed into a solution of an oppositely charged component. Usually a charged polyelectrolyte (PE, a charged polymer) is used on this first step since it can cover large area of substrate and can form a charged cushion layer on the surface for subsequent deposition of more rigid materials. Some of the typical PEs used in LBL assembly are shown in Figure 2. The exposure time lasts typically from a few seconds to 10s of minutes. Subsequently (Step 2), the substrate is rinsed with pure solvent to remove weakly bound material and dried if desired. Following the rinsing step, the substrate is transferred into solution of an oppositely charged species (Step 3) to that used in the initial step. The exposure time is again similar to that in Step 1, i.e. seconds to minutes. Finally (Step 4), the substrate is once again rinsed with pure solvent. After completion of Step 4, under optimum conditions, the substrate is covered with a pair of oppositely charged layers of materials (a bilayer) with the top surface charge being returned to the original, starting point. With the recovery of the surface charge, this cycle can be repeated until a film of desired thickness or structure is obtained. The sketch in Figure 1B shows the structure of LBL growth of a hybrid organic/inorganic, polymer/nanosheet composite after 1 and 5 cycles of deposition.

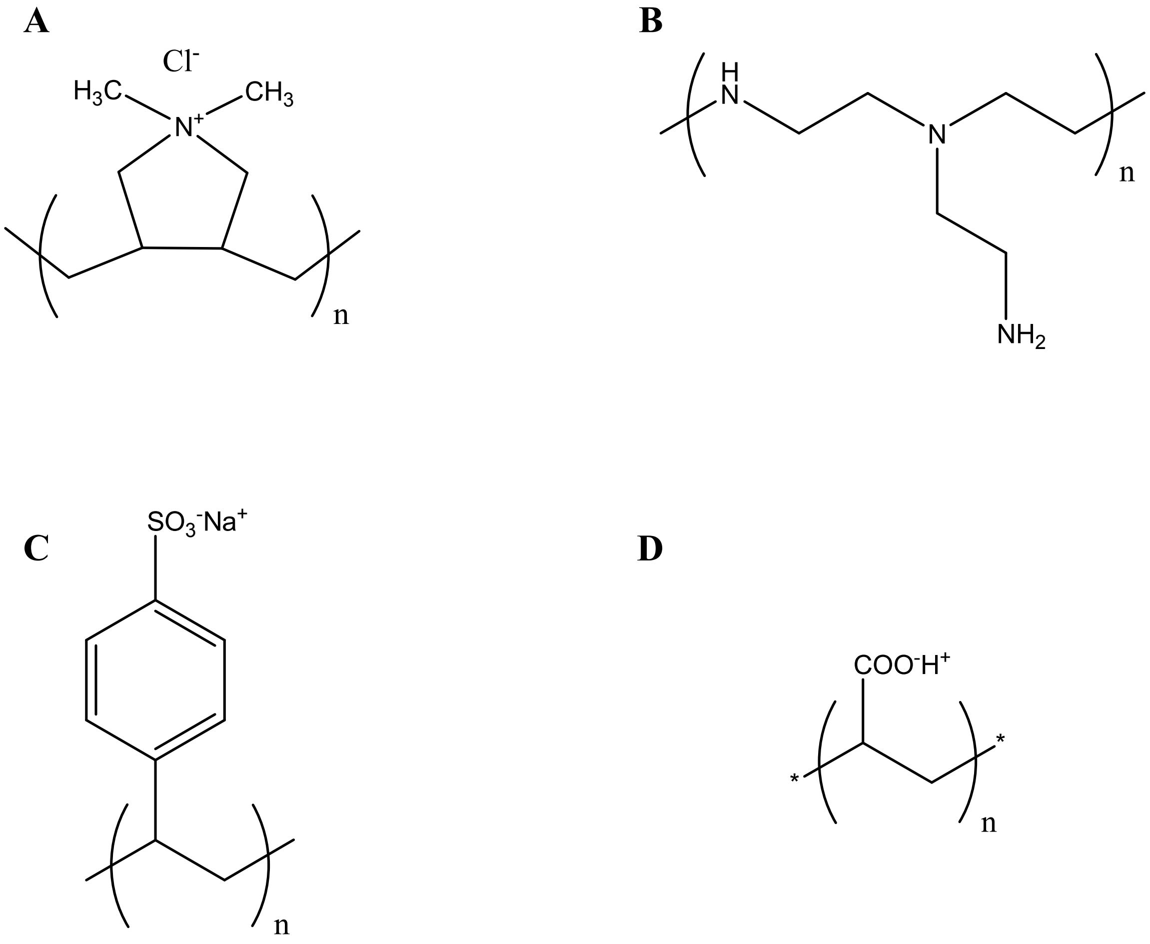

Figure 2. Common charged polymers used in LBL assembly. (A) poly(diallyldimethylammonium chloride) (PDDA), (B) branched poly(ethyleneimine) (PEI), (C) poly(styrenesulfonate) sodium salt (PSS), and (D) poly(acrylic acid) (PAA). (A) and (C) are considered strong polyelectrolytes while (B) and (D) are considered weak.

The growth of multilayer stack is achieved due to the electrostatic attraction and van-der-Waals interactions between the oppositely-charged components. For a successful LBL process to occur two major requirements have to be fulfilled: (1) colloidal solutions of oppositely charged species have to be used and (2) complete recharge of the surface must be attained on each deposition step. The latter means that after adsorption of a new layer during LBL deposition the surface charge has to change sign. When both of these demands are satisfied, formation of films with thicknesses from nanometer to micrometers with uniform structures is possible through the LBL assembly procedure. There seems to be no limitation to the maximum number of layers that can be deposited, and films with up to 1000 layers have been made.[49-51] The coverage area is limited only by the substrate size and polyelectrolyte solution volume. When dried the obtained films are stable and mechanically strong. The alternations in the dipping sequence allow for the preparation of many different variations on the LBL films. Three-dimensional heterostructures may also be created with photolithography, soft-lithography, and inkjet printing techniques.[52,53]

Besides polymers, this method has been successfully applied to many other systems. To this date, nearly any imaginable organic and inorganic macromolecular species has been used as assembly components, including: inorganic molecular clusters,[54] nanoparticles,[55] nanotubes and nanowires,[56] nanoplates,[57,58] organic dyes,[59] organic nanocrystals,[60,61] dendrimers,[62] porphyrin,[63] polysaccharides,[64,65] polypeptides,[66] nucleic acids and DNA,[67] proteins,[68,69] and viruses[70].[71] The simplicity and universality of LBL method has made it an attractive alternative to many thin film deposition methods, such as Langmuir-Blodget deposition, spin-coating, and sputtering.

Remarkable versatility has led to a number of novel designs and applications of the LBL-based materials, such as: superhydrophobic surfaces,[72] chemical sensors and semi-permeable membranes,[71,73-75] drug and biomolecules delivery systems,[71,76-78] memory devices,[79] optically active and responsive films,[61,80-82] cell and protein adhesion resistant coatings,[71,83] fuel cells and photovoltaic materials,[84,85] biomimetic and bio-responsive coatings,[86,87] and many more.[71,88]

2. Polymer/Polymer LBL Multilayers

Multilayered films composed of organic compounds on solid substrates have been studied since the mid 20th century for their potential in the preparation of tailored multicomposite materials. Classical methods used for this task such as Langmuir-Blodgett and chemisorption do not provide diversity in starting materials, since they require certain classes of molecules. It is not surprising then that the initial works on LBL assembly have been done with PE/PE systems.[44-48,89]

Polyelectrolyte multilayers can be obtained on many different supports. The roughness of the initially deposited layers will be close to that of the substrate. Nevertheless, continuation in the dipping procedure under carefully chosen conditions will result in the production of a smoother film substrate.[90] The roughness of the obtained PE films also depends on the ionic strength of the solution. The addition of NaCl into an aqueous dispersion of fully ionized strong polyelectrolyte results in the screening of its charges, which leads to coiling and entangling and, consequently, absorption of a thicker PE layer of greater roughness.[57,91] On the other hand, when an already prepared film is immersed in a salt solution it results in its swelling. The degree of swelling is a strong function of the LBL assembly composition and can be explained by the interpenetration of Na^+ and Cl^- ions inside of the film structure. When the ionic strength of the solution is high enough, a smoothing of the film surface is observed.[92,93]

When a weak PE is used for LBL stack preparation, the pH of its dispersion becomes the factor affecting the growth process and structure of the obtained film. At a pH range where the PE is fully ionized, formation of smooth thin layer is observed. A shift in pH value away from its optimum range results in PE molecule entangling. This leads to the formation of a thick film with greater degree of roughness.

Even when polyelectrolytes are assembled sequentially onto a surface during an LBL deposition, it has been reported that the structure of the assembled multilayers can be highly interpenetrated.[94-98] Poly(allylamine) (PAH)/poly(styrene sulfonate) (PSS) multilayers deposited from salt-containing solutions displayed an interpenetration between the polymer layers on the same order as the individual layer thicknesses.[94,95] These multilayers formed from one pair of PE have been described as "fussy".[48] However, in multilayers consisting of different pairs of polyelectrolytes, separate layers have a stratified structure.[98] This stratification is consistent with the evidence of interpenetration on the order of an individual layer thickness but not more.

Interactions other than electrostatic between oppositely charged molecules can also be used in LBL assembly. The successful growth of films, made of polyaniline (Pan) alternated with nonionic water-soluble polymers, has been demonstrated.[99] The authors presumed that the LBL growth of the films occurred because of hydrogen bonding between PAn and a non-ionic polymer such as poly(vinyl pyrrolidone) (PVP), poly(vinyl alcohol) (PVA), poly(acryl amide) (PAAm), and poly(ethylene oxide) (PEO), which were used in that study. Films have also been prepared with PVP and PAA. The formation of hydrogen bonding interactions was identified using infrared (IR) spectroscopy. It is also possible to utilize polymers having respectively electron-donating and electron-accepting pendant groups for LBL assembly.[100]

One more interesting example of multilayered LBL films, formed by interactions other than electrostatic, is in protein multicomponent films. Interactions between the biological molecules or between the biomolecules and the polyelectrolytes are employed in formation of these multilayers. It has been reported that immunoglobulin G can be assembled with anionic PSS at pH values above and below its isoelectric point. This fact reflects the non-electrostatic nature of the LBL process.[101] In addition, the LBL deposition of avidin and biotin-labeled polyamines creates a multilayered structure through avidin-biotin complexation[68,102-104] even in the presence of electrostatic repulsion arising from the net positive charges of the avidin (isoelectric point at pH 9.0 – 10.0) and polyamines.[102,103]

3. Multilayers from "Exponential" LBL Assembly

While a vast majority of LBL systems undergo linear growth (l-LBL), there are also some quite special combinations of polyelectrolytes which exhibit so called "exponential growth" (e-LBL). The l-LBL method has been studied/applied most extensively and thus covers most of LBL publications. Substantially smaller and more recent subset of LBL literature is related to e-LBL films. Historically, e-LBL was observed for the first time in 1999 by Elbert et al.[105] for poly(L-lysine) (PLL) and alginate (AG) polyelectrolytes pair. The authors observed that the thickness of dried films increased exponentially with the number of deposited layers. To explain the results the authors have evoked a possibility of formation of a PLL/AG complex coacervate, a type of gel, on the film surface during the successive deposition. Subsequently, Ruths et al.[106] observed exponential growth in PSS/PAH multilayer assembled onto a Langmuir monolayer which they have attributed to increasing film roughness with increasing thickness. Pardo-Yissar et al.[107] have also observed nonlinear buildup of a PLL/PAA multilayer system, and their explanation was the swelling of the film and increased absorbance of water. Finally, Picart et al.[108,109] and Lavalle et al.[110-112] have suggested a formation mechanism and later presented a proof of an "in-and-out" diffusion of the polyelectrolytes. In the studied system, the authors have found that the polycation diffuses into the film during the deposition and then out of the film during rinsing and further out during polyanion deposition. When immersed into the polyanion solution, as the diffusing polycation reaches the outer surface of the film, it interacts with the incoming polyanion to form a polycation/polyanion complex layer. The thickness of this new layer was found to be proportional to the amount of the polycation that diffused out of the film.

The fundamental understanding of the growth mechanism has spurred development of novel structures and applications of the resulting films. For example, Boulmedais et al.[66] have shown controlled switching of random-to-α-helical structure of poly(L-glutamic acid) (PLGA) in a PLGA/PAH e-LBL. Garza et al.[113,114] have also shown preparation of multi-compartment e-LBL films while Hübsch et al.[115] and later others[116] have shown the ability to control the l-LBL vs. e-LBL growth behavior of the films. The e-LBL films have also shown interesting stability dependence in response to ferrocyanide and ferricyanide ions.[117,118] Kujawa et al. and others have shown dependence of the e-LBL film thickness on the molecular weight of the polyelectrolytes.[119,120] The e-LBL interdiffusion of polyelectrolytes have been shown to induce spontaneous ordering and exchange of viruses incorporated in the films,[70] which has been applied to the formation of battery electrodes by Nam et al.[121] Most recently, several novel applications of e-LBL have been presented. These include: strengthening of wood fibers,[122] drug and DNA delivery platforms,[123-126] preparation of superhydrophobic surfaces,[127] mechanically responsive nanovalves,[128] and a novel platform for spontaneous assembly of rod-shaped viruses.[70]

One can quickly notice that all of the above-mentioned e-LBL structures were based on purely polymeric or organic precursors. The types of polyelectrolyte pairs engaged in e-LBL thus appear to be limited, while it would be quite interesting to expand the functionality of the exponentially grown films to a greater number of LBL-capable species, e.g. NPs. Preparation of hybrid organic/inorganic e-LBL materials is also addressed in this thesis.

4. Hybrid Polymer/Nanoparticles Multilayers

The LBL assembly method has been extensively utilized for the preparation of hybrid organic/inorganic films. Exfoliated clay materials, metal oxide, semiconductor NPs, and metallic NPs have been utilized for this task.[55,57,58,129-134] Most typically, the common requirement for a successful assembly of these materials is the presence of charge bearing groups on the inorganic surface. If the surface is uncharged, additional surface treatment may be applied.

The first investigation of the assembly of negatively charged exfoliated minerals such as hectorite, α-zirconium phosphate or montmorillonite (MTM), have shown that they can be assembled using positively charged PEs, such as PDDA or PAH.[57,58,130-132] It is also important to note that the sheets were found to adsorb parallel to the surface covering large areas of the previously adsorbed layer. These sheets were shown to produce composites with unusually high mechanical properties similar to those of seashell nacre and lamellar bones.[135] In fact, the mechanical properties of this material (σ_{UTS} = 100 ± 10 MPa and E = 11 ± 2 GPa), exceed those of many clay composites prepared by simple dispersion and gave a precedence for studying these structures for preparation of ultra-strong composites.[136,137] As a result, in a recent report we have shown preparation of a transparent clay nanocomposite with record-high strength and stiffness for this class of materials: σ_{UTS} = 400 ± 40 MPa and E = 106 ± 11 GPa.[138] The results of this investigation are presented in this thesis. The ability of MTM to work as nanoscale armor for other types of nanoparticles was also used in assemblies of MTM and magnetite or Ag NPs films.[139,140] LBL films utilizing insulating functionality of alumosilicate sheets were made with gold NPs.[141] Other examples of LBL assemblies incorporating MTM nanosheets include preparation of LBL films of myoglobin or horseradish peroxide for voltammetry studies, photocontrollable magnetic thin films, chemiluminescent thin films for sensory applications, or perm-selective membranes.[142-147]

Extensive work has also been carried out on LBL assemblies of CNTs. In 2002, Mamedov *et al.* have shown for the first time that SWNTs can be assembled into multilayered structures with uniform and homogeneous loadings of the nanotubes up to 50 vol.%. Characterization of the mechanical properties revealed that the composites had σ_{UTS} = 220 ± 40 MPa with some reading as high as 325 MPa and E as high as 35 GPa.[56] These exceptional values prompted subsequent investigations of LBL assemblies from MWNTs[148] and vapor grown carbon fibers[149] for preparation of novel composite thin-films. The added beneficial properties of CNTs, such as the electrical conductivity, have further led to additional investigations of applicability of the LBL films for strain and corrosion sensing,[150] optoelectronic devices,[151] neuroprosthetic devices,[152,153] antibacterial coatings,[154] superhydrophobic coatings,[155] fuel cells membranes,[85] and stem cells culture substrates.[156]

Another type of inorganic NPs is metal oxides. The LBL growth of the film built from metal oxide NPs proceeds in a linear fashion. The thickness of the adsorbed layer increases with increasing ionic strength of the solution. NPs with negatively charged surfaces, like silica or titania at high pH, have been assembled with positively charged PEs, such as PDDA and PEI. It was also demonstrated in the same work that the surface charge of pure silica colloids can be controlled by wrapping them in PDDA before the LBL assembly process.[157] Positively charged metal oxide NPs such as ceria and titania can be assembled with negatively charged PEs, like PAA and PSS in acidic media.[50,55]

Contrary to metal oxide NPs, which generally have surface charge, metallic and semiconductor NPs synthesized in solution, are not charged. In such a case, the choice of the stabilizing agent is important for the formation of charged nanostructures. Several reports on the LBL assembly of acid-stabilized metallic and semiconductor NPs have been published.[55,158,159] Furthermore, alternating PE/NP bilayers with PE/PE spacers allows for the preparation of distinctly layered composite structures.

As in the case of PE/PE multilayers, the growth of the inorganic nanomaterial containing films can be obtained through non-electrostatic interactions. Hydrogen-bonding, protein-antibody interactions *etc.* are possible, when the surface of the inorganic component is modified with a corresponding stabilizing or coordinating agent. Utilization of the LBL method gives the opportunity to produce a large variety of PE/PE films with fine control over their structure by modulating the adsorption conditions and by choosing polyelectrolytes with desired properties. The availability of non-ionized groups of PE inside of the prepared assemblies as well as the possibility of swelling in the resulting films gives an opportunity to use them as nanoreactors for the *in situ* synthesis of inorganic nanoparticles. As an example, the synthesis of cobalt hydroxide ($Co(OH)_2$), iron oxyhydroxide (β- and γ-FeOOH) and lead sulfide (PbS) NPs has been presented utilizing PDDA/PSS multilayers.[160,161] The *in situ* synthesis of inorganic nanomaterials provides a simple way of preparing composite organic/inorganic materials. However, utilization of this method does not provide total control over the structure of the resulting material as in the direct assembly.

5. Nanoparticles/Nanoparticles Multilayers

The explosion of interest in LBL materials has led to a recent revival of the all-nanoparticle structures, i.e. LBL assembly of oppositely charged NPs only, without the use of polyelectrolytes. This effort has been especially driven by the research group of M. F. Rubner.[162] In the first study by the group, Lee *et al.* have shown that LBL assembled structures from TiO_2 and SiO_2 NPs exhibit antireflective, antifogging, and self-cleaning properties from superhydrophilicity.[162] In another report they have shown an opposite effect, self-cleaning and transparent coatings based on superhydrophobicity (extreme water repulsion) from oppositely charged SiO_2 NPs.[163] The authors have further published several investigations detailing fundamental aspects of growth kinetics and structures of the films.[164,165] In the most recent reports they have demonstrated mechanical robustness of the all-NPs LBL films[166] and preparation of tunable Bragg stacks.[167] Overall, these reports showed that the properties of the all-NPs films can be tuned by the choice of the NPs sizes and surface chemistries. Given the wide variety of

NPs available, the revival of NP/NP LBL structures will surely lead to new and exciting materials.

D. Purpose and Research Overview

The previous discussion provided a brief account of state-of-the-art in the nanocomposites and LBL deposition method. The possibility of control of the growing film at each adsorption step has been emphasized. Large variety of organic and inorganic nanomaterials available opens the doors for the preparation of films with wide spectra of possible applications ranging from advanced catalytic materials to artificial biological membranes. Each of the colloidal dispersions used in this process requires individual approach when high quality films are needed. There is a continual interest and need in tuning the properties and structure of the LBL multilayers as well as in understanding of actual interactions and arrangements of the separate interlayers.

This work focuses on the development of polymer/NPs and polymer/polymer NC-thin films utilizing the layer-by-layer assembly method. The goals of this work are: (1) to use the LBL method as a model system to study the mechanics of NCs with high volume fractions of NPs, (2) to show ability of the LBL assembly method to effectively harness the exceptional mechanical properties of NPs, and (3) to show that the thin-film fabrication method can be extended to preparation of macro-scale composites via hierarchical structuring. Successful fulfillment of these goals demonstrates the capabilities of the LBL assembly method in NCs preparation and realizes its advantages for the preparation of complex structures based on inorganic nanomaterials and organic PEs.

The research, presented in this work can be generally divided into three main themes: preparation of novel LBL assemblies, characterization of properties, and applications. Chapter II describes development and mechanical characterization of nanostructured composites by LBL assembly of MTM as a means of understanding the nanoscale mechanics in clay composites. Biomedical application of polymer/clay LBL assembled thin film is also demonstrated. Chapter III describes parallel research on preparation and mechanics of nanocomposites based on cellulose nanocrystals. In addition to preparation and mechanics, a novel application of the nanocrystals as antireflective coating is presented. Chapter IV describes preparation of high-toughness and hierarchically structured composites. Preparation of LBL structures using an "exponential" LBL process and polyurethanes as a fundamentally new building block for the assembly is stressed in this chapter. The final chapter concludes this work and suggests some future research directions.

Reference List

1. Sattler, K. The energy gap of clusters, nanoparticles, and quantum dots. 5 ed.; 2002; pp 61-97.

2. Kumbhojkar, N.; Kshirsagar, A. Optical properties of II-VI semi-conducting quantum dots. 2001; pp 191-205.

3. Talapin, D. V.; Rogach, A. L.; Mekis, I.; Haubold, S.; Kornowski, A.; Haase, M.; Weller, H. Synthesis and surface modification of amino-stabilized CdSe, CdTe and InP nanocrystals. *Colloids and Surfaces, A: Physicochemical and Engineering Aspects* **2002,** *202* (2-3), 145-154.

4. Talapin, D. V.; Haubold, S.; Rogach, A. L.; Kornowski, A.; Haase, M.; Weller, H. A Novel Organometallic Synthesis of Highly Luminescent CdTe Nanocrystals. *Journal of Physical Chemistry B* **2001,** *105* (12), 2260-2263.

5. Ingert, D.; Motte, L.; Pileni, M. P. Metal chalcogenides. CdS and CdTe nanoparticles made in reverse micelles: Preparation modes and optical properties. *Surfactant Science Series* **2000,** *92* (Fine Particles), 217-234.

6. Gaponik, N. P.; Talapin, D. V.; Rogach, A. L.; Eychmuller, A. Electrochemical synthesis of CdTe nanocrystal/polypyrrole composites for optoelectronic applications. *Journal of Materials Chemistry* **2000,** *10* (9), 2163-2166.

7. Gao, M.; Kirstein, S.; Rogach, A. L.; Weller, H.; Mohwald, H. Photoluminescence and electroluminescence of CdSe and CdTe nanoparticles. *Advances in Science and Technology (Faenza, Italy)* **1999,** *27* (Innovative Light Emitting Materials), 347-358.

8. Iijima, S. Helical microtubules of graphitic carbon. *Nature (London, United Kingdom)* **1991,** *354* (6348), 56-58.

9. Smalley, R. E. Buckytubes! - new materials and new devices from carbon. Book of Abstracts, 215th ACS National Meeting, Dallas, March 29-April 2 , CHED-330. 1998.
   Ref Type: Abstract

10. Collins, P. G.; Zettl, A.; Bando, H.; Thess, A.; Smalley, R. E. Nanotube nanodevice. *Science (Washington, D. C.)* **1997,** *278* (5335), 100-103.

11. Odom, T. W.; Huang, J. L.; Kim, P.; Lieber, C. M. Atomic structure and electronic properties of single-walled carbon nanotubes. *Nature (London)* **1998,** *391* (6662), 62-64.

12. Dai, H. Carbon Nanotubes: Synthesis, Integration, and Properties. *Accounts of Chemical Research* **2002,** *35* (12), 1035-1044.

13. Javey, A.; Guo, J.; Wang, Q.; Lundstrom, M.; Dai, H. Ballistic carbon nanotube field-effect transistors. *Nature (London, United Kingdom)* **2003,** *424* (6949), 654-657.

14. Dresselhaus, M. S.; Endo, M. Relation of carbon nanotubes to other carbon materials. 80 ed.; 2001; pp 11-28.

15. Dekker, C. Carbon nanotubes as molecular quantum wires. *Physics Today* **1999,** *52* (5), 22-28.

16. Kam, N. W. S.; O'Connell, M.; Wisdom, J. A.; Dai, H. Carbon nanotubes as multifunctional biological transporters and near-infrared agents for selective cancer cell destruction. *Proceedings of the National Academy of Sciences of the United States of America* **2005,** *102* (33), 11600-11605.

17. Holt, J. K.; Park, H. G.; Wang, Y.; Stadermann, M.; Artyukhin, A. B.; Grigoropoulos, C. P.; Noy, A.; Bakajin, O. Fast Mass Transport Through Sub-2-Nanometer Carbon Nanotubes. *Science (Washington, DC, United States)* **2006,** *312* (5776), 1034-1037.

18. Fornasiero, F.; Park, H. G.; Holt, J. K.; Stadermann, M.; Grigoropoulos, C. P.; Noy, A.; Bakajin, O. Ion exclusion by sub-2-nm carbon nanotube pores. *Proceedings of the National Academy of Sciences of the United States of America, Early Edition* **2008,** (June 6 2008), 1-6, 6.

19. Treacy, M. M. J.; Ebbesen, T. W.; Gibson, J. M. Exceptionally high Young's modulus observed for individual carbon nanotubes. *Nature (London)* **1996,** *381* (6584), 678-680.

20. Yu, M. F.; Files, B. S.; Arepalli, S.; Ruoff, R. S. Tensile loading of ropes of single wall carbon nanotubes and their mechanical properties. *Physical Review Letters* **2000,** *84* (24), 5552-5555.

21. Cheng, M.; Chen, W.; Weerasooriya, T. Mechanical Properties of Kevlar KM2 Single Fiber. *Journal of Engineering Materials and Technology* **2005,** *127* (2), 197-203.

22. Yue, C. Y.; Sui, G. X.; Looi, H. C. Effects of heat treatment on the mechanical properties of Kevlar-29 fibre. *Composites Science and Technology* **2000,** *60* (3), 421-427.

23. Hindeleh, A. M.; Abdo, S. Relationship between crystalline structure and mechanical properties in Kevlar 49 fibers. *Polymer Communications* **1989,** *30* (6), 184-186.

24. Wagner, H. D.; Vaia, R. A. Nanocomposites: issues at the interface. *Materials Today (Oxford, United Kingdom)* **2004,** *7* (11), 38-42.

25. Van Lier, G.; Van Alsenoy, C.; Van Doren, V.; Geerlings, P. Ab initio study of the elastic properties of single-walled carbon nanotubes and graphene. *Chemical Physics Letters* **2000,** *326* (1,2), 181-185.

26. Sturcova, A.; Davies, G. R.; Eichhorn, S. J. Elastic Modulus and Stress-Transfer Properties of Tunicate Cellulose Whiskers. *Biomacromolecules* **2005,** *6* (2), 1055-1061.

27. Manevitch, O. L.; Rutledge, G. C. Elastic Properties of a Single Lamella of Montmorillonite by Molecular Dynamics Simulation. *Journal of Physical Chemistry B* **2004,** *108* (4), 1428-1435.

28. Balazs, A. C.; Emrick, T.; Russell, T. P. Nanoparticle Polymer Composites: Where Two Small Worlds Meet. *Science (Washington, DC, United States)* **2006,** *314* (5802), 1107-1110.

29. Usuki, A.; Kojima, Y.; Kawasumi, M.; Okada, A.; Fukushima, Y.; Kurauchi, T.; Kamigaito, O. Synthesis of nylon 6-clay hybrid. *Journal of Materials Research* **1993,** *8* (5), 1179-1184.

30. Yu, M. F.; Lourie, O.; Dyer, M. J.; Moloni, K.; Kelly, T. F.; Ruoff, R. S. Strength and breaking mechanism of multiwalled carbon nanotubes under tensile load. *Science (Washington, D. C.)* **2000,** *287* (5453), 637-640.

31. Ajayan, P. M.; Stephan, O.; Colliex, C.; Trauth, D. Aligned carbon nanotube arrays formed by cutting a polymer resin-nanotube composite. *Science (Washington, DC, United States)* **1994,** *265* (5176), 1212-1214.

32. Suhr, J.; Koratkar, N.; Keblinski, P.; Ajayan, P. Viscoelasticity in carbon nanotube composites. *Nature Materials* **2005,** *4* (2), 134-137.

33. Ago, H.; Petritsch, K.; Shaffer, M. S. P.; Windle, A. H.; Friend, R. H. Composites of carbon nanotubes and conjugated polymers for photovoltaic devices. *Advanced Materials (Weinheim, Germany)* **1999,** *11* (15), 1281-1285.

34. Ericson, L. M.; Fan, H.; Peng, H.; Davis, V. A.; Zhou, W.; Sulpizio, J.; Wang, Y.; Booker, R.; Vavro, J.; Guthy, C.; Parra-Vasquez, A. N.; Kim, M. J.; Ramesh, S.; Saini, R. K.; Kittrell, C.; Lavin, G.; Schmidt, H.; Adams, W. W.; Billups, W. E.; Pasquali, M.; Hwang, W. F.; Hauge, R. H.; Fischer, J. E.; Smalley, R. E. Macroscopic, Neat, Single-Walled Carbon Nanotube Fibers. Science (Washington, DC, United States) 305[5689], 1447-1450. 2004. Ref Type: Journal (Full)

35. Stankovich, S.; Dikin, D. A.; Dommett, G. H. B.; Kohlhaas, K. M.; Zimney, E. J.; Stach, E. A.; Piner, R. D.; Nguyen, S. T.; Ruoff, R. S. Graphene-based composite materials. *Nature (London, United Kingdom)* **2006,** *442* (7100), 282-286.

36. Breuer, O.; Sundararaj, U. Big returns from small fibers: A review of polymer/carbon nanotube composites. *Polymer Composites* **2004,** *25* (6), 630-645.

37. Dalton, A. B.; Collins, S.; Munoz, E.; Razal, J. M.; Ebron, V. H.; Ferraris, J. P.; Coleman, J. N.; Kim, B. G.; Baughman, R. H. Super-tough carbon-nanotube fibers. *Nature (London, United Kingdom)* **2003,** *423* (6941), 703.

38. Moniruzzaman, M.; Chattopadhay, J.; Billups, W. E.; Winey, K. I. Tuning the Mechanical Properties of SWNT/Nylon 6,10 Composites with Flexible Spacers at the Interface. *Nano Letters* **2007,** *7* (5), 1178-1185.

39. Kojima, Y.; Usuki, A.; Kawasumi, M.; Okada, A.; Fukushima, Y.; Kurauchi, T.; Kamigaito, O. Mechanical properties of nylon 6-clay hybrid. *Journal of Materials Research* **1993,** *8* (5), 1185-1189.

40. Liff, S. M.; Kumar, N.; McKinley, G. H. High-performance elastomeric nanocomposites via solvent-exchange processing. *Nature Materials* **2007,** *6* (1), 76-83.

41. Iler, R. K.; Colloid, J. Multilayers of colloidal particles. *Interface Sci.* **1966,** *21* (6), 569-594.

42. Golander, C. G.; Arwin, H.; Eriksson, J. C.; Lundstrom, I.; Larsson, R. Heparin surface film formation through adsorption of colloidal particles studied by ellipsometry and scanning electron microscopy. *Colloids and Surfaces* **1982,** *5* (1), 1-16.

43. Tredgold, R. H.; Winter, C. S.; El-Badawy, Z. I. Multiple monolayer adsorption - a new technique for the production of noncentrosymmetric films. *Electronics Letters* **1985,** *21* (13), 554-555.

44. Decher, G.; Hong, J. D. Buildup of ultrathin multilayer films by a self-assembly process: II. Consecutive adsorption of anionic and cationic bipolar amphiphiles and polyelectrolytes on charged surfaces. *Berichte der Bunsen-Gesellschaft* **1991,** *95* (11), 1430-1434.

45. Decher, G.; Hong, J. D. Buildup of ultrathin multilayer films by a self-assembly process. 1. Consecutive adsorption of anionic and cationic bipolar amphiphiles on charged surfaces. *Makromolekulare Chemie, Macromolecular Symposia* **1991,** *46* (Eur. Conf. Organ. Org. Thin Films, 3rd, 1990), 321-327.

46. Lvov, Y.; Decher, G.; Moehwald, H. Assembly, structural characterization, and thermal behavior of layer-by-layer deposited ultrathin films of poly(vinyl sulfate) and poly(allylamine). *Langmuir* **1993,** *9* (2), 481-486.

47. Lvov, Y.; Haas, H.; Decher, G.; Moehwald, H.; Kalachev, A. Assembly of polyelectrolyte molecular films onto plasma-treated glass. *Journal of Physical Chemistry* **1993,** *97* (49), 12835-12841.

48. Decher, G. Fuzzy nanoassemblies: toward layered polymeric multicomposites. *Science (Washington, D. C.)* **1997,** *277* (5330), 1232-1237.

49. Liu, Y.; Wang, A.; Claus, R. Molecular Self-Assembly of TiO2/Polymer Nanocomposite Films. *Journal of Physical Chemistry B* **1997,** *101* (8), 1385-1388.

50. Liu, Y.; Wang, A.; Claus, R. O. Layer-by-layer electrostatic self-assembly of nanoscale Fe3O4 particles and polyimide precursor on silicon and silica surfaces. *Applied Physics Letters* **1997,** *71* (16), 2265-2267.

51. Lenahan, K. M.; Wang, Y. X.; Liu, Y. J.; Claus, R. O.; Heflin, J. R.; Marciu, D.; Figura, C. Novel polymer dyes for nonlinear optical applications using ionic self-assembled monolayer technology. *Advanced Materials (Weinheim, Germany)* **1998,** *10* (11), 853-855.

52. Jiang, X.; Hammond, P. T. Selective Deposition in Layer-by-Layer Assembly: Functional Graft Copolymers as Molecular Templates. *Langmuir* **2000,** *16* (22), 8501-8509.

53. Clark, S. L.; Hammond, P. T. Engineering the microfabrication of layer-by-layer thin films. *Advanced Materials (Weinheim, Germany)* **1998,** *10* (18), 1515-1519.

54. Ingersoll, D.; Kulesza, P. J.; Faulkner, L. R. Polyoxometallate-based layered composite films on electrodes. Preparation through alternate immersions in modification solutions. *Journal of the Electrochemical Society* **1994,** *141* (1), 140-147.

55. Kotov, N. A.; Dekany, I.; Fendler, J. H. Layer-by-Layer Self-Assembly of Polyelectrolyte-Semiconductor Nanoparticle Composite Films. *Journal of Physical Chemistry* **1995,** *99* (35), 13065-13069.

56. Mamedov, A. A.; Kotov, N. A.; Prato, M.; Guldi, D. M.; Wicksted, J. P.; Hirsch, A. Molecular design of strong single-wall carbon nanotube/polyelectrolyte multilayer composites. *Nature Materials* **2002,** *1* (3), 190-194.

57. Keller, S. W.; Kim, H. N.; Mallouk, T. E. Layer-by-Layer Assembly of Intercalation Compounds and Heterostructures on Surfaces: Toward Molecular \"Beaker\" Epitaxy. *Journal of the American Chemical Society* **1994,** *116* (19), 8817-8818.

58. Kleinfeld, E. R.; Ferguson, G. S. Stepwise formation of multilayered nanostructural films from macromolecular precursors. *Science (Washington, DC, United States)* **1994,** *265* (5170), 370-373.

59. Cooper, T. M.; Campbell, A. L.; Crane, R. L. Formation of polypeptide-dye multilayers by electrostatic self-assembly technique. *Langmuir* **1995,** *11* (7), 2713-2718.

60. Podsiadlo, P.; Choi, S. Y.; Shim, B.; Lee, J.; Cuddihy, M.; Kotov, N. A. Molecularly Engineered Nanocomposites: Layer-by-Layer Assembly of Cellulose Nanocrystals. *Biomacromolecules* **2005,** *6* (6), 2914-2918.

61. Podsiadlo, P.; Sui, L.; Elkasabi, Y.; Burgardt, P.; Lee, J.; Miryala, A.; Kusumaatmaja, W.; Carman, M. R.; Shtein, M.; Kieffer, J.; Lahann, J.; Kotov, N. A. Layer-by-Layer Assembled Films of Cellulose Nanowires with Antireflective Properties. *Langmuir* **2007,** *23* (15), 7901-7906.

62. He, J. A.; Valluzzi, R.; Yang, K.; Dolukhanyan, T.; Sung, C.; Kumar, J.; Tripathy, S. K.; Samuelson, L.; Balogh, L.; Tomalia, D. A. Electrostatic Multilayer Deposition of a Gold-Dendrimer Nanocomposite. *Chemistry of Materials* **1999,** *11* (11), 3268-3274.

63. Araki, K.; Wagner, M. J.; Wrighton, M. S. Layer-by-Layer Growth of Electrostatically Assembled Multilayer Porphyrin Films. *Langmuir* **1996,** *12* (22), 5393-5398.

64. Lvov, Y.; Onda, M.; Ariga, K.; Kunitake, T. Ultrathin films of charged polysaccharides assembled alternately with linear polyions. *Journal of Biomaterials Science, Polymer Edition* **1998,** *9* (4), 345-355.

65. Richert, L.; Lavalle, P.; Vautier, D.; Senger, B.; Stoltz, J. F.; Schaaf, P.; Voegel, J. C.; Picart, C. Cell Interactions with Polyelectrolyte Multilayer Films. *Biomacromolecules* **2002,** *3* (6), 1170-1178.

66. Boulmedais, F.; Ball, V.; Schwinte, P.; Frisch, B.; Schaaf, P.; Voegel, J. C. Buildup of Exponentially Growing Multilayer Polypeptide Films with Internal Secondary Structure. *Langmuir* **2003,** *19* (2), 440-445.

67. Lvov, Y.; Decher, G.; Sukhorukov, G. Assembly of thin films by means of successive deposition of alternate layers of DNA and poly(allylamine). *Macromolecules* **1993,** *26* (20), 5396-5399.

68. Hong, J. D.; Lowack, K.; Schmitt, J.; Decher, G. Layer-by-layer deposited multilayer assemblies of polyelectrolytes and proteins: From ultrathin films to protein arrays. *Progress in Colloid & Polymer Science* **1993,** *93* (TRENDS IN COLLOID AN), 98-102.

69. Lvov, Y.; Ariga, K.; Kunitake, T. Layer-by-layer assembly of alternate protein/polyion ultrathin films. *Chemistry Letters* **1994,** (12), 2323-2326.

70. Yoo, P. J.; Nam, K. T.; Qi, J.; Lee, S. K.; Park, J.; Belcher, A. M.; Hammond, P. T. Spontaneous assembly of viruses on multilayered polymer surfaces. *Nature Materials* **2006,** *5* (3), 234-240.

71. Tang, Z.; Wang, Y.; Podsiadlo, P.; Kotov, N. A. Biomedical applications of layer-by-layer assembly: from biomimetics to tissue engineering. *Advanced Materials (Weinheim, Germany)* **2006,** *18* (24), 3203-3224.

72. Zhai, L.; Cebeci, F. C.; Cohen, R. E.; Rubner, M. F. Stable Superhydrophobic Coatings from Polyelectrolyte Multilayers. *Nano Letters* **2004,** *4* (7), 1349-1353.

73. Ellis, D. L.; Zakin, M. R.; Bernstein, L. S.; Rubner, M. F. Conductive Polymer Films as Ultrasensitive Chemical Sensors for Hydrazine and Monomethylhydrazine Vapor. *Analytical Chemistry* **1996,** *68* (5), 817-822.

74. Constantine, C. A.; Mello, S., V; Dupont, A.; Cao, X.; Santos, D., Jr.; Oliveira, O. N., Jr.; Strixino, F. T.; Pereira, E. C.; Cheng, T.; Defrank, J. J.; Leblanc, R. M. Layer-by-layer self-assembled chitosan/poly(thiophene-3-acetic acid) and organophosphorus hydrolase multilayers. *Journal of the American Chemical Society* **2003,** *125* (7), 1805-1809.

75. Koktysh, D. S.; Liang, X.; Yun, B. G.; Pastoriza-Santos, I.; Matts, R. L.; Giersig, M.; Serra-Rodriguez, C.; Liz-Marzan, L. M.; Kotov, N. A. Biomaterials by design: Layer-by-layer assembled ion-selective and biocompatible films of TiO2 nanoshells for neurochemical monitoring. *Advanced Functional Materials* **2002,** *12* (4), 255-265.

76. Wood, K. C.; Chuang, H. F.; Batten, R. D.; Lynn, D. M.; Hammond, P. T. Controlling interlayer diffusion to achieve sustained, multiagent delivery from layer-by-layer thin films. *Proceedings of the National Academy of Sciences of the United States of America* **2006,** *103* (27), 10207-10212.

77. Jewell, C. M.; Zhang, J.; Fredin, N. J.; Lynn, D. M. Multilayered polyelectrolyte films promote the direct and localized delivery of DNA to cells. *Journal of Controlled Release* **2005,** *106* (1-2), 214-223.

78. Wood, K.; Zacharia, N. S.; Schimidt, D. J.; Wrightman, S. N.; Andaya, B. J.; Hammond, P. T. Electroactive controlled release thin films. *Proceedings of the National Academy of Sciences of the United States of America* **2008,** *105* (7), 2280-2285.

79. Lee, J. S.; Cho, J.; Lee, C.; Kim, I.; Park, J.; Kim, Y. M.; Shin, H.; Lee, J.; Caruso, F. Layer-by-layer assembled charge-trap memory devices with adjustable electronic properties. *Nature Nanotechnology* **2007,** *2* (12), 790-795.

80. Hiller, J.; Mendelsohn, J. D.; Rubner, M. F. Reversibly erasable nanoporous anti-reflection coatings from polyelectrolyte multilayers. *Nature Materials* **2002,** *1* (1), 59-63.

81. DeLongchamp, D. M.; Hammond, P. T. High-contrast electrochromism and controllable dissolution of assembled Prussian blue/polymer nanocomposites. *Advanced Functional Materials* **2004,** *14* (3), 224-232.

82. Moriguchi, I.; Fendler, J. H. Characterization and Electrochromic Properties of Ultrathin Films Self-Assembled from Poly(diallyldimethylammonium) Chloride and Sodium Decatungstate. *Chemistry of Materials* **1998,** *10* (8), 2205-2211.

83. Heuberger, R.; Sukhorukov, G.; Voeroes, J.; Textor, M.; Moehwald, H. Biofunctional polyelectrolyte multilayers and microcapsules: control of non-specific and bio-specific protein adsorption. *Advanced Functional Materials* **2005,** *15* (3), 357-366.

84. Tokuhisa, H.; Hammond, P. T. Solid-state photovoltaic thin films using TiO2, organic dyes, and layer-by-layer polyelectrolyte nanocomposites. *Advanced Functional Materials* **2003,** *13* (11), 831-839.

85. Michel, M.; Taylor, A.; Sekol, R.; Podsiadlo, P.; Ho, P.; Kotov, N.; Thompson, L. High-performance nanostructured membrane electrode assemblies for fuel cells made by layer-by-layer assembly of carbon nanocolloids. *Advanced Materials (Weinheim, Germany)* **2007,** *19* (22), 3859-3864.

86. Zhang, J.; Senger, B.; Vautier, D.; Picart, C.; Schaaf, P.; Voegel, J. C.; Lavalle, P. Natural polyelectrolyte films based on layer-by layer deposition of collagen and hyaluronic acid. *Biomaterials* **2005,** *26* (16), 3353-3361.

87. Zhai, L.; Berg, M. C.; Cebeci, F. C.; Kim, Y.; Milwid, J. M.; Rubner, M. F.; Cohen, R. E. Patterned Superhydrophobic Surfaces: Toward a Synthetic Mimic of the Namib Desert Beetle. *Nano Letters* **2006,** *6* (6), 1213-1217.

88. Hammond, P. T. Form and function in multilayer assembly: New applications at the nanoscale. *Advanced Materials (Weinheim, Germany)* **2004,** *16* (15), 1271-1293.

89. Decher, G.; Maclennan, J.; Reibel, J.; Sohling, U. Highly ordered ultrathin LC multilayer films on solid substrates. *Advanced Materials (Weinheim, Germany)* **1991,** *3* (12), 617-619.

90. Decher, G.; Lvov, Y.; Schmitt, J. Proof of multilayer structural organization in self-assembled polycation-polyanion molecular films. *Thin Solid Films* **1994,** *244* (1-2), 772-777.

91. Loesche, M.; Schmitt, J.; Decher, G.; Bouwman, W. G.; Kjaer, K. Detailed Structure of Molecularly Thin Polyelectrolyte Multilayer Films on Solid Substrates as Revealed by Neutron Reflectometry. *Macromolecules* **1998,** *31* (25), 8893-8906.

92. Dubas, S. T.; Schlenoff, J. B. Factors Controlling the Growth of Polyelectrolyte Multilayers. *Macromolecules* **1999,** *32* (24), 8153-8160.

93. Dubas, S. T.; Schlenoff, J. B. Swelling and Smoothing of Polyelectrolyte Multilayers by Salt. *Langmuir* **2001,** *17* (25), 7725-7727.

94. Schmitt, J.; Gruenewald, T.; Decher, G.; Pershan, P. S.; Kjaer, K.; Loesche, M. Internal structure of layer-by-layer adsorbed polyelectrolyte films: a neutron and x-ray reflectivity study. *Macromolecules* **1993,** *26* (25), 7058-7063.

95. Loesche, M.; Schmitt, J.; Bouwman, W. G.; Kjaer, K.; Decher, G. Internal structure of molecularly layered polyelectrolyte interface films. *Book of Abstracts, 212th ACS National Meeting, Orlando, FL, August 25-29* **1996,** COLL-177.

96. Kellogg, G. J.; Mayes, A. M.; Stockton, W. B.; Ferreira, M.; Rubner, M. F.; Satija, S. K. Neutron Reflectivity Investigations of Self-Assembled Conjugated Polyion Multilayers. *Langmuir* **1996,** *12* (21), 5109-5113.

97. Rodriguez, L. N. J.; De Paul, S. M.; Barrett, C. J.; Reven, L.; Spiess, H. W. Fast magic-angle spinning and double-quantum 1H solid-state NMR spectroscopy of polyelectrolyte multilayers. *Advanced Materials (Weinheim, Germany)* **2000,** *12* (24), 1934-1938.

98. Baur, J. W.; Rubner, M. F.; Reynolds, J. R.; Kim, S. Foerster energy transfer studies of polyelectrolyte heterostructures containing conjugated polymers: A means to estimate layer interpenetration. *Langmuir* **1999,** *15* (19), 6460-6469.

99. Stockton, W. B.; Rubner, M. F. Molecular-Level Processing of Conjugated Polymers. 4. Layer-by-Layer Manipulation of Polyaniline via Hydrogen-Bonding Interactions. *Macromolecules* **1997,** *30* (9), 2717-2725.

100. Shimazaki, Y.; Mitsuishi, M.; Ito, S.; Yamamoto, M. Preparation and Characterization of the Layer-by-Layer Deposited Ultrathin Film Based on the Charge-Transfer Interaction in Organic Solvents. *Langmuir* **1998,** *14* (10), 2768-2773.

101. Caruso, F.; Niikura, K.; Furlong, D. N.; Okahata, Y. Assembly of Alternating Polyelectrolyte and Protein Multilayer Films for Immunosensing. *Langmuir* **1997,** *13* (13), 3427-3433.

102. Anzai, J. i.; Nishimura, M. Layer-by-layer deposition of avidin and polymers on a solid surface to prepare thin films: significant effects of molecular geometry of the polymers on the deposition behavior. *Journal of the Chemical Society, Perkin Transactions 2: Physical Organic Chemistry* **1997,** (10), 1887-1889.

103. Anzai, J. i.; Kobayashi, Y.; Nakamura, N.; Nishimura, M.; Hoshi, T. Layer-by-Layer Construction of Multilayer Thin Films Composed of Avidin and Biotin-Labeled Poly(amine)s. *Langmuir* **1999,** *15* (1), 221-226.

104. Cassier, T.; Lowack, K.; Decher, G. Layer-by-layer assembled protein/polymer hybrid films: nanoconstruction via specific recognition. *Supramolecular Science* **1998,** *5* (3-4), 309-315.

105. Elbert, D. L.; Herbert, C. B.; Hubbell, J. A. Thin Polymer Layers Formed by Polyelectrolyte Multilayer Techniques on Biological Surfaces. *Langmuir* **1999,** *15* (16), 5355-5362.

106. Ruths, J.; Essler, F.; Decher, G.; Riegler, H. Polyelectrolytes I: Polyanion/Polycation Multilayers at the Air/Monolayer/Water Interface as Elements for Quantitative Polymer Adsorption Studies and Preparation of Hetero-superlattices on Solid Surfaces. *Langmuir* **2000,** *16* (23), 8871-8878.

107. Pardo-Yissar, V.; Katz, E.; Lioubashevski, O.; Willner, I. Layered Polyelectrolyte Films on Au Electrodes: Characterization of Electron-Transfer Features at the Charged Polymer Interface and Application for Selective Redox Reactions. *Langmuir* **2001,** *17* (4), 1110-1118.

108. Picart, C.; Lavalle, P.; Hubert, P.; Cuisinier, F. J. G.; Decher, G.; Schaaf, P.; Voegel, J. C. Buildup Mechanism for Poly(L-lysine)/Hyaluronic Acid Films onto a Solid Surface. *Langmuir* **2001,** *17* (23), 7414-7424.

109. Picart, C.; Mutterer, J.; Richert, L.; Luo, Y.; Prestwich, G. D.; Schaaf, P.; Voegel, J. C.; Lavalle, P. Molecular basis for the explanation of the exponential growth of polyelectrolyte multilayers. *Proceedings of the National Academy of Sciences of the United States of America* **2002,** *99* (20), 12531-12535.

110. Lavalle, P.; Gergely, C.; Cuisinier, F. J. G.; Decher, G.; Schaaf, P.; Voegel, J. C.; Picart, C. Comparison of the Structure of Polyelectrolyte Multilayer Films Exhibiting a Linear and an Exponential Growth Regime: An in Situ Atomic Force Microscopy Study. *Macromolecules* **2002,** *35* (11), 4458-4465.

111. Lavalle, P.; Picart, C.; Mutterer, J.; Gergely, C.; Reiss, H.; Voegel, J. C.; Senger, B.; Schaaf, P. Modeling the Buildup of Polyelectrolyte Multilayer Films Having Exponential Growth. *Journal of Physical Chemistry B* **2004,** *108* (2), 635-648.

112. Lavalle, P.; Vivet, V.; Jessel, N.; Decher, G.; Voegel, J. C.; Mesini, P. J.; Schaaf, P. Direct Evidence for Vertical Diffusion and Exchange Processes of Polyanions and Polycations in Polyelectrolyte Multilayer Films. *Macromolecules* **2004,** *37* (3), 1159-1162.

113. Garza, J. M.; Schaaf, P.; Muller, S.; Ball, V.; Stoltz, J. F.; Voegel, J. C.; Lavalle, P. Multicompartment films made of alternate polyelectrolyte multilayers of exponential and linear growth. *Langmuir* **2004,** *20* (17), 7298-7302.

114. Garza, J. M.; Jessel, N.; Ladam, G.; Dupray, V.; Muller, S.; Stoltz, J. F.; Schaaf, P.; Voegel, J. C.; Lavalle, P. Polyelectrolyte Multilayers and Degradable Polymer Layers as Multicompartment Films. *Langmuir* **2005,** *21* (26), 12372-12377.

115. Huebsch, E.; Ball, V.; Senger, B.; Decher, G.; Voegel, J. C.; Schaaf, P. Controlling the Growth Regime of Polyelectrolyte Multilayer Films: Changing

from Exponential to Linear Growth by Adjusting the Composition of Polyelectrolyte Mixtures. *Langmuir* **2004,** *20* (5), 1980-1985.

116. Porcel, C.; Lavalle, P.; Ball, V.; Decher, G.; Senger, B.; Voegel, J. C.; Schaaf, P. From Exponential to Linear Growth in Polyelectrolyte Multilayers. *Langmuir* **2006,** *22* (9), 4376-4383.

117. Ball, V.; Huebsch, E.; Schweiss, R.; Voegel, J. C.; Schaaf, P.; Knoll, W. Interactions between Multivalent Ions and Exponentially Growing Multilayers: Dissolution and Exchange Processes. *Langmuir* **2005,** *21* (18), 8526-8531.

118. Huebsch, E.; Fleith, G.; Fatisson, J.; Labbe, P.; Voegel, J. C.; Schaaf, P.; Ball, V. Multivalent Ion/Polyelectrolyte Exchange Processes in Exponentially Growing Multilayers. *Langmuir* **2005,** *21* (8), 3664-3669.

119. Kujawa, P.; Moraille, P.; Sanchez, J.; Badia, A.; Winnik, F. M. Effect of molecular weight on the exponential growth and morphology of hyaluronan/chitosan multilayers: a surface plasmon resonance spectroscopy and atomic force microscopy investigation. *Journal of the American Chemical Society* **2005,** *127* (25), 9224-9234.

120. Porcel, C.; Lavalle, P.; Decher, G.; Senger, B.; Voegel, J. C.; Schaaf, P. Influence of the Polyelectrolyte Molecular Weight on Exponentially Growing Multilayer Films in the Linear Regime. *Langmuir* **2007,** *23* (4), 1898-1904.

121. Nam, K. T.; Kim, D. W.; Yoo, P. J.; Chiang, C. Y.; Meethong, N.; Hammond, P. T.; Chiang, Y. M.; Belcher, A. M. Virus-Enabled Synthesis and Assembly of Nanowires for Lithium Ion Battery Electrodes. *Science (Washington, DC, United States)* **2006,** *312* (5775), 885-888.

122. Eriksson, M.; Notley, S. M.; Wagberg, L. The influence on paper strength properties when building multilayers of weak polyelectrolytes onto wood fibers. *Journal of Colloid and Interface Science* **2005,** *292* (1), 38-45.

123. Vodouhe, C.; Le Guen, E.; Garza, J. M.; Francius, G.; Dejugnat, C.; Ogier, J.; Schaaf, P.; Voegel, J. C.; Lavalle, P. Control of drug accessibility on functional polyelectrolyte multilayer films. *Biomaterials* **2006,** *27* (22), 4149-4156.

124. Jessel, N.; Oulad-Abdelghani, M.; Meyer, F.; Lavalle, P.; Haikel, Y.; Schaaf, P.; Voegel, J. C. Multiple and time-scheduled in situ DNA delivery mediated by b-cyclodextrin embedded in a polyelectrolyte multilayer. *Proceedings of the National Academy of Sciences of the United States of America* **2006,** *103* (23), 8618-8621.

125. Boulmedais, F.; Tang, C. S.; Keller, B.; Voros, J. Controlled electrodissolution of polyelectrolyte multilayers: a platform technology towards the surface-initiated delivery of drugs. *Advanced Functional Materials* **2006,** *16* (1), 63-70.

126. Dimitrova, M.; Arntz, Y.; Lavalle, P.; Meyer, F.; Wolf, M.; Schuster, C.; Haikel, Y.; Voegel, J. C.; Ogier, J. Adenoviral gene delivery from multilayered polyelectrolyte architectures. *Advanced Functional Materials* **2007,** *17* (2), 233-245.

127. Ji, J.; Fu, J.; Shen, J. Fabrication of a superhydrophobic surface from the amplified exponential growth of a multilayer. *Advanced Materials (Weinheim, Germany)* **2006,** *18* (11), 1441-1444.

128. Mertz, D.; Hemmerle, J.; Mutterer, J.; Ollivier, S.; Voegel, J. C.; Schaaf, P.; Lavalle, P. Mechanically Responding Nanovalves Based on Polyelectrolyte Multilayers. *Nano Letters* **2007,** *7* (3), 657-662.

129. Pastoriza-Santos, I.; Koktysh, D. S.; Mamedov, A. A.; Giersig, M.; Kotov, N. A.; Liz-Marzan, L. M. One-pot synthesis of Ag@TiO2 core-shell nanoparticles and their layer-by-layer assembly. *Langmuir* **2000,** *16* (6), 2731-2735.

130. Kleinfeld, E. R.; Ferguson, G. S. Healing of Defects in the Stepwise Formation of Polymer/Silicate Multilayer Films. *Chemistry of Materials* **1996,** *8* (8), 1575-1578.

131. Lvov, Y.; Ariga, K.; Ichinose, I.; Kunitake, T. Formation of Ultrathin Multilayer and Hydrated Gel from Montmorillonite and Linear Polycations. *Langmuir* **1996,** *12* (12), 3038-3044.

132. Kotov, N. A.; Haraszti, T.; Turi, L.; Zavala, G.; Geer, R. E.; Dekany, I.; Fendler, J. H. Mechanism of and Defect Formation in the Self-Assembly of Polymeric Polycation-Montmorillonite Ultrathin Films. *Journal of the American Chemical Society* **1997,** *119* (29), 6821-6832.

133. Cassagneau, T.; Fendler, J. H. Preparation and Layer-by-Layer Self-Assembly of Silver Nanoparticles Capped by Graphite Oxide Nanosheets. *Journal of Physical Chemistry B* **1999,** *103* (11), 1789-1793.

134. McKenzie, K. J.; Marken, F.; Hyde, M.; Compton, R. G. Nanoporous iron oxide membranes: layer-by-layer deposition and electrochemical characterisation of processes within nanopores. *New Journal of Chemistry* **2002,** *26* (5), 625-629.

135. Tang, Z.; Kotov, N. A.; Magonov, S.; Ozturk, B. Nanostructured artificial nacre. *Nature Materials* **2003,** *2* (6), 413-418.

136. Podsiadlo, P.; Liu, Z.; Paterson, D.; Messersmith, P. B.; Kotov, N. A. Fusion of seashell nacre and marine bioadhesive analogs: high-strength nanocomposite by layer-by-layer assembly of clay and L-3,4-dihydroxyphenylalanine polymer. *Advanced Materials (Weinheim, Germany)* **2007,** *19* (7), 949-955.

137. Podsiadlo, P.; Tang, Z.; Shim, B. S.; Kotov, N. A. Counterintuitive Effect of Molecular Strength and Role of Molecular Rigidity on Mechanical Properties of

Layer-by-Layer Assembled Nanocomposites. *Nano Letters* **2007,** *7* (5), 1224-1231.

138. Podsiadlo, P.; Kaushik, A. K.; Arruda, E. M.; Waas, A. M.; Shim, B. S.; Xu, J.; Nandivada, H.; Pumplin, B. G.; Lahann, J.; Ramamoorthy, A.; Kotov, N. A. Ultrastrong and Stiff Layered Polymer Nanocomposites. *Science (Washington, DC, United States)* **2007,** *318* (5847), 80-83.

139. Mamedov, A. A.; Kotov, N. A. Free-Standing Layer-by-Layer Assembled Films of Magnetite Nanoparticles. *Langmuir* **2000,** *16* (13), 5530-5533.

140. Podsiadlo, P.; Paternel, S.; Rouillard, J. M.; Zhang, Z.; Lee, J.; Lee, J. W.; Gulari, E.; Kotov, N. A. Layer-by-Layer Assembly of Nacre-like Nanostructured Composites with Antimicrobial Properties. *Langmuir* **2005,** *21* (25), 11915-11921.

141. Malikova, N.; Pastoriza-Santos, I.; Schierhorn, M.; Kotov, N. A.; Liz-Marzan, L. M. Layer-by-Layer Assembled Mixed Spherical and Planar Gold Nanoparticles: Control of Interparticle Interactions. *Langmuir* **2002,** *18* (9), 3694-3697.

142. Lvov, Y.; Ariga, K.; Ichinose, I.; Kunitake, T. Assembly of Multicomponent Protein Films by Means of Electrostatic Layer-by-Layer Adsorption. *Journal of the American Chemical Society* **1995,** *117* (22), 6117-6123.

143. Ku, B. C.; Froio, D.; Steeves, D.; Kim, D. W.; Ahn, H.; Ratto, J. A.; Blumstein, A.; Kumar, J.; Samuelson, L. A. Cross-linked Multilayer Polymer-Clay Nanocomposites and Permeability Properties. *Journal of Macromolecular Science, Pure and Applied Chemistry* **2004,** *A41* (12), 1401-1410.

144. Kim, D. W.; Choi, H. S.; Lee, C.; Blumstein, A.; Kang, Y. Investigation on methanol permeability of Nafion modified by self-assembled clay-nanocomposite multilayers. *Electrochimica Acta* **2004,** *50* (2-3), 659-662.

145. Guo, Z.; Shen, Y.; Zhao, F.; Wang, M.; Dong, S. Electrochemical and electrogenerated chemiluminescence of clay nanoparticles/Ru(bpy)32+ multilayer films on ITO electrodes. *Analyst (Cambridge, United Kingdom)* **2004,** *129* (7), 657-663.

146. Yamamoto, T.; Umemura, Y.; Sato, O.; Einaga, Y. Photomagnetic Co-Fe Prussian blue thin films fabricated by the modified Langmuir-Blodgett technique. *Chemistry Letters* **2004,** *33* (5), 500-501.

147. Li, Z.; Hu, N. Direct electrochemistry of heme proteins in their layer-by-layer films with clay nanoparticles. *Journal of Electroanalytical Chemistry* **2003,** *558*, 155-165.

148. Olek, M.; Ostrander, J.; Jurga, S.; Moehwald, H.; Kotov, N.; Kempa, K.; Giersig, M. Layer-by-Layer Assembled Composites from Multiwall Carbon Nanotubes with Different Morphologies. *Nano Letters* **2004,** *4* (10), 1889-1895.

149. Shim, B. S.; Starkovich, J.; Kotov, N. Multilayer composites from vapor-grown carbon nano-fibers. *Composites Science and Technology* **2006,** *66* (9), 1174-1181.

150. Loh, K. J.; Kim, J.; Lynch, J. P.; Kam, N. W. S.; Kotov, N. A. Multifunctional layer-by-layer carbon nanotube-polyelectrolyte thin films for strain and corrosion sensing. *Smart Materials and Structures* **2007,** *16* (2), 429-438.

151. Shim, B. S.; Tang, Z.; Morabito, M. P.; Agarwal, A.; Hong, H.; Kotov, N. A. Integration of Conductivity, Transparency, and Mechanical Strength into Highly Homogeneous Layer-by-Layer Composites of Single-Walled Carbon Nanotubes for Optoelectronics. *Chemistry of Materials* **2007,** *19* (23), 5467-5474.

152. Gheith, M. K.; Sinani, V. A.; Wicksted, J. P.; Matts, R. L.; Kotov, N. A. Single-walled carbon nanotube polyelectrolyte multilayers and freestanding films as a biocompatible platform for neuroprosthetic implants. *Advanced Materials (Weinheim, Germany)* **2005,** *17* (22), 2663-2670.

153. Gheith, M. K.; Pappas, T. C.; Liopo, A. V.; Sinani, V. A.; Shim, B. S.; Motamedi, M.; Wicksted, J. P.; Kotov, N. A. Stimulation of neural cells by lateral currents in conductive layer-by-layer films of single-walled carbon nanotubes. *Advanced Materials (Weinheim, Germany)* **2006,** *18* (22), 2975-2979.

154. Nepal, D.; Balasubramanian, S.; Simonian, A. L.; Davis, V. A. Strong Antimicrobial Coatings: Single-Walled Carbon Nanotubes Armored with Biopolymers. *Nano Letters* **2008,** *8* (7), 1896-1901.

155. Liao, K. S.; Wan, A.; Batteas, J. D.; Bergbreiter, D. E. Superhydrophobic Surfaces Formed Using Layer-by-Layer Self-Assembly with Aminated Multiwall Carbon Nanotubes. *Langmuir* **2008,** *24* (8), 4245-4253.

156. Jan, E.; Kotov, N. A. Successful Differentiation of Mouse Neural Stem Cells on Layer-by-Layer Assembled Single-Walled Carbon Nanotube Composite. *Nano Letters* **2007,** *7* (5), 1123-1128.

157. Lvov, Y.; Ariga, K.; Onda, M.; Ichinose, I.; Kunitake, T. Alternate Assembly of Ordered Multilayers of SiO2 and Other Nanoparticles and Polyions. *Langmuir* **1997,** *13* (23), 6195-6203.

158. Schmitt, J.; Decher, G.; Dressick, W. J.; Brandow, S. L.; Geer, R. E.; Shashidhar, R.; Calvert, J. M. Metal nanoparticle/polymer superlattice films. Fabrication and control of layer structure. *Advanced Materials (Weinheim, Germany)* **1997,** *9* (1), 61-65.

159. Mamedov, A. A.; Belov, A.; Giersig, M.; Mamedova, N. N.; Kotov, N. A. Nanorainbows. Graded semiconductor films from quantum dots. *Journal of the American Chemical Society* **2001,** *123* (31), 7738-7739.

160. Dante, S.; Hou, Z.; Risbud, S.; Stroeve, P. Nucleation of Iron Oxy-Hydroxide Nanoparticles by Layer-by-Layer Polyionic Assemblies. *Langmuir* **1999,** *15* (6), 2176-2182.

161. Dutta, A. K.; Jarero, G.; Zhang, L.; Stroeve, P. In-situ nucleation and growth of g-FeOOH nanocrystallites in polymeric supramolecular assemblies. *Chemistry of Materials* **2000,** *12* (1), 176-181.

162. Lee, D.; Rubner, M. F.; Cohen, R. E. All-Nanoparticle Thin-Film Coatings. *Nano Letters* **2006,** *6* (10), 2305-2312.

163. Bravo, J.; Zhai, L.; Wu, Z.; Cohen, R. E.; Rubner, M. F. Transparent Superhydrophobic Films Based on Silica Nanoparticles. *Langmuir* **2007,** *23* (13), 7293-7298.

164. Lee, D.; Omolade, D.; Cohen, R. E.; Rubner, M. F. pH-Dependent Structure and Properties of TiO2/SiO2 Nanoparticle Multilayer Thin Films. *Chemistry of Materials* **2007,** *19* (6), 1427-1433.

165. Lee, D.; Gemici, Z.; Rubner, M. F.; Cohen, R. E. Multilayers of oppositely charged SiO2 nanoparticles: effect of surface charge on multilayer assembly. *Langmuir* **2007,** *23* (17), 8833-8837.

166. Gemici, Z.; Shimomura, H.; Cohen, R. E.; Rubner, M. F. Hydrothermal Treatment of Nanoparticle Thin Films for Enhanced Mechanical Durability. *Langmuir* **2008,** *24* (5), 2168-2177.

167. Wu, Z.; Lee, D.; Rubner, M. F.; Cohen, R. E. Structural color in porous, superhydrophilic, and self-cleaning SiO2/TiO2 Bragg stacks. *Small* **2007,** *3* (8), 1445-1451.

Chapter II

Mechanics of “Nacre-Like” Polymer/Clay LBL Nanocomposites

A. Introduction

Nature has evolved materials which possess mechanical properties surpassing many man-made composites. Bones, teeth, spider silk, or nacre, are just a few, well-known examples of biomaterials which exhibit exceptionally high tensile strengths, hardness, or toughness.[1-6] These remarkable properties have driven scientists to study and model their architectures and compositions, from micro- to nano-scales, in the hope of developing analogous synthetic materials. Of these, probably the most studied is nacre.[4,7-15] It is composed in 95% of brittle $CaCO_3$ plates with just a few percent of organic “glue”, yet it is twice as hard and more then ~1000 times as tough as its constituent phases.[16] These exceptional mechanical properties together with macroscopic beauty and elegance of nanoscale hierarchy serve as a model for design of high performance materials.

Preparation of artificial analogs of nacre has been approached by different methods and resulting materials capture some of the characteristics of the natural composite.[17-23] In our own work, we have used a layer-by-layer assembly technique (LBL) to prepare a nanostructured analogue of nacre from inorganic, nanometer-sized sheets of Na^+-montmorillonite clay (MTM) and a polyelectrolyte, poly(diallyldimethylammonium chloride) (PDDA).[24] The structure, deformation mechanism, and mechanical properties of this material were found to be comparable with those of natural nacre and lamellar bones (tensile strength, $\sigma_{UTS} = 100 \pm 10$ MPa, and Young's modulus, $E = 11 \pm 2$ GPa). Contrary to other preparation techniques the LBL method is relatively simple and highly versatile in merging different functionalities into a single composite.[25-27] At the same time, a vast array of available assembly components allows us to generate alternative designs as a means of understanding different interactions necessary for preparation of nacre-like clay nanocomposites with application-tailored mechanical responses.

Having at hand versatility of the LBL technique and potential for use in a wide array of applications, we have set out to improve the mechanical properties of the PDDA-based composite further. In this chapter we show preparation of several different MTM-based LBL thin films as a means of systematically studying the mechanical properties of polymer-clay NCs with high volume fractions of the inorganic filler. We show several important results here: (1) under extreme confinement, the macroscale mechanical properties of the polymer matrix are less important than the molecular scale flexibility of the polymer chains and strength of binding to the inorganic phase,[28] (2) fusion of concepts from two natural materials: nacre and a marine biodhesive, can lead to high strength nacre-like NC,[29] and (3) preparation of a transparent MTM NC with record-high strength and stiffness.[30] We also demonstrate preparation of a multifunctional polymer/MTM NC for biomedical purposes, having high-strength, biocompatibility, and bacterial resistance.[25]

B. Counterintuitive Effect of Molecular Strength and Role of Molecular Rigidity on Mechanical Properties of Layer-By-Layer Assembled Nanocomposites

1. Introduction

LBL assembly has proven invaluable in its ability to merge the functionalities of multiple components. As we have discussed in Chapter I, our group has found that LBL assembly of a polyelectrolyte poly(diallyldimethylammonium chloride) (PDDA) and Na^+-montmorillonite (MTM) can lead to a free-standing film with mechanical properties similar to those of seashell nacre and lamellar bones.[24] The mechanical properties of this material (ultimate strength, $\sigma_{UTS} = 100 \pm 10$ MPa and the Young's modulus, $E = 11 \pm 2$ GPa) exceed those of many clay composites prepared by simple dispersion.

These results are encouraging for preparation of novel, high strength materials and further improvements are expected with appropriate choice of the polymer matrix. At the same time, the survey of the field also reveals two quite important issues: (1) the existing design rules[31-33] and theories are not entirely applicable to high volume fraction composites and they do not properly address the issue of interfacial interactions of components and (2) the mechanical properties of the nanocomposites are still much below those for mechanical parameters of individual nanoscale inorganic components such as nanotubes, nanowires, platelets, etc.

In an attempt at preparing an even stronger polyelectrolyte (PE)-MTM NC and with a goal of better understanding of the nanoscale and molecular mechanics of the composites, we have hypothesized that replacing PDDA with stronger PE will result in further improvement of the mechanical properties. We have chosen to work with a natural polymer, chitosan (CH), which not only possesses quite high strength ($\sigma_{UTS} \approx 110$

MPa, $E \approx 2$ GPa) in comparison to PDDA ($\sigma_{UTS} \approx 12$ MPa, $E \approx 0.2$ GPa), but also has excellent biocompatibility, biodegradability, non-toxicity and antibacterial properties.[34] At the same time, the importance of CH has already been shown in several examples of LBL films for wide variety of applications: optically active films,[35-37] biodegradable thin films,[38,39] biosensors,[40-44] electrochemical and electrochromic materials,[45-47] drug delivery multilayered capsules,[48] and coatings for improvement of cytocompatibility.[49,50]

In this study we present our results from LBL assembly of CH with MTM.[28] We show preparation of highly uniform free-standing films and mechanical strength evaluation of the resulting nanocomposite. Contrary to our expectations and theoretical predictions, the CH-MTM composite showed significantly lower mechanical properties when compared to the PDDA-MTM system, with $\sigma_{UTS} = 81$ MPa ± 12 MPa and $E = 6.1$ GPa ± 0.8 GPa. Equally surprising, the composite showed lower σ_{UTS} than the pure polymer itself. Comparison of "plane-to-plane" adhesion revealed ~4x stronger adhesion in PDDA-MTM films than in CH-MTM. In the case of PDDA-MTM system, the excellent mechanical properties were associated along with other parameters with coiled conformation of the flexible PDDA chains, which is related to the presence of sacrificial bonds in natural nacre. Apparently the flexibility of the macromolecules is also critical for efficient stress dissipation and load transfer. For the CH-MTM system, lower σ_{UTS} is attributed to high rigidity of the CH backbone which was observed in highly elongated conformation of the polymer chains by atomic force microscopy (AFM). Therefore, this study creates a criterion for future design of ultra-strong thin film composites, which may also be applicable to conventional blends.

2. Experimental Procedure

Materials

CH (MW = 6,300,000), PDDA (MW = 100,000 – 200,000, 20 wt.%), and glacial acetic acid were purchased from Sigma-Aldrich (St. Louis, MO) and used as received without further purification. 0.1% CH solutions used throughout the experiments were prepared by stirring overnight 1 g of the polymer powder in 1 L of 3 vol.% acetic acid solution in 18 MΩ*cm, pH = 5.6 de-ionized water (DI water). After preparation, pH of the solutions was further adjusted with 1 M NaOH. Na^+-Montmorillonite (MTM) was purchased from Source Clays Repository (West Lafayette, IN). 0.5 wt.% solution of PDDA was prepared by appropriately diluting the stock solution with DI water. MTM dispersion used in the experiments was prepared by dissolving 5 g of clay in DI water under vigorous stirring for 1 week prior to use. At the end of the week, MTM dispersion was left standing overnight to allow larger particles to sediment. Next day, supernatant was collected for use in experiments while precipitate was discarded. The resulting solution had pH ≈8, which was further adjusted with 1 M HCl as needed. Microscope glass slides used for CH-MTM films deposition were obtained from Fisher Scientific. Hydrogen peroxide and concentrated sulfuric acid used in the piranha cleaning solution were purchased from Sigma-Aldrich. Concentrated hydrofluoric acid (HF) was obtained from Sigma-Aldrich and a 1 vol.% HF solution used for preparation of free-standing films was prepared by appropriately diluting the stack solution with DI water. Isopropanol, A.C.S. grade, used in separation of free-standing films was purchased from Sigma-Aldrich.

Layer-by-Layer Assembly of CH-MTM Films

Prior to beginning deposition of the CH-MTM films, the microscope glass slides were cleaned by immersion in piranha solution (3:1 H_2SO_4:H_2O_2, *dangerous!*) for 1 hour, followed by thorough rinsing with DI water. In a typical sample preparation, a clean glass slide was immersed in 0.1 wt.% solution of CH, for 5 minutes, rinsed with DI water 2 x 1 minute and dried with compressed air, then immersed in 0.5 wt.% MTM dispersion, pH ~10, for 5 minutes, rinsed 2 x 1 minute, and again dried with compressed air. This procedure describes a complete deposition cycle and reversal of the surface charge to the original, negative. The cycle could then be repeated as necessary to obtain the desired number of layers. For the purpose of this work, films composed of 300 bilayers (cycles) were prepared. Preparation of the samples was accomplished using a StratoSequence IV, a robotic dipping machine, from nanoStrata Inc. (Tallahassee, FA). Free-standing films of the nanocomposites, which were subsequently used for thermo-gravimetric analysis and mechanical strength testing, were isolated with 1 vol.% HF solution (*dangerous, use care when handling!*) by utilizing a technique described in our previous publication. Briefly, a glass slide coated with a desired number of bilayers was immersed in 1 vol.% HF solution until free detachment of a free-standing film was observed. The HF solution penetrates to the interface of the glass and the film and dissolves the glass surface, thus releasing the film. As shown previously[36], HF has minimal effect on the properties of the film when detachment is performed quickly (several minutes). Prolonged exposure to HF results in degradation of the MTM platelets. With film minimally attached to the glass surface, the slide was moved to a beaker with pure DI water and thoroughly rinsed. After that, the film was placed in a dish of pure isopropanol in order to dehydrate it, which increased its stability and rigidity, allowing for safe removal without tearing. Finally, free-standing films were removed from the solvent with wafer tweezers, briefly air dried to allow solvent evaporation, and subsequently dried overnight in a drying oven at 80 ˚C.

Instrumental Analysis

LBL process was monitored using an 8453 UV-vis Chem Station spectrophotometer produced by Agilent Technologies, with data collected after each (CH-MTM) bilayer. The reference spectrum for the instrument was ambient air and collected spectra of the adsorbed material were compared to UV-vis absorbance of a fresh, piranha-cleaned glass slide. Images of CH molecules adsorbed on a silicon wafer and MTM nanoplatelets adsorbed on a CH layer were obtained using a NanoScope IIIa atomic force microscope (AFM) from Veeco Instruments (Santa Barbara, CA). For observation of single CH molecules we have diluted down the solution used in the assembly to ~0.005 wt.% and immersed a piece of silicon wafer inside for 5 min. The instrument was operated in tapping mode with silicon nitride cantilever tips (NSC16/Cr-Au, MikroMasch). Ellipsometry measurements were obtained using a BASE-160 Spectroscopic Ellipsometer produced by J. A. Woollam Co., Inc.. The instrument was calibrated to the standard silicon wafer with a thin layer of silicon dioxide and the subsequent calculations were fitted using a Cauchy's model. The samples used for ellipsometry were prepared on silicon wafers following the LBL protocol described previously. The refractive index of the multilayer was determined from a 30 nm thick sample (5 bilayers). Amount of MTM inside of the free-standing film was determined with thermo-gravimetric analyzer (TGA) Pyris 1 from PerkinElmer, with temperature ramp-up rate of 10 ºC/min while being purged with air. In-plane mechanical properties of free-standing films were analyzed by obtaining stress-strain curves with a mechanical strength tester version 100Q from TestResources Inc. (Shakopee, MN). The relative humidity in the testing facility was ~30 %. Tests were performed at a constant rate of 10 μm/s while force was recorded using a TestResources load cell with maximum capacity of 1.1 lbf (~4.9 N). The test samples were rectangular strips ~1 mm wide and 4-6 mm long. Plane-to-plane adhesion was measured using the same setup used for in-plane measurements except the bottom grip replaced by a compression platen from TestResources and the top grip with an SEM stub freely suspended on a copper wire to allow for compliance with the sample. The samples were attached flat to the larger substrate with "super glue" making sure that the glue would not spill over the sample and give false results. After drying, the top disc was attached using a much smaller drop of glue such that the adhesive would be in contact with the sample and top disc only. The surface area of the ruptured samples was measured with freeware image analysis software from National Institutes of Health, Image J. SEM images were obtained with an FEI Nova Nanolab dual-beam FIB and scanning electron microscope operated at 15 kV beam voltage. In order to avoid charging on the specimen, a few nm thick layer of gold was sputtered onto the surface of the film prior to imaging.

3. Results and Discussion

CH-MTM films were prepared following similar conditions to those of PDDA-MTM system reported previously,[24] namely 5 min immersion of a glass slide in CH solution, 2 x 1 min rinse in DI water, 1 min of air drying, and 5 min immersion in a clay dispersion followed again by rinsing and drying steps. These conditions proved to be sufficient for successful assembly giving a very uniform and homogeneous multilayer structure. AFM characterization of a single bilayer (CH + MTM layers) revealed high density of MTM platelets adsorbed parallel to the substrate on a CH surface just as in the PDDA-MTM composite presented before. (Figure 3) The AFM images also show that some of the adsorbing MTM platelets are composed of several-sheet thick stacks resulting from incomplete exfoliation of clay. Overall the surface coverage is dense and relatively uniform for a single bilayer.

Having observed chemical compatibility of CH and MTM, LBL structures were prepared on microscope glass slides and polished silicon wafers in order to characterize assembly using UV-Vis spectroscopy and ellipsometry. In typical PE-MTM assemblies, increasing number of deposited bilayers results in a linear increase of optical density. The same was observed for the CH-MTM composite (Figures 4A and 4B). We have also observed that varying the pH of MTM or CH solutions can result in substantial changes in thickness of the films. (Figures 4B and 4D) The most substantial increase in thickness was observed for low pH of MTM and/or high pH of CH solutions. This is likely to be a result of two factors: 1) Decreasing the pH of MTM results in aggregation of the platelets which increases thickness of the MTM layer. 2) The primary amino groups on CH, with pKa value of ~6.4, are sensitive to the pH of the environment, which has an effect on both adsorption of MTM and conformation of the polymer chains.[51] When using low pH of MTM solution, pH of CH layer on the glass slide is kept below its pKa value which helps in adsorption of the aggregated platelets. Increasing pH of CH de-protonates the amino groups allowing for more flexible conformation of the chains as was shown for CH adsorbing on mica and much thicker polymer layers.[51]

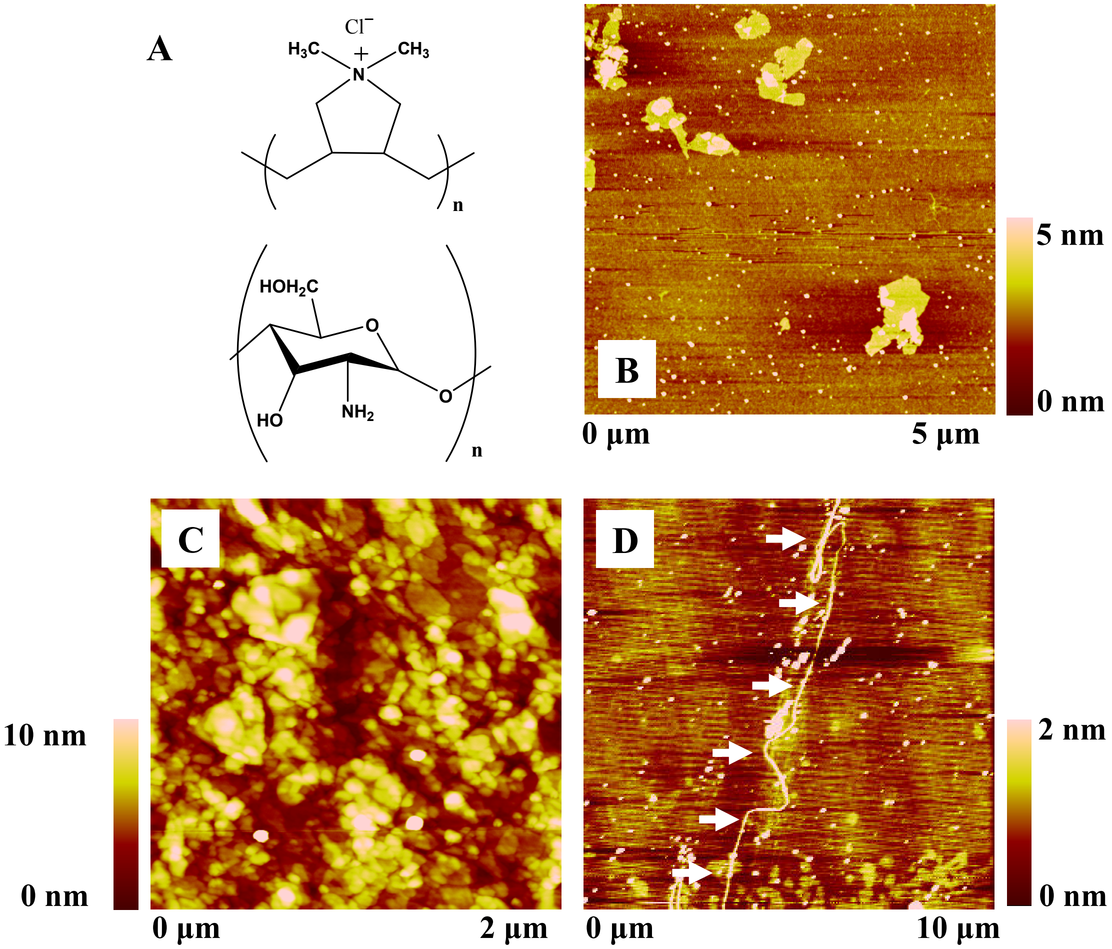

Figure 3. (A) Structure of PDDA (top) and CH (bottom) polymers. (B) AFM of a dilute solution of MTM adsorbed on a single layer of CH. (C) AFM of a single bilayer of CH+MTM adsorbed on a silicon wafer surface (height). (D) AFM image of a single chain of CH adsorbed on a silicon wafer surface.

Overall, in all of the cases, when absorbance was plotted as a function of a bilayer number for a particular wavelength, a linear growth was observed (Figure 4C). Similar results were also observed from ellipsometry. (Figure 4D) In particular, ellipsometry showed rather slow and irregular increase in thickness for low pH CH and high pH MTM. After 10 bilayers, the thickness of the film reached only ~15 nm, giving ~3 nm per bilayer on average. For high pH of CH and low pH of MTM, the thickness of the composite increased linearly at ~10 nm per bilayer.

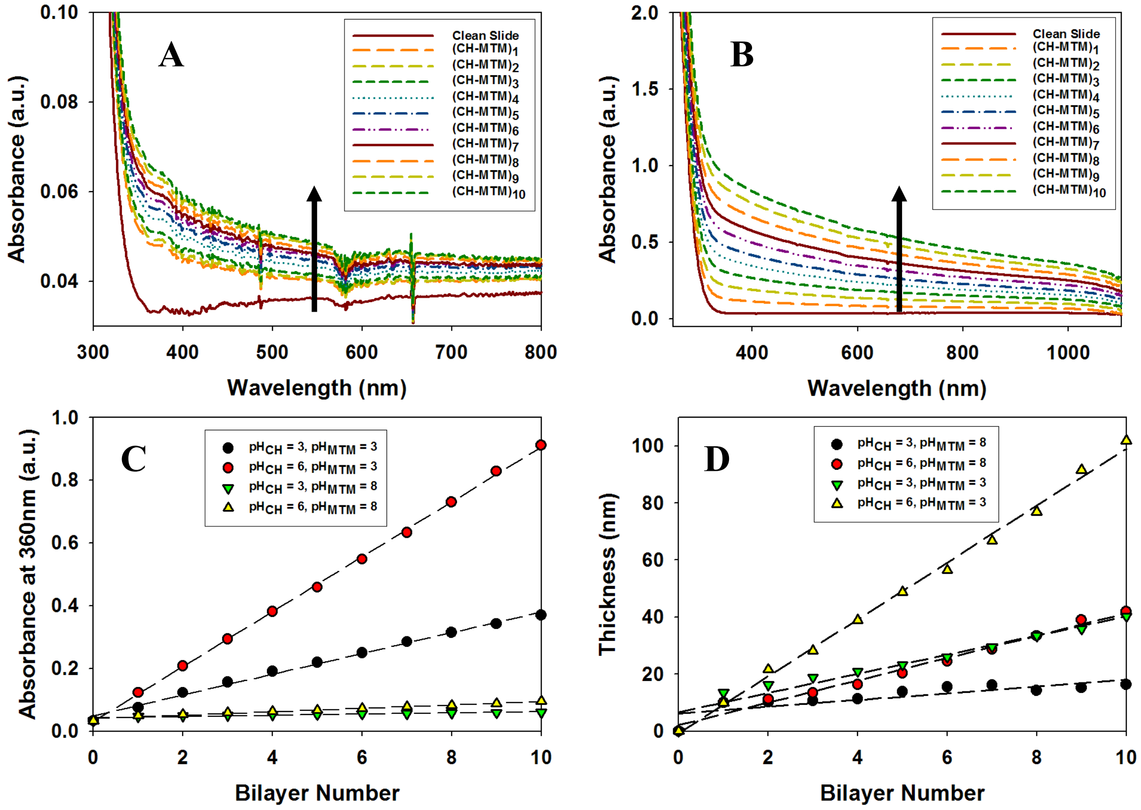

Figure 4. (A) Compilation of UV-Vis absorbance spectra for CH-MTM assembly for the first 10 bilayers with pH = 3 and pH = 8 of the two components, respectively. (B) Compilation of UV-Vis spectra for pH = 6 and pH = 3 of CH and MTM, respectively. (C) Linear regressions of absorbance vs. bilayer number for CH-MTM assembled with indicated pH conditions. (D) Ellipsometry results for CH-MTM assembly under indicated pH conditions.

For proper comparison with PDDA-MTM, CH-MTM films were prepared using the same conditions as used for the former composite: pH = 3 for CH and pH = 8 for MTM (as dissolved). Several samples of 300-bilayer films were prepared on microscope glass slides, dried at 60 ˚C for 1 hour and then were detached from the surface using a HF method described in the experimental section. The films were highly uniform and flexible. Interestingly, they were much more transparent when compared to 300-bilayer

PDDA-MTM films (Figure 5A). We believe that this effect is a result of a good dispersion of the nanoscopic filler, the nanoscale dimensions of the filler, as well as decreased surface roughness of the CH-MTM films as compared to PDDA-MTM which decreases light scattering.

SEM characterization of the free-standing films revealed uniform thickness of 2.2 µm ± 0.2 µm giving an average thickness per bilayer of ~7 nm. This thickness is higher than that reported from ellipsometry and we attribute it to the initial lag of deposition which is often present in LBL assemblies as well as increased surface roughness of the final film. The cross-section also revealed similar, well defined stratified structure which was observed previously in the PDDA-MTM composite. (Figure 5C) Given that there are no available mechanical properties data for the PDDA and high MW weight CH, we have also cast films of the two by evaporation of the solutions used for composites preparation. Both of the films, due to their hygroscopic nature, were kept well dried until testing. TGA analysis revealed exceptionally high loading of the inorganic material at ~80 wt. % (~42 vol. %). (Figure 6) Nearly identical loading was found for the PDDA-MTM composite, although PDDA showed better thermal stability in comparison to CH.

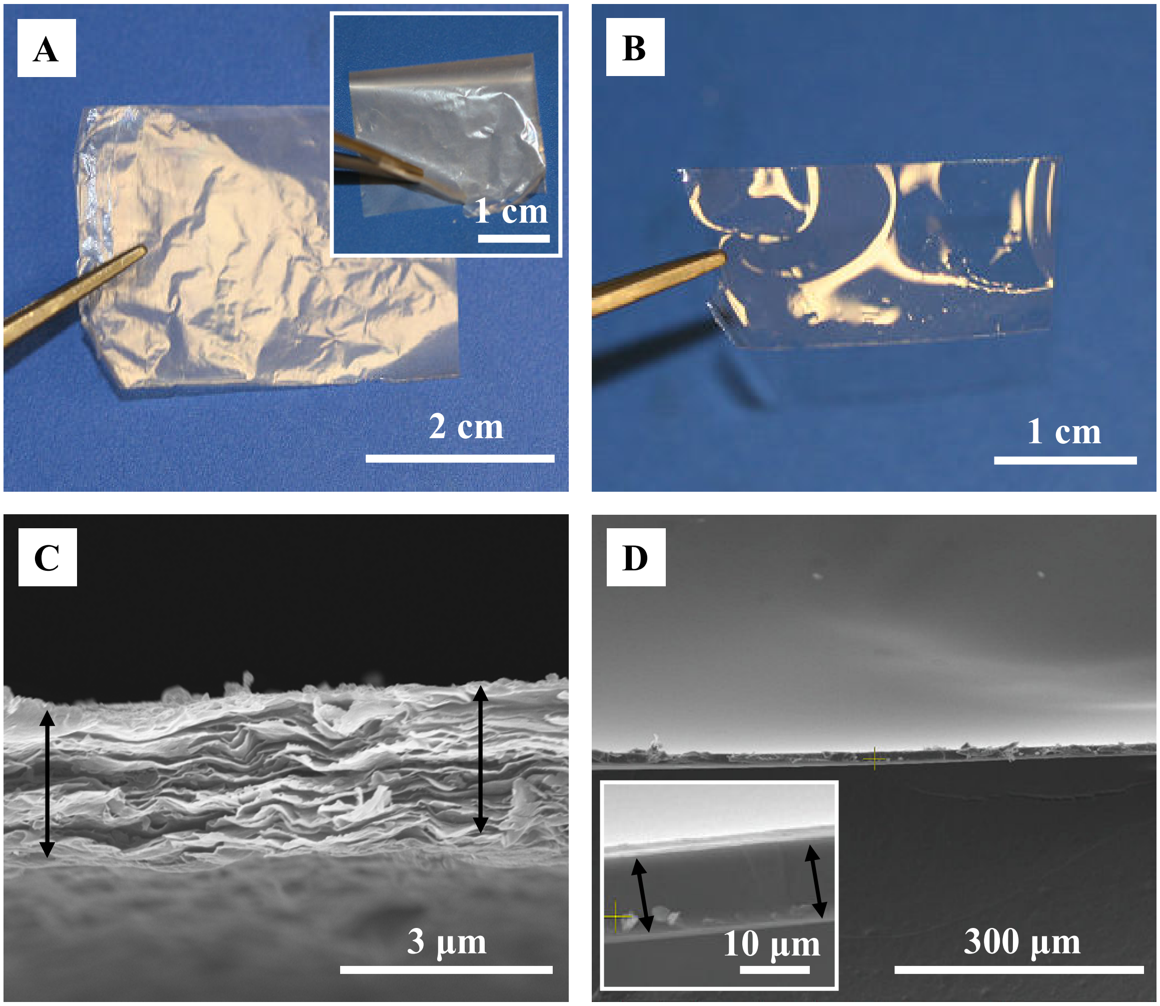

Figure 5. (A) Free-standing, 300-bilayer CH-MTM nanocomposite film. Inset shows folded film revealing good flexibility. (B) Free-standing film of CH polymer prepared by evaporation. (C) SEM image of CH-MTM composite's cross-section. (D) SEM image of CH polymer film's cross-section. Inset represents close-up of the cross-section.

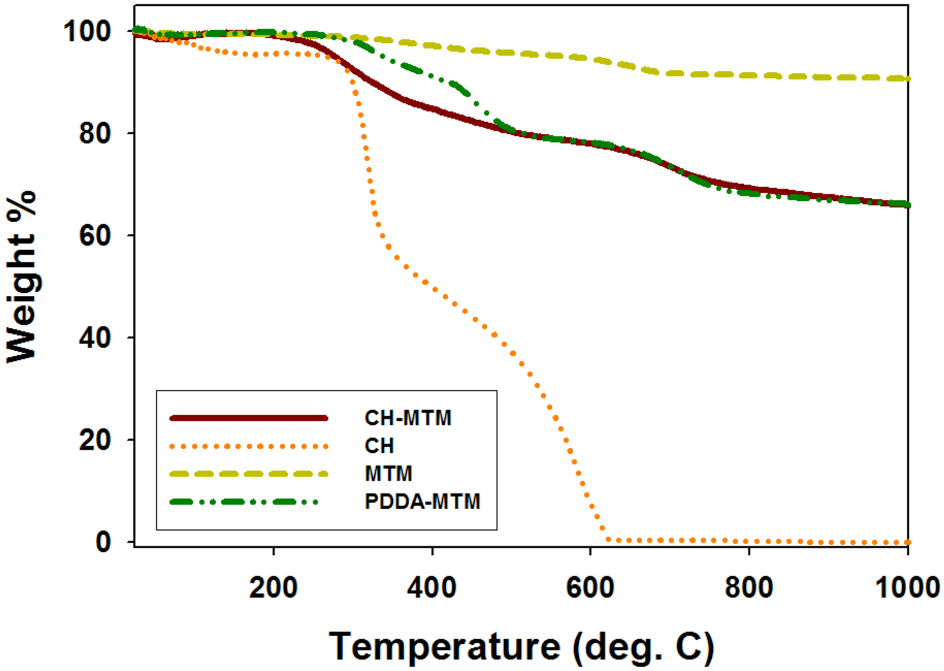

Figure 6. TGA comparison of different PE-MTM composites.

Having obtained the thickness from SEM analysis the material was cut into thin strips and subjected to a standard stretching test in order to obtain stress (σ) vs. strain (ε) plots. Figures 7A and 7B show typical stress-strain responses of PDDA, CH, PDDA-MTM, and CH-MTM, and Table 1 summarizes all of the mechanical properties. In the case of PDDA there is an order of magnitude increase in σ_{UTS} and nearly 2 orders of magnitude in E. At the same time, the toughness of the composite (estimated from the area under the curve) has decreased by an order of magnitude. In the case of CH the increase in E is not as large, only ~3x and σ_{UTS} has actually decreased by ~25 %. This is a surprising result since we have anticipated substantial increase in the stiffness and especially the ultimate strength. For comparison, literature values for mechanical properties of CH report similar or higher results for the modulus and slightly lower results for the strength, ~40-100 MPa.[52] While direct comparison can not be made between our polymer and those reported in the literature in order to confirm our results (differences in sample preparation technique, solvent, and molecular weight), the increase over the literature reported values is still very small in comparison to PDDA-MTM composite. Furthermore, theoretical predictions using the well known Halpin-Tsai's composite theory[33] or the somewhat similar continuum model of Jager-Fratzl[31] for "nacre-like" biocomposites give E ~101 GPa and E ~110 GPa, respectively, when applied to the CH-MTM system. Clearly the calculated values are more than an order of magnitude higher than those achieved.

The weakening of the material when a stronger nanoscale component is incorporated may remind of the case with classical polymer/clay nanocomposites. Inclusion of small amount of inorganic filler (usually at ≤5 wt.%) results in increase of ultimate stress, Young's modulus, and fracture strain,[53-55] while above this threshold mechanical properties decrease in most cases. This effect is attributed to the decreased degree of dispersion of clay sheets at high loadings and formation of large scale non-uniformities. In the case of LBL films the effect is likely to have a different nature because the spatial distribution of the components remains uniform.

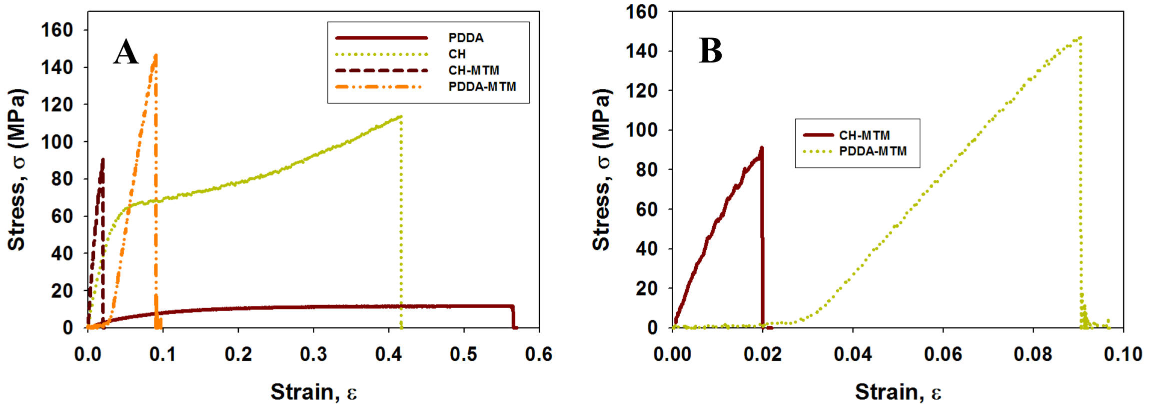

Figure 7. (A) Stress-strain curves for CH, PDDA, PDDA-MTM, and CH-MTM. (B) Close-up of CH-MTM and PDDA-MTM curves.

Table 1. Comparison of the mechanical properties for composites and pure polymers.

	Ultimate Tensile Strength, σ_{UTS} (MPa)	Young's Modulus, E (GPa)	Ultimate Strain, ε (%)	Toughness (MJ/m^3)
PDDA	12 ± 4	0.16 ± 0.03	48 ± 9	4.7 ± 2.0
CH	108 ± 15	1.9 ± 0.3	42 ± 9	31.6 ± 8.8
PDDA-MTM	100 ± 10	11 ± 2	8.4 ± 0.7	~0.5
CH-MTM	81 ± 12	6.1 ± 0.8	1.9 ± 0.6	0.9 ± 0.4

Mechanical strength of clay nanocomposites is a cumulative product of many factors, e.g. degree of clay exfoliation, homogeneity of the dispersion, or strength of polymer-clay interfacial adhesion. As can be seen from the data provided above, the loading of the clay, the degree of exfoliation, the overall homogeneity, and orientation of clay platelets in CH-MTM and PDDA-MTM are quite close to each other (Figures 3-6). To understand the reasons behind these low mechanical properties we have investigated adsorption of CH chains with AFM. Topographic AFM images revealed highly elongated chains adsorbed on the surface (Figure 3D) and can be contrasted with our results for PDDA, where we have shown that more than 85 % of chains adsorb in highly coiled conformation.[24] This can be attributed to the well-known high rigidity of CH due to its polysaccharide backbone. For PDDA-MTM we have shown that this coiled conformation is directly related to the unusual toughening mechanism of nacre or spider silk[8] due to sacrificial bonds between the different parts of the polymeric chain. One can also suggest that flexibility of the polymer directly affects the stress dissipation and load transfer from the organic matrix to the inorganic nanoscale component, i.e. MTM sheets in this case. We believe that high rigidity results in poor CH-MTM interaction, thus contributing to lowering of the mechanical properties, which is not considered in the theoretical models. The CH chain cannot find an optimal conformation on the surface of the MTM, which would result in maximum attraction due to lack of flexibility, which is possible for PDDA. (Figure 8) The attraction energies to consider here include electrostatic attraction, hydrogen bonding, and van der Waals forces. All this creates a complex, topographically uneven, and quite stochastic force field map, which is difficult to adjust to and acquire a reasonable degree of adhesion unless different parts of the backbone can move fairly independently of each other, which cannot be realized in the rigid CH molecule.

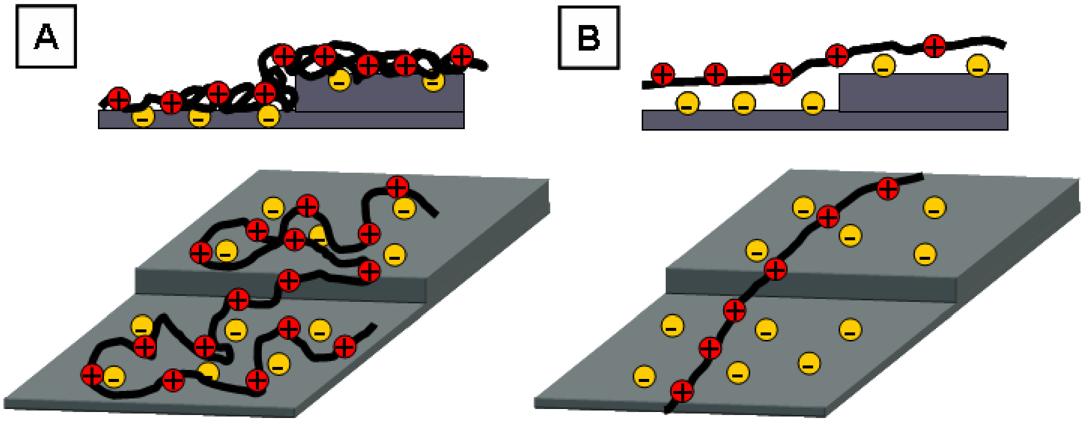

Figure 8. Graphical representation of polyelectrolyte folding and presumed structure of adsorbing chains for (A) PDDA-MTM and (B) CH-MTM nanocomposites. Top images represent a side view of an edge of a clay nanosheets adsorbed on a substrate.

To test this hypothesis we have compared the cohesive strength between CH-MTM and PDDA-MTM composites. If the hypothesis is correct, it must inevitably result in the lower adhesion of one multilayer to another. Indeed, the force required to break the contact between discs (Figure 9) showed that the strength of adhesion in PDDA-MTM composite is ~4x higher than in the CH-MTM, 2260 ± 570 kPa vs. 670 ± 250 kPa, which directly proves the fact that CH doesn’t provide as strong adhesion between the multilayers and importance of conformational freedom during adsorption. Because of the low energy of attraction between CH and MTM, the strength of individual molecules cannot come into play when films undergo in-plane deformation.

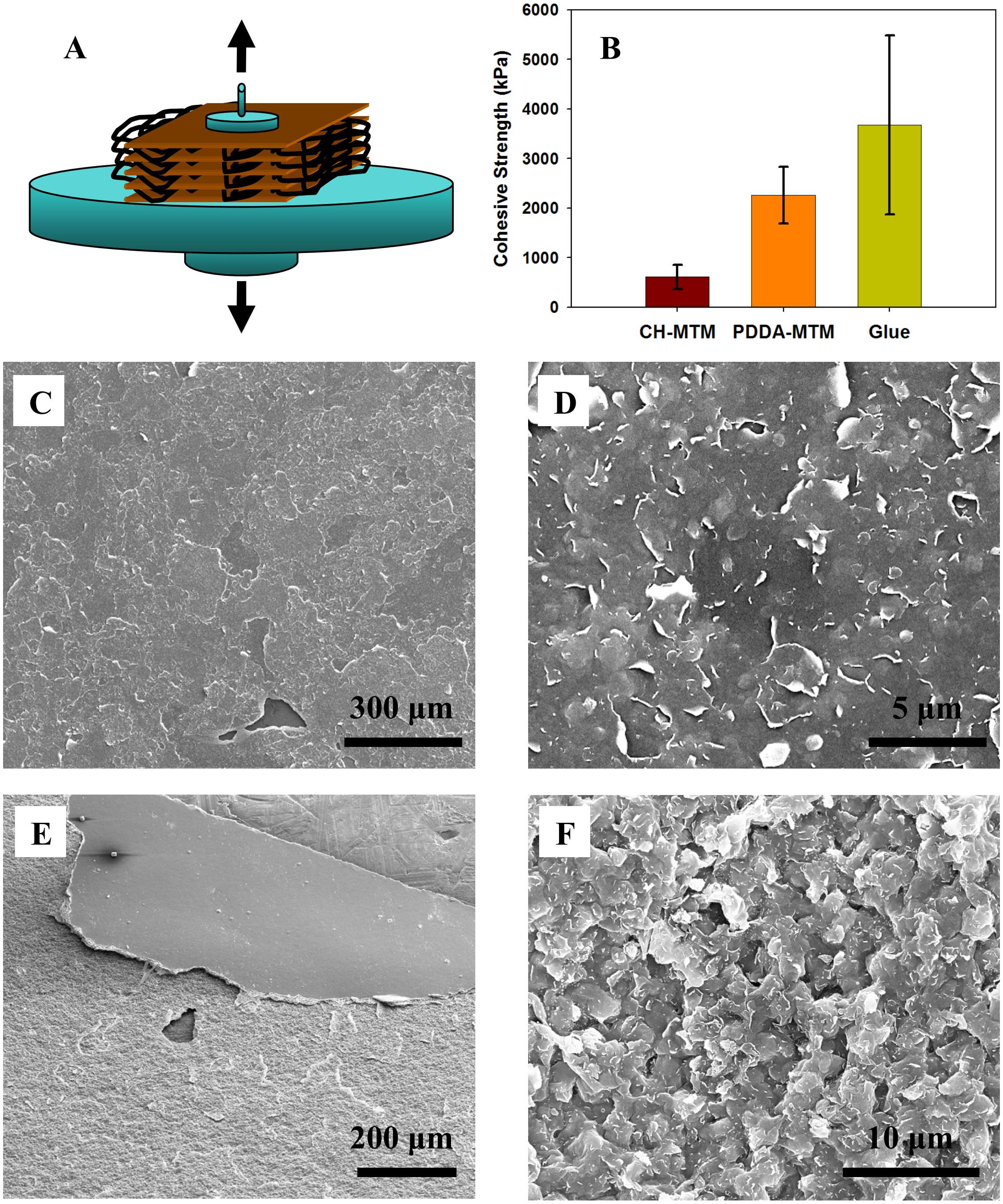

Figure 9. Cohesive strength results: (A) graphical representation of experimental setup, (B) comparison of the results, (C) and (D) CH-MTM film after planes separation, (E) and (F) PDDA-MTM film after planes separation.

4. Conclusions

LBL technique is a tool which enables manufacturing of the composite via bottom-up fabrication method, a few nanometers at a time, which in turn allows for incorporation of high amounts of the inorganic filler with homogeneous distribution throughout the composite. Also important is parallel orientation of all the platelets, which greatly helps in understanding the processes and achieving desirable mechanical characteristics. Against expectations and theoretical predictions, the mechanical properties of a new nanocomposite incorporating one of the strongest natural polymers, CH, were found to be noticeably lower than for a structurally similar composite with drastically weaker polymer, i.e. PDDA. The decrease in mechanical properties was attributed to high rigidity of the polymer resulting in the poor interfacial adhesion with the clay. This study (1) shows unorthodox nature of the behavior of nanocomposites, (2) opens the door to the detailed understanding of the mechanics at nanoscale, and (3) provides a critical criterion for the selection of the organic matrix for advanced nanocomposites necessary for a wide variety of applications from energy conversion to biotechnology.

C. Fusion of Seashell Nacre and Marine Bioadhesive Analogs: High Strength Nanocomposite by LBL Assembly of Clay and DOPA-Polymer

1. Introduction

In Section B we showed that contrary to theoretical predictions the macroscopic mechanical properties of the polymer are not as important as the molecular flexibility of the chains and strength of interfacial adhesion. We have further hypothesized that improving load transfer from the weak polymeric component to the inorganic nanosheets in our artificial nacre should increase the composite's mechanical properties even more. This required a polymer which would have potentially stronger interaction with the clay than the ionic bonds in PDDA-MTM. For inspiration we have turned to another exceptional biomaterial, the unusual protein adhesive secreted by mussels.

Mussels are notorious foulers of marine surfaces, e.g. rocks, wood, metals and even polymers, for which they secrete a byssal apparatus consisting of a series of protein threads that tether the organism onto a wet surface. Mussel holdfasts have been extensively studied by the Waite group,[56] including the specialized mussel adhesive proteins (MAPs) found at the interface between the byssal thread and the surface. MAPs serve the role of cement, which upon secretion become rapidly solidified via chemical cross-linking into an insoluble plaque, tethering the animal to surfaces. A predominant feature of MAPS is the presence of L-3,4-dihydroxyphenylalanine (DOPA),[57] a catecholic amino acid formed by posttranslational modification of tyrosine found in MAPs.[58] DOPA has been implicated in cross-linking reactions leading to solidification of the liquid protein glue,[59-61] for which there is a possible role for metal ions such as Fe^{3+} in the cross-linking reaction.[61,62] Aside from glue cross-linking, DOPA is known to have high affinity for a variety of chemically distinct surfaces: organic and inorganic, via coordination, covalent, or hydrogen bonds.[63]

The simultaneous strong binding, versatility, and hardening capability of DOPA prompted us to exploit it for preparing artificial nanostructured nacre in the hope of enhancing the interfacial clay-polymer interaction and to increase mechanical properties of the composite. Here we demonstrate, for the first time, preparation of a nanostructured composite having nacre-like architecture which takes advantage of DOPA adhesion and cross-linking strength.[64] We show that DOPA has a great effect on the strength of the nanocomposite, and the cross-linking ability allows for an even greater increase in the mechanical properties when compared to PDDA-MTM: 3 times in strength, ~40% in modulus, and 4 times in toughness.

2. Experimental Procedure

With the exception of the materials and techniques listed here, all experiments were performed as described in Section B2.

Materials

For this study Na^+-Montmorillonite, “Cloisite Na^+” (MTM), was purchased from Southern Clay Products (Gonzales, TX). $Fe(NO_3)_3$ solid and NaOH pellets were obtained from Sigma-Aldrich. 4-arm PEG-amine was purchased from SunBio, Inc. (Orinda, CA). DOPA(Ac2)-NCA and Lys(Fmoc)-NCA were prepared by following reported procedures.[65,66] PEG with comparable MW ≈ 15,000 to the DOPA containing polymer was purchased from Sigma-Aldrich.

Synthesis of 4-armed DOPA-Lys-PEG polymer

DOPA-Lys-PEG polymer was synthesized through ring-opening polymerization of N-carboxyanhydride (NCA) monomers of DOPA and Lys from the endgroups of an amine terminated 4-arm PEG polymer. 0.52 g of 4-arm PEG-NH_2 was azeotropically dried with benzene and then transferred to a 100 mL air-free flask with DOPA(Ac2)-NCA (0.37 g) and Lys(Fmoc)-NCA (0.48 g). The flask was put under vacuum and then refilled with argon. After three cycles, 30 mL anhydrous THF was added through cannula. The mixture was stirred at room temperature with argon protection for 5 days. The clear solution was dropped into cold ether and the light gray precipitate was collected. To a 100 mL air-free flask were added the obtained precipitate and 30 mL DMF. After the solution was bubbled by argon for 40 min, 8 mL degassed piperidine was added through cannula. The mixture was stirred at room temperature with argon protection for 1 h. The solvent was reduced to ca. 10 mL by high vacuum, and then cold dry ether was added. A light brown precipitate was collected and dissolved in 0.1 N HCl. After dialysis (3500 dalton cutoff point) in acidic water (HCl, pH=4.5), the solution was lyophilized to give a light brown solid, yield 70%. ^1H NMR (500 MHz, DMSO-d^6): δ 6.66-6.43 (m, -$C_6H_3(OH)_2$); 4.41-4.33 (m, NH-CH(CO)-$CH_2C_6H_3(OH)_2$); 4.19 (NH-CH(CO)-$(CH_2)_4$-NH_2); 2.98 (br, -CH-CHH-$C_6H_3(OH)_2$), 2.81 (s, -CH-CHH-$C_6H_3(OH)_2$); 2.74 (br, NH-CH(CO)-$(CH_2)_3$-CH_2-NH_2), 1.79 (NH-CH(CO)-$CH_2(CH_2)_3$-NH_2); 1.53 (NH-CH(CO)-$(CH_2)_2$-CH_2-CH_2-NH_2); 1.34 (NH-CH(CO)-CH_2-CH_2-$(CH_2)_2$-NH_2). Molecular weight was determined by GPC, $\bar{M}_w$ = 16.4 k. The DOPA content of the block copolymers was determined by UV absorbance of polymer solutions in 12.1 mM HCl at the maximum absorbance wavelength of the catechol (λ_{max} = 280 nm). Solutions containing known concentrations of free DOPA amino acid were used to construct the calibration curve. Using this method, DOPA content was determined to be 21.8 wt% (1.22 mmol/g), which is approximately 5.2 DOPA amino acids per PEG arm. The Lys content was estimated by ^{1}H NMR through calculating the ratio of integral values of the peaks at 4.19 and 4.41-4.33, and found to be equimolar with respect to the DOPA content.

Synthesis of 4-armed Lys-PEG polymer

In a similar fashion, a DOPA-free Lys-PEG polymer was synthesized through ring-opening polymerization of N-carboxyanhydride (NCA) monomers of Lys(Fmoc)-NCA from the end-groups of an amine terminated 4-arm PEG polymer. 0.52 g of 4-arm PEG-NH2 was reacted with Lys(Fmoc)-NCA (0.48 g). A light brown powder was obtained, yield 60%. Molecular weight was determined by Maldi-TOF MS[67] to be 10,146 for 4-arm PEG-NH_2, and 11,339 for synthesized Lys-PEG polymer, yielding an estimated Lys content of ca. 2.3 Lys amino acids per PEG arm.

Preparation of LBL Films with DOPA and PEG

Preparation of the films consisted of following steps: i) immersion of the substrate into a 0.2 % (w/v) solution of the polymer (Figure 1A) for 5 min (pH = 3), ii) rinsing with DI water 2 x 1min (pH = 5.6), iii) drying with a stream of compressed air for 1min, iv) immersion into 0.5 % (w/v) aqueous dispersion of MTM for 5 min (pH = 10), v) rinsing with DI water 2 x 1 min, and finally vi) once again drying with a stream of compressed air for 1 min. Prior to testing films were dried at 80 ºC and subsequently equilibrated at ambient conditions for several days prior to testing.

Instrumental Analysis

DOPA-polymer molecular weights were determined by gel permeation chromatography (GPC) or by MALDI-TOF-Mass Spectrometry (Voyager system 6050, Applied Biosystems). GPC was performed on a DAWN EOS (Wyatt Technology) using Shodex-OH Pak columns in an aqueous mobile phase (50 mM phosphate buffered saline (PBS), 0.1 M NaCl, 0.05% NaN_3; pH 6.0) and an Optilab DSP (Wyatt Technology) refractive index detector. For molecular weight calculations, the experimentally determined dn/dc value of mPEG-NH_2 (MW 5000, 0.136) was used. Humidity tests were performed by pitching a plastic tent over the instrument with humidity being adjusted with boiling water. The humidity was constantly controlled with a standard thermometer and humidity meter from Oregon Scientific. Samples were equilibrated under given conditions for 1 hour prior to testing. 100% humidity was achieved by soaking samples prior to testing for 1 hour and spraying water mist on the sample immediately before the test.

3. Results and Discussion

Preparation of the DOPA-based nanocomposite was performed following similar parameters to those used for PDDA-based composite.[24] Since successful and dense adsorption of MTM on the DOPA-Lys-PEG surface is necessary for deposition of subsequent layers, atomic force microscopy (AFM) was used for characterized the adsorbed MTM layer (Figure 10).

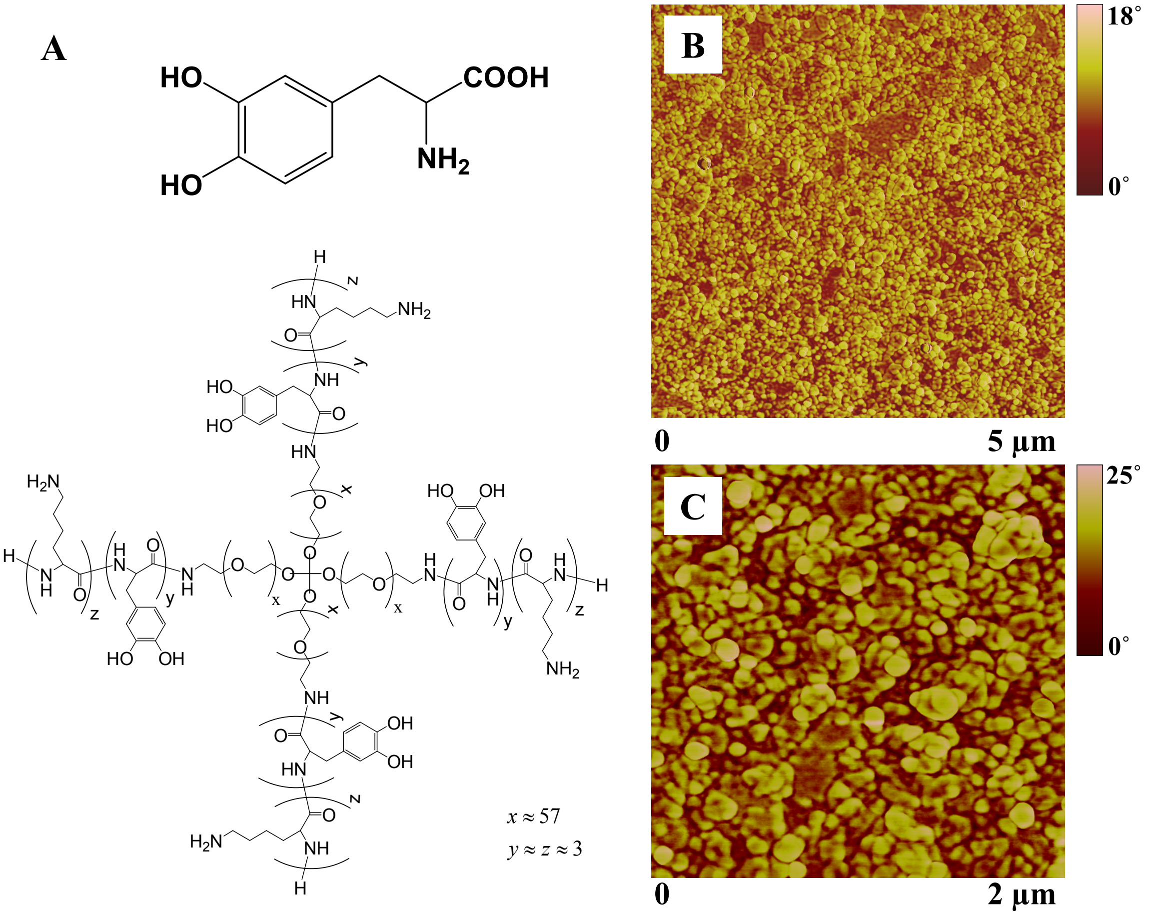

Figure 10. (A): Molecular structure of a single DOPA molecule and DOPA-Lys-PEG polymer. (B) and (C): phase AFM images of a single layer of MTM platelets adsorbed on a layer of DOPA-Lys-PEG polymer. The surface roughness (RMS) is 1.695 nm in (B) and 1.429 nm in (C).

Similarly to our previous work, MTM platelets were observed to adsorb in a form of a densely packed layer with parallel orientation to the substrate (Figures 10B and 10C). The high roughness seen in the picture is a result of short stacks of clay platelets, several sheets in thickness, which are either formed as a result of incomplete exfoliation of the clay, polymer-stimulated stacking, or stochastic build-up of adsorbing platelets.[68] Subsequent multilayer buildup was characterized with UV-Vis spectroscopy.

Compilation of the spectra showed linear increase in absorbance indicating high uniformity of the multilayer. (Figure 11A) Plotting of the absorbance as a function of a bilayer number for the maximum of absorbance wavelength could be further fitted with a linear regression. (Figure 11C) The adsorption continued in a uniform fashion for the entire assembly.

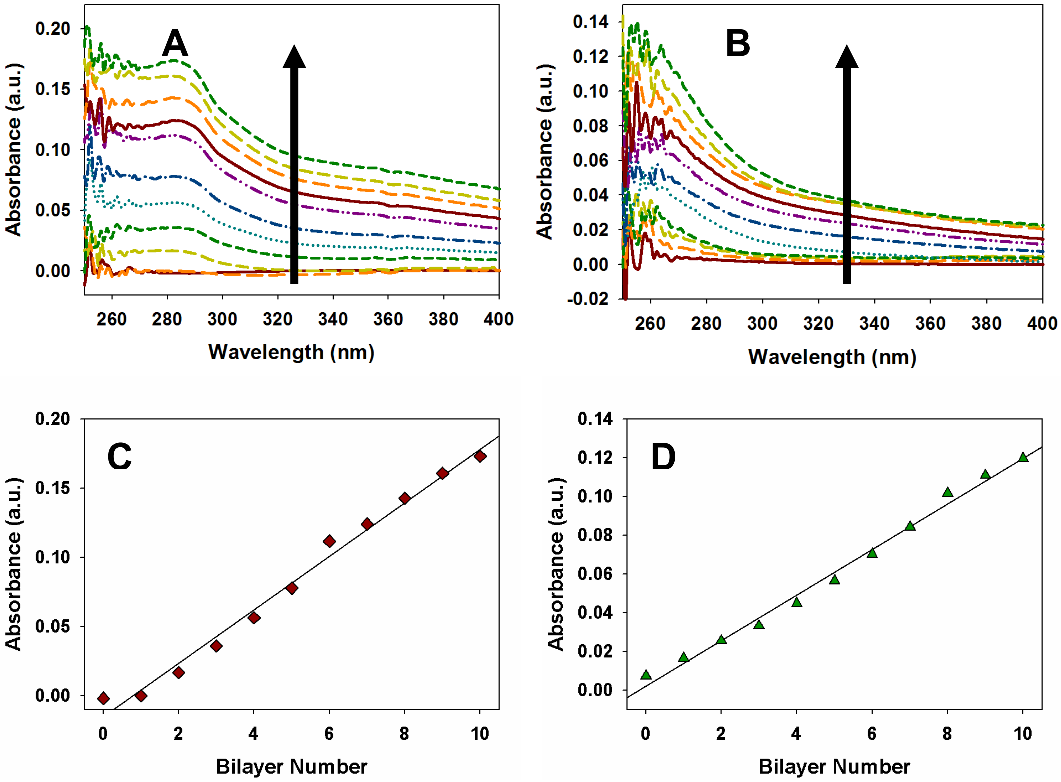

Figure 11. UV-vis spectra of DOPA-Lys-PEG/MTM and Lys-PEG/MTM films growth: (A) compilation of full UV-Vis absorbance spectra for deposition on a glass slide monitored after every bilayer (DOPA-Lys-PEG + MTM) for the first 10 bilayers (arrow indicates direction of increase of absorbance after each bilayer), (B) compilation of spectra for Lys-PEG/MTM for the first 10 bilayers, (C) absorbance at 284 nm vs. bilayer number for DOPA-Lys-PEG/MTM, and (D) absorbance at 262 nm vs. bilayer number for Lys-PEG/MTM.

For the purpose of mechanical properties evaluation, 200- and 300-bilayer films were prepared on microscope glass slides. Subsequently, the films were treated with

0.5M $Fe(NO_3)_3$ solution (pH ≈ 3) in order to allow for cross-linking of DOPA. The choice of Fe^{3+} cross-linker was based on the work of Waite's and Wilker's groups, which showed that Fe may be an important cross-linking agent of DOPA in natural environment.[61,62,69] Fe^{3+} forms complexes with DOPA, the stoichiometry of which depends on the Fe^{3+}/DOPA ratio and the pH of the system.[61,70,71] Furthermore, at alkaline pH values such as that of seawater (~8), autoxidation of DOPA through radical species formation and ultimately, covalent self-cross-linking of DOPAs is possible. Accordingly, after 30 min immersion of the glass slides in the $Fe(NO_3)_3$ solutions, the pH was raised from ~3 to ~8 by drop-wise addition of 0.1M NaOH and the films were kept under these conditions for another 30 min.

Once completed, glass slides were thoroughly washed with DI water and dried. Visual inspection of the slides showed iron treated films acquired a reddish-brown hue, similar in color to the $Fe(NO_3)_3$ solution. (Figure 12A) The color change was the first indication of Fe:DOPA complex formation. This was further supported in UV-vis absorbance spectra of films at different stages of cross-linking. (Figure 12B) It has been shown that the different complexes of Fe:DOPA give rise to distinct absorbance bands. Wilker's group showed that a 1:1 complex has two relatively weak bands at 429 nm and 700 nm. Similarly, the first band was also observed in the pH ~3 treated films in the form of a shoulder peak at ~400 nm. The plain film showed only the DOPA peak. For the 1:2 and 1:3 complexes, the first band has been shown to be shifted down to 374 nm and subsequently back up to 483 nm, respectively. While the surrounding environment of the DOPA molecules in our system is very different from the previous studies and can affect the spectroscopic results, it is plausible that the shoulder peak we have observed is actually a result of a mixture of 1:1 and 1:2 complexes. For the films cross-linked further at pH ~8, (the last curve in Figure 12B), a broad and low intensity peak emerges between 400-600 nm, which likely reflects either the 1:3 complex formation or oxidation of DOPA as we have shown previously.[72]

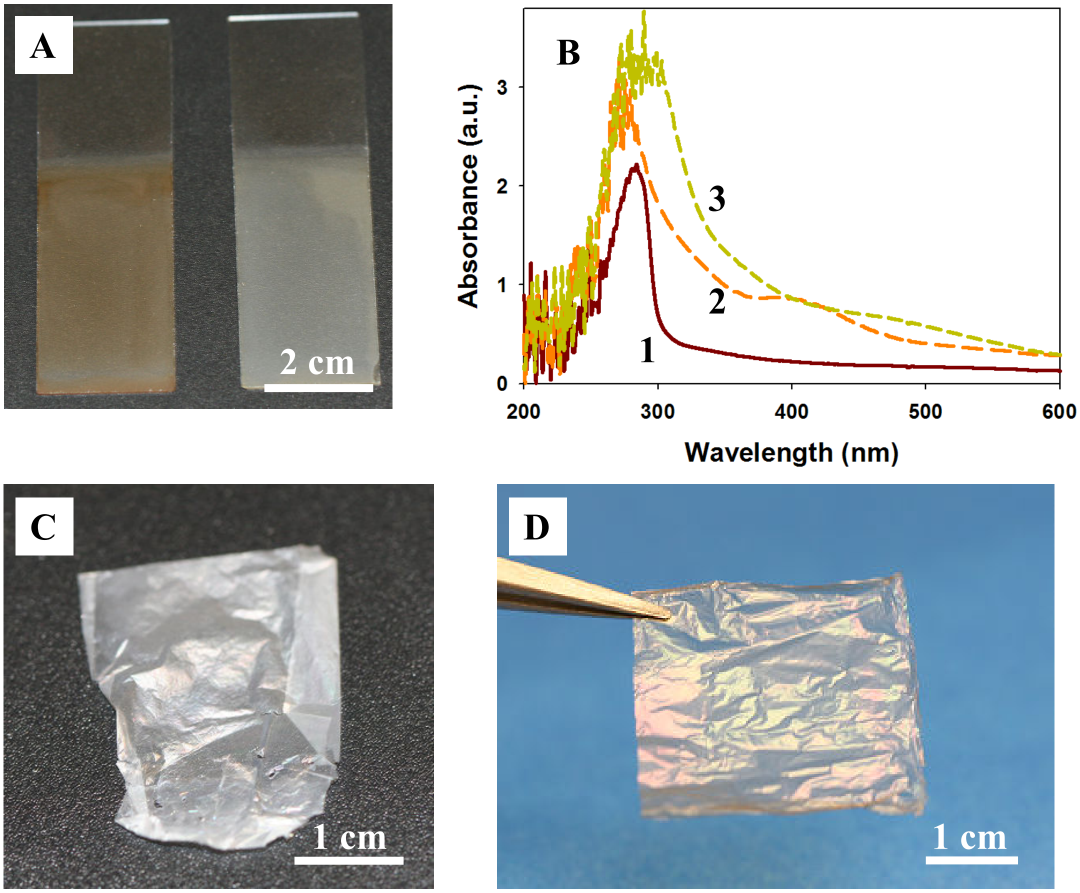

Figure 12. (A) Digital photograph of 300 bilayer DOPA-Lys-PEG/MTM films on microscope glass slides with (left) and without (right) Fe^{3+} cross-linking, (B) UV-vis spectra of 300 bilayer films of DOPA-Lys-PEG/MTM at different stages of DOPA:Fe complexation: 1) plain film, 2) pH ~3, and 3) pH ~8, (C) digital photograph of a 300 bilayer DOPA-Lys-PEG/MTM free-standing film after separation from the glass slide, and (D) digital photograph of a Fe^{3+} cross-linked 300 bilayer DOPA-Lys-PEG/MTM free-standing film.

Further proof of effective cross-linking came from evaluation of the mechanical properties of free-standing films. The 200 bilayer films appeared very thin and required careful handling. While the plain films crumbled and tore into pieces, when attempting to remove from drying solvent, the cross-linked films showed strikingly good rigidity and stability. In comparison, the 300 bilayer films were much easier to handle, and the plain films, although still fragile, could be separated in entirety and reproducibly tested. (Figures 12C and 12D) Cross-section of the films was characterized with scanning electron microscopy (SEM). The films revealed a thickness of 1.0 ± 0.1 μm and 1.5 ± 0.1 μm for the 200 and 300 bilayers thick samples, respectively. (Figure 13A) The cross-section also revealed distinct layered structure which is characteristic of MTM-based LBL films, since MTM platelets form tightly packed layers parallel to the deposition surface.

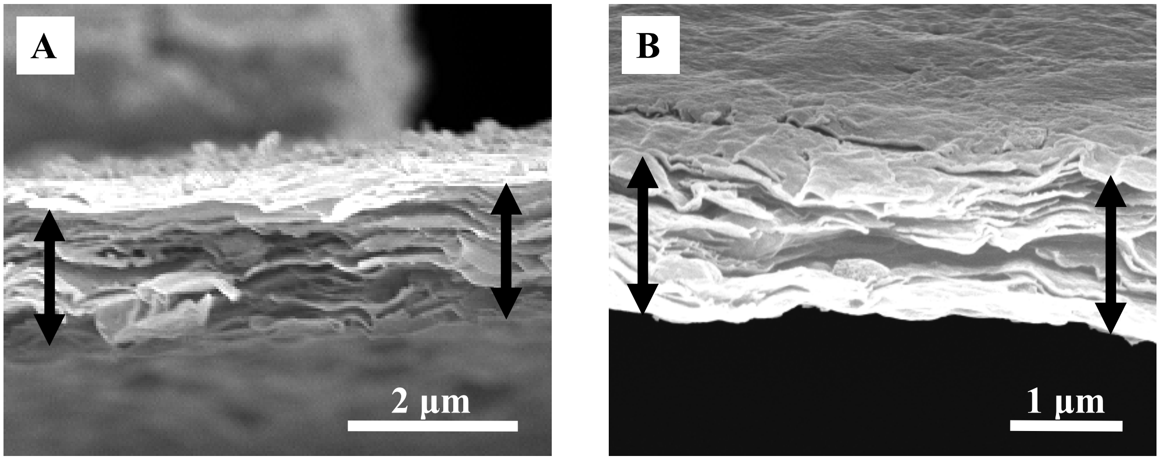

Figure 13. SEM cross-section view of 300-bilayer, Fe^{3+}-cross-linked films of (A) DOPA-Lys-PEG/MTM and (B) Lys-PEG/MTM. Arrows indicate cross-section of the films. Slight separation of the layers seen in (B) is due to a sheering force resulting from cutting samples with a razor blade during sample preparation.

Mechanical properties were evaluated by stretching strips of the films to failure and plotting the true stress vs. strain curves. Typical stress-strain curves are presented in Figure 14A and the mechanical properties are summarized in Table 2.

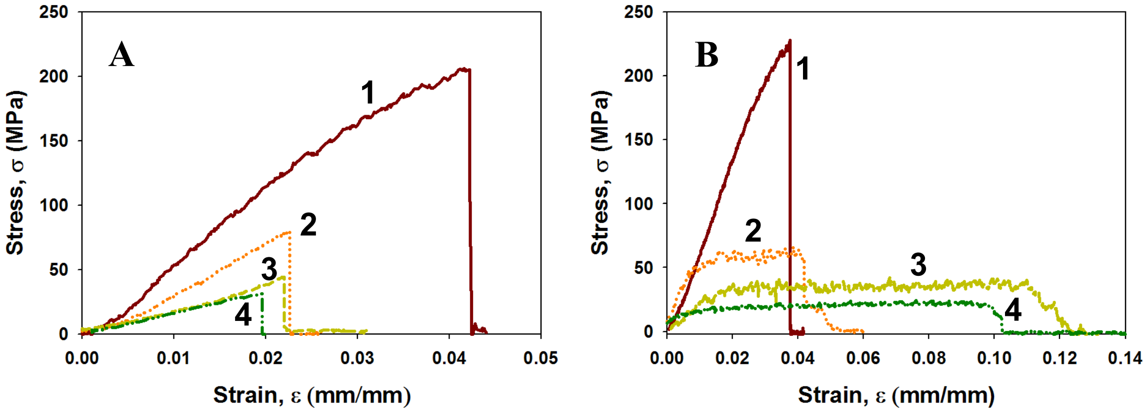

Figure 14. (A) Typical stress-strain curves for 300 bilayer composites w/ and w/o DOPA molecules and w/ or w/o Fe^{3+} cross-linking: 1) DOPA-Lys-PEG/MTM w/ Fe^{3+}, 2) DOPA-Lys-PEG/MTM plain, 3) Lys-PEG/MTM Plain, and 4) Lys-PEG/MTM w/ Fe^{3+}. (B) Typical stress-strain curves for a 300 bilayer film of DOPA-Lys-PEG/MTM cross-linked with Fe^{3+}, pH ~8, under various humidity conditions: 1) 41%, 2) 78%, 3) 92%, and 4) 100%. 100% humidity represents water soaked sample and tested while wet.

Table 2. Summary of mechanical properties for 300 bilayers DOPA-Lys-PEG/MTM and Lys-PEG/MTM composites obtained from stress-strain responses. Fe^{3+} cross-linking corresponds to pH ~8 reaction.

	Ultimate Strength, σ_{UTS} (MPa)	Young's Modulus, E (GPa)	Ultimate Strain, ε (%)	Toughness (MJ/m^3)
PDDA/MTM	100 ± 10	11 ± 2	8.4 ± 0.7	~0.5
DOPA-Lys-PEG/MTM	77 ± 29	4.6 ± 1.0	2.6 ± 0.9	1.0 ± 0.6
DOPA-Lys-PEG/MTM + Fe^{3+}	**200 ± 28**	**6.8 ± 0.9**	**3.8 ± 0.7**	**4.2 ± 1.2**
Lys-PEG/MTM	39 ± 27	2.2 ± 1.1	2.3 ± 1.7	0.7 ± 0.8
Lys-PEG/MTM + Fe^{3+}	25 ± 10	2.2 ± 0.6	1.5 ± 0.8	0.2 ± 0.2

Similarly to our previous results with PDDA/MTM nanocomposite, the DOPA-Lys-PEG/MTM films also exhibit initial plastic deformation followed by an abrupt hardening region as can be seen in the initial strain region (0 - 0.5 % strain) in Figure 14A. The plastic deformation region in DOPA films is not as pronounced as for PDDA/MTM, however the strain in the hardened region is almost 6 times greater in the

DOPA-Lys-PEG/MTM films after cross-linking. One explanation for the lack of hardening region can be found in the fact that DOPA-Lys-PEG polymer contains a very high amount of PEG polymer which can be considered as a weakly interacting in the LBL-MTM system. AFM imaging of MTM on pure, linear PEG showed sparse number of clay platelets. In PDDA/MTM films, high density of charges and flexibility of PDDA molecules allowed for coiling of the polymer and formation of ionic bridges in the polymeric matrix. Large amount of charges gave strong interaction with the MTM platelets and ionic bridging was found to be responsible for the observed toughening behavior.

The ultimate strength of the cross-linked composite is twice as high as that of the PDDA/MTM film. The tensile strength for a 200 bilayer film of PDDA/MTM (thickness of ~4.9 μm) was ~109 MPa, however for a film with comparable thickness, 50 bilayers (~1.2 μm), the strength was only ~95 MPa. Even the films without iron cross-linking display strengths of ~80 MPa, which are approaching that of PDDA/MTM. The Young's modulus however is greatly reduced. For the PDDA/MTM nanocomposite the $E \approx 13$ GPa for a 200 bilayer film and it was ~9 GPa for the 1.2 μm film, while for the DOPA films it is only ~5 GPa before and ~7 GPa after cross-linking. Once again, this result can be attributed to high amount of noninteracting PEG polymer, which is due to the composition and architecture of DOPA-containing polymer analog of MAP. The LBL films with DOPA have a significantly higher toughness which can especially be seen from the difference in the stress-strain curves. For the PDDA/MTM nanocomposites the toughness varies between ~0.5 – 0.6 MJ/m^3, while for the DOPA-Lys-PEG/MTM the toughness is about 2x greater, at 1 ± 0.6 MJ/m^3 and 8x greater for the cross-linked composite at 4.2 ± 1.2 MJ/m^3. We believe that this is a synergistic effect of smaller amount of polymer-MTM interactions which leads to reduced stiffness (slope of the curve) and greater strain, as well as due to DOPA cross-linking which produces a 3-D polymer network trapping the MTM platelets and reducing the chance of premature failure of the composite.

Overall, effectiveness of a small amount of DOPA is surprising and significant and thus prompted us to study this interaction closer. For comparison, we have synthesized an identical 4-armed PEG polymer, except without the DOPA groups - a "Lys-PEG" polymer, and prepared nanocomposite films following the same steps. Characterization of the new films showed that similarly to the DOPA-Lys-PEG polymer, the Lys-PEG/MTM assembly has uniform growth when observed with UV-vis spectroscopy. (Figures 11B and 11D) However, a clear difference can be seen in the position of the maximum absorbance peaks between the two different polymers (Figures 11A and 11B). As expected, the Lys-PEG/MTM is deprived of absorbance at ~280 nm, with its own maximum, due to MTM alone, at ~260 nm. Contrary to pure PEG, the Lys-PEG/MTM films were successfully grown and separated from the substrate into free-standing films. Characterization of the cross-section of the films revealed similar growth increment with a final thickness of ~1.6 μm for a 300 bilayer film which is very close to the DOPA-Lys-PEG/MTM composite. (Figure 13B) The mechanical properties revealed a striking difference and gave one of the most important results of this comparison. The Lys-PEG/MTM films showed nearly half the ultimate strength as compared to the DOPA-containing composite, with ultimate strength approaching ~40 MPa. The ultimate strain showed comparable value to the DOPA containing polymer (before Fe^{3+} cross-linking), ~ 2.3 %, however the Young's modulus is less than half: 2.2 GPa vs. 4.6 GPa. The difference in strength and modulus can be attributed to increased interfacial interaction and much more effective load transfer from the polymeric matrix to the stiff MTM platelets when DOPA is present. Literature reports show that the modulus of individual platelets can be as high as ~270 GPa,[73] hence it is reasonable to assume that increasing the strength of interaction with MTM platelets should increase the modulus and strength of the composite effectively. This should be especially true in our composite where loading of MTM platelets is very high, ~65 wt.%. (Figure 15)

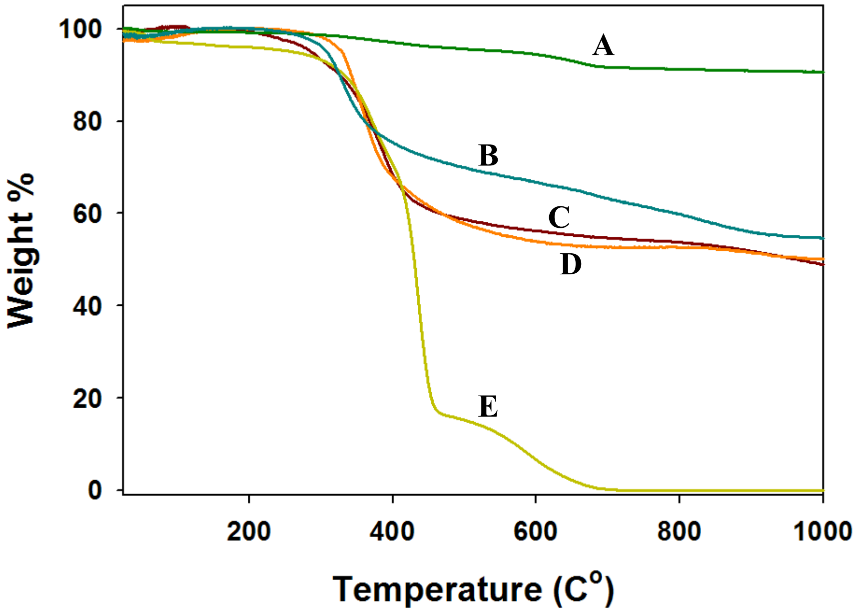

Figure 15. Thermogravimetric analysis of the DOPA-Lys-PEG/MTM nanocomposite: (A) pure montmorillonite clay, (B) Lys-PEG/MTM without cross-linking, (C) DOPA-Lys-PEG/MTM after Fe^{3+} cross-linking, (D) DOPA-Lys-PEG/MTM without cross-linking, and (E) pure DOPA-Lys-PEG polymer.

Another important result of this comparison is the effect of Fe^{3+} cross-linking of the polymeric matrix in the nanocomposite and ultimately its effect on the mechanical properties. Figure 14A is a comparison of typical curves for all of the films with and without cross-linking and Table 2 summarizes the resulting mechanical properties. Unlike in the DOPA containing films, addition of Fe^{3+} actually decreased the mechanical properties of the Lys-PEG/MTM film: the strength decreased from ~40 MPa to ~25 MPa and the ultimate strain decreased by nearly 1%. A potential explanation for this is that the trivalent Fe^{3+} ions displace some of the monovalent Lys groups from the surface and decrease the bonding of the polymer with MTM platelets. If the same effect is present in the DOPA containing composite, this would mean that the strength of DOPA-MTM platelets interaction is even stronger then could be deduced from the strength results, since some of the Lys residues could also be displaced.

At the molecular level DOPA serves a dual role: (1) an anchor that attaches the polymer to the platelets and (2) a bridge between polymer chains forming a cross-linked 3-D matrix via Fe^{3+} treatment followed by exposure to alkaline pH. As can be deduced from the cross-linking effect on mechanical properties, some of the DOPA molecules are attached to the surface and others are involved in bonding with other chains. A potential mechanism of deformation is one that upon application of load to the films, first the weaker bonds are being broken: PEG-MTM and Lys-MTM, while DOPA is still holding onto the MTM platelets. Only when much greater force is applied to these bonds the composite fails and ruptures.

Finally, since DOPA-containing marine adhesives show excellent stability under aqueous conditions we have tested our cross-linked films under varied humidity. Figure 5B summarizes results of the test. The composite gradually transitions from brittle to highly ductile as the humidity increases. This is different from the behavior of the true MAP, which is again quite likely due to PEG segments, but, at the same time, is very similar to the behavior of PDDA/C films. More interestingly, the behavior is reversible with very fast transition time. In a simple experiment, a water soaked film was simply dried off with a paper towel and immediately tested under ambient conditions. When tested, the film showed exactly the same behavior as without wetting.

4. Conclusions

In summary, we described the preparation of a novel nanostructured composite film which takes advantage of two different natural materials: layered nacre and marine adhesive of mussels. Overall, this work is a first example of fusion of two seemingly distinct concepts found in Nature into a unique composite with excellent mechanical properties. Just as in mussels, we found that DOPA molecules impart unusual adhesive strength to the clay composite and the hardening mechanism found in the natural “cement” plays an equally important role in strengthening of our “nanostructured nacre’. In comparison to our previous work with PDDA, we found that even a small amount of DOPA has a dramatic effect on the mechanical properties: the ultimate strength increased 2x and the toughness ~8x.

D. Ultrastrong and Stiff Layered Polymer Nanocomposites

1. Introduction

In Section B we showed that macroscopic mechanical properties of the polymer are not as important as the molecular flexibility of the chains and strength of interfacial adhesion. For this reason, in section C we turned our attention to a flexible polymer containing biomimetic adhesive groups in its structure in order to improve the interfacial adhesion. Interestingly, in spite of relatively low density of the adhesive groups when compared to PDDA or CH polymers, the resulting composite showed strength and stiffness approaching that of the PDDA-MTM NC. We further discovered that post-assembly ionic crosslinking of the polymer matrix resulted in a substantial improvement of strength and stiffness of the NC, resulting in 2x increase in σ_{UTS}, to ~200 MPa.

With the second result in mind, we hypothesized that LBL assembly of MTM with a polymer capable of weaker interactions with the inorganic MTM but with much greater density of crosslinkable groups should result in even greater mechanical properties. We chose to work with poly(vinyl alcohol) (PVA) which satisfies both of these requirements: (1) it contains high density of hydroxyl groups which (2) are amenable to ionic and covalent crosslinking through simple chemistries. PVA is also a readily available and inexpensive polymer. In agreement with our hypothesis, the PVA-MTM NC was successfully produced and its mechanical properties showed substantial improvement over all of the previous LBL-based MTM NCs.[30] In fact, the properties of this NC are record-high for MTM-based NCs presented until this date. This section presents the details of this experimental development as well as rigorous analysis of the observed results.

2. Experimental Procedure

Similarly as in Section C, all experimental procedures and materials used are the same as in Section B2, unless specified herein.

Materials

Polyvinyl alcohol (PVA) with molecular weight of MW ≈ 70,000 was purchased from Sigma-Aldrich (St. Louis, MO) and used as received. 25% Glutaraldehyde (GA) solution was obtained from Fluka (currently part of Sigma-Aldrich). 5 vol.% glutaraldehyde solution used in the experiments was prepared by diluting the stock solution with DI water prior to use. 1 wt.% PVA solution used for LBL assembly was prepared by dissolving 10 g of PVA powder in 1 L of 80 ºC DI water under vigorous stirring.

Preparation of Composites

In a typical sample preparation, a clean glass slide was immersed in 1 wt.% solution of PVA, for 5 minutes, rinsed with DI water 2 x 1 minute and gently dried with compressed air for 1 minute, then immersed in 0.5 wt.% MTM dispersion for 5 minutes, rinsed 2 x 1 minute, and again dried with compressed air for 1 minute. Every 10 bilayers, films were immersed into the 5 vol.% solution of glutaraldehyde for 30 minutes to allow for cross-linking. After detachment, free-standing films were further dried in a drying oven at 60 ºC and then set aside to equilibrate in ambient conditions (~65 – 75 ºF temperature and ~20 – 30% relative humidity) for at least 24 hours prior to mechanical testing. Due to the limitation of the composites' weights (~5 mg/free-standing film), the composite samples used in NMR characterization were prepared by mixing equivalent volumes of the PVA and MTM solutions and subsequent casting of the resulting solutions by air drying. GA cross-linked samples were prepared by immersion of the free-standing films in the GA solution for at 30 min.

Instrumental Analysis

IR spectra were obtained using a Nicolet 6700 spectrometer utilizing the grazing angle accessory (Smart SAGA) at a grazing angle of 85º. The Differential Scanning Calorimetry (DSC) analysis was performed using a Perkin-Elmer DSC-7 (PerkinElmer, Wellesley, MA). A small amount (5-10 mg) of the sample was encapsulated in an aluminum pan and was treated with the following heat/cool/heat method. The sample was first heated from 30 ºC to 250 ºC at a scan rate of 10 ºC/min. The sample was then cooled from 250 ºC to 30 ºC at the same rate, which was then heating of the sample from 30 ºC to 400 ºC at 10 ºC. Data acquisition and processing was done with PerkinElmer Pyris software. All the NMR experiments were performed on a Varian Chemagnetics Infinity 400 MHz spectrometer equipped with a MAS probe. The samples were packed into the 5mm Zirconia rotors and 8k MAS rotation speed was used. The ^{29}Si NMR were recorded at 79.5MHz using TMS/$CdCl_3$ (1 vol.%) as an external reference, while 104.26MHz was used for ^{27}Al NMR, and $Al(NO_3)_3/H_2O$ was used as an external standard. The carrier frequency of C13 NMR is 100.6MHz. The spectra were calibrated by the ^{13}C resonance of adamantine. XPS data were recorded on an Axis Ultra x-ray photoelectron spectrometer (Kratos Analyticals, UK) equipped with a monochromatized Al Kα x-ray source. All spectra were calibrated with respect to the binding energy of C 1s carbon core level taken at 284.6 eV.

Mechanical Testing of PVA-MTM Films

The tensile mechanical properties were analyzed by two instruments:

1) Stress-strain curves were tested in the same manner as in previous sections. Tests were performed at a rate of 0.01 mm/s with a ~4.9 N range load cell. The number of tested samples was normally 10-15 for the LBL nanocomposites and 4-5 for the pure and GA crosslinked polymer. For accurate analysis of the mechanical properties four different batches of the samples were prepared on different dates and using new solutions each time. All of the batches were tested and gave similar values for the ultimate strength. The Young's modulus could not be accurately analyzed with this instrument due to substantial mechanical compliance issues which resulted in inaccurate strain measurements.

2) The same films (same geometry and batches) were tested in parallel in tension using an in-house designed tensiometer shown in Figure 16. The tensiometer was built around a Nikon SMZ 800 dissecting microscope that was fitted with a Basler A102fc digital video camera. Dual actuators were driven by MicroMo stepper motors and mounted on Del-Tron crossed roller slides that enabled the specimen to stay in the center of view. Grips were machined out of stainless steel and placed at the end of both actuators. The specimen ends were adhered to the grips via adhesive tape. The axial

servomotors were controlled using LABVIEW software on a Dell Precision 300 pc which also synchronized data acquisition from the load element with image acquisition from the digital camera. The samples were loaded at a constant true strain rate of 0.005/sec until failure and the synchronized force and image recordings were compiled using LABVIEW. Analysis of actual material strain was achieved by electrostatically adhering 25 μm diameter glass beads on the specimen surface. The specimen images were analyzed with LABVIEW software to track the glass bead positions. The raw load vs. image data was converted to nominal stress (load/CSA) vs. nominal strain data (change in separation of glass beads/initial separation). The Young's modulus was determined by calculating the initial slope of the nominal stress vs. nominal strain data. At least 5 samples were tested in order to produce each data point for the stress-strain curves.

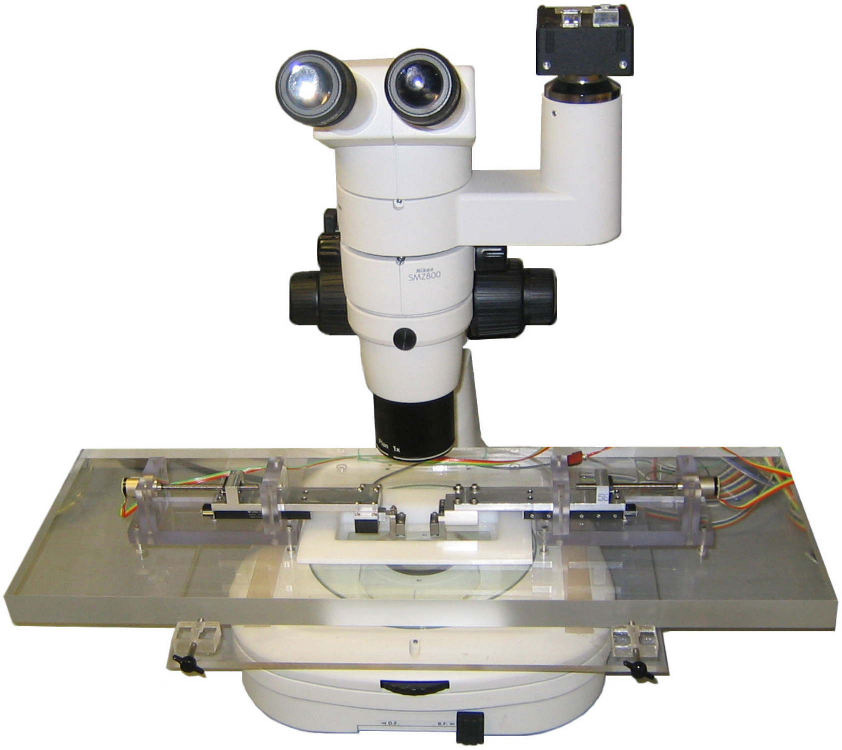

Figure 16. A custom-designed tensile tester was built around a Nikon SMZ800 dissecting microscope for measuring tensile properties. Images were acquired using a Basler digital camera. Dual stepper motors were controlled by a Lab-VIEW program which moved the crossheads which were stabilized by preloaded crossed roller slides.

Most of the attributes of the above tensile tests confirm to the ASTM standard ASTM D 882. The standard includes the testing of plastic sheets with the thickness not greater than 0.25 mm. The PVA and PVA-MTM samples tested here are within this limit. The standard calls for the measurement of specimen extension by grip extension or displacement of gage marks. Here, the gage marks are the 25 μm diameter glass beads on the specimen surface.

All of the tests were performed under similar environmental conditions with relative humidity maintained in the range of ~20 – 30 % and ambient temperature in the range of 65 – 75 ºF.

3. Results and Discussion

A traditional LBL process of sequentially coating a surface with nanometer thick layers of poly(vinyl alcohol) (PVA) and MTM by immersing a glass substrate in dilute solutions of the components was used in this study [74-76]. Ellipsometry and UV-Vis spectroscopy (Figures 17 and 18) revealed linear and uniform growth.

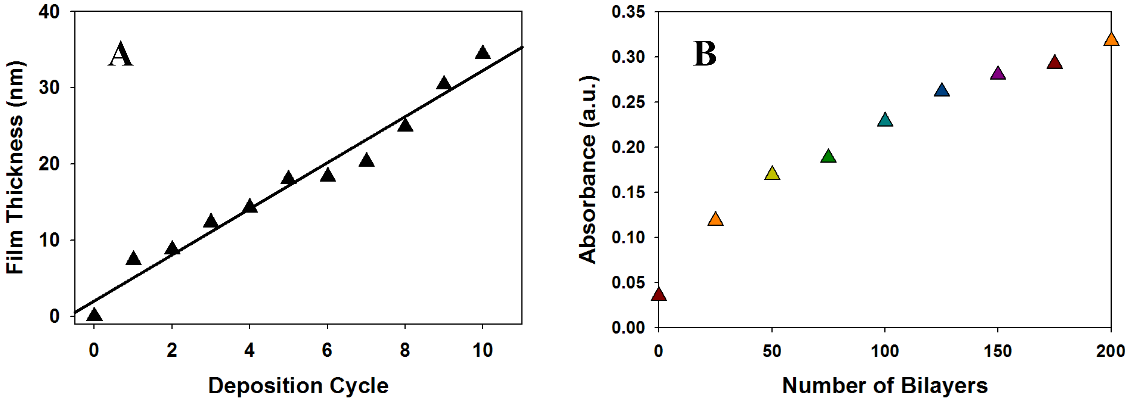

Figure 17. (A) Thickness results for PVA-MTM nanocomposite for the first 10 deposition cycles from ellipsometry. (B) Absorbance as a function of a bilayer number at 360 nm.

Characterization of the assembly using atomic force microscopy (AFM) (Figure 18) and scanning electron microscopy (Figure 19) verified dense coverage of the nanoplatelets and their strictly planar orientation. The electron microscopy characterization provided thickness measurements of 1.0 µm +/- 0.1 µm (SEM) and 1.5 µm +/- 0.1 µm (SEM) for 200- and 300-bilayer films respectively, indicating an average of ~5 nm thickness per bilayer (Figure 19A). Nearly identical thickness was obtained from ellipsometry for a 300-bilayer film grown on a silicon wafer: 1.480 µm +/- 0.004 µm (SEM). The cross-section also revealed a well-defined layered architecture.

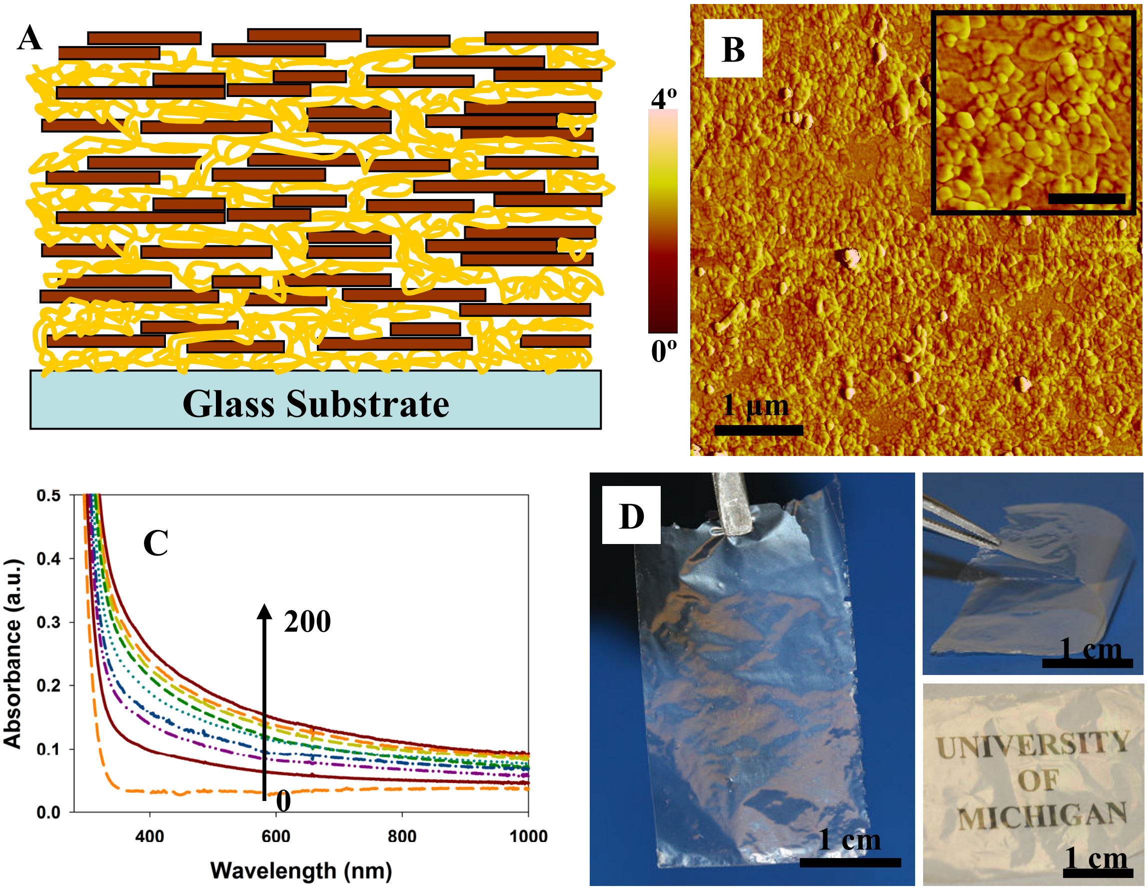

Figure 18. Preparation of PVA-MTM nanocomposites. (A) Schematic representation of the internal architecture of the PVA-MTM nanocomposite (picture shows 8 bilayers). (B) Atomic force microscopy phase image of a single PVA-MTM bilayer adsorbed on top of a silicon wafer. The inset represents a close up of the main image showing individual MTM platelets more clearly. The scale bar in the inset corresponds to 400 nm. (C) Compilation of UV-Vis absorbance spectra collected after multiples of 25 bilayers of PVA-MTM composite deposited on both sides of a microscope glass slide up to 200 bilayers. (D) Free-standing, 300-bilayer PVA-MTM composite film showing high flexibility and high transparency. Lower image is taken at an angle to show diffraction colors.

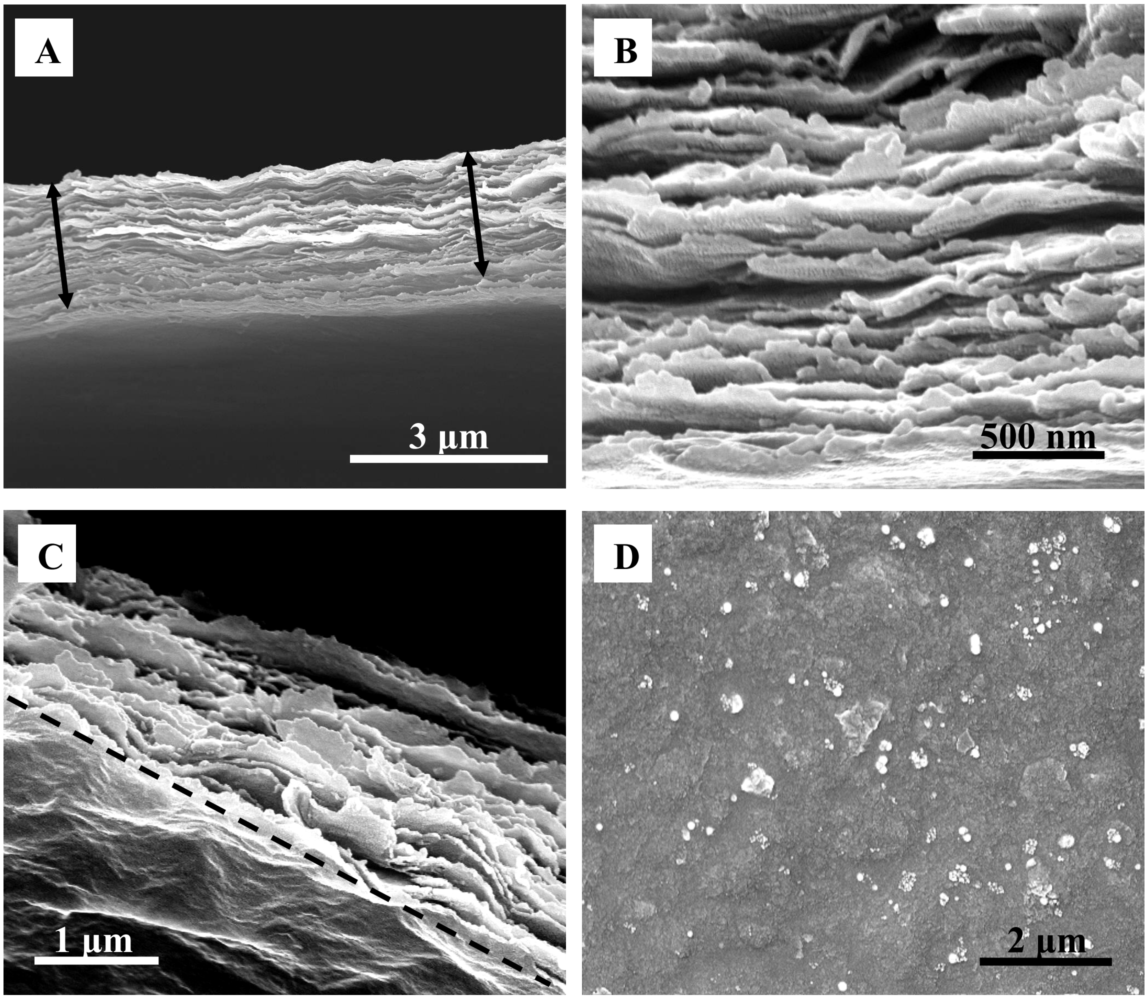

Figure 19. Scanning electron microscopy characterization of a 300-bilayer, free-standing PVA-MTM nanocomposite. (A) Cross-section of the film. Arrows indicate span of cross-section. (B) Close-up of the cross-section showing separation of layers. (C) Top-down view of a fracture edge of the composite after tensile testing. Dashed line indicates edge of the sample. (D) Top-down view of the composite's surface. Slight separation of the layers seen in (A) and (B) is due to a shearing force resulting from cutting the sample with a razor blade during SEM sample preparation.

We note that PVA is uncharged unlike many other polymeric materials used in LBL. Nevertheless, it produces a stronger composite than other polymers that undergo electrostatic attraction to the clay sheets[29,76,77]. The PVA-MTM pair has two unique properties. The first is the high efficiency of hydrogen bonding. Atomic modeling revealed that the geometry of SiO_4 tetrahedrons on the surface of the alumosilicates is conducive to cooperative H-bonding (the Velcro effect). The distance between the oxygen atoms of clay and hydrogen atoms of PVA are 2.75 and 2.65 Å, respectively, which makes H-bonding epitaxial (Figure 20).

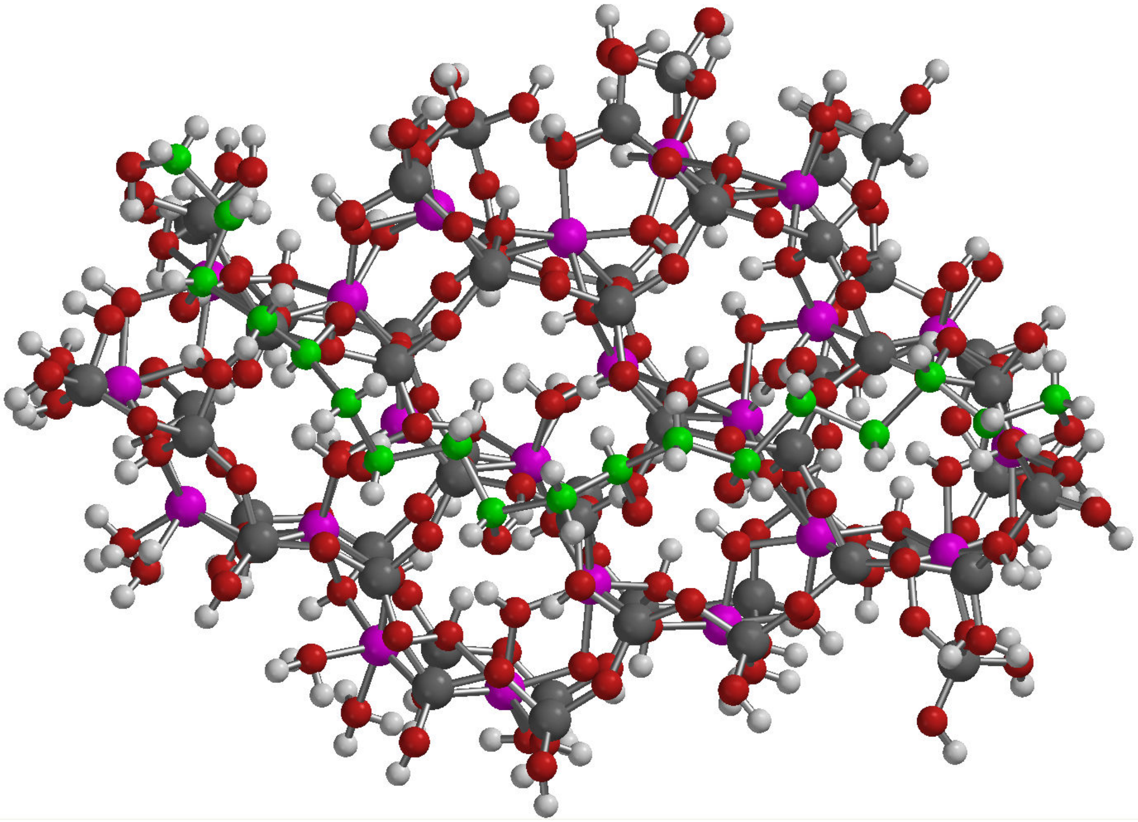

Figure 20. Energy-optimized geometry of bonding between PVA and MTM via hydrogen bonding obtained from computer calculations using AM1 semi-empirical algorithm. Atoms: Al - purple, O – red, H- light grey, Si, - dark grey, C – green. The distance between the OH groups on PVA matches very well that between oxygen atoms in the coordination sphere of silicon atoms on the surface of clay platelets. No defects or substitution atoms were included in the consideration of the hydrogen bonding.

Secondly, a significant part of the efficient load transfer between the polymer and the inorganic building block is attributed to the cyclic cross-linking to Al substitution present on the surface of MTM sheets and to Al atoms located along the edges of the MTM platelets[78]. These Al atoms are easily accessible (Figure 21A) to the macromolecules, unlike similar groups in the middle of the sheets. An atom of Al, two atoms of oxygen and three atoms of carbon from PVA participating in this bond form a 6-member ring structure, which is known to be particularly stable (Figure 21A). Experimental data from Fourier transform infrared spectroscopy (FTIR), nuclear magnetic resonance (NMR), and x-ray photoelectron scattering spectroscopy (XPS), point to the formation of the Al-PVA covalent linkages. As such, we see a characteristic shift in the XPS spectra of Al from 74.4 to 74.9 eV (Figure 21B: 1, 2); concomitantly, the change in ratio of carbon XPS peaks at 284.8 eV (-$\underline{C}$-H_2) and 286.2 eV (-$\underline{C}$-O-H) was observed (Figure 21C). The formation of Al-PVA bonds can be further confirmed by the appearance of the characteristic FTIR vibration of Al-O-C (Figure 21D, inset) at 848 cm^{-1} [78], and strong suppression of the C–O-H band at 3290 cm^{-1} (Figure 21E) which correlate nicely with condensation of hydroxyls at Al sites with those from PVA groups.

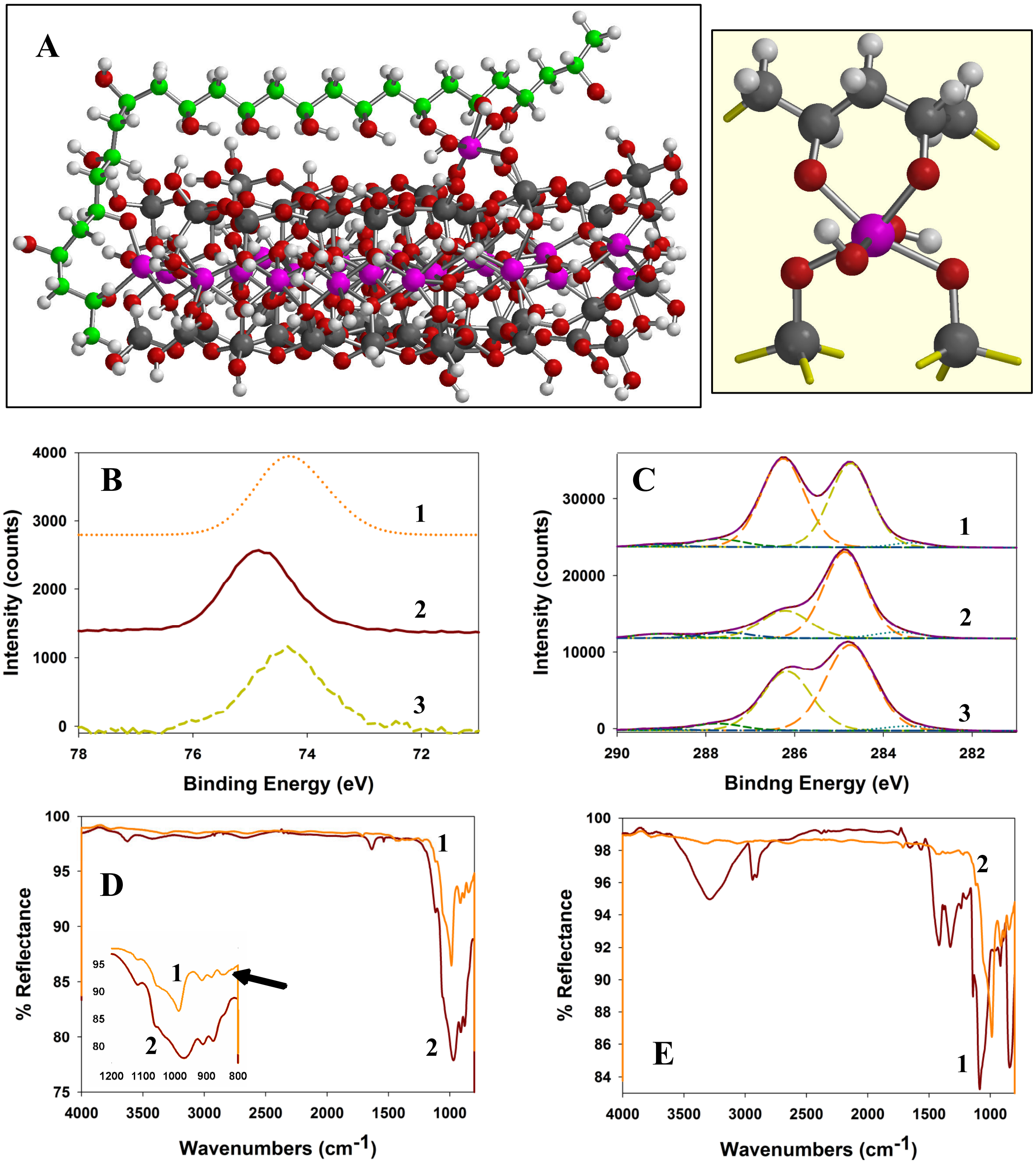

Figure 21. Characterization of PVA and MTM molecular interactions. (A) Energy-optimized geometry of bonding between PVA and MTM via Al substitution sites obtained by computer calculations using the AM1 semi-empirical algorithm. In the inset: enlarged portion of the 6-member cycle formed between PVA and MTM. Atoms: Al - purple, O – red, H- light grey, Si, - dark grey, C – green. (B) Al 2p XPS spectra for: (1) MTM, (2) PVA-MTM nanocomposite, and (3) PVA-MTM nanocomposite with GA cross-linking. Positive energy shift is indicative of increased oxidation state of the Al. (C) C 1s XPS spectra for: (1) PVA, (2) PVA-MTM composite, and (3) PVA-MTM composite with glutaraldeyhe (GA) cross-linking. XPS spectra were deconvoluted in component peaks corresponding to the different oxidation states of C. The major peaks at 284.8 eV and 286.2 eV correspond to -$\underline{C}$-H_2 and -$\underline{C}$-O-H carbons. (D) Comparison of

FTIR spectra for (1) PVA-MTM composite and (2) MTM. Inset shows a close-up of the major peaks. Arrow points to the characteristic vibration peak at 848 cm^{-1}. (E) Comparison of FTIR spectra for pure PVA (1) and PVA-MTM composite (2). The spectrum of PVA-MTM shows suppression of the C-O-H vibrations due to covalent binding with MTM surface.

The NMR spectra of ^{27}Al (Figure 22) remain the same as expected, since the coordination environment of Al (i.e. octahedral) did not change. Note that the nanometer scale organization and the layered structure of the composite provide the necessary conditions for formation of multiples of such cyclic linkages.

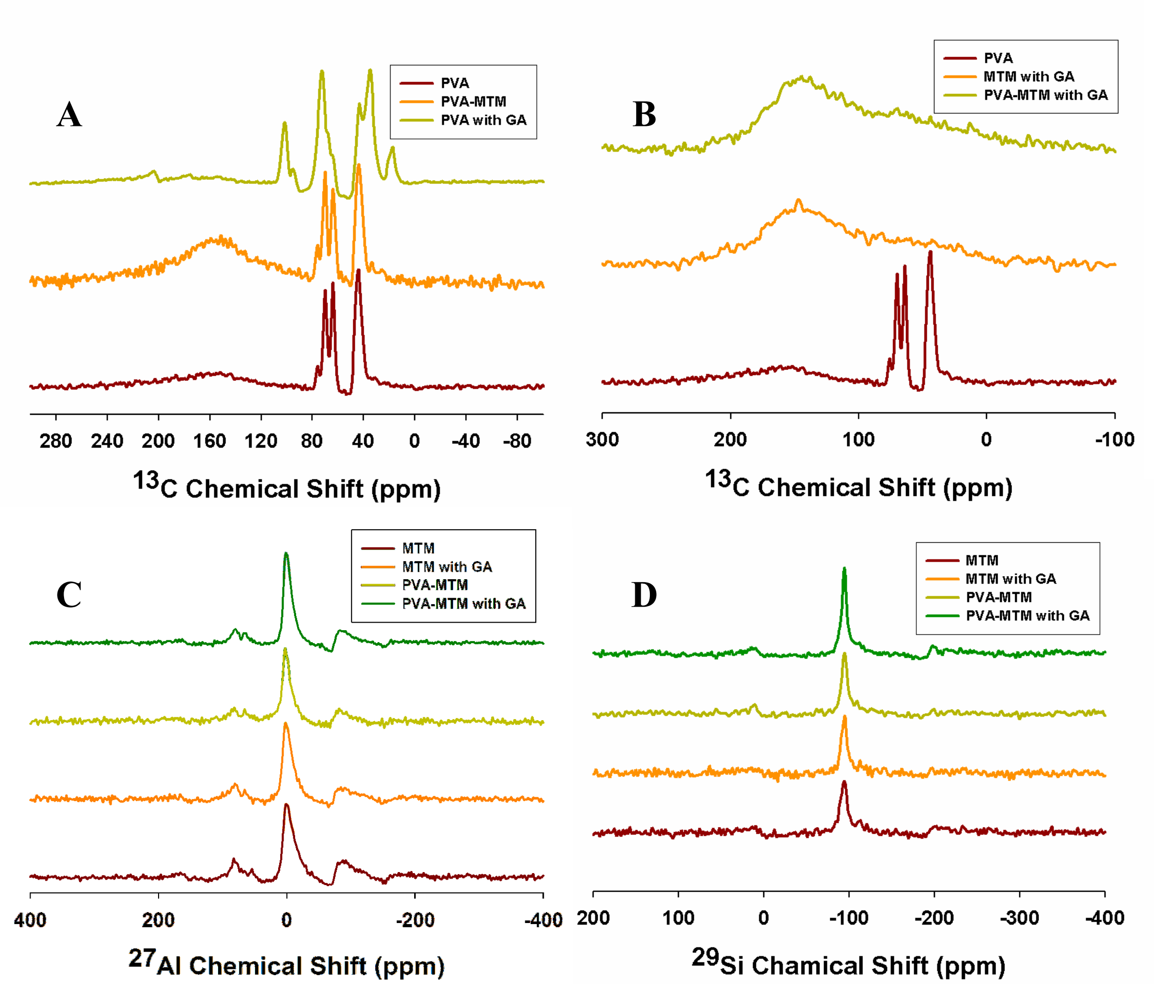

Figure 22. (A) and (B) ^{13}C, (C) ^{27}Al, and (D) ^{29}Si solid-state NMR spectra of the indicate samples.

Films were treated with glutaraldehyde (GA) after LBL assembly to further the bonding and load transfer between the –OH groups and clay surface. GA is a highly efficient cross-linking agent for PVA [79,80] that forms covalent acetal bridges between –OH groups of the polymer chains (Figure 23) as well as the hydroxyl groups present on the MTM sheets and particularly on their edges. Solid-state NMR analyses revealed dramatic changes in the spectra before and after GA treatment (Figure 22). We can also see clear evidence of a reaction between GA and clay from NMR (Figure 22) and FTIR (Figure 24), which means that this type of cross-linking further increases connectivity between PVA and clay sheets as well as the clay particles themselves.

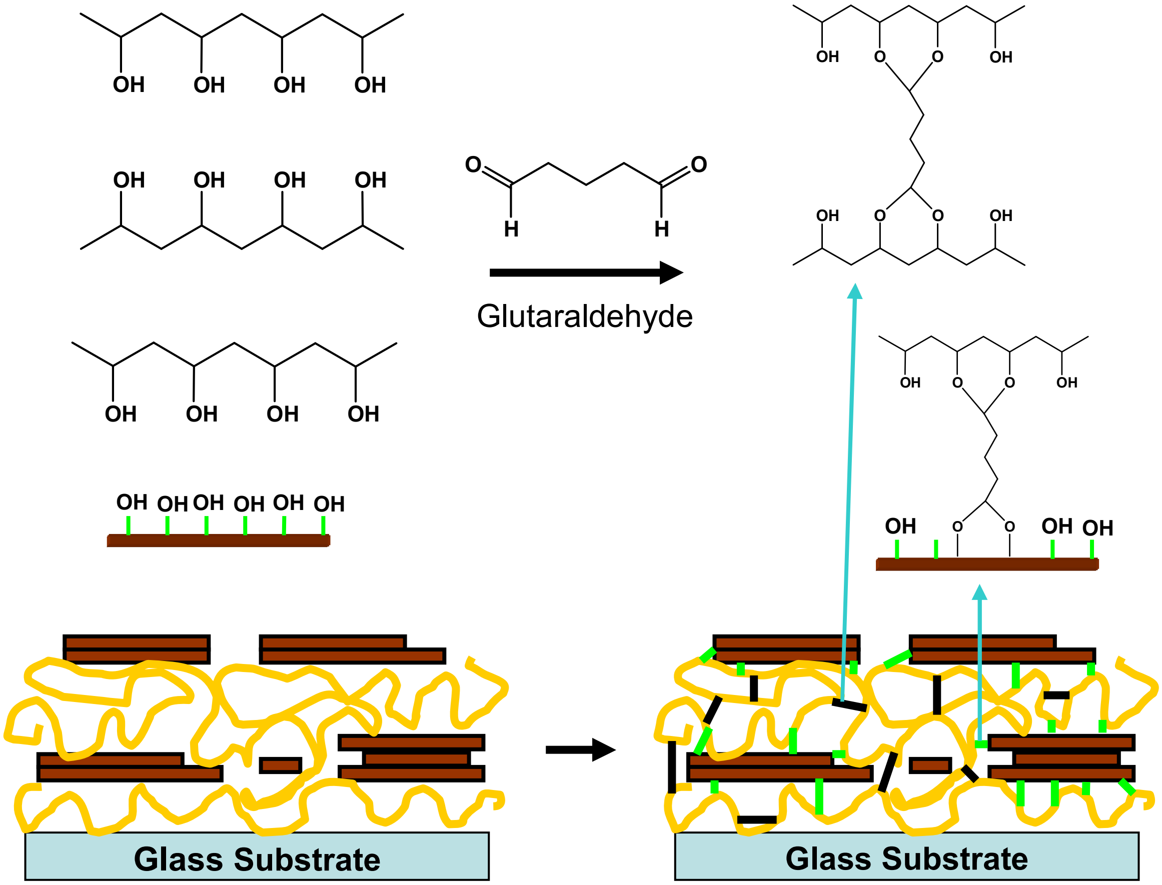

Figure 23. Schematic of glutaraldehyde cross-linking in the PVA-MTM nanocomposite.

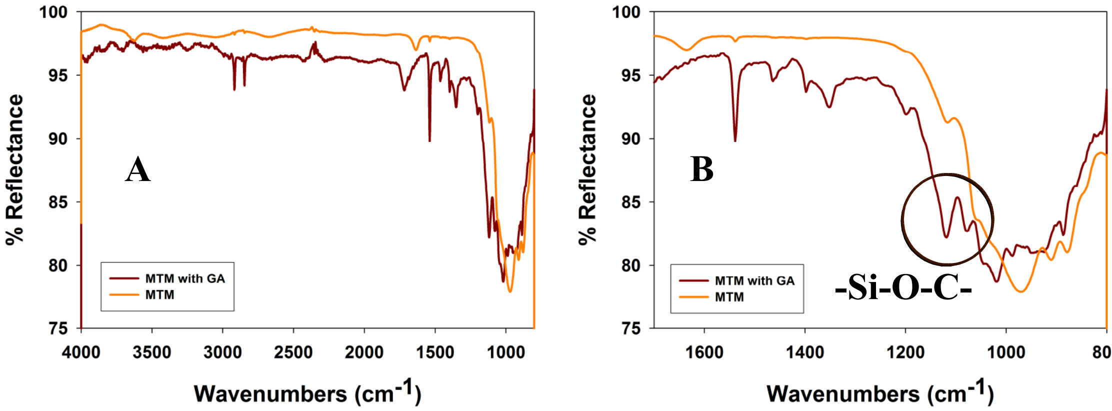

Figure 24. FTIR comparison of MTM and MTM reacted with GA: (A) full spectra and (B) closeup of the spectrum in (A). The appearance of new peaks in the MTM with GA spectrum can be associated with formation of –Si-O-C- bonds.[81]

Cross-linked free-standing films showed high uniformity, strength, flexibility, and remarkable transparency (Figure 18D). UV-Vis spectra of the 300-bilayer free-standing films showed 80-90% transparency across the visible light spectrum while pure PVA showed 90-95% (Figure 25). Thermo-gravimetric analysis showed that the same films were composed in ~70 wt.% (~50 vol.%) of the MTM (Figure 26). This can be explained by the nano-scale dimensions of the inorganic phase, the nearly perfect orientation, and fine dispersion of the nanoplatelets. UV-Vis spectroscopy also showed Fabry-Perot patterns [82,83], which are a further indication of high uniformity of the film.

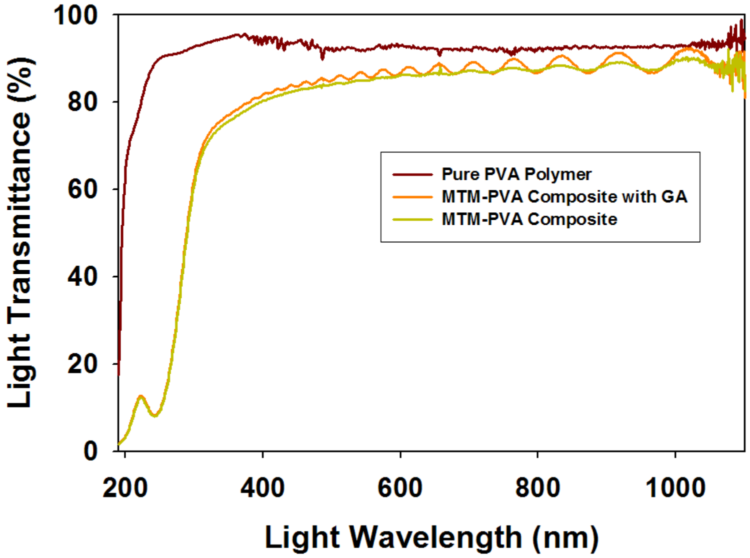

Figure 25. UV-Vis transmittance spectra of pure PVA cast film, 300-bilayer PVA-MTM film, and a 300-bilayer PVA-MTM film with GA cross-linking.

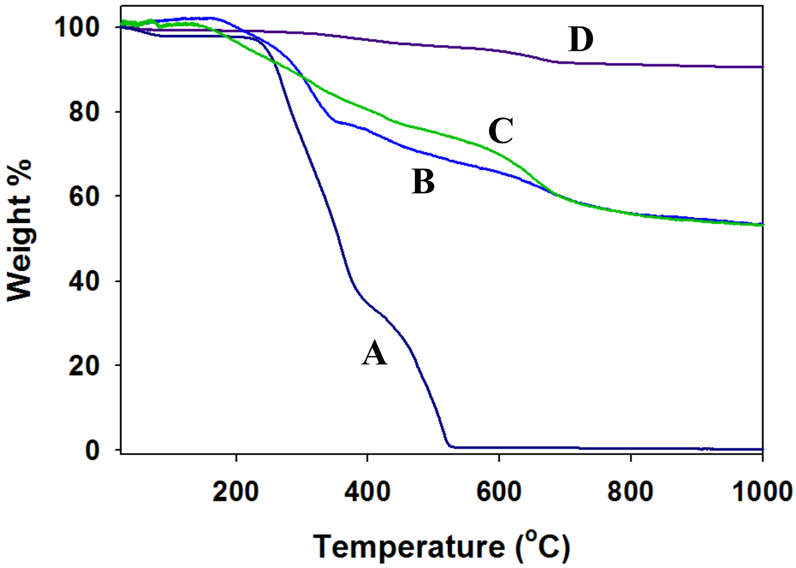

Figure 26. TGA results for (A) pure PVA polymer, (B) 300-bilayer PVA-MTM film, (C) 300-bilayer PVA-MTM film with GA cross-linking, and (D) MTM clay powder.

Evaluation of mechanical properties by microtensile tests gave remarkable results even without GA cross-linking (Table 3 and Figure 27). The nanocomposite displayed ~4x higher strength and nearly an order of magnitude higher modulus when compared to pure PVA polymer. GA cross-linking increased the strength, stiffness, and brittleness of both pure PVA and the PVA-MTM composite. (Figures 27A and 27B) The ultimate tensile strength increased by nearly a factor of three over the uncross-linked PVA-MTM strength and ten times in comparison to that of pure PVA, to values as high as 480 MPa. The modulus of the PVA-MTM with GA exceeded that of uncross-linked PVA-MTM by one order of magnitude and it exceeded the modulus of pure PVA by two orders of magnitude with the highest values reaching 125 GPa. For comparison, the modulus of PVA-MTM with GA is comparable to that of various grades of Kevlar [84-86], $E \sim 80 - 220$ GPa, and exceeds the stiffness of the strongest CNT-based fibers [87]. Additionally, unlike PDDA-MTM composites, the PVA-MTM films with GA cross-linking showed exceptional stability under humid conditions (Figure 28), which is consistent with the covalent character of the bonds responsible for load transfer.

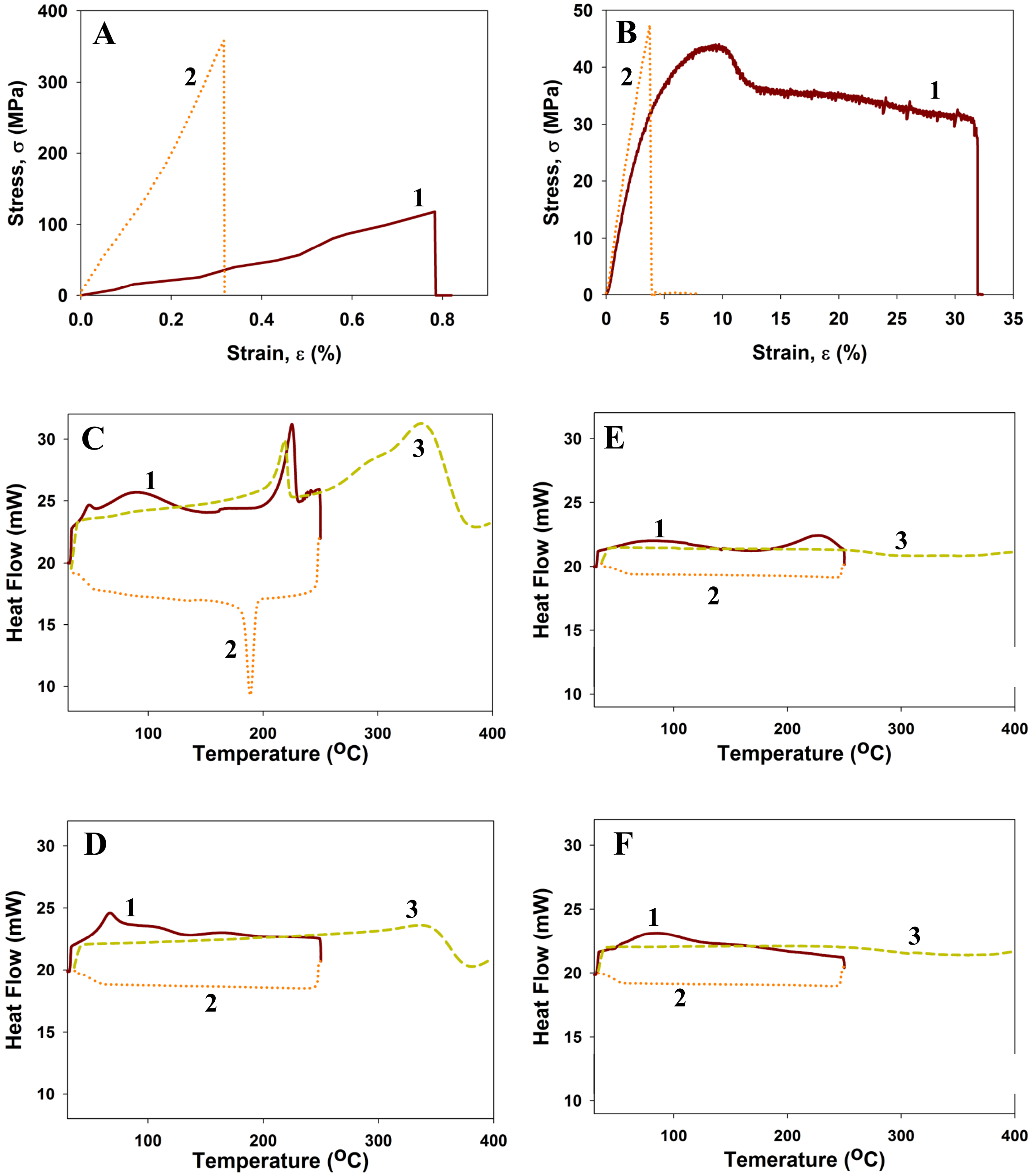

Figure 27. Mechanical and thermal properties of PVA and PVA-MTM nanocomposites. (A) Stress-strain curves for 300-bilayer PVA-MTM composites without (1) and with (2) GA cross-linking. (B) Stress-strain curves for pure PVA polymer without (1) and with (2) GA cross-linking. The stress-strain curves are obtained from a home-built tensiometer (see SOM). (C) – (F) Differential scanning calorimetric analyses results for PVA polymer without (C) and with (D) GA cross-linking and for PVA-MTM without (E) and with (F) GA crosslinking. The DSC scans follow heat (1) – cool (2) – heat (3) cycles as indicated by the numbering on the graphs.

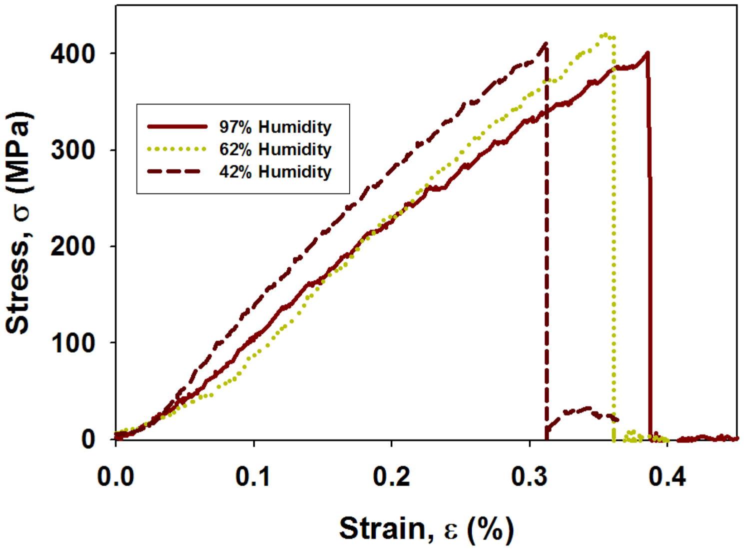

Figure 28. Comparison of mechanical properties of PVA-MTM composite with GA cross-linking under indicated humidity conditions. The samples were equilibrated for at least 30 min prior to testing.

Table 3. Summary of mechanical properties for PVA and its nanocomposites. The data are mean +/- SD. The tensile strengths reported were obtained using both: a commercially available servohydraulic test system and a custom in-house built tensiometer (Figure 16). The moduli were obtained using the custom-built tensiometer. *Data for the PDDA-MTM are the previously published results by *Tang et al.*[88] for 1.2 – 4.9µm (50 – 200 bilayers) thick samples tested at relative humidity of 32%. *N* indicates the minimum number of the experimental data points used in the statistical calculations.

Sample Type (*N*)	Tensile Strength, σ_{UTS} (MPa)	Modulus, *E'* (GPa)	Ultimate Strain, ε (%)
PVA (5)	40 ± 4	1.7 ± 0.2	35 ± 4
PVA with GA (5)	40 ± 10	2.0 ± 0.5	3.3 ± 1.3
PDDA (5)	12 ± 4	0.2 ± 0.03	48 ± 9
PDDA-MTM (*)	100 ± 10	11 ± 2	10 ± 2
PVA-MTM (5)	150 ± 40	13 ± 2	0.7 ± 0.2
PVA-MTM with GA (5)	**400 ± 40**	**106 ± 11**	**0.33 ± 0.04**

Theoretical estimates for nanocomposite properties with nanometer scale spacing of constituents in a polymer and such a large volume fraction of the filler are not available, and the currently recognized theories from the filled rubber literature are not entirely applicable [89]. We believe that the explanation of these results lies in the effective stiffening of the PVA matrix (due to constrained motion of the polymer chains) because of its close proximity to and the many interactions with the MTM platelets. The evidence of this reinforcement mechanism comes from differential scanning calorimetry (DSC) analysis (Figures 27C – 27F), which shows suppression of the thermal motion of the PVA when constrained between dispersed nanoplatelets. This effect should result in the shift in glass transition temperature (T_g) toward the higher values. However overall suppression of motions makes the actual T_g of the polymer not very well defined for such systems as can be seen in the width of the corresponding DSC peaks. Similar effect can be seen from comparison of polymer's melting temperatures (T_m) between pure PVA (Figure 27C) and PVA-MTM (Figure 27E). While the T_m in PVA is sharp and very well defined, PVA-MTM shows strong suppression and broadening of the peak. An additional consequence of such stiffening is that traditional theories of composite mechanics using the bulk properties of pure polymers are difficult to apply to composites with high contents of a uniformly distributed inorganic phase. Mechanical property enhancement in the GA cross-linked PVA-MTM is a result of an increase in the likelihood that a polymer chain in the PVA-MTM with GA system interacts strongly with two or more clay platelets, thereby improving the particle to matrix to particle load transfer process over that in the PVA-MTM system.

4. Conclusions

Reinforcement in polymer-nanoplatelet systems such as PVA-MTM is the result of several mechanisms operating at the nanoscale. The degree of structural organization (afforded by the LBL process) of the clay platelets in the composite maximizes the number of polymer/MTM interactions and constrains the polymer chain motion which results in a highly efficient load transfer between the polymer phase and the stiff MTM platelets.

E. High Strength, Transparent Nacre-Like Nanocomposites with Double Network of Sacrificial Crosslinks.

1. Introduction

In nacre both the "brick-and-mortar" architecture and the sacrificial ionic bonds that can reform after breaking are keys to its mechanical properties.[90,91] These amazing properties have inspired scientists to develop synthetic biomimetic analogs.[92,93] In the biomimetic composite reported previously by our group, the PDDA/MTM NC, ionic cross-links were introduced due to the opposite charges on MTM and PDDA. In the previous section we also showed that LBL assembly of MTM with poly(vinyl alcohol) (PVA) results in a NC with record-high mechanical properties.[94] We found that post-assembly cross-linking of PVA with glutaraldehyde (GA) increases mechanical properties to σ_{UTS} = 150 ➔ 400 MPa and E' = 15 ➔ 106 GPa. Despite the high strength, this cross-linking is covalent, which is not present in nacre, and cannot reform, which revealed itself in the low strain values of the resulting composite.

We have further posed a question: Can we improve LBL materials and potentially exceed the nature-made mechanical properties of nacre and bones using just the reformable (ionic and other) cross-links? Additionally, one can also pose a question whether bonds other than ionic can be engaged in a similar break-reform fashion?[90,91] These are important goals from both fundamental and practical points of view. Nanoscale nacres potentially afford achieving these goals because they offer a greater degree of (1) integration of organic/inorganic phases and (2) freedom in molecular design when compared to microscale lamellar materials including a wide choice of polymers.[94-96]

Here we demonstrate: (1) nacre-like composite with σ_{UTS} far greater than that of any other nacre mimics prepared until now and 2-3x stronger than natural nacre, and (2) the fact that a manifold of weaker bonds can potentially be engaged in a similar manner as sacrificial ionic bonds.

2. Experimental Procedure

The experimental procedures and materials used here are the same as in Sections B2 and D2. Additional materials and procedures are listed here. $FeCl_3$, $CaCl_2$, $AlCl_3$, and $CuCl_2$ salts used in crosslinking of the films were obtained from Sigma-Aldrich. After buildup the glass slides were immersed into the salt solutions for 24 hours at room temperature. In the case of Cu^{2+} the slide was kept in the solution for 3 days. The detached, free-standing films were further dried in a drying oven at 60 ºC and then set aside to equilibrate in ambient conditions (~65 – 75 ºF temperature and ~20 – 30% relative humidity) for at least 24 hours prior to mechanical testing.

3. Results and Discussion

As a start we used LBL films made from PVA and MTM (reported in Section D) which are bound mainly through a manifold of weak hydrogen bonds. Ionic bonds were introduced after assembly by cross-linking PVA with metal cations M^{n+}.[78,97-99] Atomic force microscopy (AFM) revealed full platelet coverage of the surface resembling that in nacre. (Figure 29E).

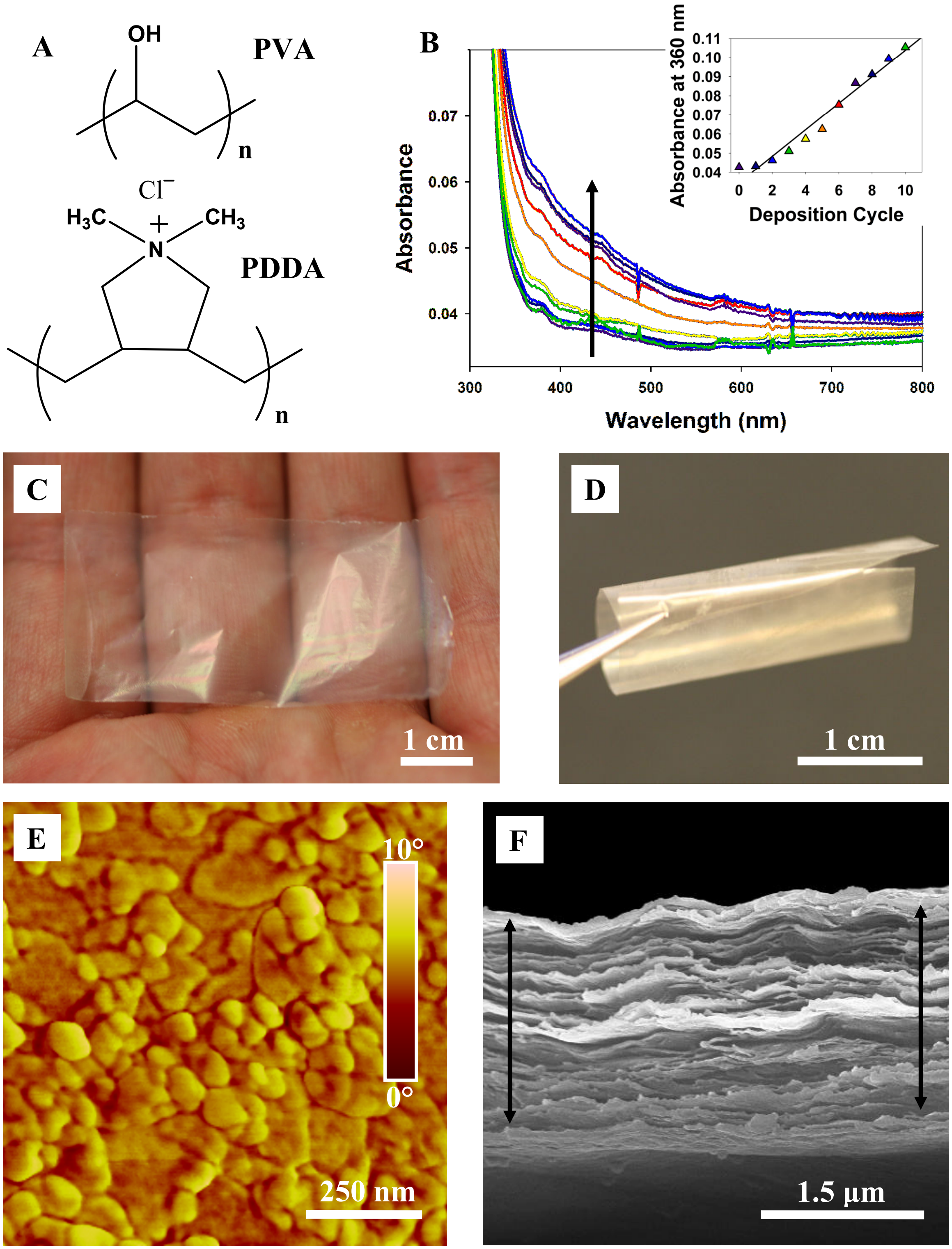

Figure 29. (A) Structure of PVA and PDDA polymers; (B) UV-vis spectra for the first 10 bilayers of deposition (arrow indicates increase of absorbance, inset represents absorbance at 360 nm as a function of bilayer); (C) and (D) optical images of a free standing film of $(PVA/MTM)_{300}$ showing very high transparency and flexibility, (E)

AFM phase image of a single PVA/MTM bilayer, (F) SEM image of cross-section of a 300-bilayer PVA/MTM composite showing laminar architecture. The films in SEM can be slightly expanded due to separation of layers resulting from the shearing force of the razor blade used for cutting test samples.

Growth profile of the films characterized with UV-vis spectroscopy and ellipsometry (Figure 29B) revealed fairly linear growth. As reported previously, ellipsometry measurements gave a thickness of ~3.5 nm per bilayer for the first 10 deposition cycles. 200 and 300 bilayer films were prepared using an automated dipping machine (nanoStrata Inc., Tallahassee, FL). Once completed, films were cross-linked with 0.5 M solutions of M^{n+}, i.e. $FeCl_3$, $CaCl_2$, $AlCl_3$, or $CuCl_2$ for 24 h. Free-standing samples were separated from the slides using a HF etching method described previously[100] and dried at 80 ºC for 10 min. Note that unlike nacre, the ionic bonds in the case of M^{n+} cross-linking are *intramolecular* with respect to PVA chains rather than between the polymer and inorganic plates.

The resulting films were found to be strong, flexible, but also highly transparent, which is attributed to the nanoscale dimensions of the inorganic phase (Figures 29C and 29D) and high orientation of MTM. Light transmittance measurements showed between 50-90% of transparency across the visible spectrum of light for the composites while for plain PVA films it was found to be 90-95%. (Figure 30) Additionally, the transmittance spectra showed Fabry-Perot fringes which are indicative of high uniformity of the films.[101,102]

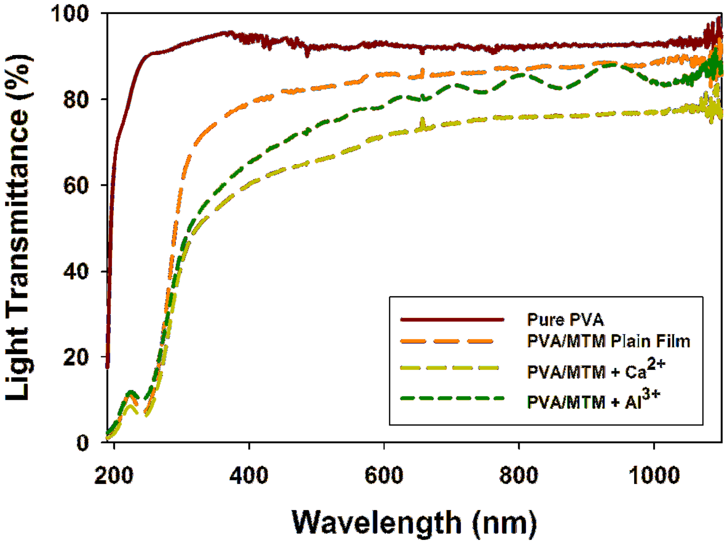

Figure 30. Comparison of UV-vis transmittances for selected $(PVA/MTM)_{300}$ films and pure PVA film.

Although no ionic bonds were involved in PVA/MTM bonding, the *non-cross-linked* films actually showed 50% higher strength then PDDA/MTM samples studied previously (Table 4).[94,100]

Table 4. Compilation of mechanical properties for PDDA/MTM and PVA-based composites.

	Ultimate Tensile Strength, σ_{UTS} (MPa)	Modulus, *E'* (GPa)	Ultimate Strain, ε (%)
Pure PDDA	12 ± 4	0.2 ± 0.03	48 ± 9
Pure PVA	40 ± 4	1.7 ± 0.2	35 ± 4
PDDA/MTM	100 ± 10	11 ± 2	10 ± 1
PVA/MTM Film	150 ± 40	13 ± 2	0.7 ± 0.2
PVA/MTM + Al^{3+}	**250 ± 50**	**41 ± 5**	0.33 ± 0.15
PVA/MTM + Cu^{2+}	**320 ± 40**	**58 ± 6**	0.28 ± 0.02

This increase is due to an abundance of hydrogen and van-der-Waals bonds that can break and reform when the polymer and clay phases slide against each other similarly to ionic bonds in nacre. They also demonstrated relatively high strains. (Figure 31)

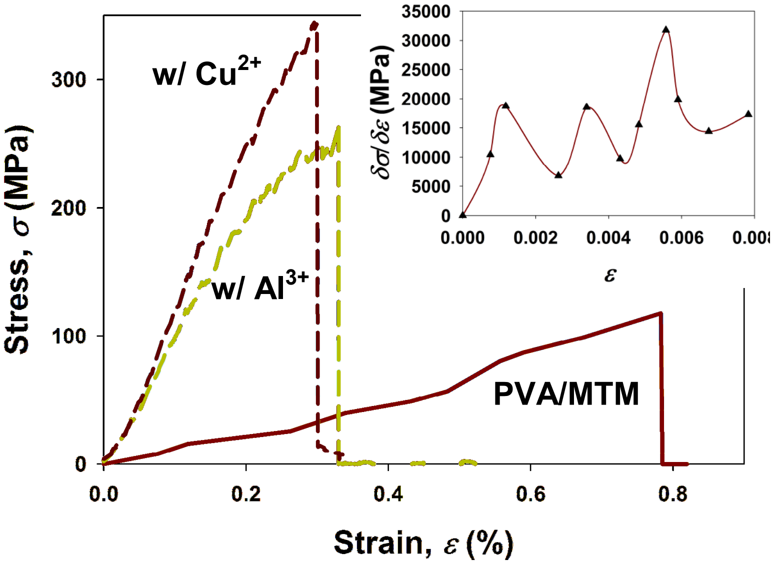

Figure 31. Comparison of stress-strain curves for PVA/MTM films with indicated cross-linkers. Inset shows the differential of the PVA/MTM stress-strain curve revealing the characteristic saw-tooth pattern.

The presence of break-reform mechanism in PVA/MTM can also be seen in differential strain curve (Figure 31, inset) with a characteristic saw-tooth pattern typical for nacre proteins.[90,91] Implementation of M^{n+} cross-linking showed dramatic increases in tensile strength and stiffness: σ_{UTS}, ~150 MPa → ~320 MPa and E', ~13 GPa → ~60 GPa (arrow indicates change after ionic cross-linking). This is especially evident for Cu^{2+} and Al^{3+} treated samples. Ca^{2+} and Fe^{3+}, while being good cross-linking agents for PVA, did not show any improvement at all, which may be attributed to partial bonding of OH groups with clay. The tensile strength of Cu^{2+} cross-linked film is more than twice as high as that of nacre ($\sigma_{UTS} \approx$ 80 - 135 MPa),[103,104] which represents a substantial improvement, and 3x greater then PDDA/MTM composite. Similarly the stiffness of the Cu^{2+} cross-linked film approaches that of nacre ($E \approx$ 60-70 GPa) and it exceeds that of the PDDA/MTM composite by 5x. Strain, however, remains similar to that seen in the PVA/MTM composites cross-linked by GA. It is also somewhat lower than that of nacre (0.8%),[104] which remains the next materials design challenge but can also be potentially improved upon using appropriate polymers.

4. Conclusions

We showed here preparation of a thin film of nacre-like clay nanocomposite which utilizes cross-links from both ionic and other weaker bonds. These cross-links are likely to break and form again in the course of the deformation, which can explain several experimental observations. Nevertheless, we need to be cautious and point out that the exact mechanism of the stretching of PVA molecules sandwiched between the parallel sheets on clay will require special study probably by spectroscopic means. Overall, we obtained material which has superior properties to the original prototype found in nature. This underscores the importance of molecular engineering of the composites and the necessity of the high degree of control over their nanoscale organization. Further directions of improvement of the mechanical performance of these materials must include control over the coiling of the polymer phase to increase extensibility of the material.

F. LBL Assembly of Nacre-Like Nanostructured Composites with Antibacterial Properties

1. Introduction

LBL assembly has also proven invaluable in the ability to merge the functionalities of its components. Through creative experimental setup, one can combine the physical properties of NPs and proteins with the mechanical properties of clays and polymers. The addition of collagen to CdTe NP assemblies, for example, has been found to increase biocompatibility,[105] and monolayers of montmorillonite clay have also been found to control interactions between layers of gold NPs.[106] Combined assemblies of montmorillonite clay and magnetite NPs have led to free-standing NPs films.[107] As demonstrated by the group of V. Tsukruk, incorporation of Au NPs in the polyectrolyte films also resulted in free-standing films with excellent mechanical properties and unique potential applications as highly sensitive acoustic membranes.[108,109]

Such assemblies are recently gaining popularity in the field of biomaterials, creating a demand for biocompatible and antimicrobial thin films as potential coatings for biomedical implants. A variety of solutions have since been developed using LBL assembly to help meet this demand. Several groups demonstrated the ability of multilayer films to control adhesion of mammalian cells.[49,110-113] Bhadra et al. have shown preparation of hollow multilayer capsules loaded with Ciprofloxacin hydrochloride for sustained delivery of this antimicrobial drug.[114] Boulmedais et al. and Kenausis et al. have both presented preparation of multilayer thin films with anti-adhesive properties for both proteins and bacteria.[115,116] Etienne et al. have prepared an active multilayer coating by incorporation of an antimicrobial peptide into the deposition sequence.[117] LBL assembly by the group of M. Bruening of polyethyleneimine-silver ion complex with a polyanion and subsequent reduction to produce *in-situ* silver NPs[118] as well as dendrimeric[119,120] silver NPs have also been successfully implemented as antimicrobial coatings to combat *E. coli*. Such biocompatible assemblies, however, have yet to be applied to a film with the free-standing mechanical properties of the PDDA/MTM artificial nacre.[100]

This study presents an antimicrobial coating for such structures using a multifunctional LBL assembly of PDDA, MTM, and biocompatible, starch-coated silver NPs prepared using a "green" synthesis strategy.[25] Film homogeneity and deposition were monitored using AFM and UV-vis spectrometry, and film stability was analyzed using ICP-MS. Cell culture testing was also performed with *E. coli* and mammalian cells to observe bactericidal activity and cytocompatibility. Such antimicrobial coatings could prove effective for a variety of biomedical devices, and help realize the potential bioapplications of these high strength "nacre-like" composites.

2. Experimental Procedure

The experimental procedures and materials used here are the same as in Sections B2 and D2 unless stated herein.

Materials

The polymers, PDDA, MW ~100,000 and 200,000, and poly(acrylic acid) (PAA, MW 60,000) were purchased from Sigma-Aldrich (St. Louis, MO) and used as received without further purification. Modified Na^+-Montmorillonite, Cloisite Na^+ (MTM) was purchased from Southern Clay Products (Gonzales, TX) and used as received. Polymer solutions were diluted to desired concentrations with $18M\Omega*cm^{-1}$, de-ionized water prior to use in the experiments. Starch indicator was a commercial reagent from Fisher Scientific (Hampton, NH). $AgNO_3$ and β-d-glucose, both used in the Ag NPs synthesis, were obtained from Sigma-Aldrich. Dulbecco's Modified Eagle Medium (DMEM) was purchased from Fisher Scientific, and fetal bovine serum was purchased from GIBCO (Carlsbad, CA). Ampicillin and human osteoblasts were purchased from American Type Culture Collection (ATCC, Manassas, VA).

Silver NP Synthesis

Starch-stabilized Ag NPs were synthesized based on a modified "green" synthesis method published previously.[121] Briefly, 200mL of starch indicator was combined with 3.3mL of 0.10M $AgNO_3$ under gentle heating and stirring in the absence of oxygen. Upon dissolution, 5.0mL of 0.10M β-d-glucose reducing agent was added, and the reaction was allowed to proceed for 24 hours. The resulting solution was deep yellow-brown in color, indicating the presence of metallic silver. This mixture was then used as obtained in the layer-by-layer assembly process.

LBL Assembly of Silver NP Films

The microscope glass slides used in LBL assembly were cleaned by immersion in piranha solution (3:1 $H2SO_4$:H_2O_2, dangerous if contacted with organics) for 1 hour, then thoroughly rinsed with de-ionized water prior to use. 0.5 wt% MTM dispersion was prepared by dissolving 5g of clay powder in 1000 mL of $18M\Omega*cm^{-1}$ and stirring the solution for 1 week prior to use. In order to achieve greater charge density on the surface, slides were pre-coated with $(PDDA/PAA)_3$ prior to the deposition of PDDA/Ag NPs and PDDA/MTM/PDDA/Ag NPs layers, respectively. In the pre-coating process, the slides were immersed sequentially in 0.5 wt% solution of 100,000 MW PDDA for 10 minutes, rinsed with DI water, and dried under a stream of air, followed by a 10-minute immersion in 1.0 wt% PAA, rinsing, and drying. This sequence was repeated 3 times before continuing with composite deposition.

In a typical sample preparation, a glass slide with a $(PDDA/PAA)_3$ primer layer was immersed in 0.5wt% solution of 200,000 MW PDDA for 10 minutes, rinsed with DI water for 1 minute and dried, then immersed in 0.5 wt% MTM dispersion for 10 minutes, rinsed for 1 minute, and again dried. The procedure was then repeated using PDDA and Ag NPs solution to complete one cycle of (PDDA/MTM/PDDA/Ag NPs). This cycle could then be repeated as necessary to obtain the desired number of layers.

The layer-by-layer assembly process was monitored using an 8453 UV-Vis Chem Station spectrophotometer produced by Agilent Technologies, with data collected after each (PDDA/MTM) and (PDDA/MTM/PDDA/Ag NPs) cycle for up to 10 cycles. Images of (PDDA/MTM) and (PDDA/Ag NPs) layers were obtained using a NanoScope IIIa from Veeco Instruments (Santa Barbara, CA) atomic force microscope operated in tapping mode with silicon nitride cantilever tips.

Bacterial Inhibition Evaluation

Ampicillin-resistant gram-negative bacteria, *E. coli* XL1-Blue strain transformed with the pBluescript II KS(-) plasmid (Statagene, La Jolla, CA) were grown overnight in

50 ml of LB ampicillin (10 g/L tryptone, 10 g/L yeast extract, 5 g/L NaCl, 500 mg/L ampicillin) at 37°C under agitation (350 rpm). An aliquot was used to inoculate a 50 ml flask of fresh LB ampicillin medium. When the culture reached an optical density at 600 nm (OD600) of 0.005 – 0.01 after incubation (37°C, 350 rpm), 1 ml of culture was transferred to a sterile 5ml culture tube (0.5 cm inside diameter test tube, Fisher Scientific) containing a single piece of glass slide 25mm x ~5mm coated using LBL assembly on both sides, and incubated for 18 hours as described above (this is a modified version of the standard shake-flask test, ASTM E2149-01) After incubation, the OD600 was read using UV-Vis spectrophotometer to determine the bacterial growth.

Cell viability of the remaining culture after incubation was assessed by colony forming unit (CFU) counting. Typically, a serial dilution of the culture was plated on LB ampicillin agar plates and incubated overnight at 37°C before counting of the colonies. Fresh colonies in fresh medium were also plated for comparison with the same initial density of cells. After incubation, the viable colonies were visible with naked eye and thus could be counted manually. After counting, the number of colonies was compared with the control plates.

Biocompatibility Evaluation

Human Osteoblast cell (ATCC, CRL-11372) culture was grown until full confluence for 1 week in 13mL of 90% DMEM, 10% FBS, and 1% ampicilin medium at 37 ˚C in humidified incubator with 5% CO_2. Square pieces of glass slides (1cm x 1cm): 3x clean without coating, 3x pre-coated only with $(PDDA/PAA)_3$, and 3x coated with $(PDDA/PAA)_3(PDDA/MTM/PDDA/Ag\ NPs)_{10}$ were placed on the bottom of 3 different

12-well plates and sterilized by 70% EtOH immersion followed by 1hour UV irradiation. Cells were then seeded into each well at a density of ~$0.1*10^6$ and incubated for three days. Biocompatibility was assessed by observing the attachment and spreading of the cells on the surfaces.

3. Results and Discussion

Ag NPs Synthesis

To avoid potential problems with stabilizer toxicity, the Ag NPs were synthesized following a modified green synthesis protocol, where a macromolecule of biological origin (starch) was used as a stabilizer.[121] Successful synthesis of these starch-stabilized Ag NPs was confirmed with UV-vis absorbance, and the size of resulting NPs was verified with AFM. The UV-vis absorbance spectrum of the deep yellow-brown Ag NPs solution, which was subsequently used in the LBL procedure without modification, is shown in Figure 32. This spectrum shows an absorbance peak at 410 nm, which matches visual observations and is in agreement with the original green synthesis protocol (λ = 419 nm). The narrow nature of the observed peak also suggests a uniform mixture of NPs with little variation in particle size, which otherwise would have resulted in stretching of the Ag NPs absorbance peak. These solutions of NPs were also found to be quite stable, with no evidence of aggregation during two months of storage.

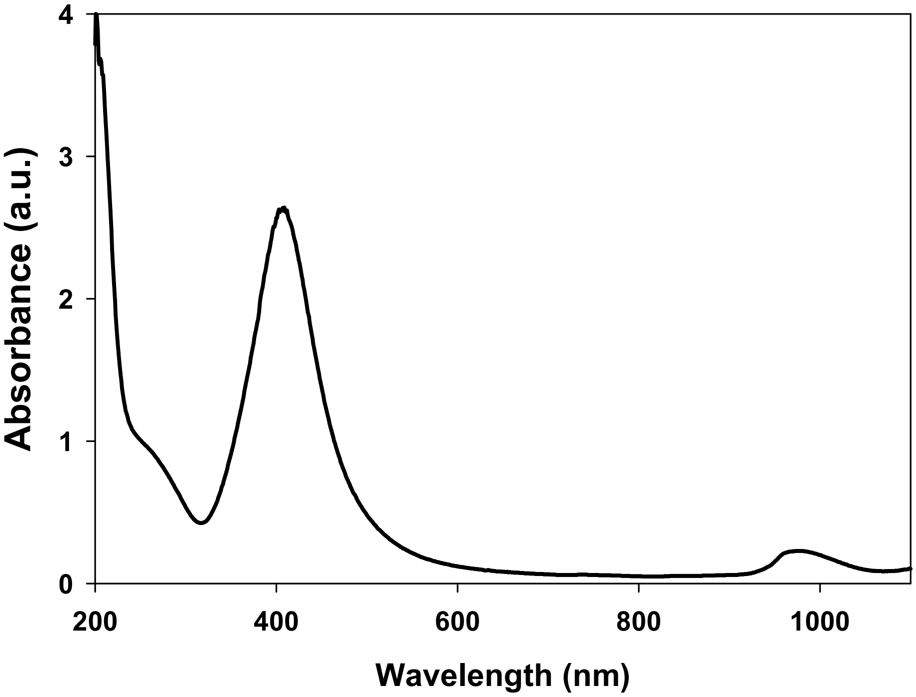

Figure 32. UV-vis absorbance spectrum of Ag NPs solution. The maximum absorbance peak occurs at 410nm.

Figure 33A shows the topographic AFM image of a (PDDA/Ag NPs)$_1$ bilayer, formed on a silica wafer using 10 minute immersions for each component. The image reveals dense packing of spherical Ag NPs, with AFM cross-sectional analysis (Figures 33C and 33D) showing an average NP diameter of 4.3 nm ± 1.5 nm (Figure 33B), which closely correlates with the size reported in the original green synthesis protocol (5.3 nm ± 2.6 nm). This uniform nanoparticle size confirms the lack of variance evidenced by the narrow UV-vis absorbance spectrum in Figure 32.

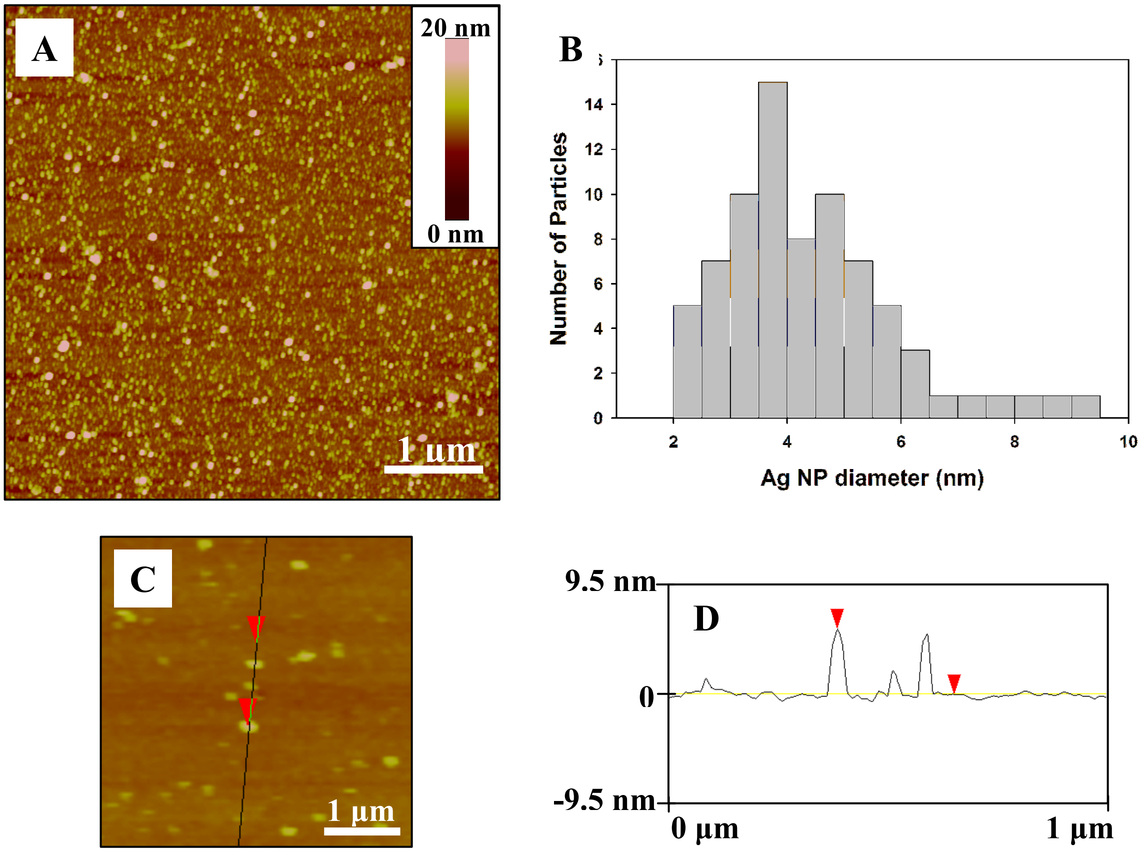

Figure 33. AFM characterization of the Ag NPs size distribution: (A) topography image of a large area, (B) Ag NPs size distribution from counting of 77 particles, (C) magnified topography image used for cross-sectional analysis, and (D) result of the cross sectional analysis on the particular Ag NPs. Average particle size was found to be 4.3nm ± 1.5 nm.

Assembly of (PDDA/MTM) Composites

To confirm proper LBL assembly of the "artificial nacre" structure (Figure 34A), $(PDDA/MTM)_{10}$ films were assembled on a microscope glass slide using ten-minute immersions for both polymer and clay components. Assembly was monitored with UV-vis absorbance measurements where, as detailed previously,[24] successful assembly resulted in linear increase of absorbance with increasing number of layers. Figure 3A is a compilation of UV-vis absorbance spectra collected after deposition of the $(PDDA/PAA)_3$ primer layer and each of the (PDDA/MTM) bilayers. The even increase in absorbance with each additional bilayer suggests regular deposition of PDDA and MTM with each immersion cycle. Successful MTM deposition was also evidenced by the glass slide gradually changing from transparent to opaque (milky color) over the course of deposition.

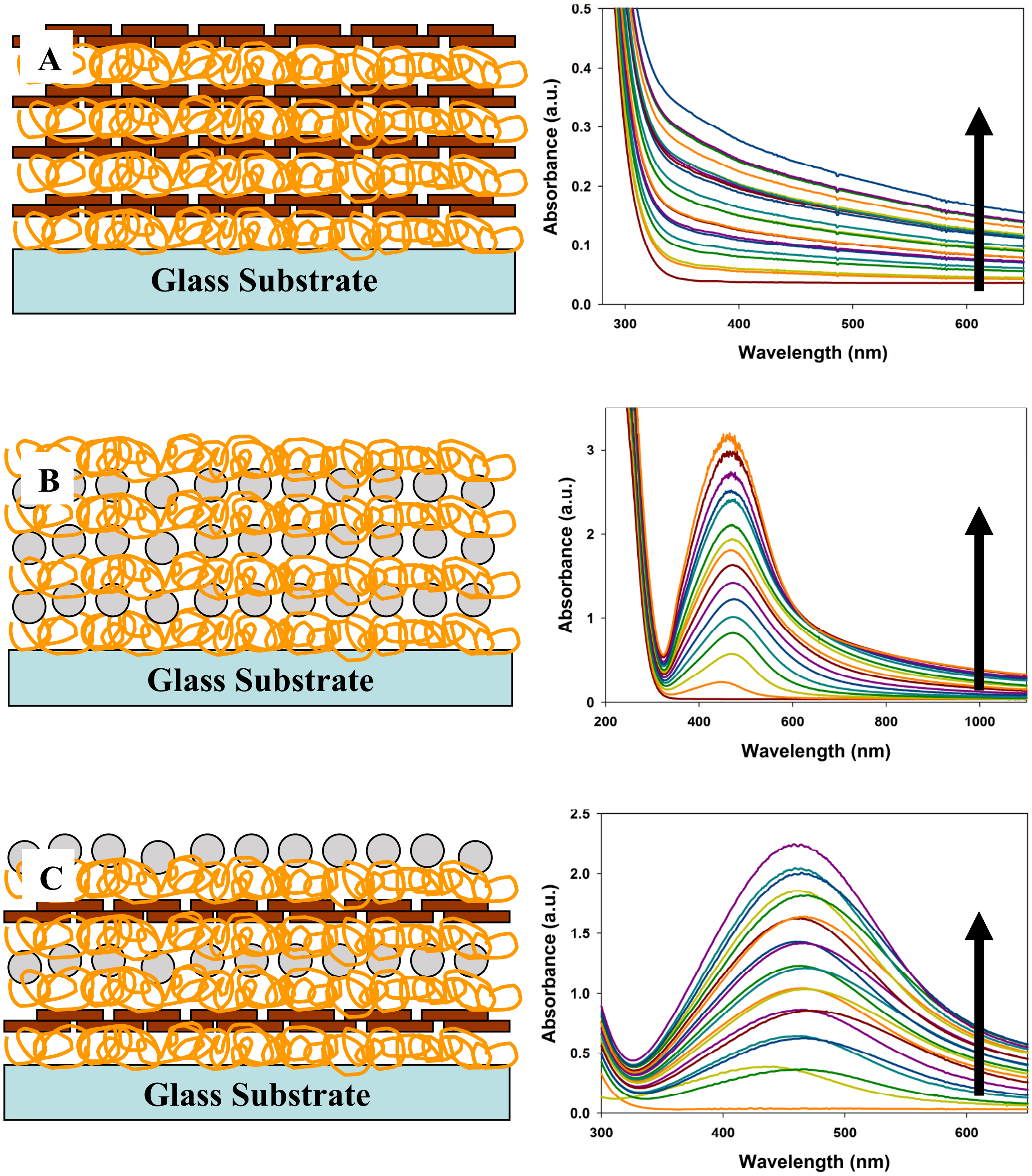

Figure 34. UV-vis absorbance spectra of Layer-by-Layer assembly. (A): schematic diagram of internal architecture and absorbance spectra for $(PDDA/MTM)_{10}$ assembly; (B): schematic diagram of internal architecture and absorbance spectra for (PDDA/Ag

NPs)$_{15}$ assembly; and (C): schematic diagram of internal architecture and absorbance spectra for the hybrid (PDDA/MTM/PDDA/Ag NPs)$_{10}$ assembly. Arrows indicate direction of increase in absorbance.

Assembly of (PDDA/Ag NPs) Composites

Prior to assembling the hybrid clay-Ag NPs composite, a PDDA-Ag NPs system (Figure 34B) was first generated in order to establish appropriate assembly conditions. Priming of the glass slides with (PDDA/PAA)$_3$ and 10 minute adsorption steps resulted in successful formation of the multilayer. Similarly to the (PDDA/MTM) system, Figure 34B shows the compilation of the UV-vis absorbance spectra of a (PDDA/Ag NPs) LBL assembly with ten-minute immersions for each layer and with data collected after each (PDDA/Ag NPs) bilayer for up to fifteen bilayers. The height of the Ag absorbance peak increases linearly with each deposited bilayer, suggesting uniform deposition of Ag NPs throughout the film. This observation was also confirmed visually, as the glass slides evenly changed from clear to a deep yellow-brown, metallic color as the number of deposited layers increased. The red shift in plasmon absorption peak maximum from 410 nm to 460 nm should be attributed to dipole resonance interactions between layers of Ag NPs, a well-documented phenomenon in noble metal NPs.[122-128]

Combined Assembly of MTM, Ag NPs, ad PDDA

Having established the optimum assembly parameters for (PDDA/Ag NPs) system, the combined assembly of (PDDA/Ag NPs/PDDA/MTM) films (Figure 34C) was realized in the same fashion, namely: 10 min adsorption steps with glass slides primed with (PDDA/PAA)$_3$. UV-Vis absorbance spectra were again collected after each

(PDDA/MTM) and (PDDA/Ag NPs) cycle to verify successful deposition. The compiled data, shown in Figure 34C, display the same incremental increases in absorbance as for the (PDDA/Ag NPs) and (PDDA/MTM) samples. A red-shift in Ag absorbance from 410 nm to 460 nm is again present, and absorbance increases linearly with each deposited layer, indicating proper Ag NPs deposition. The deposition of MTM in each cycle was found to stretch and slightly red-shift the maximum of the peak, from 460 nm to 465-470 nm. Subsequent deposition of (PDDA/Ag NPs) resulted in reversal of the effect to the original value. The slight red shift can be explained by high value of MTM's dielectric constant, $\varepsilon = 100\text{-}550$,[129] as compared to typical values for polyelectrolytes of $\varepsilon \approx 10$.[130] The groups of P. Mulvany and L. M. Liz-Marzan have developed a model for gold NPs LBL film,[128] showing that increasing volume fraction of NPs results in red-shift of the peak. At the same time it is expected that increasing separation between Ag NPs layers, will lead to a blue-shift of the spectrum.[128] MTM has been shown to increase overall dielectric constant of a polyelectrolyte composite up to 7 times at volume fractions as low as 5%.[131] In our system, we believe that we are observing a combined effect of the blue-shift from separation increase and red-shift from the MTM inclusion. It can be also expected that subsequent inclusion of the PDDA/Ag NPs layer decreases the volume fraction of MTM which leads to reversal of the effect. Similarly to previous observations, the combined film gradually turned metallic deep-brown with increasing number of layers. Opaqueness was also present with each additional MTM layer added, which was not seen in the (PDDA/Ag NPs) system. This fact is a simple visual criterion for incorporation of MTM layers and successful assembly of the hybrid.

Bactericidal Properties of the Hybrid Composites

Silver has long been known to be a potent antimicrobial agent and its beneficial effects on wound biology have in general been overlooked until recently. Silver ions and silver compounds are known to be potent antimicrobial agents against most of bacteria including *E. coli*,[132-134] while only a few rare strains are silver-resistant.[135-137] In its uncharged state, in the form of Ag NPs, silver was also found to possess antimicrobial properties. Although the mechanism of action is still unresolved, it has been shown that Ag NPs interact with the constituents of the outer membrane, causing structural changes, degradation, and finally cell death.[138] An additional beneficial effect of Ag NPs, which may present an additional advantage for wound healing around implanted material, is anti-inflammatory property.[139] While experiments against bacteria with Ag NPs in solution showed eventual depletion of silver and only growth delay,[138] LBL assembly allows for immobilization of Ag NPs in ultra thin films on complicated geometries. Combined with high strength, this coating method offers new alternative for biomedical, implantable devices.

To establish bactericidal properties of our composite, a suspension of bacterial cells (*E. coli*) was placed in a round-bottom test tube together with rectangular piece of a glass slide coated with 10 deposition cycles of the composite. Experiments were carried out both under static and dynamic (shaking) conditions. After 18 hours of incubation the concentration of cells inside the tubes was measured and compared to the inoculation conditions. When the experiments were performed under dynamic conditions, with initial bacteria concentration, OD600 = 0.0048, almost complete inhibition was observed (Table 5). The supernatant was further plated onto agar plates at 10x dilutions with fresh medium. Both original and diluted suspensions grew into viable colonies overnight with CFU reaching that of control plates. This suggests that the inhibition of bacteria can be attributed to the direct interaction of the cells with the silver immobilized in the composite. The fact that single layer of Ag NPs is much less effective then 10 layers also shows that certain concentration of silver is required for high levels of inhibition at these bacterial concentrations.

Table 5. Bacterial inhibition with a hybrid composite under dynamic conditions. Initial optical densities were OD600 = 0.0048 and 0.066. OD 600 measurements of bacterial suspensions were measured after 18 hours of incubation. Comparison was against bare glass slides (Control) and to glass slides coated with $(PDDA/PAA)_3$ (Precoat). Control solutions which reached high OD600 were diluted 30 times before taking the measurement. At least 3 measurements were performed for 3 samples each time and the results are shown as averages of these results.

Inoculation OD_{600}		OD_{600}
0.0048	Control	2.002 ± 0.267
	$(AgNPs/MTM)_{10}$	0.0071 ± 0.28
	$(AgNPs/MTM)_{10}$ + $(PDDA/MTM)_1$	0.0047 ± 0.28
0.066	Control	2.096 ± 0.101
	Precoat	2.492 ± 0.032
	$(AgNPs/MTM)_1$	2.477 ± 0.092
	$(AgNPs/MTM)_{10}$	0.193 ± 0.030

Further experiments with higher initial concentration of bacteria, OD600 = 0.066, show slightly decreased effectiveness of the composite (Table 5). In analogy to the first result, we found that single layer of silver does not present high enough concentration to provide effective inhibition. We also found that the inhibition can mostly be attributed to the presence of silver and not to any of the poly-ions (PDDA and PAA) or clay.

Under static conditions we have observed very little inhibition, <10 %. The concentration of cells in the control after 18 hours of incubation reached OD600 = 0.949 ± 0.055 whereas for the coated slides the concentration reached OD600 = 0.853 ± 0.023 (initial concentration was OD_{600} = 0.066). The overall concentration of cells was lower as compared to the agitated experiments, but this can be attributed to decreased diffusion of oxygen and thus starvation. After 18 hours, cells have settled into the meniscus below the glass slide hence avoiding contact with the composite. The growth process was most likely retarded during sedimentation were small percentage of the cells came in contact with the surface.

Silver Elution from the Hybrid Composite

Antimicrobial properties of these composites are attributed to the Ag NPs immobilized on the surface of this material. Hence, evaluation of the stability of the composite in aqueous medium is important for long term durability and effectiveness. None of the previous studies have attempted determination of the actual amount of silver eluting from such composites. This is important because high concentration of oxidized silver, Ag^+, can be toxic for human cells[140-142] and potentially cause adverse effects for long-term implants. Considering high surface energy and therefore greater chemical potential of silver in NPs, the actual amount of silver could be substantially higher than for bulk pieces of the same metal. In order to determine actual amounts of eluted silver, glass slides coated with $(PDDA/MTM/PDDA/Ag\ NPs)_{10}$ were immersed in de-ionized water for 25 days, with solution aliquots collected at regular intervals and analyzed by ICP-MS for trace levels of Ag leaching out from the composite. Samples were collected from slides placed in both light and dark conditions in order to account for possible Ag NPs photoreactivity. After 25 days, films retained their integrity and no visible change in water color was observed in either light or dark environments. ICP-MS analysis of the sample aliquots retained after different time intervals showed that silver was eluting in miniscule concentrations in the range of 0.5-2.0 and 0-3.3 μg/L for dark and light conditions correspondingly (Figure 35). Therefore, one can say that the overall silver concentration around the implanted LBL nanocomposite (PDDA/MTM/PDDA/Ag NPs)$_{10}$ does not exceed 3.0 μg/L.

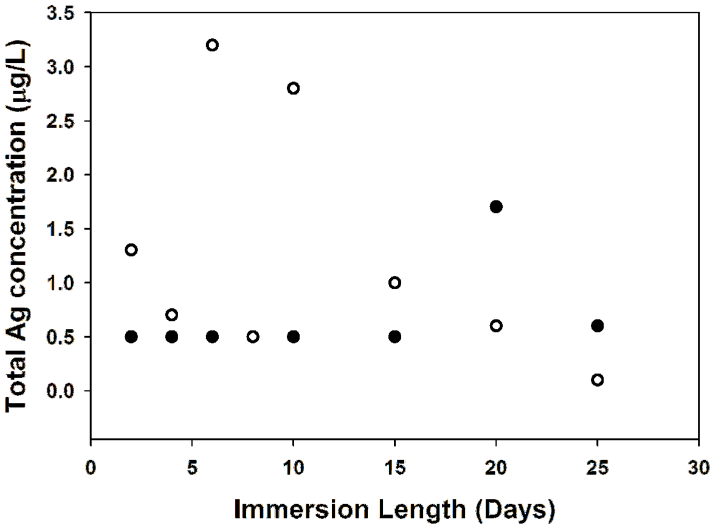

Figure 35. Analysis of the hybrid MTM-Ag NPs' composite film stability for Ag elution. ICP-MS analysis of the water solution after immersion shows levels of Ag below the detection limit of the instrument. Both Dark (filled symbol) and Light (open symbol) conditions show similar results.

Biocompatibility Evaluation

Although the concentration of eluting silver is very small, direct evaluation of the biocompatibility of the composite would be necessary for further studies of this material. Ag NPs have been shown to possess good biocompatibility with mouse fibroblasts and human osteoblasts[143] and their use for bio-applications has been widely documented.[42,144,145] To evaluate the effect of our composite, glass slides coated with the films were cut into smaller pieces and placed in the 12-well plates. Following sterilization with 70% EtOH and UV-vis irradiation, cells were seeded on top of the slides and allowed to attach and grow for 3 days. One of the indications of biocompatibility characteristics of this cell line is their attachment to the surface. Figure 36 shows cells attaching on the surface of the composite. The number of attaching cells was not as high as for the bare slides however it is possible to render the composite more biocompatible by coating with additional components. When additional capping layers were introduced on top of the composite, no change in antibacterial properties was observed (Table 5). The same experiment was repeated with 5 bilayers of (PDDA/MTM) of capping (data not shown) and the same level of inhibition was achieved. This suggests that additional, interfacing layers could be introduced on top of the composite to improve the cell attachment without having to sacrifice the bactericidal properties.

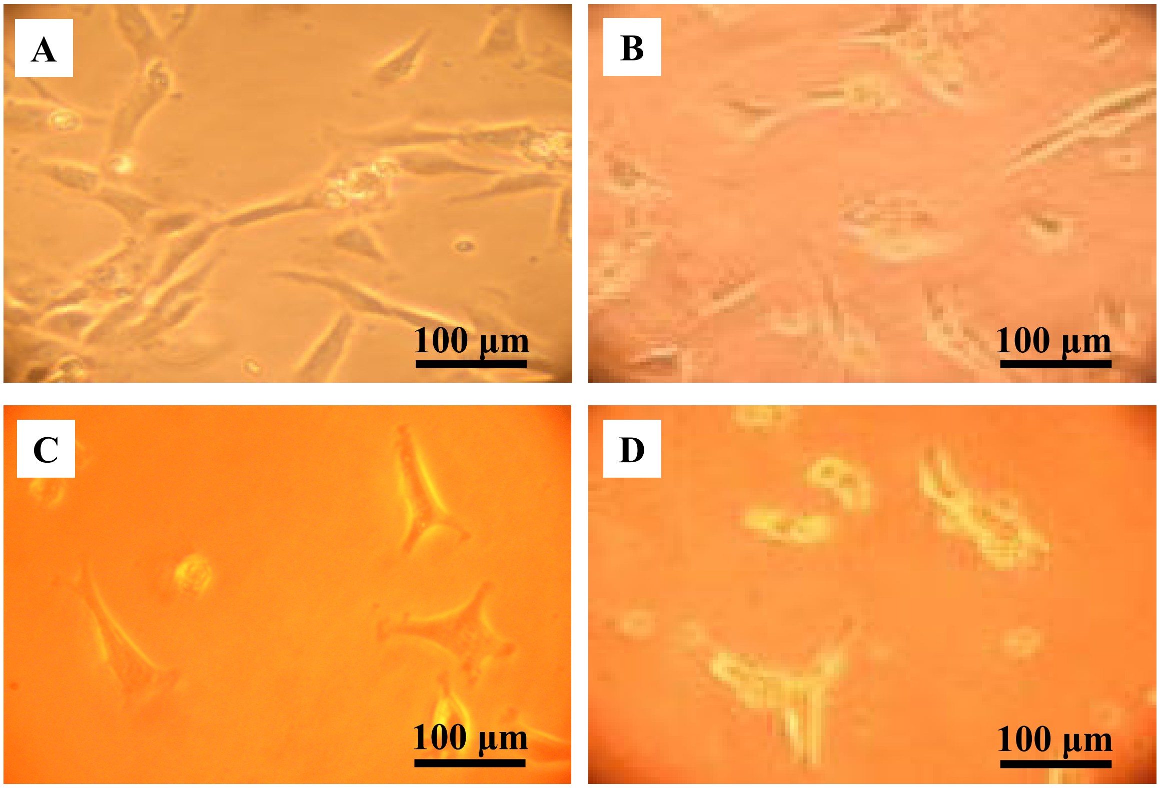

Figure 36. Optical microscopy images of Human Osteoblasts (ATCC, CRL-11372) cultured on bare glass slides ((A) and (B)) and on glass slides coated with (PDDA/MTM/PDDA/Ag NPs)$_{10}$ ((C) and (D)) for 3 days.

4. Conclusions

We have presented here preparation of a nanostructured, hybrid and multifunctional, composite containing Ag NPs with good mechanical properties based on the polymer/MTM structure. The composite possesses strong antibacterial characteristics as well as biocompatibility with human osteoblasts. With wide variety of materials available, this type of composites can be expanded to additional functionalities, e.g. controlled drug delivery.

Reference List

1. Coyne, K. J.; Qin, X. X.; Waite, J. H. Extensible collagen in mussel byssus: a natural block copolymer. *Science (Washington, D. C.)* **1997,** *277* (5333), 1830-1832.

2. Currey, J. D. Mechanical properties of mollusc shell. *Symposia of the Society for Experimental Biology* **1980,** *34*, 75-97.

3. Currey, J. Biomaterials: Sacrificial bonds heal bone. *Nature (London, United Kingdom)* **2001,** *414* (6865), 699.

4. Wang, R. Z.; Suo, Z.; Evans, A. G.; Yao, N.; Aksay, I. A. Deformation mechanisms in nacre. *Journal of Materials Research* **2001,** *16* (9), 2485-2493.

5. Shao, Z.; Vollrath, F. Surprising strength of silkworm silk. *Nature* **2002,** *418* (6899), 741.

6. Lewis, R. V. Spider silk: Ancient ideas for new biomaterials. *Chemical Reviews (Washington, DC, United States)* **2006,** ACS.

7. Aksay, I. A.; Trau, M.; Manne, S.; Honma, I.; Yao, N.; Zhou, L.; Fenter, P.; Eisenberger, P. M.; Gruner, S. M. Biomimetic pathways for assembling inorganic thin films. *Science (Washington, D. C.)* **1996,** *273* (5277), 892-898.

8. Smith, B. L.; Schaffer, T. E.; Viani, M.; Thompson, J. B.; Frederick, N. A.; Kind, J.; Belcher, A.; Stucky, G. D.; Mors, D. E.; Hansma, P. K. Molecular mechanistic origin of the toughness of natural adhesives, fibers and composites. *Nature (London)* **1999,** *399* (6738), 761-763.

9. Rousseau, M.; Lopez, E.; Stempfle, P.; Brendle, M.; Franke, L.; Guette, A.; Naslain, R.; Bourrat, X. Multiscale structure of sheet nacre. *Biomaterials* **2005,** *26* (31), 6254-6262.

10. Rousseau, M.; Lopez, E.; Coute, A.; Mascarel, G.; Smith, D. C.; Naslain, R.; Bourrat, X. Sheet nacre growth mechanism: a Voronoi model. *Journal of structural biology* **2005,** *149* (2), 149-157.

11. Katti, K. S.; Katti, D. R.; Pradhan, S. M.; Bhosle, A. Platelet interlocks are the key to toughness and strength in nacre. *Journal of Materials Research* **2005,** *20* (5), 1097-1100.

12. Song, F.; Soh, A. K.; Bai, Y. L. Structural and mechanical properties of the organic matrix layers of nacre. *Biomaterials* **2003,** *24* (20), 3623-3631.

13. Nassif, N.; Pinna, N.; Gehrke, N.; Antonietti, M.; Jaeger, C.; Coelfen, H. Amorphous layer around aragonite platelets in nacre. *Proceedings of the National*

Academy of Sciences of the United States of America **2005,** *102* (36), 12653-12655.

14. Evans, A. G.; Suo, Z.; Wang, R. Z.; Aksay, I. A.; He, M. Y.; Hutchinson, J. W. Model for the robust mechanical behavior of nacre. *Journal of Materials Research* **2001,** *16* (9), 2475-2484.

15. Li, X.; Chang, W. C.; Chao, Y. J.; Wang, R.; Chang, M. Nanoscale Structural and Mechanical Characterization of a Natural Nanocomposite Material: The Shell of Red Abalone. *Nano Letters* **2004,** *4* (4), 613-617.

16. Jackson, A. P.; Vincent, J. F. V.; Turner, R. M. The Mechanical Design of Nacre. *Proceedings of the Royal Society of London Series B-Biological Sciences* **1988,** *234* (1277), 415-&.

17. Sellinger, A.; Weiss, P. M.; Anh, N.; Lu, Y.; Assink, R. A.; Gong, W.; Brinker, C. J. Continuous self-assembly of organic-inorganic nanocomposite coatings that mimic nacre. *Nature (London)* **1998,** *394* (6690), 256-260.

18. Deville, S.; Saiz, E.; Nalla, R. K.; Tomsia, A. P. Freezing as a Path to Build Complex Composites. *Science (Washington, DC, United States)* **2006,** *311* (5760), 515-518.

19. Zhang, X.; Liu, C.; Wu, W.; Wang, J. Evaporation-induced self-assembly of organic-inorganic ordered nanocomposite thin films that mimic nacre. *Materials Letters* **2006,** *60* (17-18), 2086-2089.

20. Volkmer, D.; Harms, M.; Gower, L.; Ziegler, A. Morphosynthesis of nacre-type laminated CaCO3 thin films and coatings. *Angewandte Chemie, International Edition* **2005,** *44* (4), 639-644, S639-1.

21. Pezzotti, G.; Asmus, S. M. F.; Ferroni, L. P.; Miki, S. In situ polymerization into porous ceramics: a novel route to tough biomimetic materials. *Journal of Materials Science: Materials in Medicine* **2002,** *13* (8), 783-787.

22. Wang, C. A.; Huang, Y.; Zan, Q.; Guo, H.; Cai, S. Biomimetic structure design - a possible approach to change the brittleness of ceramics in nature. *Materials Science & Engineering, C: Biomimetic and Supramolecular Systems* **2000,** *C11* (1), 9-12.

23. Zhang, S.; Zhang, J.; Zhang, Z.; Dang, H.; Liu, W.; Xue, Q. Preparation and characterization of self-assembled organic-inorganic nacre-like nanocomposite thin films. *Materials Letters* **2004,** *58* (17-18), 2266-2269.

24. Tang, Z.; Kotov, N. A.; Magonov, S.; Ozturk, B. Nanostructured artificial nacre. *Nature Materials* **2003,** *2* (6), 413-418.

25. Podsiadlo, P.; Paternel, S.; Rouillard, J. M.; Zhang, Z.; Lee, J.; Lee, J. W.; Gulari, E.; Kotov, N. A. Layer-by-Layer Assembly of Nacre-like Nanostructured Composites with Antimicrobial Properties. *Langmuir* **2005,** *21* (25), 11915-11921.

26. Mamedov, A.; Ostrander, J.; Aliev, F.; Kotov, N. A. Stratified Assemblies of Magnetite Nanoparticles and Montmorillonite Prepared by the Layer-by-Layer Assembly. *Langmuir* **2000,** *16* (8), 3941-3949.

27. Kachurina, O.; Knobbe, E.; Metroke, T. L.; Ostrander, J. W.; Kotov, N. A. Corrosion protection with synergistic LBL/ormosil nano-structured thin films. *International Journal of Nanotechnology* **2004,** *1* (3), 347-365.

28. Podsiadlo, P.; Tang, Z.; Shim, B. S.; Kotov, N. A. Counterintuitive Effect of Molecular Strength and Role of Molecular Rigidity on Mechanical Properties of Layer-by-Layer Assembled Nanocomposites. *Nano Letters* **2007,** *7* (5), 1224-1231.

29. Podsiadlo, P.; Liu, Z.; Paterson, D.; Messersmith, P. B.; Kotov, N. A. Fusion of seashell nacre and marine bioadhesive analogs: high-strength nanocomposite by layer-by-layer assembly of clay and L-3,4-dihydroxyphenylalanine polymer. *Advanced Materials (Weinheim, Germany)* **2007,** *19* (7), 949-955.

30. Podsiadlo, P.; Kaushik, A. K.; Arruda, E. M.; Waas, A. M.; Shim, B. S.; Xu, J.; Nandivada, H.; Pumplin, B. G.; Lahann, J.; Ramamoorthy, A.; Kotov, N. A. Ultrastrong and Stiff Layered Polymer Nanocomposites. *Science (Washington, DC, United States)* **2007,** *318* (5847), 80-83.

31. Gao, H.; Ji, B.; Jager, I. L.; Arzt, E.; Fratzl, P. Materials become insensitive to flaws at nanoscale: Lessons from nature. *Proceedings of the National Academy of Sciences of the United States of America* **2003,** *100* (10), 5597-5600.

32. Jager, I.; Fratzl, P. Mineralized collagen fibrils: a mechanical model with a staggered arrangement of mineral particles. *Biophysical Journal* **2000,** *79* (4), 1737-1746.

33. Halpin, J. C.; Kardos, J. L. The Halpin-Tsai equations: a review. *Polymer Engineering and Science* **1976,** *16* (5), 344-352.

34. Kumar, M. N. V. R. A review of chitin and chitosan applications. *Reactive & Functional Polymers* **2000,** *46* (1), 1-27.

35. Camilo, C. S.; dos Santos, D. S., Jr.; Rodrigues, J. J., Jr.; Vega, M. L.; Campana Filho, S. P.; Oliveira, O. N., Jr.; Mendonca, C. R. Surface-Relief Gratings and Photoinduced Birefringence in Layer-by-Layer Films of Chitosan and an Azopolymer. *Biomacromolecules* **2003,** *4* (6), 1583-1588.

36. dos Santos, D. S., Jr.; Bassi, A.; Rodrigues, J. J., Jr.; Misoguti, L.; Oliveira, O. N., Jr.; Mendonca, C. R. Light-Induced Storage in Layer-by-Layer Films of Chitosan and an Azo Dye. *Biomacromolecules* **2003,** *4* (6), 1502-1505.

37. Sotero Dos Santos, D., Jr.; Bassi, A.; Misoguti, L.; Ginani, M. F.; Novais De Oliveira, O., Jr.; Mendonca, C. R. Spontaneous birefringence in layer-by-layer films of chitosan and azo dye Sunset Yellow. *Macromolecular Rapid Communications* **2002,** *23* (16), 975-977.

38. Serizawa, T.; Yamaguchi, M.; Akashi, M. Enzymatic Hydrolysis of a Layer-by-Layer Assembly Prepared from Chitosan and Dextran Sulfate. *Macromolecules* **2002,** *35* (23), 8656-8658.

39. Tachaboonyakiat, W.; Serizawa, T.; Endo, T.; Akashi, M. The influence of molecular weight over the ultrathin films of biodegradable polyion complexes between chitosan and poly(g-glutamic acid). *Polymer Journal (Tokyo)* **2000,** *32* (6), 481-485.

40. Constantine, C. A.; Gattas-Asfura, K. M.; Mello, S. V.; Crespo, G.; Rastogi, V.; Cheng, T. C.; Defrank, J. J.; Leblanc, R. M. Layer-by-layer biosensor assembly incorporating functionalized quantum dots. *Langmuir* **2003,** *19* (23), 9863-9867.

41. Constantine, C. A.; Mello, S., V; Dupont, A.; Cao, X.; Santos, D., Jr.; Oliveira, O. N., Jr.; Strixino, F. T.; Pereira, E. C.; Cheng, T.; Defrank, J. J.; Leblanc, R. M. Layer-by-layer self-assembled chitosan/poly(thiophene-3-acetic acid) and organophosphorus hydrolase multilayers. *Journal of the American Chemical Society* **2003,** *125* (7), 1805-1809.

42. Xu, X. H.; Han, B.; Fu, Y. S.; Han, J.; Shi, H. B.; Wu, B.; Han, S.; Chen, Q. Preparation of chitosan/glucose oxidase nanolayered films for electrode modification by the technique of layer-by-layer self-assembly. *Journal of Materials Science Letters* **2003,** *22* (9), 695-697.

43. dos Santos, D. S., Jr.; Riul, A., Jr.; Malmegrim, R. R.; Fonseca, F. J.; Oliveira, O. N., Jr.; Mattoso, L. H. C. A layer-by-layer film of chitosan in a taste sensor application. *Macromolecular Bioscience* **2003,** *3* (10), 591-595.

44. Riul, A.; de Sousa, H. C.; Malmegrim, R. R.; dos Santos, D. S.; Carvalho, A. C. P. L.; Fonseca, F. J.; Oliveira, O. N.; Mattoso, L. H. C. Wine classification by taste sensors made from ultra-thin films and using neural networks. *Sensors and Actuators, B: Chemical* **2004,** *B98* (1), 77-82.

45. Huguenin, F.; dos Santos, D. S., Jr.; Bassi, A.; Nart, F. C.; Oliveira, O. N., Jr. Charge storage capability in nanoarchitectures of V2O5/chitosan/poly(ethylene oxide) produced using the layer-by-layer technique. *Advanced Functional Materials* **2004,** *14* (10), 985-991.

46. Huguenin, F.; Nart, F. C.; Gonzalez, E. R.; Oliveira, O. N., Jr. Using the Quadratic Logistic Equation To Analyze Intercalation of Lithium Ions in Layer-by-Layer V2O5 Films. *Journal of Physical Chemistry B* **2004,** *108* (49), 18919-18924.

47. Huguenin, F.; Gonzalez, E. R.; Oliveira, O. N., Jr. Electrochemical and Electrochromic Properties of Layer-by-Layer Films from WO3 and Chitosan. *Journal of Physical Chemistry B* **2005,** *109* (26), 12837-12844.

48. Ye, S.; Wang, C.; Liu, X.; Tong, Z. Deposition temperature effect on release rate of indomethacin microcrystals from microcapsules of layer-by-layer assembled chitosan and alginate multilayer films. *Journal of Controlled Release* **2005,** *106* (3), 319-328.

49. Zhu, Y.; Gao, C.; He, T.; Liu, X.; Shen, J. Layer-by-Layer Assembly To Modify Poly(L-lactic acid) Surface toward Improving Its Cytocompatibility to Human Endothelial Cells. *Biomacromolecules* **2003,** *4* (2), 446-452.

50. Liu, Y.; He, T.; Gao, C. Surface modification of poly(ethylene terephthalate) via hydrolysis and layer-by-layer assembly of chitosan and chondroitin sulfate to construct cytocompatible layer for human endothelial cells. *Colloids and Surfaces, B: Biointerfaces* **2005,** *46* (2), 117-126.

51. Claesson, P. M.; Ninham, B. W. pH-dependent interactions between adsorbed chitosan layers. *Langmuir* **1992,** *8* (5), 1406-1412.

52. Lazaridou, A.; Biliaderis, C. G. Thermophysical properties of chitosan, chitosan-starch and chitosan-pullulan films near the glass transition. *Carbohydrate Polymers* **2002,** *48* (2), 179-190.

53. Srivastava, S. K.; Pramanik, M.; Acharya, H. Ethylene/vinyl acetate copolymer/clay nanocomposites. *Journal of Polymer Science, Part B: Polymer Physics* **2006,** *44* (3), 471-480.

54. Jordan, J.; Jacob, K. I.; Tannenbaum, R.; Sharaf, M. A.; Jasiuk, I. Experimental trends in polymer nanocomposites-a review. *Materials Science & Engineering, A: Structural Materials: Properties, Microstructure and Processing* **2005,** *A393* (1-2), 1-11.

55. Ray, S. S.; Bousmina, M. Biodegradable polymers and their layered silicate nanocomposites: In greening the 21st century materials world. *Progress in Materials Science* **2005,** *50* (8), 962-1079.

56. Waite, J.; Andersen, N.; Jewhurst, S.; Sun, C. Mussel Adhesion: Finding the Tricks Worth Mimicking. *Journal of Adhesion* **2005,** *81* (3-4), 297-317.

57. Waite, J. H.; Tanzer, M. L. Polyphenolic substances of Mytilus edulis: novel adhesive containing L-dopa and hydroxyproline. *Science (Washington, DC, United States)* **1981,** *212* (4498), 1038-1040.

58. Waite, J. H. Evidence for a repeating 3,4-dihydroxyphenylalanine- and hydroxyproline-containing decapeptide in the adhesive protein of the mussel, Mytilus edulis L. *Journal of Biological Chemistry* **1983,** *258* (5), 2911-2915.

59. Yu, M.; Hwang, J.; Deming, T. J. Role of L-3,4-Dihydroxyphenylalanine in Mussel Adhesive Proteins. *Journal of the American Chemical Society* **1999,** *121* (24), 5825-5826.

60. Burzio, L. A.; Waite, J. H. Cross-Linking in Adhesive Quinoproteins: Studies with Model Decapeptides. *Biochemistry* **2000,** *39* (36), 11147-11153.

61. Sever, M. J.; Weisser, J. T.; Monahan, J.; Srinivasan, S.; Wilker, J. J. Metal-mediated cross-linking in the generation of a marine-mussel adhesive. *Angewandte Chemie, International Edition* **2004,** *43* (4), 448-450.

62. Taylor, S. W.; Chase, D. B.; Emptage, M. H.; Nelson, M. J.; Waite, J. H. Ferric Ion Complexes of a DOPA-Containing Adhesive Protein from Mytilus edulis. *Inorganic Chemistry* **1996,** *35* (26), 7572-7577.

63. Lee, H.; Scherer, N. F.; Messersmith, P. B. Single-molecule mechanics of mussel adhesion. *PNAS* **2006,** *103* (35), 12999-13003.

64. Podsiadlo, P.; Liu, Z.; Paterson, D.; Messersmith, P. B.; Kotov, N. A. Fusion of seashell nacre and marine bioadhesive analogs: high-strength nanocomposite by layer-by-layer assembly of clay and L-3,4-dihydroxyphenylalanine polymer. *Advanced Materials (Weinheim, Germany)* **2007,** *19* (7), 949-955.

65. Fuller, W. D.; Verlander, M. S.; Goodman, M. A procedure for the facile synthesis of amino-acid N-carboxy anhydrides. *Biopolymers* **1976,** *15* (9), 1869-1871.

66. Fuller, W. D.; Verlander, M. S.; Goodman, M. DOPA-containing polypeptides. I. Improved synthesis of high-molecular-weight poly(L-DOPA) and water-soluble copolypeptides. *Biopolymers* **1978,** *17* (12), 2939-2943.

67. Montaudo, G.; Montaudo, M. S.; Puglisi, C.; Samperi, F. Characterization of Polymers by Matrix-Assisted Laser Desorption Ionization-Time of Flight Mass Spectrometry. End Group Determination and Molecular Weight Estimates in Poly(ethylene glycols). *Macromolecules* **1995,** *28* (13), 4562-4569.

68. Kotov, N. A.; Haraszti, T.; Turi, L.; Zavala, G.; Geer, R. E.; Dekany, I.; Fendler, J. H. Mechanism of and Defect Formation in the Self-Assembly of Polymeric Polycation-Montmorillonite Ultrathin Films. *Journal of the American Chemical Society* **1997,** *119* (29), 6821-6832.

69. Monahan, J.; Wilker, J. J. Cross-Linking the protein precursor of marine mussel adhesives: Bulk measurements and reagents for curing. *Langmuir* **2004,** *20* (9), 3724-3729.

70. Taylor, S. W.; Luther, G. W., III; Waite, J. H. Polarographic and Spectrophotometric Investigation of Iron(III) Complexation to 3,4-Dihydroxyphenylalanine-Containing Peptides and Proteins from Mytilus edulis. *Inorganic Chemistry* **1994,** *33* (25), 5819-5824.

71. Sever, M. J.; Wilker, J. J. Absorption spectroscopy and binding constants for first-row transition metal complexes of a DOPA-containing peptide. *Dalton Transactions* **2006,** (6), 813-822.

72. Lee, B. P.; Dalsin, J. L.; Messersmith, P. B. Synthesis and Gelation of DOPA-Modified Poly(ethylene glycol) Hydrogels. *Biomacromolecules* **2002,** *3* (5), 1038-1047.

73. Manevitch, O. L.; Rutledge, G. C. Elastic Properties of a Single Lamella of Montmorillonite by Molecular Dynamics Simulation. *Journal of Physical Chemistry B* **2004,** *108* (4), 1428-1435.

74. Hammond, P. T. Form and function in multilayer assembly: New applications at the nanoscale. *Advanced Materials (Weinheim, Germany)* **2004,** *16* (15), 1271-1293.

75. Jiang, C.; Tsukruk, V. V. Freestanding nanostructures via layer-by-layer assembly. *Advanced Materials (Weinheim, Germany)* **2006,** *18* (7), 829-840.

76. Tang, Z.; Wang, Y.; Podsiadlo, P.; Kotov, N. A. Biomedical applications of layer-by-layer assembly: from biomimetics to tissue engineering. *Advanced Materials (Weinheim, Germany)* **2006,** *18* (24), 3203-3224.

77. Podsiadlo, P.; Tang, Z.; Shim, B. S.; Kotov, N. A. Counterintuitive Effect of Molecular Strength and Role of Molecular Rigidity on Mechanical Properties of Layer-by-Layer Assembled Nanocomposites. *Nano Letters* **2007,** *7* (5), 1224-1231.

78. Bonapasta, A. A.; Buda, F.; Colombet, P. Cross-Linking of Poly(vinyl alcohol) Chains by Al Ions in Macro-Defect-Free Cements: A Theoretical Study. *Chemistry of Materials* **2000,** *12* (3), 738-743.

79. Nagy, M.; Wolfram, E.; Varadi, T. Effect of poly(vinylpyrrolidone) on the structure and some physical properties of chemically cross-linked poly(vinyl alcohol) gels. *Progress in Colloid & Polymer Science* **1976,** *60*, 138-146.

80. Braun, D.; Walter, E. Intra- and intermolecular crosslinking of poly(vinyl alcohol) with dialdehydes. *Colloid and Polymer Science* **1980,** *258* (7), 795-801.

81. Li, Y. S.; Wang, Y.; Tran, T.; Perkins, A. Vibrational spectroscopic studies of (3-mercaptopropyl)trimethoxysilane sol-gel and its coating. *Spectrochimica Acta, Part A: Molecular and Biomolecular Spectroscopy* **2005,** *61A* (13-14), 3032-3037.

82. Guan, Y.; Yang, S.; Zhang, Y.; Xu, J.; Han, C. C.; Kotov, N. A. Fabry-Perot Fringes and Their Application To Study the Film Growth, Chain Rearrangement, and Erosion of Hydrogen-Bonded PVPON/PAA Films. *Journal of Physical Chemistry B* **2006,** *110* (27), 13484-13490.

83. Mamedov, A.; Ostrander, J.; Aliev, F.; Kotov, N. A. Stratified Assemblies of Magnetite Nanoparticles and Montmorillonite Prepared by the Layer-by-Layer Assembly. *Langmuir* **2000,** *16* (8), 3941-3949.

84. Cheng, M.; Chen, W.; Weerasooriya, T. Mechanical Properties of Kevlar KM2 Single Fiber. *Journal of Engineering Materials and Technology* **2005,** *127* (2), 197-203.

85. Yue, C. Y.; Sui, G. X.; Looi, H. C. Effects of heat treatment on the mechanical properties of Kevlar-29 fibre. *Composites Science and Technology* **2000,** *60* (3), 421-427.

86. Hindeleh, A. M.; Abdo, S. Relationship between crystalline structure and mechanical properties in Kevlar 49 fibers. *Polymer Communications* **1989,** *30* (6), 184-186.

87. Dalton, A. B.; Collins, S.; Munoz, E.; Razal, J. M.; Ebron, V. H.; Ferraris, J. P.; Coleman, J. N.; Kim, B. G.; Baughman, R. H. Super-tough carbon-nanotube fibers. *Nature (London, United Kingdom)* **2003,** *423* (6941), 703.

88. Tang, Z.; Kotov, N. A.; Magonov, S.; Ozturk, B. Nanostructured artificial nacre. *Nature Materials* **2003,** *2* (6), 413-418.

89. Bergstrom, J. S.; Boyce, M. C. Mechanical behavior of particle filled elastomers. *Rubber Chemistry and Technology* **1999,** *72* (4), 633-656.

90. Smith, B. L.; Schaffer, T. E.; Viani, M.; Thompson, J. B.; Frederick, N. A.; Kind, J.; Belcher, A.; Stucky, G. D.; Mors, D. E.; Hansma, P. K. Molecular mechanistic origin of the toughness of natural adhesives, fibers and composites. *Nature (London)* **1999,** *399* (6738), 761-763.

91. Thompson, J. B.; Kindt, J. H.; Drake, B.; Hansma, H. G.; Morse, D. E.; Hansma, P. K. Bone indentation recovery time correlates with bond reforming time. *Nature (London, United Kingdom)* **2001,** *414* (6865), 773-776.

92. Sellinger, A.; Weiss, P. M.; Anh, N.; Lu, Y.; Assink, R. A.; Gong, W.; Brinker, C. J. Continuous self-assembly of organic-inorganic nanocomposite coatings that mimic nacre. *Nature (London)* **1998,** *394* (6690), 256-260.

93. Deville, S.; Saiz, E.; Nalla, R. K.; Tomsia, A. P. Freezing as a Path to Build Complex Composites. *Science (Washington, DC, United States)* **2006,** *311* (5760), 515-518.

94. Podsiadlo, P.; Kaushik, A. K.; Arruda, E. M.; Waas, A. M.; Shim, B. S.; Xu, J.; Nandivada, H.; Pumplin, B. G.; Lahann, J.; Ramamoorthy, A.; Kotov, N. A. Ultrastrong and Stiff Layered Polymer Nanocomposites. *Science (Washington, DC, United States)* **2007,** *318* (5847), 80-83.

95. Podsiadlo, P.; Tang, Z.; Shim, B. S.; Kotov, N. A. Counterintuitive Effect of Molecular Strength and Role of Molecular Rigidity on Mechanical Properties of Layer-by-Layer Assembled Nanocomposites. *Nano Letters* **2007,** *7* (5), 1224-1231.

96. Podsiadlo, P.; Liu, Z.; Paterson, D.; Messersmith, P. B.; Kotov, N. A. Fusion of seashell nacre and marine bioadhesive analogs: high-strength nanocomposite by layer-by-layer assembly of clay and L-3,4-dihydroxyphenylalanine polymer. *Advanced Materials (Weinheim, Germany)* **2007,** *19* (7), 949-955.

97. Kandori, K.; Ishikawa, T. Study on the hydrothermal reaction of FeCl3 solution in the presence of poly(vinyl alcohol). *Colloid and Polymer Science* **2004,** *282* (10), 1118-1125.

98. Bonapasta, A. A.; Buda, F.; Colombet, P.; Guerrini, G. Cross-Linking of Poly(Vinyl Alcohol) Chains by Ca Ions in Macro-Defect-Free Cements. *Chemistry of Materials* **2002,** *14* (3), 1016-1022.

99. Gong, J.; Luo, L.; Yu, S. H.; Qian, H.; Fei, L. Synthesis of copper/cross-linked poly(vinyl alcohol) (PVA) nanocables via a simple hydrothermal route. *Journal of Materials Chemistry* **2006,** *16* (1), 101-105.

100. Tang, Z.; Kotov, N. A.; Magonov, S.; Ozturk, B. Nanostructured artificial nacre. *Nature Materials* **2003,** *2* (6), 413-418.

101. Mamedov, A.; Ostrander, J.; Aliev, F.; Kotov, N. A. Stratified Assemblies of Magnetite Nanoparticles and Montmorillonite Prepared by the Layer-by-Layer Assembly. *Langmuir* **2000,** *16* (8), 3941-3949.

102. Guan, Y.; Yang, S.; Zhang, Y.; Xu, J.; Han, C. C.; Kotov, N. A. Fabry-Perot Fringes and Their Application To Study the Film Growth, Chain Rearrangement, and Erosion of Hydrogen-Bonded PVPON/PAA Films. *Journal of Physical Chemistry B* **2006,** *110* (27), 13484-13490.

103. Wang, R. Z.; Suo, Z.; Evans, A. G.; Yao, N.; Aksay, I. A. Deformation mechanisms in nacre. *Journal of Materials Research* **2001,** *16* (9), 2485-2493.

104. Barthelat, F.; Li, C. M.; Comi, C.; Espinosa, H. D. Mechanical properties of nacre constituents and their impact on mechanical performance. *Journal of Materials Research* **2006,** *21* (8), 1977-1986.

105. Mamedov, A. A.; Kotov, N. A. Free-Standing Layer-by-Layer Assembled Films of Magnetite Nanoparticles. *Langmuir* **2000,** *16* (13), 5530-5533.

106. Sinani, V. A.; Koktysh, D. S.; Yun, B. G.; Matts, R. L.; Pappas, T. C.; Motamedi, M.; Thomas, S. N.; Kotov, N. A. Collagen Coating Promotes Biocompatibility of Semiconductor Nanoparticles in Stratified LBL Films. *Nano Letters* **2003,** *3* (9), 1177-1182.

107. Malikova, N.; Pastoriza-Santos, I.; Schierhorn, M.; Kotov, N. A.; Liz-Marzan, L. M. Layer-by-Layer Assembled Mixed Spherical and Planar Gold Nanoparticles: Control of Interparticle Interactions. *Langmuir* **2002,** *18* (9), 3694-3697.

108. Jiang, C.; Markutsya, S.; Pikus, Y.; Tsukruk, V. V. Freely suspended nanocomposite membranes as highly sensitive sensors. *Nature Materials* **2004,** *3* (10), 721-728.

109. Jiang, C.; Markutsya, S.; Tsukruk, V. V. Compliant, robust, and truly nanoscale free-standing multilayer films fabricated using spin-assisted layer-by-layer assembly. *Advanced Materials (Weinheim, Germany)* **2004,** *16* (2), 157-161.

110. Yang, S. Y.; Lee, D.; Cohen, R. E.; Rubner, M. F. Bioinert Solution-Cross-Linked Hydrogen-Bonded Multilayers on Colloidal Particles. *Langmuir* **2004,** *20* (14), 5978-5981.

111. Yang, S. Y.; Berg, M. C.; Hammond, P. T.; Rubner, M. F. Primary hepatocytes and fibroblasts response to polyelectrolyte multilayers with polyacrylamide containing polymers. 2003; pp 79-80.

112. Richert, L.; Lavalle, P.; Vautier, D.; Senger, B.; Stoltz, J. F.; Schaaf, P.; Voegel, J. C.; Picart, C. Cell Interactions with Polyelectrolyte Multilayer Films. *Biomacromolecules* **2002,** *3* (6), 1170-1178.

113. Kidambi, S.; Lee, I.; Chan, C. Engineering polyelectrolyte multilayer (PEM) surfaces to create cell resistant and adhesive surfaces. 2004; pp 88-89.

114. Bhadra, D.; Gupta, G.; Bhadra, S.; Umamaheshwari, R. B.; Jain, N. Multicomposite ultrathin capsules for sustained ocular delivery of ciprofloxacin hydrochloride. *Journal of Pharmacy & Pharmaceutical Sciences* **2004,** *7* (2), 241-251.

115. Boulmedais, F.; Frisch, B.; Etienne, O.; Lavalle, P.; Picart, C.; Ogier, J.; Voegel, J. C.; Schaaf, P.; Egles, C. Polyelectrolyte multilayer films with pegylated polypeptides as a new type of anti-microbial protection for biomaterials. *Biomaterials* **2004,** *25* (11), 2003-2011.

116. Kenausis, G. L.; Voeroes, J.; Elbert, D. L.; Huang, N.; Hofer, R.; Ruiz-Taylor, L.; Textor, M.; Hubbell, J. A.; Spencer, N. D. Poly(L-lysine)-g-Poly(ethylene glycol) Layers on Metal Oxide Surfaces: Attachment Mechanism and Effects of Polymer Architecture on Resistance to Protein Adsorption. *Journal of Physical Chemistry B* **2000,** *104* (14), 3298-3309.

117. Etienne, O.; Picart, C.; Taddei, C.; Haikel, Y.; Dimarcq, J. L.; Schaaf, P.; Voegel, J. C.; Ogier, J. A.; Egles, C. Multilayer polyelectrolyte films functionalized by insertion of defensin: a new approach to protection of implants from bacterial colonization. *Antimicrobial Agents and Chemotherapy* **2004,** *48* (10), 3662-3669.

118. Dai, J.; Bruening, M. L. Catalytic Nanoparticles Formed by Reduction of Metal Ions in Multilayered Polyelectrolyte Films. *Nano Letters* **2002,** *2* (5), 497-501.

119. Shi, Z.; Neoh, K. G.; Kang, E. T. Surface-grafted viologen for precipitation of silver nanoparticles and their combined bactericidal activities. *Langmuir* **2004,** *20* (16), 6847-6852.

120. Balogh, L.; Swanson, D. R.; Tomalia, D. A.; Hagnauer, G. L.; McManus, A. T. Dendrimer-Silver Complexes and Nanocomposites as Antimicrobial Agents. *Nano Letters* **2001,** *1* (1), 18-21.

121. Raveendran, P.; Fu, J.; Wallen, S. L. Completely green synthesis and stabilization of metal nanoparticles. *Journal of the American Chemical Society* **2003,** *125* (46), 13940-13941.

122. Zhao, L.; Kelly, K. L.; Schatz, G. C. The Extinction Spectra of Silver Nanoparticle Arrays: Influence of Array Structure on Plasmon Resonance Wavelength and Width. *Journal of Physical Chemistry B* **2003,** *107* (30), 7343-7350.

123. Jensen, T.; Kelly, L.; Lazarides, A.; Schatz, G. C. Electrodynamics of noble metal nanoparticles and nanoparticle clusters. *Journal of Cluster Science* **1999,** *10* (2), 295-317.

124. Kobayashi, Y.; Katakami, H.; Mine, E.; Nagao, D.; Konno, M.; Liz-Marzan, L. M. Silica coating of silver nanoparticles using a modified Stober method. *Journal of Colloid and Interface Science* **2005,** *283* (2), 392-396.

125. Liz-Marzan, L. M.; Lado-Tourino, I. Reduction and Stabilization of Silver Nanoparticles in Ethanol by Nonionic Surfactants. *Langmuir* **1996,** *12* (15), 3585-3589.

126. Pastoriza-Santos, I.; Liz-Marzan, L. M. Formation and Stabilization of Silver Nanoparticles through Reduction by N,N-Dimethylformamide. *Langmuir* **1999,** *15* (4), 948-951.

127. Pastoriza-Santos, I.; Gomez, D.; Perez-Juste, J.; Liz-Marzan, L. M.; Mulvaney, P. Optical properties of metal nanoparticle coated silica spheres: a simple effective medium approach. *Physical Chemistry Chemical Physics* **2004,** *6* (21), 5056-5060.

128. Ung, T.; Liz-Marzan, L. M.; Mulvaney, P. Gold nanoparticle thin films. *Colloids and Surfaces, A: Physicochemical and Engineering Aspects* **2002,** *202* (2-3), 119-126.

129. Arroyo, F. J.; Carrique, F.; Jimenez-Olivares, M. L.; Delgado, A. V. Rheological and Electrokinetic Properties of Sodium Montmorillonite Suspensions. *Journal of Colloid and Interface Science* **2000,** *229* (1), 118-122.

130. Anderson, M. R.; Davis, R. M.; Taylor, C. D.; Parker, M.; Clark, S.; Marciu, D.; Miller, M. Thin Polyimide Films Prepared by Ionic Self-Assembly. *Langmuir* **2001,** *17* (26), 8380-8385.

131. Lu, J.; Zhao, X. Electrorheological behavior of polyaniline-montmorillonite clay nanocomposite. *International Journal of Modern Physics B: Condensed Matter Physics, Statistical Physics, Applied Physics* **2002,** *16* (17 & 18), 2521-2527.

132. Slawson, R. M.; Van Dyke, M. I.; Lee, H.; Trevors, J. T. Germanium and silver resistance, accumulation, and toxicity in microorganisms. *Plasmid* **1992,** *27* (1), 72-79.

133. Zhao, G.; Stevens, S. E., Jr. Multiple parameters for the comprehensive evaluation of the susceptibility of Escherichia coli to the silver ion. *BioMetals* **1998,** *11* (1), 27-32.

134. Spadaro, J. A.; Berger, T. J.; Barranco, S. D.; Chapin, S. E.; Becker, R. O. Antibacterial effects of silver electrodes with weak direct current. *Antimicrobial Agents and Chemotherapy* **1974,** *6* (5), 637-642.

135. Pooley, F. D. Bacteria accumulate silver during leaching of sulfide ore minerals. *Nature (London, United Kingdom)* **1982,** *296* (5858), 642-643.

136. Slawson, R. M.; Trevors, J. T.; Lee, H. Silver accumulation and resistance in Pseudomonas stutzeri. *Archives of Microbiology* **1992,** *158* (6), 398-404.

137. Klaus, T.; Joerger, R.; Olsson, E.; Granqvist, C. G. Silver-based crystalline nanoparticles, microbially fabricated. *Proceedings of the National Academy of Sciences of the United States of America* **1999,** *96* (24), 13611-13614.

138. Sondi, I.; Salopek-Sondi, B. Silver nanoparticles as antimicrobial agent: A case study on E. coli as a model for Gram-negative bacteria. *Journal of Colloid and Interface Science* **2004,** *275* (1), 177-182.

139. Bhol, K. C.; Schechter, P. J. Topical nanocrystalline silver cream suppresses inflammatory cytokines and induces apoptosis of inflammatory cells in a murine

model of allergic contact dermatitis. *British Journal of Dermatology* **2005,** *152* (6), 1235-1242.

140. Locci, P.; Marinucci, L.; Lilli, C.; Belcastro, S.; Staffolani, N.; Bellocchio, S.; Damiani, F.; Becchetti, E. Biocompatibility of alloys used in orthodontics evaluated by cell culture tests. *Journal of Biomedical Materials Research* **2000,** *51* (4), 561-568.

141. Wataha, J. C.; Lockwood, P. E.; Schedle, A. Effect of silver, copper, mercury, and nickel ions on cellular proliferation during extended, low-dose exposures. *Journal of Biomedical Materials Research* **2000,** *52* (2), 360-364.

142. Cortizo, M. C.; de Mele, M. F.; Cortizo, A. M. Metallic dental material biocompatibility in osteoblastlike cells: Correlation with metal ion release. *Biological Trace Element Research* **2004,** *100* (2), 151-168.

143. Alt, V.; Bechert, T.; Steinrucke, P.; Wagener, M.; Seidel, P.; Dingeldein, E.; Domann, E.; Schnettler, R. An in vitro assessment of the antibacterial properties and cytotoxicity of nanoparticulate silver bone cement. *Biomaterials* **2004,** *25* (18), 4383-4391.

144. Vo-Dinh, T.; Yan, F.; Wabuyele, M. B. Surface-enhanced Raman scattering for medical diagnostics and biological imaging. *Journal of Raman Spectroscopy* **2005,** *36* (6/7), 640-647.

145. Ren, C.; Song, Y.; Li, Z.; Zhu, G. Hydrogen peroxide sensor based on horseradish peroxidase immobilized on a silver nanoparticles/cysteamine/gold electrode. *Analytical and Bioanalytical Chemistry* **2005,** *381* (6), 1179-1185.

Chapter III

LBL Nanocomposites from Cellulose Nanocrystals

A. Introduction

In Chapter I we have pointed out that carbon nanotubes (CNTs) have received wide attention thanks to their low density, as well as excellent mechanical and electrical properties.[1-11] However, as we noted, utilization of this material for the preparation of hybrid composites is problematic due to the difficulty of generating stable dispersions, because of their highly hydrophobic surface.[12-16] In addition, for the purpose of large scale production, CNTs are prohibitively expensive, and until cheaper synthesis techniques will be developed, it is unlikely that they will find utilization in large scale manufacturing besides some niche, high value–added applications.

An alternative may be found in natural and renewable materials. As such, in Chapter II we have presented an extensive study on mechanics and applications of LBL-assembled, MTM clay-based NCs. Another natural nanomaterial, the cellulose nanocrystals (CNRs), is also gaining momentum recently due to the combination of its natural and renewable origins as well as equally impressive mechanical properties when compared to CNTs: bending strength of ~10 GPa and E ~150 GPa,[17,18] which are only about 10x smaller then those of SWNTs (σ_{UTS} ~300 GPa at E ~1 TPa,[1,11] and bending strength of 63 GPa[1]).

The CNRs have been receiving growing interest in the recent years. This is because the virtually ideal crystalline structure of the cellulose rods, resulting from alignment of polymer chains, imparts them with exceptional mechanical as well as unique optical properties. Given their natural origins and inherently low cost, they have been studied for development of reinforced NCs for variety of applications in automotive, railways, or aviation industries, just to name a few.[19-21] Compared to other inorganic reinforcing fillers, CNRs have additional advantages, including positive ecological: low energy consumption, ease of recycling by combustion, high sound attenuation, and comparatively easy processability due to their nonabrasive nature, which allows high filling levels, in turn resulting in significant cost savings.[21] All of this makes CNRs an attractive nanomaterial for the preparation of low cost, light-weight, and high-strength hybrid composites for multitude of applications. They are also of interest for their liquid crystals chereacteristics[22-24] and are being researched for different applications, one example of which was presented recently for preparation of security paper.[25]

Since cellulose is so pervasive throughout the living world, numerous reports detailing preparation of CNRs from diverse sources such as: cotton,[26] tunicate (a sea animal),[27,28] algae,[29,30] bacteria,[31,32] and wood;[26,33,34] have already been presented. Depending on the source, they are available in a wide variety of aspect ratios (ratio of length to diameter), e.g. ~200-300 nm long and 5 nm in lateral dimension[26] and up to several microns long and 15 nm in lateral dimension[27,28] from cotton and tunicate respectively.

This chapter describes initial studies into the LBL assemblies of CNRs and establishes precedence for preparation of CNRs multilayers. First, we show the feasibility of LBL assembly of NCs from cotton CNRs as a first stage in an effort of preparing the high-strength composites.[35] Further, we discuss initial investigation into mechanical properties of these assemblies. Finally, we demonstrate feasibility of LBL assembly of long CNRs from tunicate with unique application as an anti-reflective coating.

B. LBL Assembly of Cellulose Nanocrystals

1. Introduction

From the purely mechanical point of view, recent work has shown preparation of composites from micro fibrillated cellulose possessing bending strength as high as 370 MPa and *E* up to 19 GPa[36] and CNRs in combination with silk fibroin resulted in a composite with tensile strength (σ) as high as 160 MPa and *E* approaching 12 GPa.[37] Clearly, these results in mechanical reinforcement are far from the values that are expected given the properties of CNRs. The problem once again arises from the poor matrix connectivity of the material with the host polymer similarly to CNTs.

Having in mind the results obtained with clay LBL assemblies in Chapter II, we have attempted LBL assembly of the CNRs in order to generate even stronger composites in perspective. Here, we report for first time the LBL assembly of nanostructured composite from CNRs and PDDA as a first stage in an effort of preparing high strength, low-cost and light-weight thin-films. The sequential deposition of the CNRs with LBL technique opens a new route for nanoscale organization of the material which may potentially lead to other, new developments.

2. Experimental Procedure

Materials

The polymer, poly(diallyldimethylammonium chloride) (PDDA) with molecular weight of MW ~100,000 was purchased from Sigma-Aldrich (St. Louis, MO) and used as received (20 wt.% solution) without further purification. Prior to use in the experiments, the stock polymer solution was diluted to 0.5 wt.% with 18 MΩ, de-ionized under vigorous stirring for 2 hours. Whatman No.1 filter paper and microscope glass slides were both obtained from Fisher Scientific (Hampton, NH). Hydrogen peroxide and concentrated sulfuric acid used in the piranha solution were both purchased from Sigma-Aldrich.

Cellulose Nanocrystals Preparation

Cellulose nanocrystals were prepared by sulfuric acid hydrolysis of Whatman No. 1 filter paper powder (98% cotton) as described previously.[26] Briefly, 5g of the ground paper was mixed with 100mL of 64% w/v sulfuric acid and stirred at 45 °C for 1 h. The acid solution was subsequently removed by multiple centrifugation, decantation of the supernatant, and redispersion steps. Purified material was finally redissolved in 100 mL of deionized water and stored in the refrigerator until further use. Prior to use in experiments, suspension with the crystals were redispersed by brief ultra-sonic treatment of the solution with an ultrasonic processor (Cole-Parmer) in order to break up any of the aggregated material.[26]

Layer-by-Layer Assembly

The microscope glass slides used in LBL assembly were cleaned by boiling in piranha solution (3:1 H_2SO_4:H_2O_2) for 1 hour, followed by thorough rinsing with de-ionized water prior to use. Cleaned glass slides were then sequentially immersed into: 1) 0.5 wt.% PDDA solution for 10 min, 2) DI water for 2 minutes in order to rinse any weakly adsorbed material, 3) cellulose nanocrystals solution for 10 min, and 4) DI water for 2 minutes to rinse away any weakly adsorbed CNRs. The entire cycle was then repeated up to ten times for the purpose of the present study although the deposition can be repeated indefinitely. The pH of the rinsing water after CNRs deposition was adjusted to pH = 2-3, in the range of CNRs solution pH, because it showed more uniform growth of the multilayer. After every rinsing step, glass slides were thoroughly dried with compressed air stream before proceeding to the next deposition.

Instrumental Analysis

Scanning electron microscopy (SEM) images were taken with a FEI Nova Nanolab Dualbeam FIB. SEM sample consisted of a single PDDA/CNRs bilayer which was deposited on a piece of a piranha cleaned silicon wafer following the same procedure as with glass slides. Prior to taking images, sample was coated with a thin layer of gold using a vacuum gold ion sputterer to avoid the charging effect on the sample with the electron beam.

Atomic force microscopy (AFM) imaging was performed in air with a Nanoscope III (Digital Instruments/Veeco Metrology Group) operated in tapping mode using silicon/nitride tips. The sample was prepared in the same manner as for SEM analysis except no gold coating was required.

UV-vis spectroscopy was performed with an 8453 UV-Vis Chem Station spectrophotometer produced by Agilent Technologies. The measurements were obtained by acquiring the absorbance spectrum for a sample deposited on a clean glass slide from 200 nm to 1000 nm after each deposition of a material and comparing the spectrum to that of a pure glass slide. For the purpose of spectrum acquisition, the glass slide was placed directly in the path of light between the light source and the detector.

Ellipsometry measurements were obtained using a BASE-160 Spectroscopic Ellipsometer produced by J. A. Woollam Co., Inc.. The samples used for ellipsometry were similar to those used for SEM and AFM. In particular, layers were deposited on the silicon wafer in the same manner as on glass slides and a scan was obtained after every CNRs layer up to 10 bilayers. The refractive index of the multilayer was determined from a thick sample. This value was then used for the thickness calculation of thin layers. The instrument was calibrated to the standard silicon wafer with a thin layer of silicon dioxide and the overall thickness on the wafer was then fitted using a Cauchy's model.

3. Results and Discussion

For the purpose of preparation of the hybrid composite we chose to work with PDDA since it has received wide attention in the LBL community. PDDA is widely available and its polymer chains contain high density of positive charges per unit length which renders preparation of the multilayers easier as opposed to other weakly charged polyelectrolytes. Sulfuric acid hydrolysis of cotton fibers results in partial conversion of the hydroxyl groups to sulfates, thus imparting negative charges to the nanocrystals and requiring positively charged partner for the assembly. Gray *et al.* has also reported a study of adhesion forces on the surface of the CNRs/PDDA samples, which gave a suggestion that assembly with PDDA polymer should be feasible.[38]

In a typical assembly, we have used 10 min adsorption intervals since we have found this to be adequate in many other systems we have prepared previously. To monitor proper assembly, we have used the classical approach and measured UV-vis absorbance spectrum after each deposited bilayer on a glass slide. (Figure 37A). When absorbance at 360nm wavelength was plotted as a function of a bilayer number the graph gave nearly straight regression, indicating uniform assembly and distribution of CNRs in each bilayer. (Figure 37A) The absorbance of the composite reached nearly 0.35 OD after deposition of 10 bilayers, indicating high loading of the CNRs and rapid LBL deposition, which can be contrasted with quite slow deposition of SWNTs due to small surface charge.

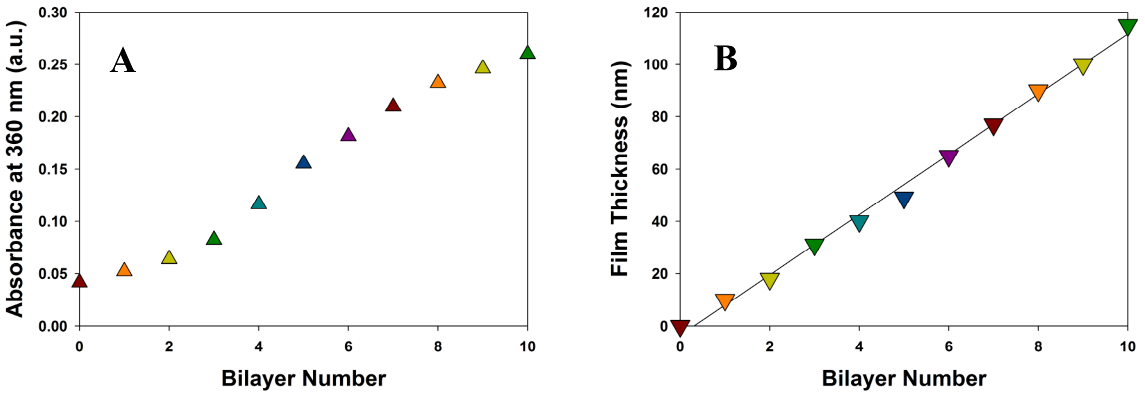

Figure 37. Evolution of a growing composite determined using (A) UV-vis absorbance at 360 nm and (B) with an ellipsometer after each deposition of cellulose nanocrystals.

We have also characterized the thickness of each individual bilayer in the composite using ellipsometry. We have found that an individual bilayer is 11 nm thick and this thickness was consistent for every additional bilayer added to the composite. A plot of the thickness data obtained from ellipsometry once again shows, as expected, a straight line. (Figure 37B) This result is in good agreement with the UV-vis data collected.

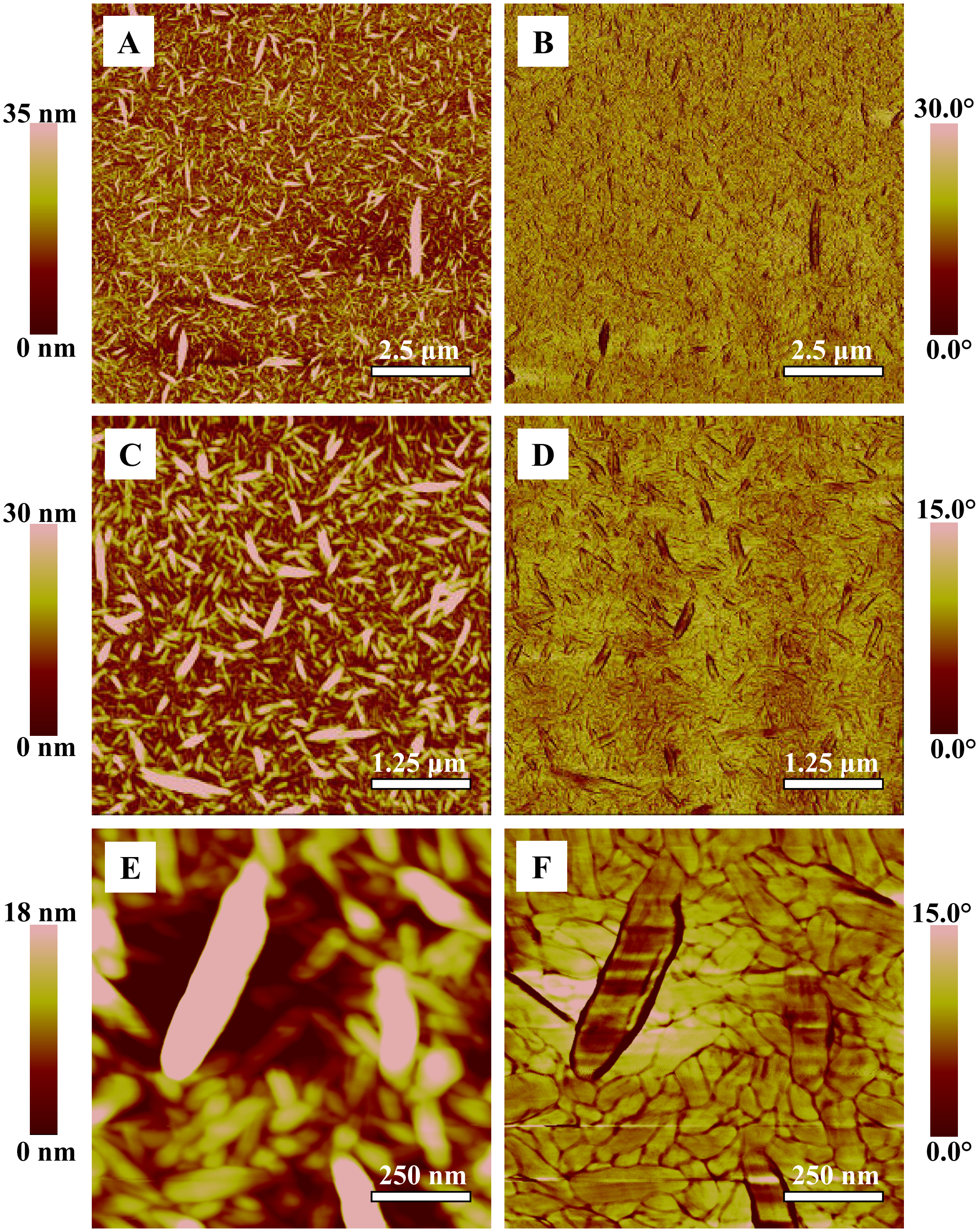

Figure 38. Tapping mode Atomic Force Microscopy image of surface topography for a single PDDA/CNRs bilayer on silicon substrate. (A) and (B) topography and phase images of 10 µm * 10 µm area; (C) and (D) topography and phase images of 5 µm * 5 µm area; (E) and (F) topography and phase images of 1 µm * 1 µm area.

Surface morphology and topology of LBL layers of CNRs was characterized by atomic force microscopy (AFM) as well as scanning electron microscopy (SEM). Following previously reported suggestions we have obtained AFM images while operating in tapping mode, since CNRs have been found to be easily adsorbed on the tip of the probe operating in the contact mode when PDDA is present.[38] Characterization of a single bilayer adsorbed on a silicon wafer revealed very high density and uniform coverage. (Figure 38) In our experience with CNTs assembly, we have not previously observed such high density of coverage with a single bilayer. SEM characterization confirmed high uniformity and dense packing obtained from AFM analysis (Figure 39).

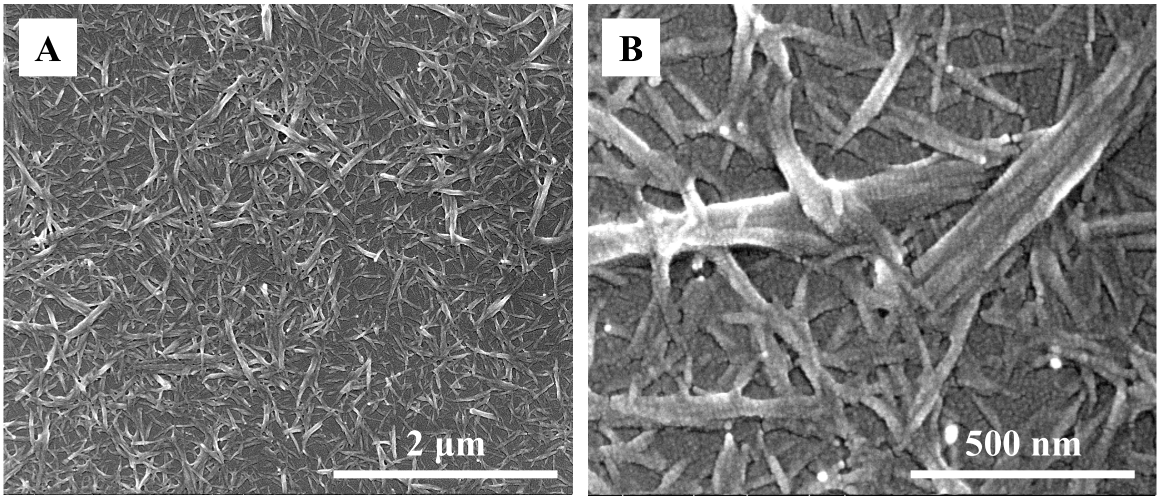

Figure 39. Scanning Electron Microscopy images of a single PDDA/CNRs bilayer on a silicon substrate at 50k (A) and 200k (B) magnifications.

CNRs obtained from cotton have been reported to be 5 nm in diameter and 100-300 nm long.[26] Both SEM and AFM are in agreement with these reports. SEM and AFM also show larger crystals which following a closer look (Figures 39A and 39B) clearly show that these are aggregates of CNRs resulting from incomplete digestion of cotton. To avoid these larger aggregates, further purification may be applied. The network morphology of the films is very encouraging structural feature for the creation of ultrastrong materials provided that methods of efficient load transfer and debundling of CNRs are found. These problems are identical to those seen for CNT composites, although approaches to their solutions can be drastically different due to substantially more chemically active structure of CNR backbone.

4. Conclusions

In conclusion, we have presented here initial results from successful LBL assembly of cellulose nanocrystals and PDDA polycation in an effort of generating a new class of multilayered composites. In the preliminary study, characterization of the multilayer structure revealed tightly packed CellNs layers with high loading of the nanocrystals. Formation of a uniform layer can potentially allow for direct assembly of the nanocrystals with other nanocolloids without the need for polymeric interlayer which will be exploited in the future work. Given their natural origins, CellNs have wide potential for applications in biomedical community as well.

C. High-Speed Preparation of High-Strength Mutilayered Nanocomposites from Cellulose Nanocrystals

1. Introduction

In Section B2 of this chapter we presented results from a “proof-of-concept” study on layer-by-layer assembly of CNRs and a PDDA polymer.[35] The feasibility of LBL assembly of the nanocrystals prompts further investigation of nanocomposites from this material. In this section we show that unlike the assemblies from MTM clay in

Chapter II, assembly of CNRs is highly robust and fast. We show that free-standing PDDA/CNRs films can be prepared with as few as 5 sec dipping intervals as opposed to 5 min for polymer/MTM. The free-standing films display high homogeneity, optical transparency, high loading of CNRs, and high mechanical properties: σ_{UTS} = 130 ± 35 MPa, E as high as 10 GPa, and toughness ~4.2 ± 2.6 MJ/m^3. These mechanical properties can be favorably compared to PDDA/MTM and MWNTs-based LBL composites and are significantly greater than those of any CNRs based composites prepared until now by conventional techniques.[39,40]

2. Experimental Procedure

Unless additionally stated in this section, the materials, extraction of CNRs, and preparation of the NCs are the same as described in Section B2. The mechanical properties were evaluated in the same manner and instrument setup as discussed in Chapter II.

Cellulose Nanocrystals Preparation

The extraction method of CNRs for this part of work was slightly modified to reduce the umber of aggregates and to improve segregation of individual nanocrystals. Similarly as in Section B2, the CNRs were prepared by sulfuric acid hydrolysis of Whatman No. 1 filter paper powder. A modification was made in the sulfuric acid digestion step. We observed that increasing the volume of sulfuric acid solution to 200 ml instead of 100 ml and digestion time to 2 h instead of 1h, greatly improved the quality of final suspension.

Layer-by-Layer Assembly

The deposition of multilayers was performed both by hand and by automatic dipping robots as described in Chapter II. Briefly, cleaned microscope glass slides were sequentially immersed into: 1) 0.5 wt.% PDDA solution for 10 min, 2) DI water for 2 minutes in order to rinse any weakly adsorbed material, 3) cellulose nanocrystals solution for 10 min, and 4) DI water for 2 minutes to rinse away any weakly adsorbed CNRs. After every rinsing step, glass slides were thoroughly dried with compressed air stream before proceeding to the next deposition. Following thorough characterization of the assembly, the dipping time into the polymer and CNRs solutions was reduced to as few as ~1sec. The entire cycle was then repeated until a desired number of layers were deposited (100 – 300 bilayers).

3. Results and Discussion

As described in the Experimental Procedure Section, preparation of the PDDA/CNRs films was performed following similar conditions to those used in our previous report, namely: (a) immersion of the glass or silicon substrate into 0.5 wt.% solution of PDDA, (b) 30 sec rinse with DI water, (c) compressed air drying, (d) immersion of the substrate into CNRs dispersion, (e) 30 sec rinse in DI water, and finally (f) once again drying using stream of compressed air. This sequence constitutes a single deposition cycle (a bilayer) and as we have shown previously, for the PDDA polyelectrolyte (PE), it results in adsorption of a densely packed layer of the nanocrystals, approx. 10 nm in thickness. To simplify the procedure, in the current work we have used plain, pH ~5.6 DI water instead of the pH ~2-3, since there was no observable difference in adsorption between these two conditions. Another and much more important change we have made in the assembly was decreasing the adsorption time for the CNRs and PDDA.

Previously, we used 10 min immersions for both the PDDA and CNRs components. These conditions were chosen because they proved to be versatile for many of the PE-nanocolloid systems we have prepared in the past, including the MTM-based LBL assemblies described in Chapter II.[41-44] After more extensive evaluation of the adsorption behavior for various PE-CNRs systems, we found that even < 1 sec long immersion into CNRs dispersion is sufficient for covering the surface of the substrate with comparable density to that we showed previously for 10 min. By the same analogy, PE adsorption was also reduced to 1 min. Atomic force microscopy imaging of a silicon wafer surface coated with a single bilayer of PDDA/CNRs following the three different time intervals: (a) 1 min, (b) 5 sec, and (c) instantaneous dipping showed identical morphology and crystal density. (Figures 40A, 40B, and 40C)

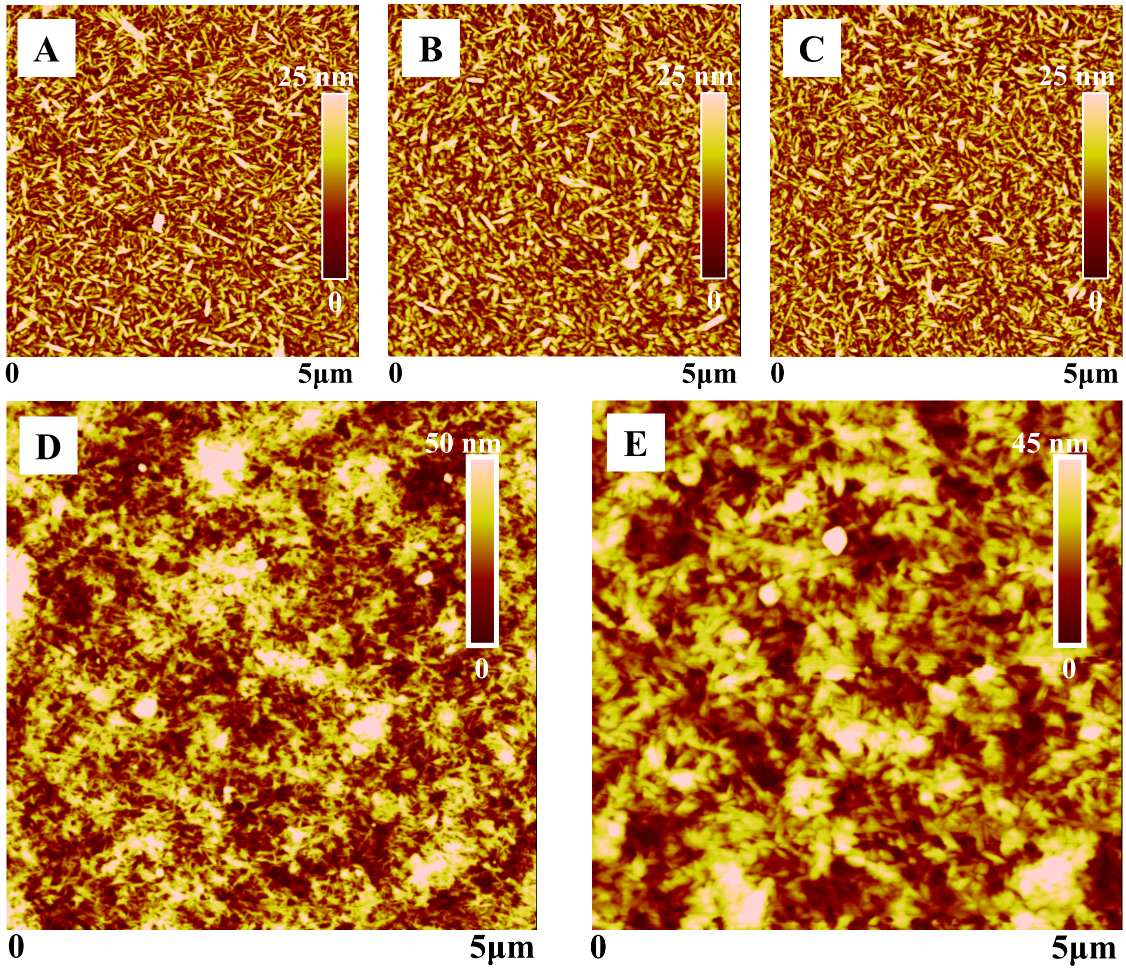

Figure 40. Tapping mode AFM images of surface topographies for PDDA/CNRs multilayers. (A), (B), and (C): Topography images for a single bilayer of PDDA/CNRs on top of a silicon wafer deposited with (A) 1min, (B) 5 sec, and (C) < 1 sec dipping intervals. The images show planar orientation and dense coverage of the nanocrystals on the surfaces. (D) and (C): Topography images for ~1 µm thick PDDA/CNRs LBL film consisting of 95 bilayers deposited on the surface of a silicon wafer.

This result has a profound impact on speed of preparation of the NC. In other high-strength LBL nanocomposites, e.g. from CNTs or MTM nanosheets, a single bilayer deposition required more then 20 min (including rinsing and drying steps) which meant that preparation of free-standing films composed of 200 or 300 bilayers took several days of continuous deposition. Extending the high-speed adsorption finding to multilayer buildup would reduce this preparation time by an order of magnitude. An explanation for this behavior has been suggested in a recent work by Gray's group on comparison of the LBL assembly of poly(allylamine hydrochloride) (PAH) with CNRs between LBL and spin-assisted LBL methods.[45] Cranston and Gray have suggested that an explanation for the much higher thickness per bilayer in our system as opposed to theirs may lie in several factors: incomplete separation of the fibers into crystallites, using acidic solution of crystallites, presence of a highly charged polymer, and using higher concentration of the CNRs which renders the system non-diffusion limited. While incomplete separation of crystallites could be seen in the SEM images in the previous section, only the remaining three factors are true and significant in this work.

As we have noted in the Experimental Procedures section, we have slightly modified the CNRs extraction method to reduce the aggregation problem. We found that decreasing the concentration of cotton in the digestion solution from 5 g/100 ml to 5 g/200 ml and increasing the digestion time from 1h to 2h resulted in excellent separation of the nanocrystals. Evidence of this was observed from AFM (Figure 40) as well as SEM characterization of the multilayers. (Figure 41) As can be seen in the images, unlike in Figure 39B, the films are composed of well isolated individual nanocrystals having small size distribution.

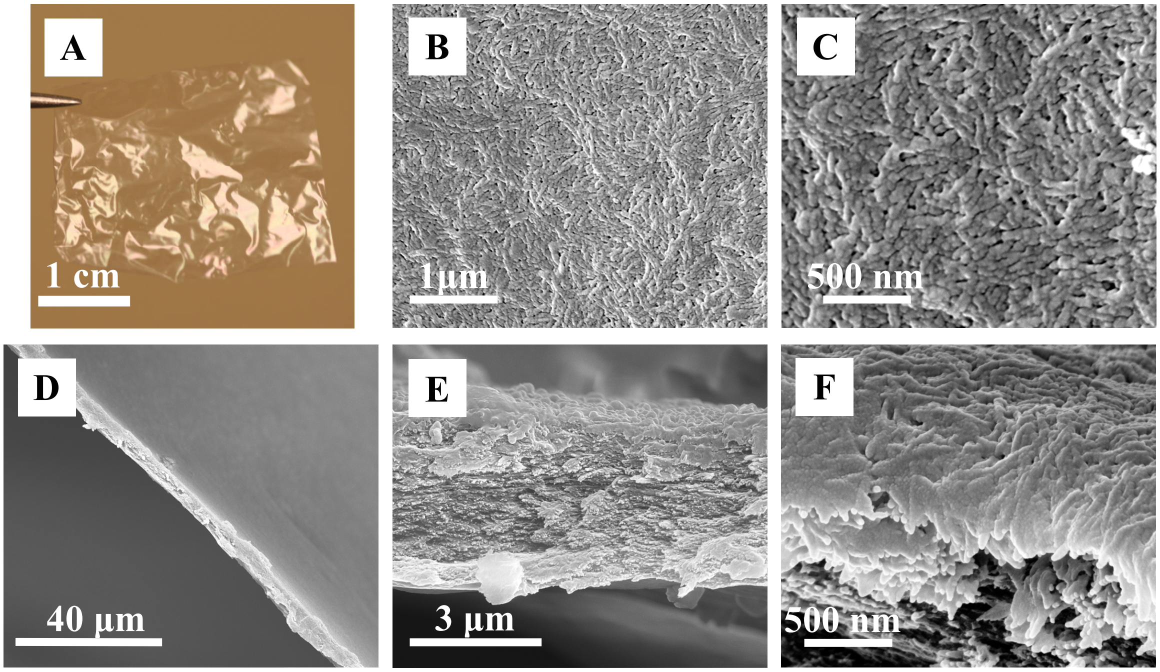

Figure 41. Optical and SEM images of a 300-bilayer PDDA/CNRs free-standing LBL film. (A): A photograph of a free standing film showing high transparency. (B) and (C): SEM images of surface morphology of the free-standing film from (A). (D) and (E): SEM cross-sectional images of the $(PDDA/CNRs)_{300}$ LBL film showing uniformity in thickness and a layered structure of the film. (F): SEM cross-sectional image of the $(PDDA/CNRs)_{300}$ LBL film after tensile test showing pullout of individual CNRs.

This improvement of the isolation had also a direct impact on the optical properties of the NC. Investigation of the UV-vis absorbance of a glass slide coated with the multilayer showed much smaller overall increase in the absorbance with increasing number of layers as well as a sinusoidal function of absorbance change vs. number of deposited bilayers. (Figure 42A) The sinusoidal pattern appears to have a well defined periodic nature with the maxima falling at specific thicknesses of the film for the given wavelength. The maxima appear to correspond to the constructive light interference according to the Bragg’s Law, which is especially evident for the 360 nm wavelength, where the maxima fall at thicknesses of (1) ~7-8 bilayers = ~90 nm = 360 nm/4 and (2) 16 bilayers = ~180 nm = 360 nm/2 (each bilayers has a thickness of ~11 nm).

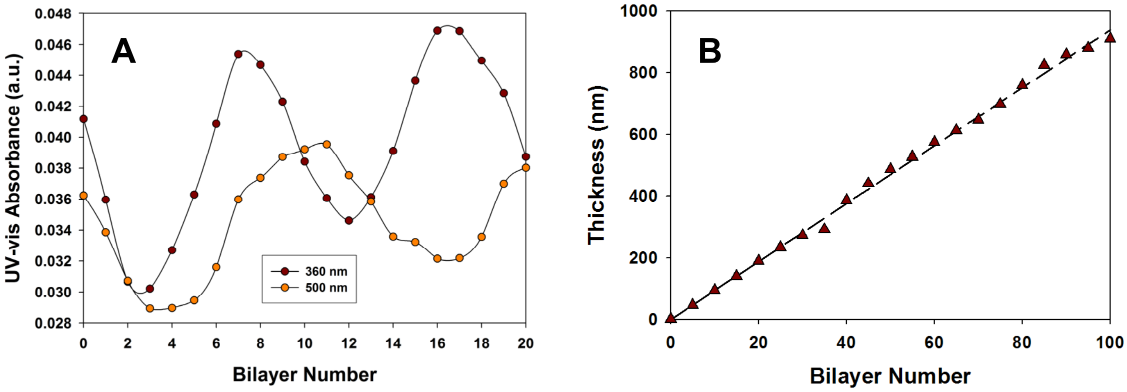

Figure 42. UV-vis and ellipsometry characterization of PDDA/CNRs multilayer growth. (A) UV-vis absorbance plot as a function of increasing number of bilayers. Points are plotted for absorbance at 360 nm and 500 nm. (B) Thickness of the multilayer obtained from ellipsometry as a function bilayers number showing linear growth up to 100 bilayers.

Following the initial characterization, we have proceeded with growing thick films for testing the mechanical properties. In spite of the dramatically faster preparation, ellipsometry measurements showed linear and consistent growth extending up to 100 bilayers. (Figure 42B) AFM characterization of a 95-bilayer film deposited on a silicon wafer showed that the CNRs remain well isolated with planar orientation with respect to the substrate. Contrary to the speculations of Cranston and Gray, the growth increment remained at 11 nm per bilayers, suggesting that the only influential factors affecting thickness of our films could be greater charge of PDDA polymer and higher concentration of the CNRs solution. This suggest that LBL assembly of CNRs is system dependent, i.e. choice of the polymer affects the growth behavior, and requires further studies for better understanding.

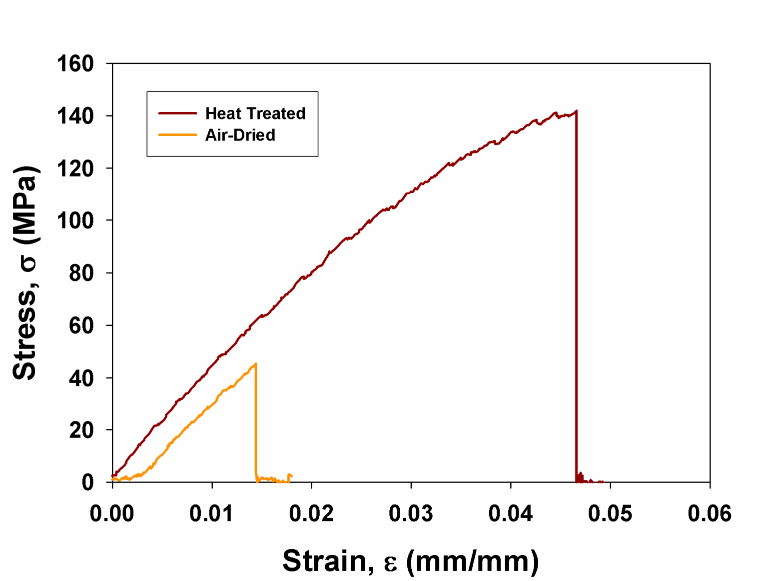

Figure 43. Stress-strain response of a 300-bilayer PDDA/CNRs free-standing LBL films. The heat-treated films were prepared vacuum drying of a free-standing film at 180 °C.

Similarly to the work on MTM-based NCs, we have prepared 300-bilayer LBL films on microscope glass slides for mechanical properties evaluation, using an automatic dipping robot. Note that preparation of the composite took only a few hours as opposed to days for the MTM clay based NCs. Free-standing films were subsequently isolated using the same HF separation technique as described in Chapter II, and characterized with SEM and mechanical testing apparatus. (Figures 41 and 43) Free-standing films showed excellent stability and nearly complete optical transparency as can be seen in Figure 41A. SEM characterization revealed a very uniform structure and distribution of the nanocrystals with high loading of the nanomaterial.

Characterization of the mechanical properties showed that as detached and air-dried LBL films had ultimate strength of, $\sigma_{UTS} = 52 \pm 21$ MPa and Young's modulus of, $E = 3.0 \pm 1.1$ GPa. (Table 6) These were encouraging results since in comparison, the strength of pure PDDA is at least 4x lower and the modulus of elasticity is 15x lower.

Further drying of the films under vacuum and at a temperature of 180 °C showed substantial improvement in the properties to σ_{UTS} = 128 ± 35 MPa and E = 2.8 ± 0.9 GPa. These results can be favorably compared to the previous results with PDDA/MTM clay-based material and as a preliminary study; they suggest that further improvement of mechanical properties should be possible as was demonstrated for MTM-based LBL assemblies in Chapter II.

Table 6. Comparison of mechanical properties of PDDA/CNRs composite and PDDA.

	Ultimate Tensile Strength, σ_{UTS} (MPa)	Young's Modulus, E (GPa)	Ultimate Tensile Strain, ε (%)	Toughness (MJ/m^3)
Pure PDDA	~12	~0.2	~50	~5
Air-Dried	52 ± 21	3.0 ± 1.1	2.3 ± 1.4	0.65 ± 0.75
Heat Treated	128 ± 35	2.8 ± 0.9	6.1 ± 1.7	4.2 ± 2.6

4. Conclusions

We presented here results from initial investigation of mechanical properties in polyelectrolyte-CNRs, LBL-assembled nanocomposite. Modification of the preparation method led to improvement in the separation of the nanocrystals, yielding a film with unique optical properties, and assembly length of the films was reduced by an order of magnitude. Preparation of free-standing films was demonstrated and their structure was characterized as a tightly packed assembly of CNRs. The structure of the film appears to have nanoscale porosity which could be exploited in future work for preparation of separation membranes. Evaluation of mechanical properties showed that the films exceed properties of previously reported PDDA/MTM nanocomposite. This result combined with the unique transparency offers an opportunity for development of high-performance and transparent NCs similarly to work presented in Chapter II. Organic nature of the CNRs also presents opportunities for chemical modification which are not as easily accessible in the inorganic MTM nanosheets.

D. Layer-by-Layer Assembled Films of Cellulose Nanowires with Antireflective Properties

1. Introduction

In Sections B and C of this chapter we discussed preparation of LBL assemblies from short, cotton CNRs. In this final section, we turn our attention to preparation of the assemblies from high-aspect-ratio cellulose nanowires (CNWs) from tunicate and we discuss a novel property of this multilayer: the antireflectivity.

Antireflection (AR) surfaces and coatings have been widely utilized to maximize the transmission of light through optical surfaces for many years now. They are especially important for such applications as: flat-panel displays, solar cells, lasers, or other opto-electronic devices.[46-48] The principle of AR is the interference of the reflected light from air-coating and a coating-substrate interfaces.[49,50] An ideal homogeneous single-layer AR coating satisfies the following conditions: the thickness of the coating is λ/4, where λ is the wavelength of the incident light, and $n_c = (n_a n_s)^{1/2}$, where n_c, n_a, and n_s, are refractive indices of the coating, air, and substrate, respectively.[49-51] To satisfy these conditions, with $n_a = 1$, for an effective AR coating on glass or plastics which have $n_s \sim 1.5$, n_c should be ~1.22. Unfortunately, the lowest refractive index of homogeneous dielectric materials is only about 1.34. To achieve the required low refractive index, processes that produce nanoporous materials are often utilized. Some of the examples presented to this date include: phase separation and etching,[52,53] sol-gel assembly,[54,55] reactive twin-magnetron sputtering,[56] interference lithography,[57] and reactive ion etching of substrates.[58]

LBL technique[59] is an attractive method for preparation of AR materials because it can produce large-area, uniform, and defect-free nanoporous coatings on essentially any type of surface, including 3-D, with precise control over the thickness and optical properties. The first demonstration of the LBL-AR was shown by Hattori in 2001 with deposition of silica or polymer nanoparticles (NPs) onto glass substrates.[60] Since then, other researchers have described LBL-AR preparation from double-layer nanoparticle-based coatings,[61] multilayer assembly of silica sols and NPs,[51,62-65] all-NPs assemblies,[66] and nanoporous polyelectrolyte multilayers.[67] Overall, with the exception of the nanoporous polyelectrolyte assemblies,[67] all of the LBL-AR coatings presented until today relied on spherical NPs in their preparation. Note that mechanical properties are very essential for optical coatings and incorporation of nanoscale components with promising mechanical properties is quite essential.

Here, we show that equally effective coatings can be prepared by LBL assembly of high-aspect-ratio axial colloids and we demonstrate this by LBL assembly of cellulose nanowires from tunicate (a sea animal) (CNWs). The morphology of CNWs is also quite remarkable. Their uniformity and high aspect ratio can be very favorably compared with synthetic nanowires (NWs),[68-73] while their preparation is very simple. They can be an example of naturally perfect nanostructures. We show that the layered architecture of the coating and parallel orientation of the microns-long and stiff CNWs with respect to the coated surface, result in formation of a porous structure with film-thickness dependent porosity and optical properties. In simplest terms, the structure of the coating can be compared to that of a “flattened matchsticks pile”. The underlying physics of AR effect is certainly the same as in the other AR coatings, however the structure of LBL assembled CNWs has a decisively new morphology. Additionally, incorporation of CNWs opens the door for improvement of their mechanical properties and preparation of optically active coatings with multifunctional properties, such as electrically driven responsiveness.[74,75]

2. Experimental Procedure

Materials

Microscope glass slides used for the deposition were obtained from Fisher Scientific. 50 wt.% solution of polyethyleneimine (PEI), branched, MW = 750,000 (light scattering) was obtained from Sigma-Aldrich. Chitosan (CH) and polyallylamine (PAH) used for preparation of thin films for mechanical properties evaluation were obtained from Sigma-Aldrich. 1 wt.% solutions of PEI and PAH used in this work were prepared by diluting the stock solution with 18 $M\Omega*cm^{-1}$, pH = 5.6 de-ionized water (DI water). 0.5 wt.% solution of CH was obtained by dissolving appropriate amount of the solid in 3 vol.% acetic acid solution (Sigma-Aldrich). Hydrogen peroxide and concentrated sulfuric acid used in the piranha cleaning solution were both purchased from Sigma-Aldrich. All of the reagents used for extraction of the cellulose nanocrystals: KOH pellets, sodium perchlorate solution, NaOH pellets, and glacial acetic acid, were obtained from Sigma-Aldrich. Tunicate specimens of *Didemnum* sp. were collected at Sandwich, Massachusetts, near the east entrance to the Cape Cod Canal in October of 2006. Colonies were attached to granitic rocks in a vast, rocky intertidal pool area that is exposed at low tide and covered with 3 m of water at high tide. A stainless steel spatula was used to remove the colonies from the rocks. Specimens were rinsed with seawater, enrolled in white paper towels, placed in individual 500 ml plastic jars, and preserved in anhydrous, denatured ethanol until further use.

Cellulose NWs Extraction

The colloidal suspensions of CNWs in water were prepared following a modified method of Chanzy et al.[76] Briefly, the animals were gutted and their tunic isolated and cut into small, ~1 cm x 1 cm fragments. The fragments were thoroughly rinsed with DI water to remove remaining sea debris and then deproteinized by four successive bleaching treatments. Details of the procedure were as follows:

a) 22 g of wet tunic was placed into 200 ml of 5% KOH/water solution and stirred overnight;

b) Next day, 300 ml of a bleaching mixture consisting of 2.55 g of sodium perchlorate, 4.05 g of NaOH, and 11 mL of glacial acetic acid were prepared and the resulting solution was heated to 70 ºC;

c) The KOH treated pieces of tunic were separated, rinsed with pure DI water, and the KOH/water solution was discarded;

d) Tunicate fragments were added to the bleaching solution and allowed to stir at 70 ºC for 2 hours;

f) The bleaching solution was replaced with fresh solution every 2 hours, for a total of 3 bleachings

e) steps a) – f) were repeated 3 more times after which the tunicate fragments were separated and rinsed with DI water.

Following the bleaching treatments tunicate fragments became highly porous with a white-yellow tint. The bleached fragments were subsequently disintegrated into a homogeneous suspension in ~100 ml of DI water with a commercial blender and separated using centrifugation. Resulting paste was then set aside and in the mean time, 200 ml of 50 % (v/v) concentrated H_2SO_4/DI water solution was prepared (careful!, highly exothermic reaction). The solution was first allowed to cool down and subsequently heated up to a stable temperature of 70 ºC. When the final temperature was reached, the tunicate paste was added to the solution and allowed to stir at the 70 ºC for 2 hours under vigorous stirring. In this step, the strong acid oxidizes the amorphous regions of cellulose much faster leaving the crystallites intact and at the same time introduces sulfate groups in the place of hydroxyls on the surface of the NWs giving them a net negative charge. Following the reaction, the NWs were separated using high-speed centrifugation (~20,000 xg) and washed with 3 redispersion and centrifugation steps in pure DI water. Finally, the resulting dispersion of the tunicate NWs was treated for ~1min with ultrasonication while on ice to give a homogeneous suspension of the NWs. Suspension was very stable and could be stored for long (at least months) periods of time in refrigerator prior to use.

LBL Deposition

Preparation of the films consisted of following steps: i) immersion of the substrate (Si or microscope glass slide) into a polymer solution for 1 min, ii) rinsing with the DI water for 1min, iii) drying with a stream of compressed air for 1min, iv) immersion into aqueous dispersion of CNWs for 1 min, v) rinsing with DI water for 1 min, and finally vi) once again drying with a stream of compressed air for 1 min. Prior to beginning deposition, the glass slides were cleaned by immersion into "piranha" solution (3:1 H_2SO_4:H_2O_2, dangerous if contacted with organics!) for 1 hour, followed by thorough rinsing with DI water. For PAH/CNWs, free-standing films were removed from the glass substrate with 1 vol.% HF solution as described in our previous publications.[39]

Instrumental Analysis

LBL process was monitored using an 8453 UV-Vis Chem Station spectrophotometer from Agilent Technologies, with data collected after each (PEI/CNWs) bilayer deposition. The reference spectrum for the instrument was that of a fresh, piranha-cleaned glass slide and collected spectra of the adsorbed material were compiled into a single plot for comparison. Atomic Force Microscopy (AFM) images were obtained using a NanoScope IIIa atomic force microscope (AFM) from Veeco Instruments (Santa Barbara, CA). The instrument was operated in tapping mode and images were obtained using silicon nitride cantilever tips (NSC16/Cr-Au, MikroMasch). Imaging was performed on films deposited on top of Si wafers and on top of a microscope glass slide in the case of a 12 bilayer film. Scanning electron microscopy (SEM) was used to characterize the cross-section dimensions of the free-standing films. The images were obtained with an FEI Nova Nanolab dual-beam FIB and scanning electron microscope. Due to nonconductive nature of the specimens, a few nm thick layer of gold was sputtered onto the surface of the film prior to imaging. Ellipsometry measurements were obtained using two instruments: 1) BASE-160 Spectroscopic Ellipsometer produced by J. A. Woollam Co., Inc. and 2) EP3-SW Imaging Ellipsometer (Nanofilm Technologie GmbH, Germany). The samples used for ellipsometry were either deposited on top of a glass slide or the Si wafer. The thickness progression of the LBL assembly was characterized with the BASE-60 ellipsometer. The instrument was calibrated to the standard silicon wafer with a thin layer of silicon dioxide and the subsequent calculations were fitted using a Cauchy's model. The samples used for ellipsometry were prepared on silicon wafers following the LBL protocol described previously. The refractive index of the multilayer was determined from a 5 bilayers sample. The refractive index of the films was obtained using the EP3-SW Ellipsometer. The ellipsometric parameters for this instrument, delta and psi, were recorded at a wavelength of 532 nm from a sample deposited on the glass slides. Four-zone nulling experiments were performed at multiple angles of incidence (48º to 68º every 2 degrees), and an anisotropic Cauchy model was also used to model the thickness and refractive index in this case. Zeta potential of the CNWs was obtained using a Zetasizer Nano ZS from Malvern Instruments, Great Britain. Light reflectance measurements were obtained using an in-house constructed system with a UV-NIR deuterium-halogen light source, DH-2000-BAL and a USB2000 miniature fiber optic spectrometer from Ocean Optics Inc., Dunedin, FL. The data were collected at a normal incidence light with a reference spectrum of polished Si wafer. Mechanical properties of free-standing PAH/CNWs films were analyzed by obtaining stress-strain curves with a mechanical strength tester version 100Q from TestResources Inc. (Shakopee, MN). The relative humidity in the testing facility was ~30 %. Tests were performed at a constant rate of 10 μm/s while force was recorded using a TestResources load cell with maximum capacity of 1.1 lbf (~4.9 N). The test samples were rectangular strips ~1 mm wide and 4-6 mm long. Brillouin scattering spectra were collected for CH/CNWs samples deposited on Si wafer with illumination in a 180° backscattering setup using a Coherent Verdi solid-state laser with a wavelength of 532 nm and power intensities of 40 - 90 mW. The laser light was focused onto the sample with a focusing spot of ~30 μm^2. The scattered light was collected over a period of 20 – 60 min, and analyzed using a Sandercock tandem 6 pass Fabry-Perot interferometer.

3. Results and Discussion

In Section B we showed ”proof-of-concept” demonstration of LBL assembly of short CNRs from cotton.[35] We showed the feasibility of LBL assembly of the crystals with PDDA polycation and we found the preparation to be simple and robust. Similarly, Gray *et al.* in their subsequent publications showed more detailed characterization of the LBL and “spin-assisted” LBL assembly of the cotton CNRs with other polymers as well.[45,77] We believe that the structural perfection and large aspect ratio of tunicate NWs is a very attractive property of this unique natural nanomaterial, which is likely to be a decisive factor in performance characteristics of CNW-materials.

In light of our previous results on cotton CNRs, we have first characterized adsorption of the tunicate NWs with atomic force microscopy (AFM) and scanning electron microscopy (SEM). For this purpose we have pre-coated small pieces of silicone wafer with 1 wt.% solution of polyethyleneimine (PEI) for 1 min and then after thorough rinsing with DI water and drying with compressed air, the Si pieces were quickly dipped into the CNWs dispersion for about a fraction of a second in order to adsorb isolated individual whiskers. The choice of PEI for this work was arbitrary and we want to note that we have obtained similar results with other polycations, including PDDA, polyallylamine (PAH), or Chitosan. To our surprise, unlike virtually all other LBL assemblies of nanocolloids, for which adsorption requires sometimes even tens of minutes, both AFM and SEM revealed densely covered surface of microns-long and highly rigid NWs. (Figure 44)

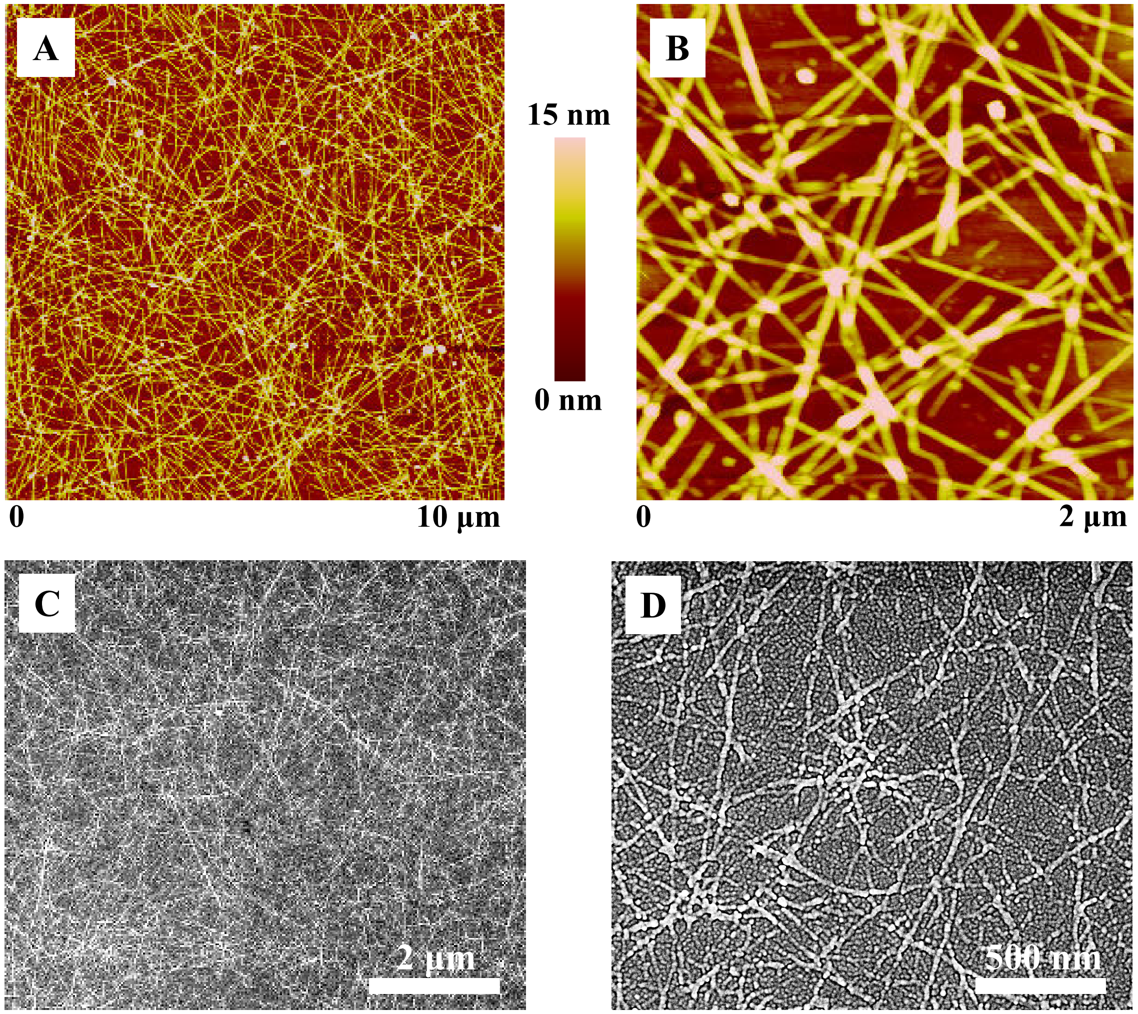

Figure 44. AFM and SEM characterization of a single PEI/tunicate bilayer adsorbed on a surface of a Si wafer with 1 min PEI and instantaneous tunicate immersions. (A) and (B): height AFM images. (C) and (D): SEM micrographs.

Similarly to the results in Section C, we believe that this fast adsorption is a result of several factors: a) high concentration of the CNWs, b) high surface charge, and c) acidity of the dispersion from incomplete removal of the strong sulfuric acid. High concentration of the CNWs drives the Langmuir adsorption while low pH protonates the amine groups of PEI and increases strength of attraction to the CNWs. Zeta potential measurements showed highly negative surface charge of -30-40 mV which supports this hypothesis. For the purpose of multilayers preparation, this behavior presents a unique advantage by dramatically shortening the necessary time of preparation. As can be seen from the images, the CNWs are several microns long and they are very rigid. Cross-sectional analysis of the AFM images revealed somewhat smaller dimensions then those reported in the literature: 3-4 nm (Figure 45) as opposed to 15 nm.[27,28] Altogether the high density of adsorbing nanocrystals create a dense, percolated network, and this feature enables preparation of the LBL-AR structure.

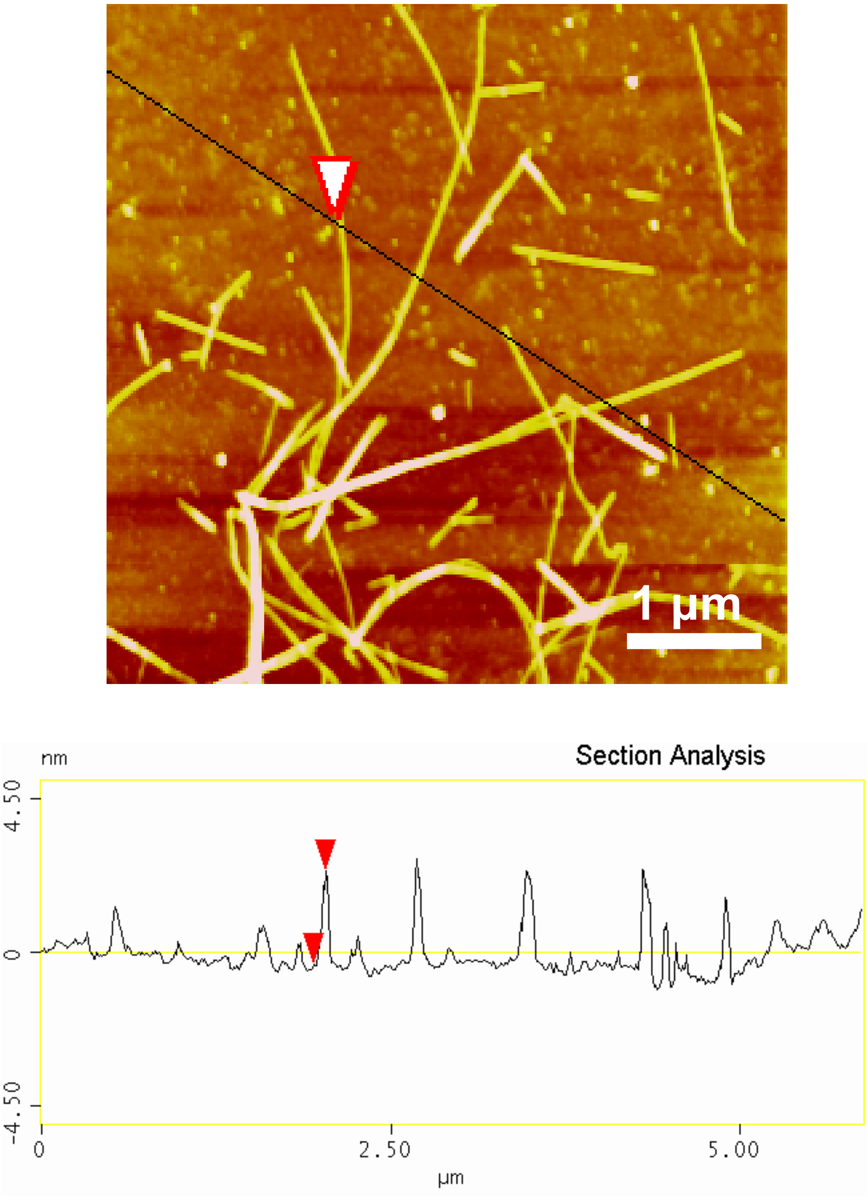

Figure 45. Cross-sectional analysis of individual CNWs. The cross-section reveals the thickness of the nanowires to be between 3-4 nm.

Having established dense and uniform adsorption of the CNWs, LBL films were grown on microscope glass slides and silicon wafers. The multilayer film growth was characterized with both UV-vis spectroscopy and ellipsometry. With the fast and dense adsorption, films were grown using only 1 min immersions for both the polymer and CNWs. UV-vis characterization (Figure 46) revealed linearly increasing light transmittance across the visible range of light when compared to an uncoated glass slide, which is characteristic of LBL-AR coatings. The maximum of transmittance is reached after ~12 bilayers, requiring only ~30 min for total preparation of the coating including the rinsing and drying steps. (Figure 47) The transmittance results are nearly identical to those observed by Rubner's group for SiO_2 nanoparticles LBL-AR although the nanoscale component, topology of nanomaterial, and mechanism of pore formation in the PEI/CNWs multilayer are very different.[62]

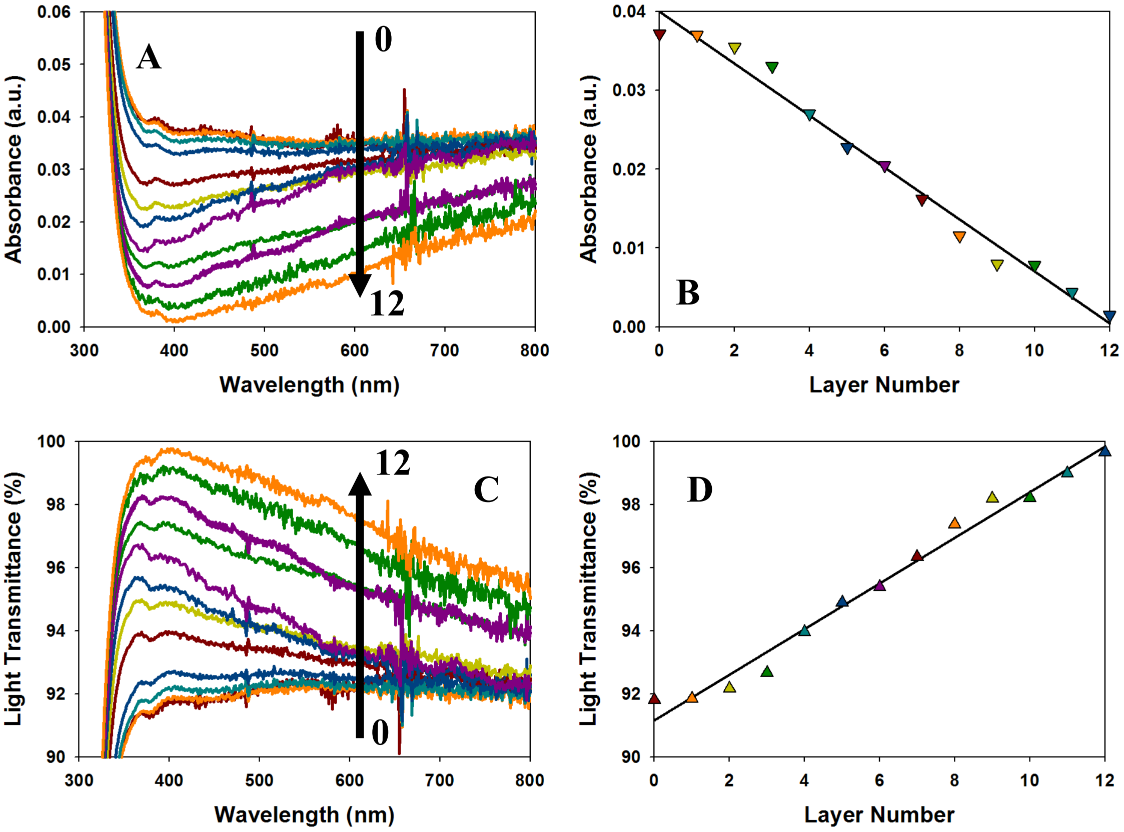

Figure 46. UV-vis characterization of PEI/CNWs assembly on a microscope glass slide: (A) compilation of absorbance spectra for the first 12 bilayers, (B) absorbance at 400 nm as function of bilayer number, (C) corresponding transmittance spectra for the first 12 bilayers, and (D) light transmittance at 400 nm as a function of a bilayer number.

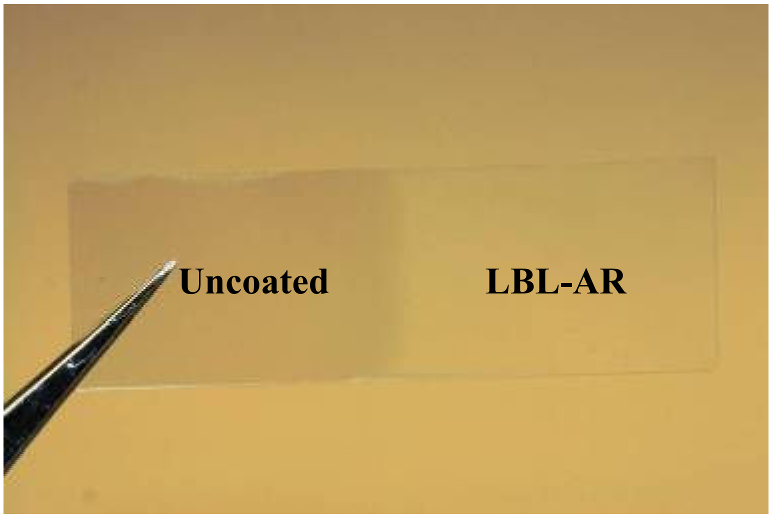

Figure 47. Photograph of a 1” x 3” microscope glass slide coated with 12 bilayers of PEI/CNWs as indicated.

With the good linearity observed from UV-vis spectroscopy it is expected to have linear thickness growth of the LBL-AR film as a function of the bilayer number. Ellipsometry measurements showed in fact linear growth of the film with an average increment of ~7 nm per bilayer (Figure 48A). This is a reasonable result given that the diameter of the CNWs is only 3-4 nm. The ellipsometry also showed rather small increment after polymer layer deposition suggesting that the effective thickness is a result of up to 2 overlapping NWs on average. Similarly to the studies on SiO_2 nanoparticles, the maximum transmittance peak also red-shifts accounting for increased film thickness and light scattering. (Figure 48B) The refractive index for the 12-bilayer film from ellipsometry gave a value of 1.28 at 532 nm, which is closely matching the required value of 1.22 for AR coatings. Similarly, the thickness for the 12-bilayer film is ~85 nm which is closely matching the λ/4 requirement of ~100 nm for the maximum transmittance of 400 nm. The same calculation can be used for the 20 bilayer film in Figure 48B which shows a transmittance maximum at ~570 nm. The λ/4 = ~143 nm which is in excellent agreement with the ellipsometry results in Figure 48A. Complementary to transmittance, reflectance characterization shows exact match of the minimum of reflectance for the 12 bilayers at ~400 nm. (Figure 48C) The results also show that the onset of AR is with the deposition of the first bilayer and the effect increases until the minimum required thickness is achieved.

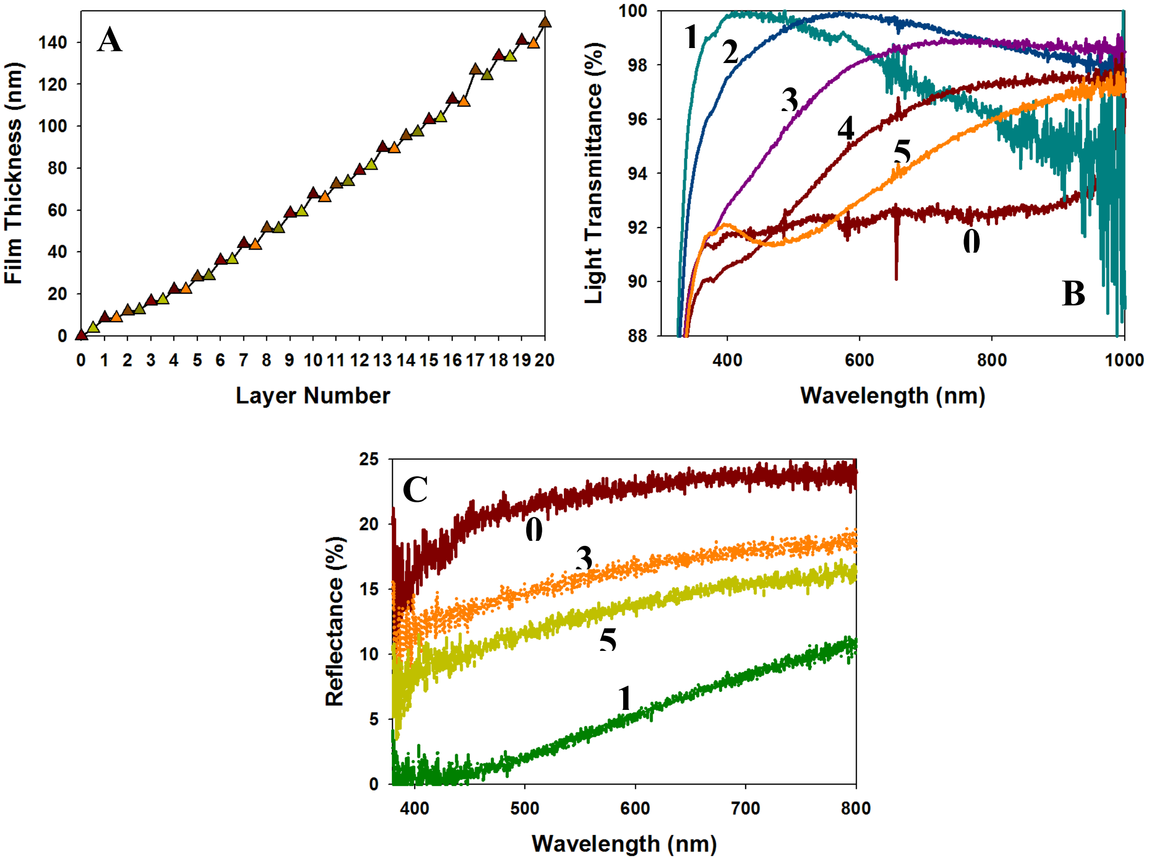

Figure 48. (A) Thickness of the PEI/CNWs film characterized with ellipsometry after every PEI and CNWs adsorbed layers. (B) UV-vis transmittance spectra collected after indicated number of (PEI/CNWs) bilayers. (C) Reflectance spectra collected after indicated number of (PEI/CNWs) bilayers. Curves identified by 0 are spectra of an uncoated glass slide.

Characterization of the multilayered films with AFM and SEM revealed highly porous structure characteristic of other porous AR coatings. (Figures 49 and 50) Both SEM and AFM show decrease in the pore size from 0 to 12 and to 20 bilayers which is directly related to the formation mechanism. As can be seen in the schematics in Figures 49A-C the overlapping NWs resemble rigid rods which when piled up create the necessary porous structure for an effective AR coating. As the pile becomes too tall, the porosity decreases, resulting in the observed decrease in transparency and increase of light scattering. The LBL assembly enables formation of this type of structure by restricting adsorption of the NWs to planar, 2-D orientation. Planar orientation of the long NWs ensures discrete and uniform thickness of the adsorbing layers with relatively low variation in the overall film thickness. One can imagine that this type of structure can only be possible with very long and rigid NWs suggesting that a critical, minimum length of this building block is necessary. If the NWs were too short, just as in our previous work on cotton CNRs, the NWs would just fill in the holes leaving little porosity, which in turn would result in much higher refractive index and light scattering. This is also important because unlike the nanoparticle-based assemblies, LBL structures composed of long NWs offer unique percolated network which could potentially allow for engineering of other functionalities and certainly contribute to improving mechanical resilience of this type of coatings. As expected, results from evaluation of mechanical properties of free-standing PAH/CNWs films show ultimate tensile strength as high as 110 MPa and a modulus of elasticity of ~6 GPa, while Brillouin light scattering measurements on LBL CNWs films show an in-plane modulus between 20 and 30 GPa. (Figure 51) The latter represent potentially more appropriate characteristics of the coatings, because it describes mechanical properties of undisturbed coating.

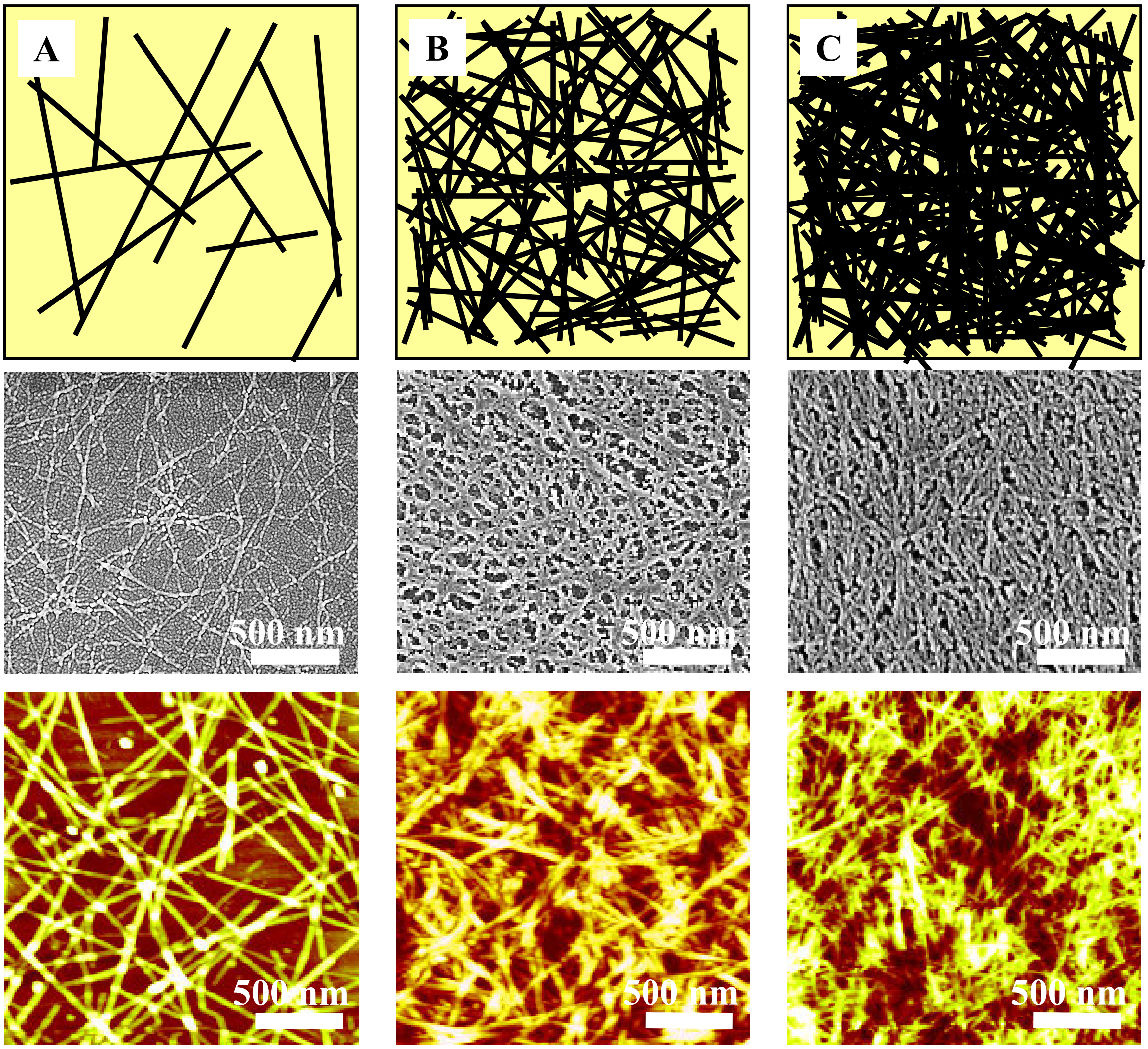

Figure 49. Graphical representation and microscopy images of the of the PEI/CNWs LBL-AR coatings with (A) 1 bilayer, (B) 12 bilayers, and (C) 20 bilayers.

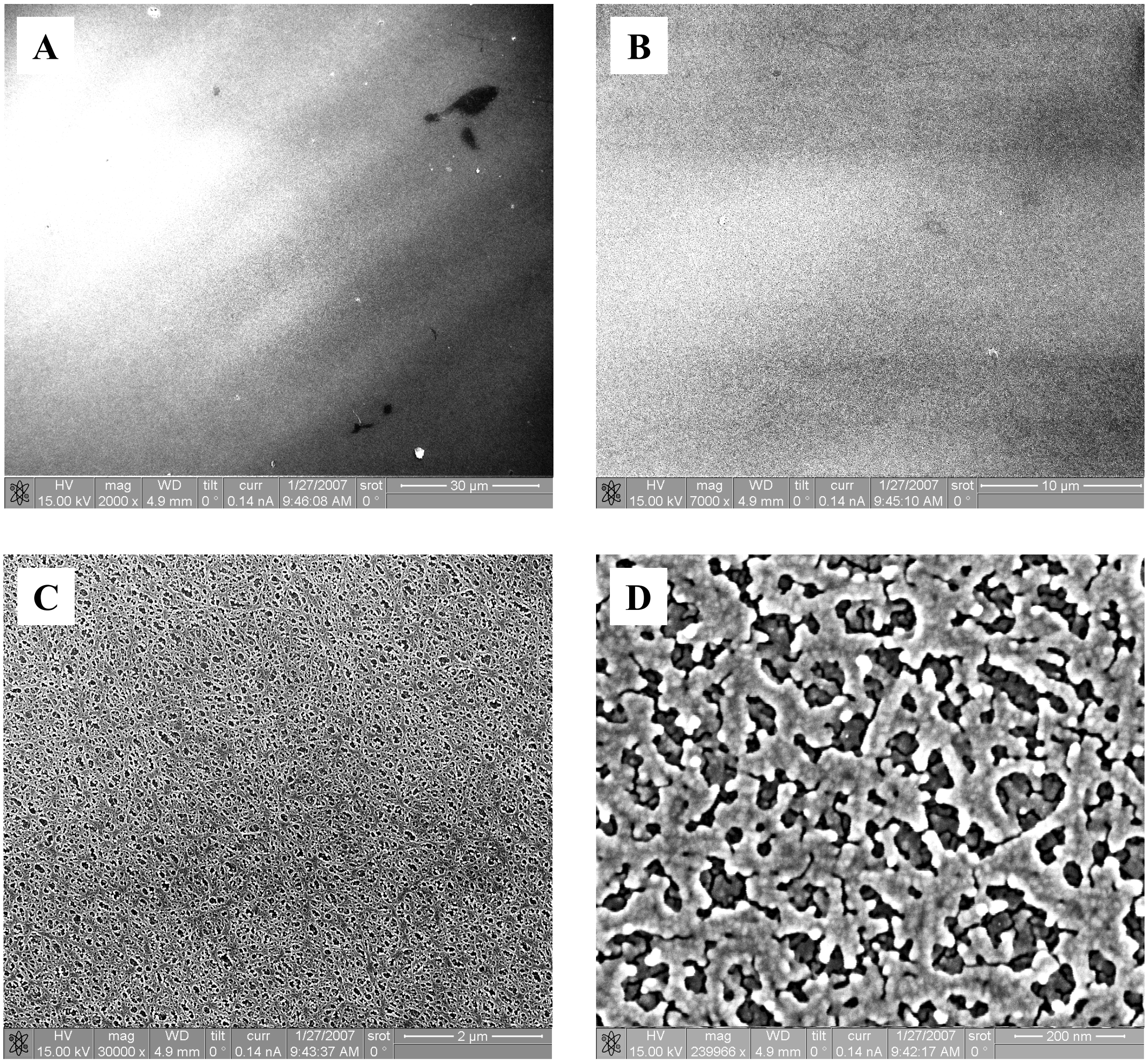

Figure 50. SEM images of 12 bilayers of PEI/CNWs at different magnifications showing uniformity of the coating: (A) 2000x, (B) 7000x, (C) 30000x, and (D) 240,000x. The cracks in (D) are caused by the electron beam.

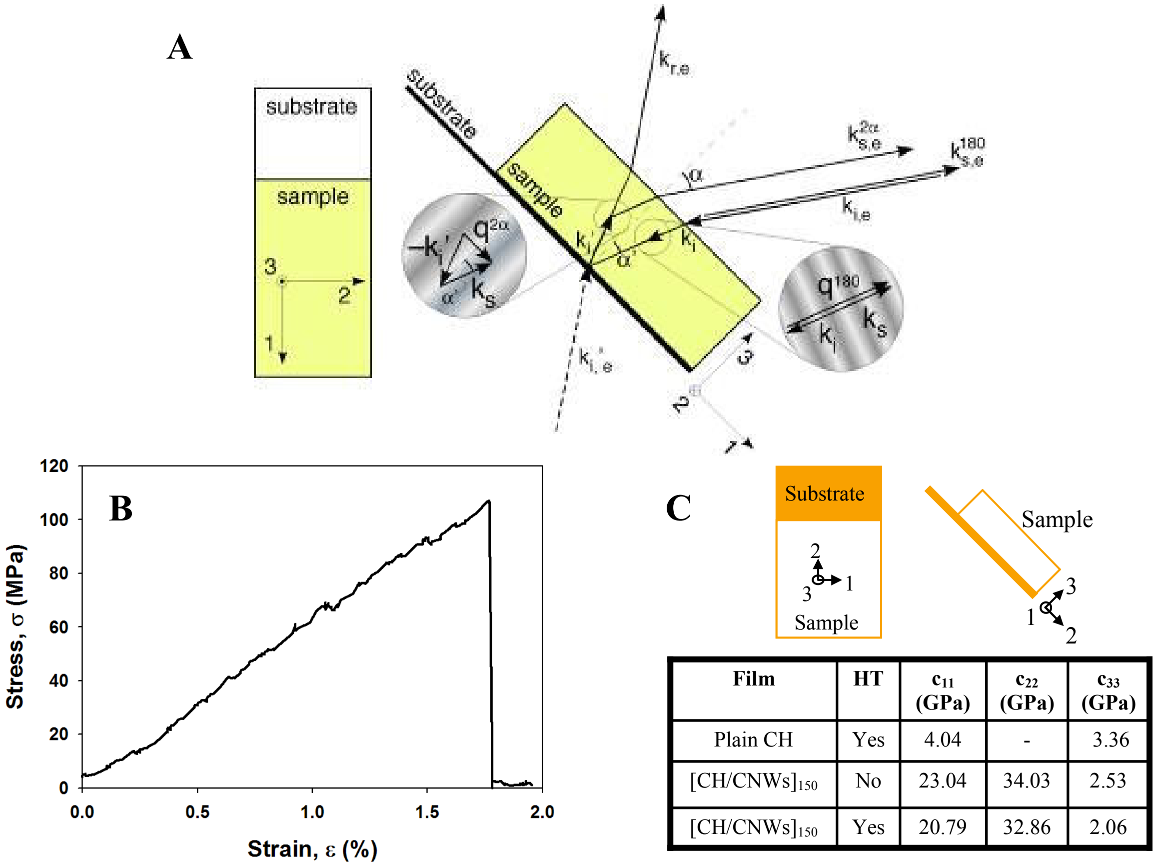

Film	HT	c_{11} (GPa)	c_{22} (GPa)	c_{33} (GPa)
Plain CH	Yes	4.04	-	3.36
$[CH/CNWs]_{150}$	No	23.04	34.03	2.53
$[CH/CNWs]_{150}$	Yes	20.79	32.86	2.06

Figure 51. (A) Backscattering setup for Brillouin scattering. k_i, k_s, and k_r are the incident, scattered, and reflected beams; 1 and 2 directions are in the growth plane of the sample, and direction 3 is normal to the growth plane; α is the angle k_i makes with the 3 direction; q is the phonon propagation direction. (B) Typical stress-strain response of a PAH/CNWs free-standing film. (C) Elastic constants of CH and CH/CNWs films from Brillouin scattering experiments. HT indicates heat treatment of the sample.

4. Conclusions

We showed here the first preparation of thin films of stiff and rigid tunicate cellulose NWs by LBL assembly. The resulting films have morphology of a porous matchsticks pile which brings about strong anti-reflective properties. Overall, the unique mechanical properties of CNWs combined with other stiff axial colloids, such as semiconductor NWs, can potentially greatly enrich and improve the functionalities of AR coatings.[68]

Reference List

1. Wong, E. W.; Sheehan, P. E.; Lieber, C. M. Nanobeam mechanics: elasticity, strength, and toughness of nanorods and nanotubes. *Science (Washington, D. C.)* **1997,** *277* (5334), 1971-1975.

2. Popov, V. N.; Van Doren, V. E.; Balkanski, M. Elastic properties of single-walled carbon nanotubes. *Physical Review B: Condensed Matter and Materials Physics* **2000,** *61* (4), 3078-3084.

3. Baughman, R. H.; Cui, C.; Zakhidov, A. A.; Iqbal, Z.; Barisci, J. N.; Spinks, G. M.; Wallace, G. G.; Mazzoldi, A.; De Rossi, d.; Rinzler, A. G.; Jaschinski, O.; Roth, S.; Kertesz, M. Carbon nanotube actuators. *Science (Washington, D. C.)* **1999,** *284* (5418), 1340-1344.

4. Qian, D.; Dickey, E. C.; Andrews, R.; Rantell, T. Load transfer and deformation mechanisms in carbon nanotube-polystyrene composites. *Applied Physics Letters* **2000,** *76* (20), 2868-2870.

5. Yu, M. F.; Files, B. S.; Arepalli, S.; Ruoff, R. S. Tensile loading of ropes of single wall carbon nanotubes and their mechanical properties. *Physical Review Letters* **2000,** *84* (24), 5552-5555.

6. Salvetat, J. P.; Kulik, A. J.; Bonard, J. M.; Briggs, G. A.; Stoeckli, T.; Metenier, K.; Bonnamy, S.; Beguin, F.; Burnham, N. A.; Forro, L. Elastic modulus of ordered and disordered multiwalled carbon nanotubes. *Advanced Materials (Weinheim, Germany)* **1999,** *11* (2), 161-165.

7. Van Lier, G.; Van Alsenoy, C.; Van Doren, V.; Geerlings, P. Ab initio study of the elastic properties of single-walled carbon nanotubes and graphene. *Chemical Physics Letters* **2000,** *326* (1,2), 181-185.

8. Hernandez, E.; Goze, C.; Bernier, P.; Rubio, A. Elastic Properties of C and BxCyNz Composite Nanotubes. *Physical Review Letters* **1998,** *80* (20), 4502-4505.

9. Treacy, M. M. J.; Ebbesen, T. W.; Gibson, J. M. Exceptionally high Young's modulus observed for individual carbon nanotubes. *Nature (London)* **1996,** *381* (6584), 678-680.

10. Krishnan, A.; Dujardin, E.; Ebbesen, T. W.; Yianilos, P. N.; Treacy, M. M. J. Young's modulus of single-walled nanotubes. *Physical Review B: Condensed Matter and Materials Physics* **1998,** *58* (20), 14013-14019.

11. Yu, M. F.; Lourie, O.; Dyer, M. J.; Moloni, K.; Kelly, T. F.; Ruoff, R. S. Strength and breaking mechanism of multiwalled carbon nanotubes under tensile load. *Science (Washington, D. C.)* **2000,** *287* (5453), 637-640.

12. Penumadu, D.; Dutta, A.; Pharr, G. M.; Files, B. Mechanical properties of blended single-wall carbon nanotube composites. *Journal of Materials Research* **2003,** *18* (8), 1849-1853.

13. Ajayan, P. M.; Zhou, O. Z. Applications of carbon nanotubes. *Topics in Applied Physics* **2001,** *80* (Carbon Nanotubes), 391-425.

14. Ajayan, P. M.; Charlier, J. C.; Rinzler, A. G. Carbon nanotubes. From macromolecules to nanotechnology. *Proceedings of the National Academy of Sciences of the United States of America* **1999,** *96* (25), 14199-14200.

15. Ajayan, P. M.; Schadler, L. S.; Giannaris, C.; Rubio, A. Single-walled carbon nanotube-polymer composites: strength and weakness. *Advanced Materials (Weinheim, Germany)* **2000,** *12* (10), 750-753.

16. Kis, A.; Csanyi, G.; Salvetat, J. P.; Lee, T. N.; Couteau, E.; Kulik, A. J.; Benoit, W.; Brugger, J.; Forro, L. Reinforcement of single-walled carbon nanotube bundles by intertube bridging. *Nature Materials* **2004,** *3* (3), 153-157.

17. Sturcova, A.; Davies, G. R.; Eichhorn, S. J. Elastic Modulus and Stress-Transfer Properties of Tunicate Cellulose Whiskers. *Biomacromolecules* **2005,** *6* (2), 1055-1061.

18. Helbert, W.; Cavaille, J. Y.; Dufresne, A. Thermoplastic nanocomposites filled with wheat straw cellulose whiskers. Part I: Processing and mechanical behavior. *Polymer Composites* **1996,** *17* (4), 604-611.

19. De Souza Lima, M. M.; Borsali, R. Rodlike cellulose microcrystals: structure, properties, and applications. *Macromolecular Rapid Communications* **2004,** *25* (7), 771-787.

20. Dufresne, A. Comparing the mechanical properties of high performances polymer nanocomposites from biological sources. *Journal of Nanoscience and Nanotechnology* **2006,** *6* (2), 322-330.

21. Samir, M. A. S. A.; Alloin, F.; Dufresne, A. Review of Recent Research into Cellulosic Whiskers, Their Properties and Their Application in Nanocomposite Field. *Biomacromolecules* **2005,** *6* (2), 612-626.

22. Revol, J. F.; Bradford, H.; Giasson, J.; Marchessault, R. H.; Gray, D. G. Helicoidal self-ordering of cellulose microfibrils in aqueous suspension. *International Journal of Biological Macromolecules* **1992,** *14* (3), 170-172.

23. Gray, D. G. Chiral nematic ordering of polysaccharides. *Carbohydrate Polymers* **1994,** *25* (4), 277-284.

24. Roman, M.; Gray, D. G. Parabolic Focal Conics in Self-Assembled Solid Films of Cellulose Nanocrystals. *Langmuir* **2005,** *21* (12), 5555-5561.

25. Revol, J.-F.; Godbout, J. D. L.; Gray, D. G. Solidified liquid crystals of cellulose with optically variable properties. WO A1 9521901, 1995.

26. Fengel, D.; Wegener, G. *Wood: Chemistry, Ultrastructure, Reactions;* 1984.

27. Favier, V.; Chanzy, H.; Cavaille, J. Y. Polymer Nanocomposites Reinforced by Cellulose Whiskers. *Macromolecules* **1995,** *28* (18), 6365-6367.

28. Terech, P.; Chazeau, L.; Cavaille, J. Y. A Small-Angle Scattering Study of Cellulose Whiskers in Aqueous Suspensions. *Macromolecules* **1999,** *32* (6), 1872-1875.

29. Revol, J. F. On the cross-sectional shape of cellulose crystallites in Valonia ventricosa. *Carbohydrate Polymers* **1982,** *2* (2), 123-134.

30. Hanley, S. J.; Giasson, J.; Revol, J. F.; Gray, D. G. Atomic force microscopy of cellulose microfibrils: comparison with transmission electron microscopy. *Polymer* **1992,** *33* (21), 4639-4642.

31. Tokoh, C.; Takabe, K.; Fujita, M.; Saiki, H. Cellulose synthesized by Acetobacter xylinum in the presence of acetyl glucomannan. *Cellulose* **1998,** *5* (4), 249-261.

32. Grunert, M.; Winter, W. T. Nanocomposites of cellulose acetate butyrate reinforced with cellulose nanocrystals. *Journal of Polymers and the Environment* **2002,** *10* (1/2), 27-30.

33. Araki, J.; Wada, M.; Kuga, S.; Okano, T. Flow properties of microcrystalline cellulose suspension prepared by acid treatment of native cellulose. *Colloids and Surfaces A-Physicochemical and Engineering Aspects* **1998,** *142* (1), 75-82.

34. Beck-Candanedo, S.; Roman, M.; Gray, D. G. Effect of Reaction Conditions on the Properties and Behavior of Wood Cellulose Nanocrystal Suspensions. *Biomacromolecules* **2005,** *6* (2), 1048-1054.

35. Podsiadlo, P.; Choi, S. Y.; Shim, B.; Lee, J.; Cuddihy, M.; Kotov, N. A. Molecularly Engineered Nanocomposites: Layer-by-Layer Assembly of Cellulose Nanocrystals. *Biomacromolecules* **2005,** ***6*** (6), 2914-2918.

36. Nakagaito, A. N.; Yano, H. Novel high-strength biocomposites based on microfibrillated cellulose having nano-order-unit web-like network structure. *Applied Physics A: Materials Science & Processing* **2004,** *80* (1), 155-159.

37. Noishiki, Y.; Nishiyama, Y.; Wada, M.; Kuga, S.; Magoshi, J. Mechanical properties of silk fibroin-microcrystalline cellulose composite films. *Journal of Applied Polymer Science* **2002,** *86* (13), 3425-3429.

38. Lefebvre, J.; Gray, D. G. AFM of adsorbed polyelectrolytes on cellulose I surfaces spin-coated on silicon wafers. *Cellulose (Dordrecht, Netherlands)* **2005,** *12* (2), 127-134.

39. Tang, Z.; Kotov, N. A.; Magonov, S.; Ozturk, B. Nanostructured artificial nacre. *Nature Materials* **2003,** *2* (6), 413-418.

40. Olek, M.; Ostrander, J.; Jurga, S.; Moehwald, H.; Kotov, N.; Kempa, K.; Giersig, M. Layer-by-Layer Assembled Composites from Multiwall Carbon Nanotubes with Different Morphologies. *Nano Letters* **2004,** *4* (10), 1889-1895.

41. Podsiadlo, P.; Paternel, S.; Rouillard, J. M.; Zhang, Z.; Lee, J.; Lee, J. W.; Gulari, E.; Kotov, N. A. Layer-by-Layer Assembly of Nacre-like Nanostructured Composites with Antimicrobial Properties. *Langmuir* **2005,** *21* (25), 11915-11921.

42. Podsiadlo, P.; Liu, Z.; Paterson, D.; Messersmith, P. B.; Kotov, N. A. Fusion of seashell nacre and marine bioadhesive analogs: high-strength nanocomposite by layer-by-layer assembly of clay and L-3,4-dihydroxyphenylalanine polymer. *Advanced Materials (Weinheim, Germany)* **2007,** *19* (7), 949-955.

43. Podsiadlo, P.; Tang, Z.; Shim, B. S.; Kotov, N. A. Counterintuitive Effect of Molecular Strength and Role of Molecular Rigidity on Mechanical Properties of Layer-by-Layer Assembled Nanocomposites. *Nano Letters* **2007,** *7* (5), 1224-1231.

44. Podsiadlo, P.; Kaushik, A. K.; Arruda, E. M.; Waas, A. M.; Shim, B. S.; Xu, J.; Nandivada, H.; Pumplin, B. G.; Lahann, J.; Ramamoorthy, A.; Kotov, N. A. Ultrastrong and Stiff Layered Polymer Nanocomposites. *Science (Washington, DC, United States)* **2007,** *318* (5847), 80-83.

45. Cranston, E. D.; Gray, D. G. Morphological and optical characterization of polyelectrolyte multilayers incorporating nanocrystalline cellulose. *Biomacromolecules* **2006,** *7* (9), 2522-2530.

46. Lowdermilk, W. H.; Milam, D. Graded-index antireflection surfaces for high-power laser applications. *Applied Physics Letters* **1980,** *36* (11), 891-893.

47. Zheng, Y.; Kikuchi, K.; Yamasaki, M.; Sonoi, K.; Uehara, K. Two-layer wideband antireflection coatings with an absorbing layer. *Applied Optics* **1997,** *36* (25), 6335-6338.

48. Bilyalov, R.; Stalmans, L.; Poortmans, J. Comparative Analysis of Chemically and Electrochemically Formed Porous Si Antireflection Coating for Solar Cells. *Journal of the Electrochemical Society* **2003,** *150* (3), G216-G222.

49. Clapham, P. B.; Hutley, M. C. Reduction of Lens Reflection by Moth Eye Principle. *Nature* **1973,** *244* (5414), 281-282.

50. Macleod, H. A. *Thin-Film Optical Filters. 2nd Ed;* 1986.

51. Yancey, S. E.; Zhong, W.; Heflin, J. R.; Ritter, A. L. The influence of void space on antireflection coatings of silica nanoparticle self-assembled films. *Journal of Applied Physics* **2006,** *99* (3), 034313-1-034313/10.

52. Walheim, S.; Schaffer, E.; Mlynek, J.; Steiner, U. Nanophase-separated polymer films as high-performance antireflection coatings. *Science (Washington, D. C.)* **1999,** *283* (5401), 520-522.

53. Ibn-Elhaj, M.; Schadt, M. Optical polymer thin films with isotropic and anisotropic nano-corrugated surface topologies. *Nature (London, United Kingdom)* **2001,** *410* (6830), 796-799.

54. Schelle, C.; Mennig, M.; Krug, H.; Jonschker, G.; Schmidt, H. One step antiglare sol-gel coating for screens by sol-gel techniques. *Journal of Non-Crystalline Solids* **1997,** *218*, 163-168.

55. Chen, D. Anti-reflection (AR) coatings made by sol-gel processes: A review. *Solar Energy Materials and Solar Cells* **2001,** *68* (3-4), 313-336.

56. Szczyrbowski, J.; Braeuer, G.; Teschner, G.; Zmelty, A. Antireflective coatings on large scale substrates produced by reactive twin-magnetron sputtering. *Journal of Non-Crystalline Solids* **1997,** *218*, 25-29.

57. Hadobas, K.; Kirsch, S.; Carl, A.; Acet, M.; Wassermann, E. F. Reflection properties of nanostructure-arrayed silicon surfaces. *Nanotechnology* **2000,** *11* (3), 161-164.

58. Aydin, C.; Zaslavsky, A.; Sonek, G. J.; Goldstein, J. Reduction of reflection losses in ZnGeP2 using motheye antireflection surface relief structures. *Applied Physics Letters* **2002,** *80* (13), 2242-2244.

59. Decher, G. Fuzzy nanoassemblies: toward layered polymeric multicomposites. *Science (Washington, D. C.)* **1997,** *277* (5330), 1232-1237.

60. Hattori, H. Anti-reflection surface with particle coating deposited by electrostatic attraction. *Advanced Materials (Weinheim, Germany)* **2001,** *13* (1), 51-54.

61. Koo, H. Y.; Yi, D. K.; Yoo, S. J.; Kim, D. Y. A snowman-like array of colloidal dimers for antireflecting surfaces. *Advanced Materials (Weinheim, Germany)* **2004,** *16* (3), 274-277.

62. Cebeci, F. C.; Wu, Z.; Zhai, L.; Cohen, R. E.; Rubner, M. F. Nanoporosity-Driven Superhydrophilicity: A Means to Create Multifunctional Antifogging Coatings. *Langmuir* **2006,** *22* (6), 2856-2862.

63. Rouse, J. H.; Ferguson, G. S. Preparation of Thin Silica Films with Controlled Thickness and Tunable Refractive Index. *Journal of the American Chemical Society* **2003,** *125* (50), 15529-15536.

64. Yu, H. H.; Wu, H. B.; Li, X. F.; Zhu, Y. Z.; Jiang, D. S. Self-assembly and optical properties of silica nanoparticulate thin films. *Acta Physico-Chimica Sinica* **2001,** *17* (12), 1057-1061.

65. Wu, Z.; Walish, J.; Nolte, A.; Zhai, L.; Cohen, R. E.; Rubner, M. F. Deformable antireflection coatings from polymer and nanoparticle multilayers. *Advanced Materials (Weinheim, Germany)* **2006,** *18* (20), 2699-2702.

66. Lee, D.; Rubner, M. F.; Cohen, R. E. All-Nanoparticle Thin-Film Coatings. *Nano Letters* **2006,** *6* (10), 2305-2312.

67. Hiller, J.; Mendelsohn, J. D.; Rubner, M. F. Reversibly erasable nanoporous anti-reflection coatings from polyelectrolyte multilayers. *Nature Materials* **2002,** *1* (1), 59-63.

68. Tang, Z.; Kotov, N. A.; Giersig, M. Spontaneous organization of single CdTe nanoparticles into luminescent nanowires. *Science (Washington, DC, United States)* **2002,** *297* (5579), 237-240.

69. Park, M. S.; Wang, G. X.; Kang, Y. M.; Wexler, D.; Dou, S. X.; Liu, H. K. Preparation and electrochemical properties of SnO2 nanowires for application in lithium-ion batteries. *Angewandte Chemie, International Edition* **2007,** *46* (5), 750-753, S750-1.

70. Gao, F.; Yuan, Y.; Wang, K. F.; Chen, X. Y.; Chen, F.; Liu, J. M.; Ren, Z. F. Preparation and photoabsorption characterization of BiFeO3 nanowires. *Applied Physics Letters* **2006,** *89* (10), 102506-1-102506/3.

71. Liu, S.; Yue, J.; Gedanken, A. Synthesis of long silver nanowires from AgBr nanocrystals. *Advanced Materials (Weinheim, Germany)* **2001,** *13* (9), 656-658.

72. Lu, Q.; Gao, F.; Zhao, D. One-Step Synthesis and Assembly of Copper Sulfide Nanoparticles to Nanowires, Nanotubes, and Nanovesicles by a Simple Organic Amine-Assisted Hydrothermal Process. *Nano Letters* **2002,** *2* (7), 725-728.

73. Kim, H.; Sigmund, W. Zinc oxide nanowires on carbon nanotubes. *Applied Physics Letters* **2002,** *81* (11), 2085-2087.

74. Yun, S.; Zhao, L.; Wang, N.; Kim, J. Hybrid electro-active papers of cellulose and carbon nanotubes for bio-mimetic actuators. *Key Engineering Materials* **2006,** *324-325* (Pt. 2, Fracture and Damage Mechanics V), 843-846.

75. Kim, J.; Yun, S.; Ounaies, Z. Discovery of Cellulose as a Smart Material. *Macromolecules* **2006,** *39* (12), 4202-4206.

76. Sugiyama, J.; Chanzy, H.; Maret, G. Orientation of cellulose microcrystals by strong magnetic fields. *Macromolecules* **1992,** *25* (16), 4232-4234.

77. Cranston, E. D.; Gray, D. G. Formation of cellulose-based electrostatic layer-by-layer films in a magnetic field. *Science and Technology of Advanced Materials* **2006,** *7* (4), 319-321.

Chapter IV

Flexible, High Toughness and Hierarchically Structured Nanocomposites

A. Introduction

As we have discussed in previous chapters, LBL assembly[1] can generate unique materials with high degree of nanoscale organization and unique mechanical, electrical, optical, and many other properties.[2-10] While suitable for a number of sophisticated applications, small thicknesses of typical LBL sheets prohibit their utilization in a variety of biomedical technologies, advanced engineering, and aviation/space applications. Resolution of this problem would indicate a paradigm change in the practice of LBL and/or composite material manufacturing.

Additionally, while all of the nanocomposites presented in Chapters II and III showed exceptional strengths and stiffnesses, they all showed low ductility, i.e. small strain values, and toughness. Low ductility appears to be a general characteristic of all LBL assemblies, and many applications, such as flexible electronics and biomedical devices, would greatly benefit from flexible and tough/durable LBL coatings.

In this final chapter we address these two issues by focusing on the exponential LBL assembly (e-LBL) which greatly accelerates the multilayer growth process and offers new opportunities for materials' design. The e-LBL assembly has been thus far utilized solely for organic components and in this chapter we show for the first time preparation of hybrid organic/inorganic e-LBL assemblies.[11] We show that composites' thicknesses can be as high as hundreds of microns for 200-bilayer films offering orders of magnitude acceleration of the assembly process. The films also display unusually high hardness and stiffness when compared to the traditional, linear LBL assemblies. We further show that in spite of the very dynamic nature of the e-LBL systems, resulting from the "in-and-out" diffusion of the polyelectrolytes, the films are capable of self-organization allowing for formation of unique and novel architectures. We demonstrate this by preparation of a hybrid polymer/MTM clay e-LBL assembly having internal structure reminiscent of that found in natural nacre, however with reversed roles of the organic and inorganic phases.

In the second half of this chapter we focus on preparation of LBL composites using new assembly components: water-soluble polyurethanes (PUs). PUs are well-known for their strength and toughness and they found broad applications in construction, transportation, household appliances, packaging, electronics, and implantable biomedical devices, to name a few. PUs have never been used in LBL assembly, and thus, represent an important new component of LBL technique with a variety of potential research venues.

As such, first we demonstrate preparation of highly flexible nanostructured films from LBL assembly of oppositely charged PUs. The resulting films display average strains of ~630 %, which are more than 2 orders of magnitude greater than any LBL assemblies prepared thus far. Further, we extend the e-LBL assembly to a cationic PU as a route to preparation of high toughness, flexible, and hierarchically structured composites. The hierarchical organization is accomplished via consolidation of individual LBL sheets allowing for fast preparation of macro-scale materials having thicknesses at least in the millimeters range. The resulting laminates are homogenous, transparent, ductile, and display nearly 3x higher strength and toughness when compared to the original polymeric materials. The consolidation of individual films opens the road to development of a large family of hierarchically organized composites combining nano/micro scale organization originating from LBL technique and meso/macroscale ordering from the consolidation step. The hierarchical organization can also be applied as a unique tool for in-situ visualization of deformation mechanics with high spatial resolution, accuracy, and speed.

B. Exponential Growth of LBL Films with Incorporated Inorganic Sheets

1. Introduction

As we have mentioned in Chapter I, analysis of the exiting literature on e-LBL assembly shows that the types of polyelectrolyte pairs capable of the exponential assembly appear to be limited, and it would be quite beneficial to expand the functionality of this type of films to a greater number of LBL-capable species. As such, it would be very interesting to include nanoscale inorganic components in the e-LBL films, for instance, nanosheets of Na^+-motmorillonite (MTM). This is especially important for nacre-like composites, where it would be useful if MTM multilayers formed faster as in exponential growth mode.

As such, we have asked a question of whether it is actually feasible to generate hybrid organic/inorganic e-LBL films? The conundrum here is that MTM films have been shown to produce very effective diffusion barriers,[12] which are expected to strongly hinder the diffusion in the LBL films. According to the current understanding of e-LBL mechanism, this should make e-LBL impossible. To our great surprise this understanding is not true and MTM does allow for "in-and-out" diffusion process of macromolecules to occur.

Here, we present results from e-LBL assembly of a hybrid system composed of poly(ethyleneimine) (PEI), poly(acrylic acid) (PAA), and MTM with the following deposition sequence: $(PEI/PAA/PEI/MTM)_n$, where n is the number of deposition cycles and in this tri-component system it corresponds to 2 pairs (bilayers) of oppositely charged compounds per cycle. The assembly and film architecture was characterized with scanning electron microscopy (SEM), small angle x-ray scattering (SAXS), and laser scanning confocal microscopy, and it was compared with its organic counterpart, i.e. $(PEI/PAA)_n$ and a "nacre-like" analogue $(PEI/MTM)_n$. Mechanical properties of the different films were also characterized with nanoindentation. The $(PEI/PAA/PEI/MTM)_n$ system exhibits initial exponential growth followed by linear buildup, but with unusually thick individual bilayers, which were recently reported for a subset of e-LBL films incorporating high molecular weight polyelectrolytes.[13] In the present system, the growth rate was established to be nearly identical for $(PEI/PAA/PEI/MTM)_n$ with and without MTM, with total film-thicknesses reaching 200 μm for $n = 100$ and deposition intervals of 10 min, suggesting that inclusion of the MTM nanosheets have surprisingly little effect on the "in-and-out" diffusion mechanism of e-LBL film formation. Similar to the previous publications,[14] fluorescently labeled PEI was found to be diffusing through the film, thus further confirming the "in-and-out" diffusion mechanism. The nanoindentation experiments also showed that the films have unusually high modulus and hardness, which is technologically very important for a variety of coatings. Surprisingly, the properties of the e-LBL films are even higher when compared to the traditional linear systems with much greater inorganic contents and other LBL layers characterized in a similar way before.[15]

2. Experimental Procedure

Materials

35 wt.% aqueous solution of poly(acrylic acid) (PAA) with MW = 250,000, 50 wt.% aqueous solution of branched polyethleneimine (PEI) with MW = 750,000 (from light scattering), NaOH pellets, and dimethylsulfoxide (DMSO) were all purchased from Sigma-Aldrich (St. Louis, MO) and used as received without further purification. Na^+-Montmorillonite (Cloisite-Na^+, MTM) was purchased from Southern Clay Products (Gonzales, TX). 1 wt.% solutions of PAA and PEI used throughout the experiments, were prepared by appropriately diluting the stock solutions with 18 MΩ*cm, pH = 5.6 de-ionized water (DI water). MTM dispersion used in the experiments was prepared by dissolving 5 g of clay in DI water under vigorous stirring for 1 week prior to use. At the end of the week, MTM dispersion was left standing overnight to allow larger particles to sediment. Next day, supernatant was collected for use in experiments while precipitate was discarded. The pH of the resulting solutions was: 9.5, 2.9, and 10, for MTM, PAA, and PEI, respectively. Fluorescein isothiocyanate isomer I (FITC) was obtained from Sigma-Aldrich. *N*-(5-aminopentyl)-4-amino-3,6- disulfo-1,8-naphthalimide, dipotassium salt (lucifer yellow cadaverine, LYC) was obtained from Invitrogen (Carlsbad, CA). 1-

ethyl-3-(3-dimethylaminopropyl)-carbodiimide, hydrochloride (EDC) used in the fluorescent dye-PE conjugation was obtained from Invitrogen. *N*-hydroxysuccinimide (NHS) used to extend the activity of EDAC was obtained from Pierce (Rockford, IL). Dialysis membrane Spectra/Por 7 (Spectrum Laboratories Inc.) with a molecular weight cut off size of 1,000 used in the dye-PE conjugates purification was obtained from Fisher Scientific. Microscope glass slides used for films deposition were obtained from Fisher Scientific. Hydrogen peroxide and concentrated sulfuric acid used in the piranha cleaning solution were purchased from Sigma-Aldrich.

Preparation of PE-Dye Conjugates

FITC fluorescent probe was conjugated to the PEI polymer via condensation of the isothiocyanate groups of FITC and the primary amines[16] of the PEI. In the reaction, 100 ml of aqueous 1 wt.% PEI solution was mixed together with appropriate amount of FITC dissolved in 1 ml of pure DMSO and the mixture was stirred in darkness for 24 hours at room temperature. The pH of the mixture was adjusted to 8 immediately after mixing of the two components. The molar ratio of FITC and $–NH_2$ groups of PEI was chosen at 1 : 100 in order to have sufficient fluorescent signal and not to disturb PEI's physico-chemical properties. Following the 24 hours, the conjugate was dialyzed against DI water for at least 4 days in order to remove unbound FITC.

PAA was labeled with LYC via peptide bond condensation of the cadaverine's: $–NH_2$ and PAA's: –COOH groups through zero-length cross-linking with EDC/NHS.[16] Appropriate amounts of EDC and NHS in this order were added to 100 ml of 1 wt.% PAA solution such that the molar ratio of the –COOH groups to the EDC and NHS was

100 : 2 : 2. After addition, the pH of the solution was quickly raised to 8 with 1M NaOH. The solution was allowed to stir at room temperature for 20 min after which an appropriate amount of LYC dissolved in 1 ml of DMSO was added in a molar ratio of –COOH groups to the dye of 100 : 1. The resulting solution was allowed to stir overnight after which the conjugate was dialyzed against DI water for at least 4 days in order to remove unbound dye and remaining EDC and NHS.

Layer-by-Layer Assembly

The microscope glass slides used for the film preparation were cleaned with piranha solution (3:1 H_2SO_4:H_2O_2, *dangerous!*) for 1 hour, followed by thorough rinsing with DI water. In a typical sample preparation a clean glass slide was: (a) immersed in the PEI solution for 30 sec, 2 min, 5 min, or 10 min, (b) rinsed with DI water for 2 min, (c) immersed in 0.5 wt.% MTM dispersion for 30 sec, 2 min, 5 min, or 10 min, (d) rinsed with DI water for 2 min, (e) again immersed in PDDA or PEI solution for 30 sec, 2 min, 5 min, or 10 min, (f) rinsed with DI water for 2 min, and finally (g) immersed for 30 sec, 2 min, 5 min, or 10 min in PAA solution, followed by (h) another DI water rinse for 2 min. Preparation of pure PE samples was performed in the same manner except the MTM immersion step was replaced by PAA. This procedure describes a complete deposition cycle which was then repeated as necessary to obtain the desired number of layers. Preparation of the samples was accomplished using a Midas II automatic slide stainer from EM Sciences. In a typical set, 10 slides were loaded onto the stainer and a slide was removed every 10 cycles for SEM characterization. Samples used in the characterization of the polymer diffusion with laser scanning confocal microscopy were 100-cycles films.

The dye-labeled polymer was deposited on top of the films by immersing the glass slide in the conjugate solution for 30 min. After immersion the films were allowed to air-dry at room temperature. Free-standing films of the nanocomposites, which were subsequently used for thermo-gravimetric analysis and x-ray analysis, were detached from the glass support with a razor blade. The PEI/MTM films were detached using dilute, 0.5% HF solution as described previously for the PDDA/MTM system.

Instrumental Analysis

Thickness of the films was characterized with scanning electron microscopy (SEM) and ellipsometry. The images were obtained with an FEI Nova Nanolab dual-beam FIB and scanning electron microscope operated at 15 kV beam voltage. In order to avoid charging on the specimen, a few nm thick layer of gold was sputtered onto the surface of the film prior to imaging. Ellipsometry measurements were obtained using a BASE-160 Spectroscopic Ellipsometer produced by J. A. Woollam Co., Inc. The instrument was calibrated to the standard silicon wafer with a thin layer of silicon dioxide and the subsequent calculations were fitted using a Cauchy's model. The samples used for ellipsometry were prepared on silicon wafers following the LBL protocol described previously. The refractive index of the multilayer was determined from a 100 nm thick sample. Diffusion of the dye-labeled polyelectrolytes was characterized by obtaining cross-sectional images of the films with a Leica SP2 confocal microscope. Amount of MTM inside of the free-standing film was determined with thermo-gravimetric analyzer (TGA) Pyris 1 from PerkinElmer, with temperature ramp-up rate of 10 ºC/min while being purged with air. Small-angle x-ray studies (SAXS) were performed at the G1 beamline station at the Cornell High Energy Synchrotron Source (CHESS). The wavelength of the x-rays was 0.1239 nm, and the sample to detector distance was 956 mm, calibrated with silver behenate (first order scattering vector of q of 1.076nm^{-1}, with $q = 4\pi \sin(\theta/\lambda)$ where 2θ is the scattering angle and λ is the wavelength). Slit collimation was used to achieve a resulting beam spot that is approximately 0.2 mm in height and 0.4 mm in width (the y- and x-axes, respectively). A slow-scan CCD-based x-ray detector, home built by Drs. M.W. Tate and S.M. Gruner of the Cornell University Physics Department, was used for data collection. We used regular transmission SAXS not GISAXS, just so there is not confusion. The measurements in this experimental setup were found to be sensitive to background subtraction. The mechanical properties of the LBL films were tested using a Nanoinstruments NanoIndenter II model provided by MTS Nanoinstruments Inc., Oak Ridge, TN. A Berkovoich shape indenter was used, and the stiffness, hardness and Young's modulus were calculated and recorded.

3. Results and Discussion

In our previous work with $(PDDA/MTM)_n$ thin films we have shown that the MTM nanosheets interact strongly with the PDDA through a manifold of ionic bonds leading to the formation of nanocomposite with excellent mechanical properties.[3] We have also observed that the MTM nanosheets form a densely packed layer of plates during each adsorption, creating a surface which can be compared to a "ceramic-tile floor". In this structure, the MTM sheets are oriented parallel to the substrate and in respect to the e-LBL they are perpendicular to the path of the diffusing polymer. One can wonder what would be the implications for e-LBL process in this system? Most certainly, such orientation appears to hinder the diffusion of macromolecules through the multilayers, which is not favorable to e-LBL. Note that LBL assembly of PEI and PAA has been shown to give exponential growth.[17,18] To answer the questions of feasibility of e-LBL assembly in this system, we have proceeded with the preparation of hybrid films from PEI, as well as purely polymeric films without the MTM inclusions, all in parallel. For comparison $(PEI/MTM)_n$ films were also prepared.

The films were assembled following similar conditions to the previously reported and well characterized composite of $(PDDA/MTM)_n$, i.e. concentrations of solutions and deposition procedure.[3] Note that pH of the PEI and PAA solutions was adjusted to maximize the protonation of the $–NH_2$ and -COOH functional groups in order to decrease the charges on the polymers, which appears to be one of the requirements for e-LBL process. In a typical assembly we used: 5 min immersion of a glass slide in PEI, 2 min rinse with DI water, 5 min immersion into a PAA, 2 min rinse with DI water, 5 min immersion into a PEI, another 2 min rinse with DI water, a 5 min immersion into a MTM dispersion, followed by a final 2 min rinse with DI water. This sequence after being repeated ***n***-times produced $(PEI/PAA/PEI/MTM)_{\boldsymbol{n}}$ composite. The purely polymeric systems were prepared following the same sequence except that every MTM layer was replaced with a PAA layer and the same total number of layers was assembled for comparison. One should also keep in mind that the clay-containing e-LBL structures are identical to the $(PDDA/MTM)_n$ or $(PEI/MTM)_n$ except that every other layer of negatively charged MTM has been replaced by negatively charged PAA. To keep the system as close as possible to the previously reported $(PDDA/MTM)_n$, the concentrations and pH's of the polyelectrolytes and MTM solutions were also chosen to be similar to the conditions used in the $(PDDA/MTM)_n$ composites – 0.5 or 1 wt.% concentrations. For the $(PEI/MTM)_n$ system we chose 0.1 wt.% concentration for PEI since the 1 wt.% concentration has led to aggregation at these assembly conditions.

For e-LBL systems with and without clay, a set of 10 films on microscope glass slides with varied number of bilayers: ***n*** = 20 – 200, incremented by 20 bilayers was prepared. For $(PEI/MTM)_n$, the films with n = 100 and 200 were made. While all of the previous reports dealing with e-LBL have shown films composed of at most 30 bilayers and film thicknesses of no more than 15 μm, we also wanted to see if the exponential growth could be continued to much greater thicknesses. During deposition, within the first few layers, the films became strongly hydrated and had gel-like appearance which was indicative of successful e-LBL process in accordance with the work by Elbert et al..[19] All of the e-LBL films showed very large thicknesses when hydrated, several millimeters, when compared to the $(PEI/MTM)_n$ or $(PDDA/MTM)_n$. Even upon drying, the thickness of the e-LBL coatings for 200-bilayer films could be easily distinguished with naked eye (Figure 52), which otherwise was difficult to observe for the l-LBL, $(PEI/MTM)_n$ films.

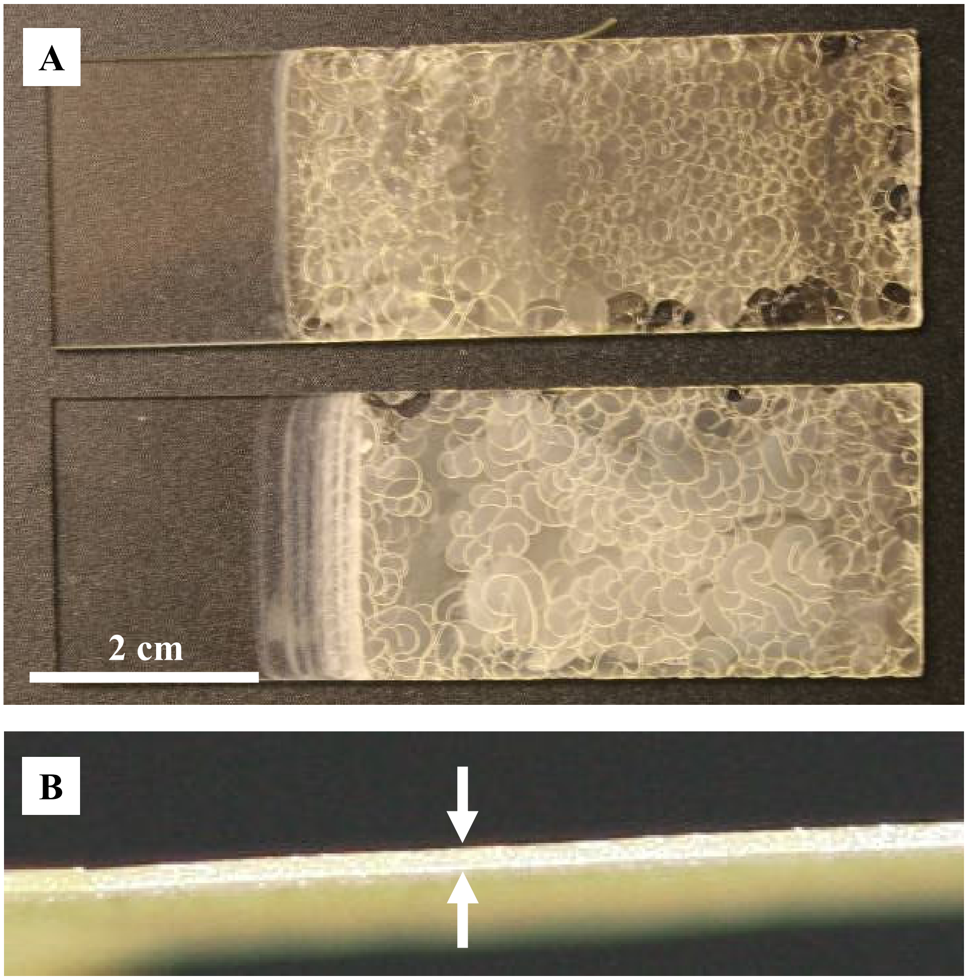

Figure 52. Optical images of exponentially grown films (A) $(PEI/PAA)_{200}$ and $(PEI/PAA/PEI/MTM)_{100}$ prepared with 2 min depositions in top and bottom parts, respectively. The circular patterns seen in the image are the observed cracks. (B) Edge-on view of a free standing film of $(PEI/PAA/PEI/MTM)_{100}$ film with 2 min depositions (arrows indicate the span of the cross-section).

Upon drying, when compared to $(PEI/MTM)_n$, the $(PEI/PAA/PEI/MTM)_n$ films showed extensive cracking (Figure 52). One can speculate that the stresses building up when water is removed from the film constitute the origin of this cracking. The $(PEI/PAA)_n$ films also appeared to be more transparent when compared to the films with MTM. Thermo-gravimetric analysis (TGA) showed the clay content in the dry films to be ~5 wt.% at 650 ºC (Figure 53), which when normalized for the loss of pure clay at this temperature, it can be estimated as high as ~10 wt.%. Overall, similarity of appearance is indicative of the similarity of growth process which can be established more diligently by microscopy and spectroscopy methods.

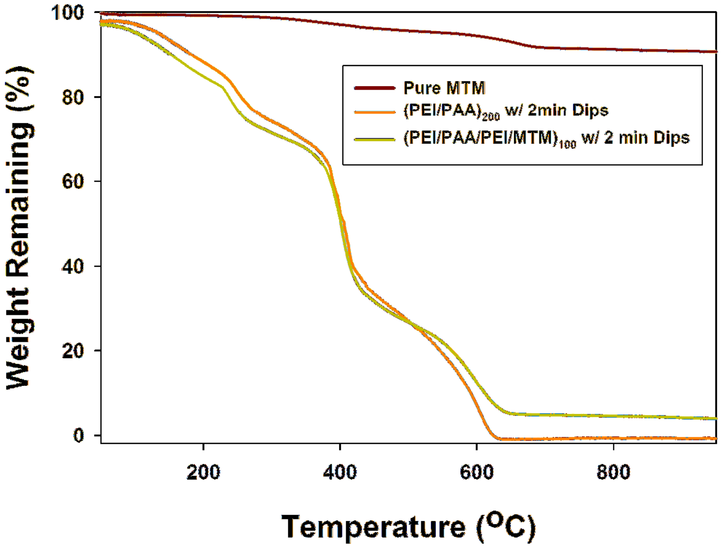

Figure 53. TGA analysis results for indicated LBL nanocomposites. All films are composed of 200 bilayers.

SEM characterization of the films' cross-sections (Figure 54) showed very large thicknesses. For 200-bilayers samples, the measured thicknesses were in excess of 100 μm for the 2, 5, and 10 min depositions. For comparison, $(PDDA/MTM)_n$ films were previously shown to have thicknesses on the order of only ~5 μm for 200 bilayers[3] and the $(PEI/MTM)_n$ showed only ~2 μm for the same number of bilayers. From the structural point of view, $(PEI/PAA)_n$ films (Figure 54A) had very uniform and homogeneous image of the cross-section. The films with MTM (Figure 54B) showed architecture with indications of stratification. This architecture is also very different when compared to the well defined and layered structure of $(PEI/MTM)_n$ films (Figure 54C). Overall on the basis of these SEM data one must conclude that, indeed, the MTM platelets were successfully incorporated into the e-LBL structure.

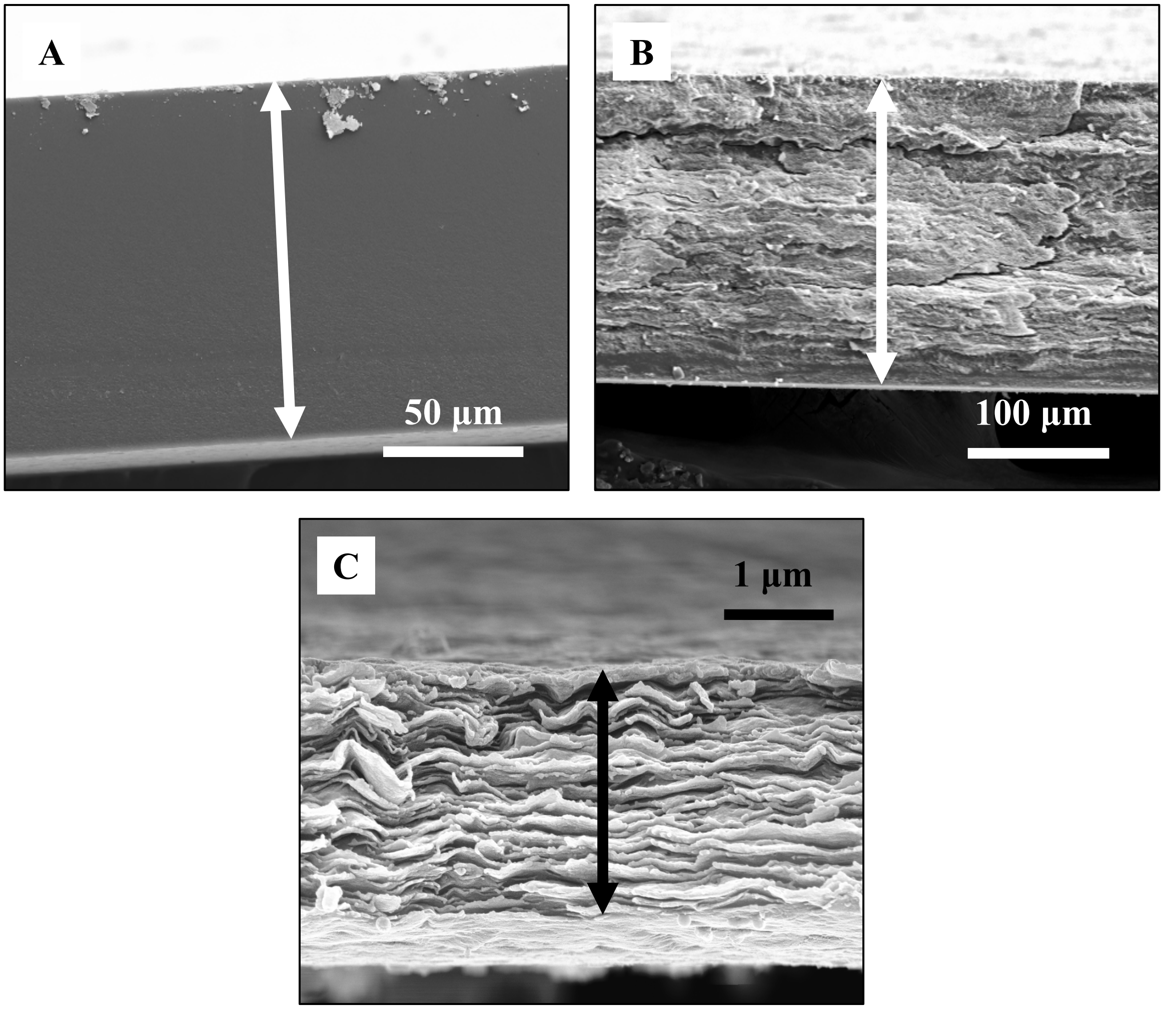

Figure 54. SEM images of cross-sections for free-standing films of: (A) $(PEI/PAA)_{200}$ with 10 min depositions; (B) $(PEI/PAA/PEI/MTM)_{100}$ with 10 min depositions; and (C) $(PEI/MTM)_{100}$ with 5 min depositions. Arrows indicate span of the cross-section.

In addition to the large thicknesses, further proof of the exponential process was obtained from ellipsometric measurements of film growth on top of polished silicon surfaces (Figure 55A). For the e-LBL films, both of the curves show a clear upswing, especially when compared to the l-LBL, $(PEI/MTM)_n$. Notably, the total film thickness for the film studied with ellipsometry is more than 10x smaller as that of the film grown for SEM/optical studies. While exponential trend is unmistakable, it is less pronounced than for the $(PEI/PAA)_n$. Here it would be appropriate to notice that drying is a critical parameter in the e-LBL and for MTM-containing layers in particular. While the films used for ellipsometry were dried after every deposition cycle, i.e. $(PEI/PAA/PEI/MTM)_1$ sequence, the films grown on top of the glass slides were only dried at the end of the process. For comparison, a film prepared with drying after every single deposited material layer showed completely linear growth for the same number of layers.

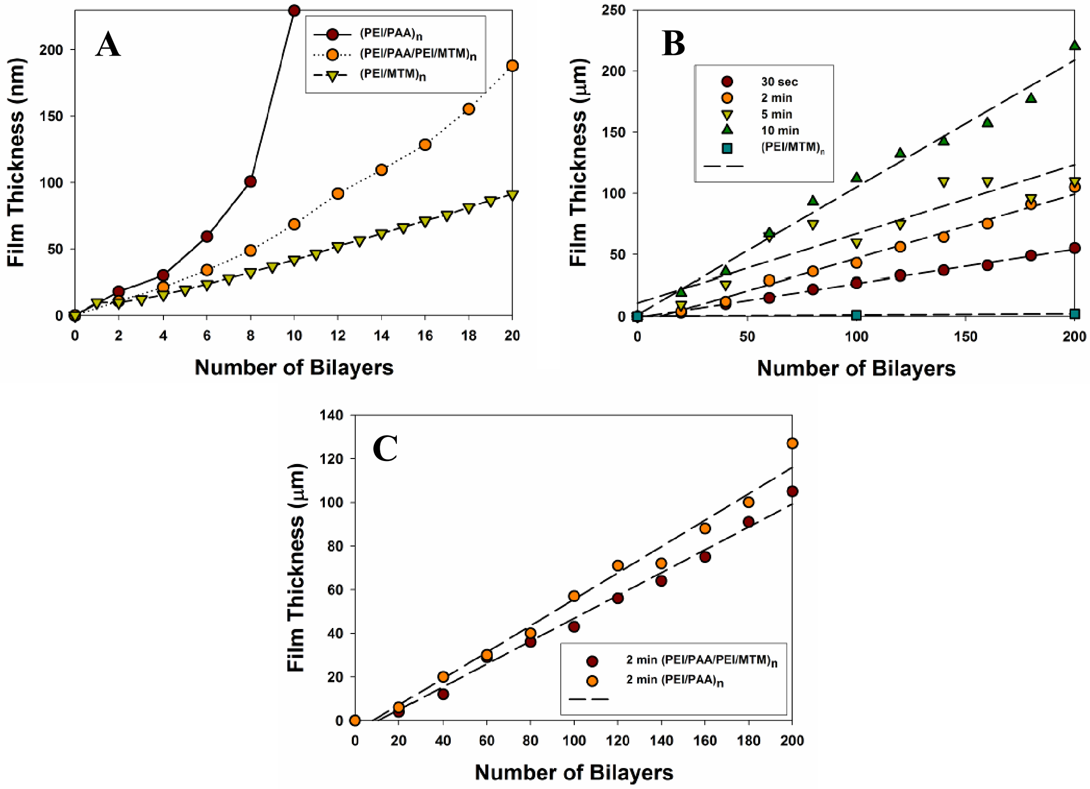

Figure 55. Compilation of thicknesses evolution of e-LBL and l-LBL films as a function of number of deposited layers and with different deposition intervals: (A) Comparison of l-LBL and e-LBL film-growth with and without MTM grown on a silicon wafer with thickness measured using ellipsometry. The "exponential" upswing of the growth curve for $(PEI/PAA/PEI/MTM)_n$ can be clearly seen. The deposition interval for e-LBL films was 2 min and for the $(PEI/MTM)_n$ it was 5 min.; (B) Comparison of thicknesses from SEM for $(PEI/PAA/PEI/MTM)_n$ films with the specified deposition intervals prepared on microscope glass slides. The $(PEI/MTM)_n$ regression is based on the thickness of a 100- and a 200-bilayer film deposited on top of a glass slide with 5 min depositions.; and

(C) Comparison of $(PEI/PAA/PEI/MTM)_n$ with and without MTM following 2 min depositions.

After the initial exponential regime, the growth appears to be relatively constant and linear. This is especially evident from the plots of thicknesses of the prepared film sets as a function of number of bilayers in Figure 55B. All of the films show linear growth however with very large increments. The same behavior was recently demonstrated for e-LBL films composed of high molecular weight polyelectrolytes.[13] Porcel et al. have shown that the e-LBL system will transition to a thick l-LBL with increasing molecular weight of the polymers. Note that the slope of this linear portion of e-LBL is strongly dependent on the length of the deposition interval. Varying the deposition from 30 sec to 10 min gave substantial changes in the total thicknesses of the films (Figure 55B) as well as the thicknesses of the individual polyelectrolyte complex layers. This observation suggested that the saturation of the film has not been reached in the allotted amount of time. The dependence on the lifetime is also indicative of the diffusion-limited nature of growth pattern.

While transition from e-LBL to l-LBL with large thicknesses of layers added in each deposition cycle is not surprising, the question arises whether MTM slows down this stage of LBL growth due to retarded diffusion of a polyelectrolyte through the MTM layers. However side-by-side comparison of films with and without MTM (Figure 55C) showed nearly identical growth kinetics. The cumulative conclusion that one can reach is that apart of greater sensitivity to drying (Figure 55A), the growth process in $(PEI/PAA)_n$ and $(PEI/PAA/PEI/MTM)_n$ systems is quite similar regardless of incorporation of significant amount of alumosilicate in the fabric of the film.

Comparison of the top surface morphologies by SEM for the dried films of $(PEI/PAA)_{20}$, $(PEI/MTM)_{20}$, and $(PEI/PAA/PEI/MTM)_{10}$ (Figure 56) shows striking differences between the three systems and gives some explanation for the distorted internal architecture in the $(PEI/PAA/PEI/MTM)_n$ system (Figure 54B). At low magnification, the $(PEI/MTM)_{20}$ film shows relatively flat surface topography (Figure 56C) when compared to its e-LBL counterparts, which is indicative of uniform distribution and parallel orientation of the platelets on the substrate. At higher magnification (Figure 56D) the presence of MTM platelets is revealed, also showing some adsorbed aggregates. The e-LBL films with and without MTM inclusions show strong, yet uniform roughness even at low magnification which presumably is a result of rapid shrinking and non uniform stresses in the film when drying the highly swollen structure. In the films containing MTM, during shrinking, the adsorbed platelets, due to their significantly smaller size, orient themselves parallel to the roughened surface, thus acquiring 3-D conformation. This “pseudo” 3-D orientation of MTM (unlike largely parallel-to-substrate orientation of platelets seen typically in LBL films of clays) further can be the cause and/or be a result of the diffusion of polylectrolytes.

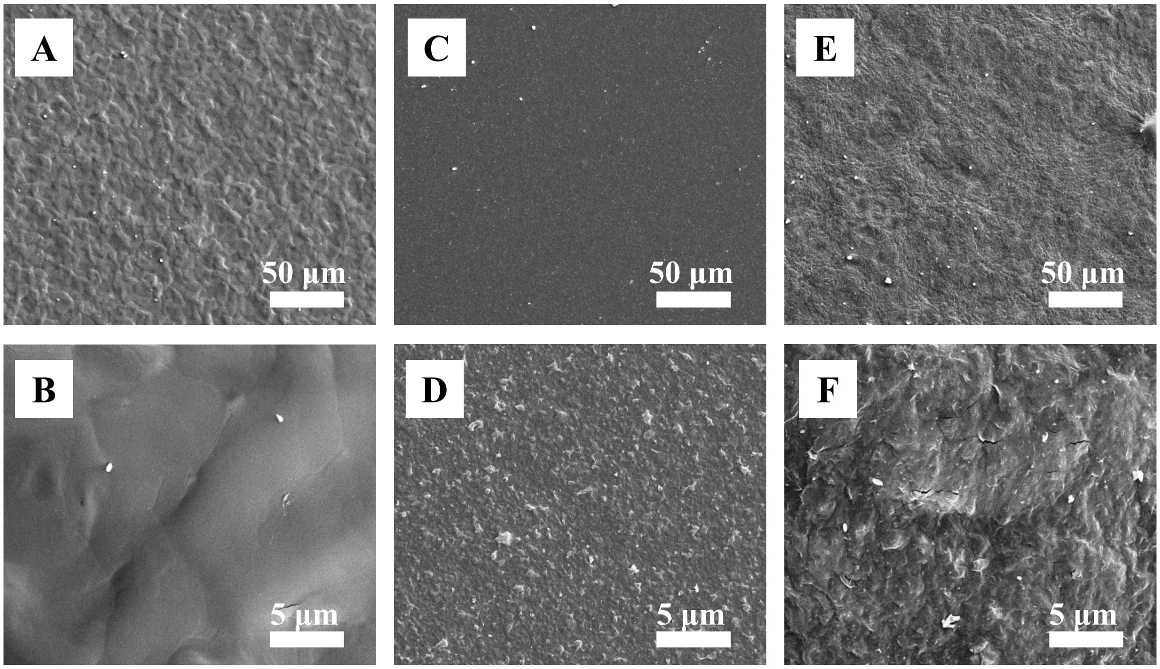

Figure 56. SEM comparison of top surface morphologies for: (A) and B) (PEI/PAA)$_{20}$; (C) and (D) (PEI/MTM)$_{20}$; and (E) and (F) (PEI/PAA/PEI/MTM)$_{10}$ films.

Based on the previous studies by Picart *et al,*[14] one can expect that the mechanism of the exponential growth in (PEI/PAA/PEI/MTM)$_{\mathbf{n}}$ films can be described as following. PEI, being a polycation, diffuses into the matrix of the previously deposited layer in the amount substantially above the limits of electroneutrality. Swelling of the films can be the cause as well as the reason for the accumulation of PEI in the composite. To some degree, the fast diffusion of the polyelectrolytes can be explained by reptation movements of similar polymers previously observed for LBL films with nanoparticles.[20] When the film is exposed to PAA or MTM, the stored amount of PEI diffuses out and forms a polyelectrolyte complex on the surface of the multilayers with PAA or MTM.

Verification of the diffusion mechanism suggested was attained in a similar fashion to previous works[46], but not without unexpected findings. PEI and PAA polymers have been conjugated with fluorescein isothiocyanate isomer I (FITC) and *N*-(5-

aminopentyl)-4-amino-3,6- disulfo-1,8-naphthalimide, dipotassium salt (lucifer yellow cadaverine, LYC) fluorescent dyes, respectively, and their diffusion through the films was observed with confocal microscopy. In this experiment, we have immersed a glass slide coated with a 200-bilayer, e-LBL film of each structure into a dye-labeled polyelectrolyte for 30 min, and after rinsing and drying we have imaged the cross-section of the film. Similarly to all previous publications on e-LBL, all of the films showed diffusion of the polycation (Figures 57A and 57B), which certainly confirms the e-LBL mechanism for MTM-containing multilayers. Note that even for the 30 min, the diffusion extends only through a portion of the film and between the two systems the depth of diffusion I nearly identical at ~30 and 27 μm. This is consistent with the molecular weight dependence of the diffusion and inability of the multilayer matrix to reach saturation of PEI accumulation, which leads to the seemingly linearly growing e-LBL producing very thick films.[13]

Interestingly, PAA seemed to have diffused throughout the film (Figures 57D and 57E) as well. Although there is no obvious fundamental restriction that polyanions cannot diffuse through the matrix of LBL layers, such process was previously underestimated for e-LBL layers although indications that it does take place were reported.[21,22] To some degree this changes significantly the mechanism that can be suggested based on literature data exclusively and need to foresee the possibility of PAA incorporation and diffusion out similarly to what was described for PEI above.

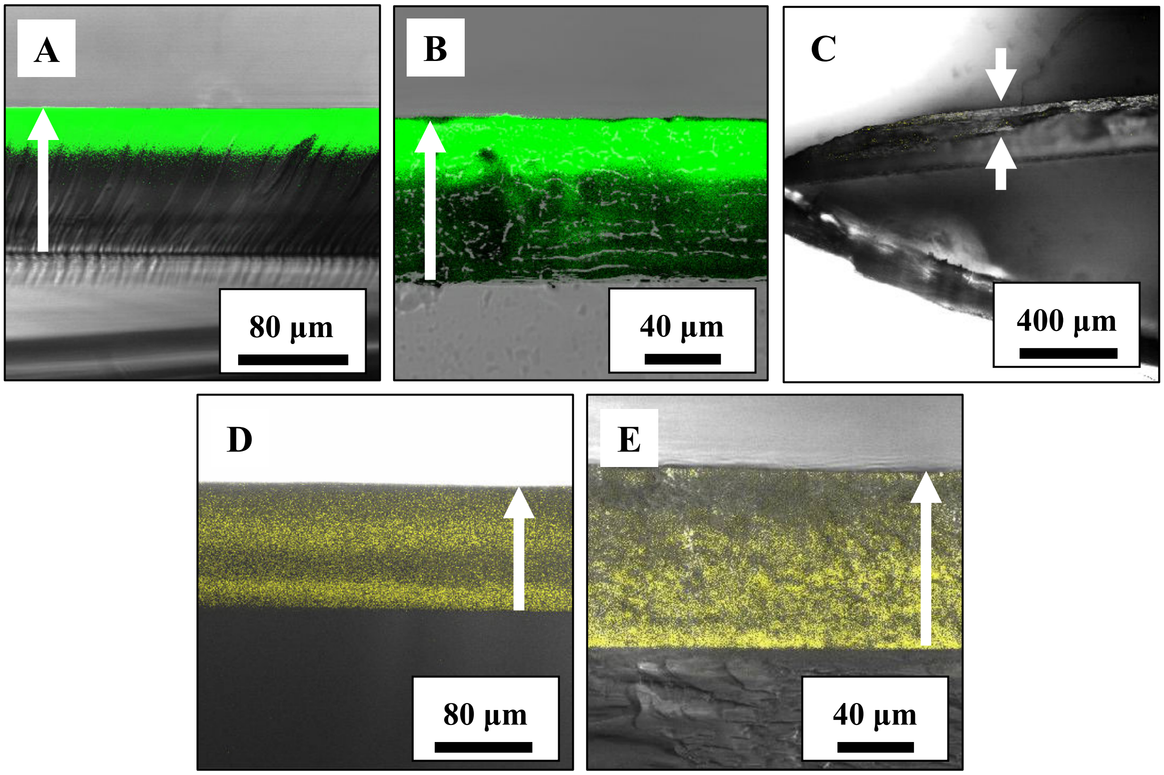

Figure 57. Laser scanning confocal microscopy characterization of dye-labeled polymer diffusion in the e-LBL systems. (A) and (B): $(PEI/PAA)_{200}$ and $(PEI/PAA/PEI/MTM)_{100}$ with top layer of FITC-PEI, respectively. (C): $(PEI/PAA/PEI/MTM)_{100}$ control without labeled polymers. (D) and (E): $(PEI/PAA/PEI/MTM)_{100}$, and $(PEI/PAA)_{200}$ with top layer of LYC-PAA, respectively. White arrow indicates growth direction of the film.

To answer the question of how the PEI and PAA is able to diffuse through the tightly packed clay layers, one needs to better understand the organization of clay sheets in order to resolve the question about permeability of the polyelectrolytes through them. It can be done by using small angle x-ray scattering (SAXS) revealing the information about internal layering morphologies of $(PEI/PAA)_n$, $(PEI/MTM)_n$, and $(PEI/PAA/PEI/MTM)_{\mathbf{n}}$ films (Figure 58). The $(PEI/PAA)_n$ film does not contain clay and thus only diffuse scattering from the polymers is observed (Figure 58A). For the films containing clay, the primary peak observed in the $(PEI/MTM)_n$ film corresponds to a basal spacing of 1.85 nm (Figures 58B and 58D), indicating significant intercalation of polymer between clay sheets. A smaller shoulder was observed indicating the presence of a smaller basal spacing at 1.35 nm, which is similar to literature values of the basal spacing for Na^+-montmorillonite.[23] Importantly, the $(PEI/PAA/PEI/MTM)_n$ film only displays a weak peak corresponding to a basal spacing of 1.35 nm indicative of lower degree of organization (Figures 58C and 58D).

The intensity of SAXS peak in the $(PEI/MTM)_n$ film is much stronger (Figure 58D), indicating a more regular structure. The lack of intense scattering from the montmorillonite in the $(PEI/PAA/PEI/MTM)_n$ film indicates either a wide range of intercalated basal spacings or exfoliation of the clay platelets. In the $(PEI/MTM)_n$ film the positively charged PEI intercalates the montmorillonite interlayer gallery by exchanging with the Na^+ ions. In this case any further intercalation of PEI into the interlayer gallery will lead to an excess positive charge. Considering diffusion data in Figure 57 and SAXS results, one can also suggest the possibility of PAA diffusing into the interlayer gallery of $(PEI/PAA/PEI/MTM)_n$ especially when large amount of PEI is accumulated in the matrix, allowing further separation of the alumosilicate sheets and corresponding larger spread of basal spacing values.

We can further quantify the orientation of the clay platelets by using Herman's orientation parameter (f).[24-26] To calculate the orientation parameter, azimuthal scans were taken over a small window around the q value. This parameter ranges from 1 to -½, in which a value of zero indicates a completely random distribution of orientations. When f is 1 or -½ the system is completely aligned parallel or perpendicular, respectively, to the chosen reference direction (in this case, normal to the substrate). The values for the orientation parameter were as follows:

$(PEI/MTM)_n$ for spacing between 1.3 and 1.4 nm: 0.27 ± 0.07

$(PEI/MTM)_n$ for spacings between 1.8 and 1.9 nm: 0.46 ± 0.07

$(PEI/PAA/PEI/MTM)_n$ with MTM for spacing between 1.3 and 1.4 nm: 0.27 ± 0.10

These trends agree well with visual inspection of the SEM images in Figures 54 and 56: the MTM platelets in the $(PEI/MTM)_n$ sample are clearly more oriented parallel to the substrate than in the $(PEI/PAA/PEI/MTM)_n$ sample, thus corroborating the SAXS data.

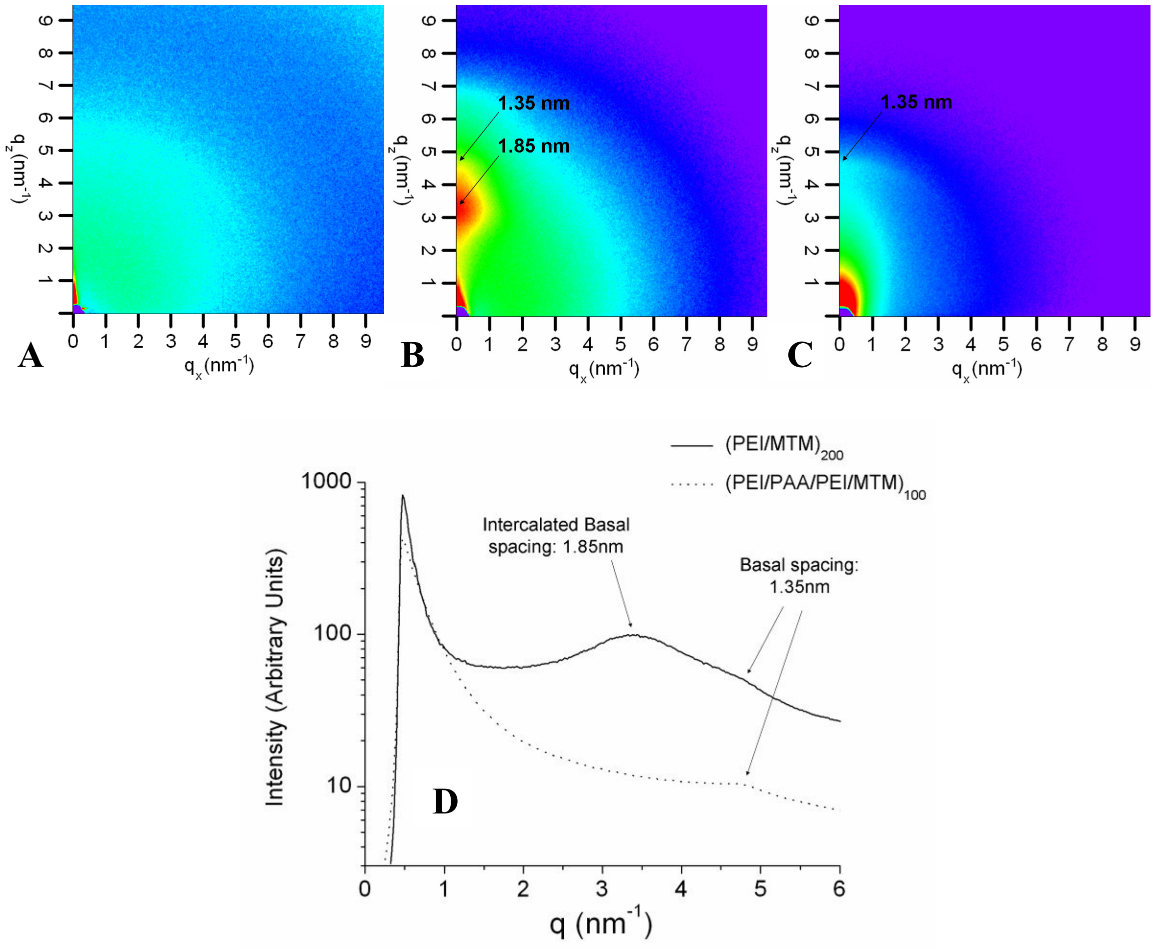

Figure 58. 2-D SAXS patterns of free-standing films of: (A) $(PEI/PAA)_{200}$; (B) $(PEI/MTM)_{200}$; and (C) $(PEI/PAA/PEI/MTM)_{100}$. The scattering features of interest are

indicated by arrows and the corresponding spacings are noted. (D) 1-D SAXS patterns of free-standing films of $(PEI/MTM)_{200}$ and $(PEI/PAA/PEI/MTM)_{100}$. These plots are radial integrations of the 2-D images shown in (B) and (C). The intensities were shifted for clarity. The intercalated basal spacing of 1.85 nm is clearly observed in the PEI/MTM film and weak basal spacings of 1.35 nm are observed in both films. The lack of intense scattering from the montmorillonite in the PEI/PAA/PEI/MTM film indicates either a wide range of intercalated basal spacings or exfoliation of the clay platelets.

Last, in addition to the dynamics of growth and the structure in these hybrid e-LBL films, we have investigated their mechanical properties as they are of great interest for accelerating the preparation process of the ultra-strong nanocomposites. Since this family of e-LBL films displayed extensive cracking (other combinations were found to be very stable in dry conditions) we found nanoindentation technique to be the most suitable to perform these measurements. The nanoindentation also allowed us to make a comparison with previous such studies on PDDA/MTM films. Previously, Advincula et al demonstrated that the PDDA/MTM films posses modulus of E = 9.5 GPa, and hardness of H = 0.46 GPa.[15] In that study, the authors found that the hardness of $(PDDA/MTM)_{100}$ films was higher than the hardness of some of the high strength polymers, e.g. isotactic polypropylene (H = 0.125 GPa) and high density polyethylene (H = 0.06 GPa), and it was on par with a soft metal, copper, (H = 0.46 GPa).[15,27] To our surprise, the e-LBL films also showed exceptionally high modulus and hardness, in spite of having much lower content of the very stiff MTM platelets. (Figure 59)

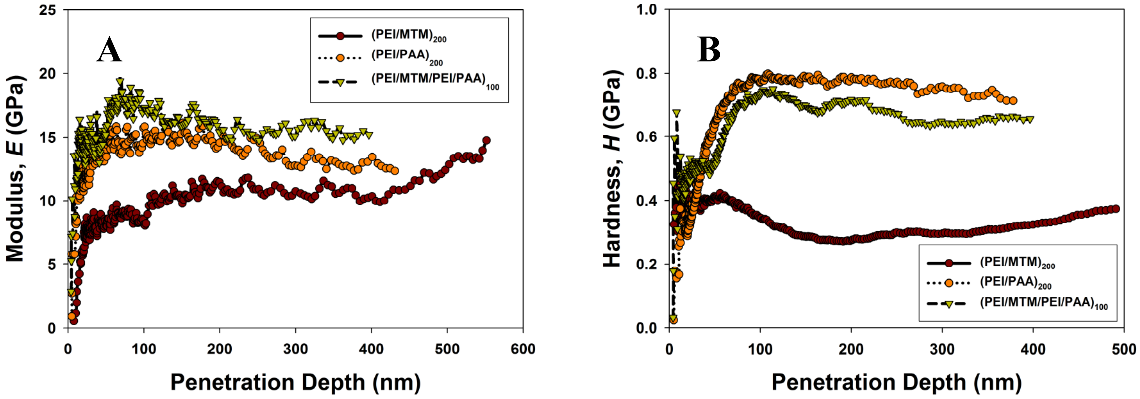

Figure 59. Typical results from nanoindentation experiments for $(PEI/MTM)_{200}$, $(PEI/PAA)_{200}$, and $(PEI/MTM/PEI/PAA)_{100}$ films with 5 min, 2min, and 10 min depositions, respectively. (A) represents the modulus as a function of penetration depth and (B) is the corresponding hardness. These results are from the "loading" (penetration as opposed to retraction of the tip) part of the experiment and the maximum load-to force was set at 2 mN, hence the different number of experimental points.

In this experiment we have compared films of $(PEI/MTM)_{200}$, $(PEI/PAA)_{200}$, and $(PEI/MTM/PEI/PAA)_{100}$ with 5 min, 2min, and 10 min depositions. For each of the samples experimental data for an array of 3 x 3 indents were collected and results from loading and unloading parts of the force-displacement curves were compared. The experimental results are summarized in Table 7 and they are compared to the previous results for $(PDDA/MTM)_n$ film.

Table 7. Experimental results from comparison of the mechanical properties of (PDDA/MTM), (PEI/MTM), (PEI/PAA), and (PEI/MTM/PEI/PAA) LBL films using nanoindentation. Data for (PDDA/MTM) are taken from Fan *et al.*.[15]

	Loading		Unloading	
Sample Type	Modulus, *E* (GPa)	Hardness, *H* (GPa)	Modulus, *E* (GPa)	Hardness, *H* (GPa)
PDDA/MTM	9.5	0.46		
PEI/MTM	13.7 ± 0.5	0.49 ± 0.22	16.9 ± 0.2	0.50 ± 0.22
PEI/PAA	15.4 ± 3.0	0.70 ± 0.23	17.0 ± 0.2	0.67 ± 0.21
PEI/MTM/PEI/MTM	15.7 ± 5.1	0.88 ± 0.45	21.4 ± 0.8	0.98 ± 0.81

The experimental data show that the $(PEI/MTM)_n$ and $(PDDA/MTM)_n$ films have relatively similar properties. Surprisingly, the e-LBL films with and without MTM inclusions have actually higher stiffness and hardness than those growing in non-exponential mechanism. This is a most unpredictable result since the loading of clay nanosheets in the e-LBL film is an order of magnitude lower than in the l-LBL structures. The explanation for this phenomenon is likely to be the fact that dynamic nature of e-LBL films allows the polymer to adjust to nanoscale topography of the clay sheets and/or the partner polymer better than in l-LBL. Such "molecular fitting" of the more flexible component to the other was shown to be critical for obtaining high mechanical properties.[4,8]

4. Conclusions

The results presented here are the first example of exponentially growing LBL structures incorporating inorganic sheet-like nanoparticles. These findings open up the door to a much greater research avenue into hybrid organic/inorganic exponential LBL structures. It was demonstrated that clay sheets despite their well-known barrier function do not prevent exponential growth of LBL films. The explanation for exponential growth phenomenon can come from the unexpectedly fast diffusion/reptation through the openings between the MTM tiles. This process is aided by a slight tilt of clay sheets when PAA is present in the system. Along with faster growth multilayers, the e-LBL mechanism also gives substantial as well as unpredictable improvement in mechanical properties, which was attributed to the closer approach to thermodynamic equilibrium in a system with greater molecular mobility. The mechanism(s) described here also have a great importance for acceleration of the manufacturing of layered composites with unique mechanical properties.

C. “Inverted Nanostructured Nacre” from Hierarchical Organization in Exponential LBL Films

1. Introduction

In previous section we showed that inorganic nanosheets of MTM clay can be successfully incorporated into the e-LBL deposition sequence of polyethyleneimine (PEI) and polyacrylic acid (PAA) with homogeneous distribution of the nanomaterial throughout the film.[11] The resulting films showed large thicknesses (more than 100 μm for 100 bilayers) as well as unusually high stiffness and hardness. Unfortunately the films have also shown very brittle behavior upon drying and the internal structure was greatly distorted as a result of the diffusion of the polymers and large volume changes of the films between the hydrated and dried states. As we have shown in Chapter II, nanoscale control over structural organization afforded by the LBL technique is the main reason for attainment of the exceptional mechanical properties in the polymer/clay films. Hence, in spite of fast growth kinetics, the in-and-out diffusion and large volume changes in the e-LBL appear to be impedance to helping in accelerating the process. Contrary to this expectation we have discovered that hybrid organic/inorganic e-LBL films are capable of self-restructuring leading to well organized hierarchical architectures.

Here, we present results from e-LBL assembly and characterization of a hybrid system composed of PDDA, PAA, and MTM. The e-LBL films showed several unusual features. Firstly, contrary to the PEI-e-LBL system, the PDDA/PAA structures were found to form mechanically robust and transparent free-standing films with high strength and toughness: yield strength, $\sigma_Y \approx 80$ MPa, ultimate tensile strength, $\sigma_{UTS} \approx 70$ MPa, Young's modulus, $E \approx 1.7$ GPa, and nearly 20% of ultimate strain. Incorporation of MTM into the films increased the strength to $\sigma_{UTS} \approx 120$ MPa and modulus to $E \approx 2.2$ GPa. Considering very low clay content of only ~3 wt. %, these mechanical properties are quite remarkable.

Perhaps the most remarkable feature of the hybrid films was found in their internal organization. Cross-sectional images revealed exceptionally-well organized and stratified structure with microns-thick polymer strata separated by thin clay layers. This structure can be best compared to that of Nacre however with reversed roles of the polymer and clay layers. Given these results, the e-LBL process provides a pathway not only to accelerating the nanocomposites preparation process but also to novel architectures.

2. Experimental Procedure

With the exception of the materials and techniques listed here, all experiments were performed as described in Section B2.

Materials and Assembly

20 wt.% aqueous solution of poly(diallyldimethylammonium chloride) (PDDA), cellulose acetate (CA) and acetone were purchased from Sigma-Aldrich (St. Louis, MO) and used as received without further purification. 1 wt.% solutions of PAA, PDDA, and PEI used throughout the experiments, were prepared by appropriately diluting the stock

solutions with 18 MΩ*cm, pH = 5.6 de-ionized water (DI water). 1wt.% solution of CA was prepared by dissolving 0.5 g of the CA powder in 50 ml of pure acetone and used immediately after preparation. The pH of solutions was: 9.5, 2.9, 10, and 4.4 for MTM, PAA, PEI, and PDDA, respectively. For isolation of free-standing films, the slides were first coated on both sides with a thin sacrificial layer of CA using spin-coating. The slides were completely covered with the solution and spun at 2000 RPM for 30 sec. The e-LBL films grown on CA layer were isolated by immersing the slides in pure acetone. While CA is stable in water, it dissolves in acetone, thus releasing free-standing films from the substrate.

Instrumental Analysis

Stress-strain curves were obtained by testing ~1 mm wide and 4-6 mm long rectangular strips of the materials with a mechanical strength tester 100Q from TestResources Inc. (Shakopee, MN). Tests were performed at a rate of 0.01 mm/s with a ~110 N maximum range load cell. The number of tested samples was normally 10.

3. Results and Discussion

The e-LBL films were assembled following similar conditions to the PEI-e-LBL assembly described in Section B of this chapter.[11] In a typical assembly, we used: 5 min immersion of a glass slide in PDDA, 2 min rinse with DI water, 5 min immersion into PAA, 2 min rinse with DI water, 5 min immersion into PDDA, another 2 min rinse with DI water, a 5 min immersion into MTM dispersion, followed by a final 2 min rinse with DI water. The concentrations and pH's of the polyelectrolytes and MTM solutions were also chosen to be similar to the conditions used in the $(PDDA/MTM)_n$ composites in order to make a proper comparison, i.e. 1 wt.% concentration. Purely polymeric films of $(PDDA/PAA)_n$ and the previously reported $(PDDA/MTM)_n$ were also prepared using the same solutions. Overall, 4 sets of e-LBL films with MTM were prepared with varied deposition times, i.e. 30 sec, 2 min, 5 min, and 10 min. Each set consisted of 10 samples with varied number of layers from 20 to 200 bilayers (10 – 100 deposition cycles) incremented by 20 bilayers. A fifth set of films of PDDA/PAA only was prepared for comparison using 5 min depositions.

In addition to the films assembled on the glass slides, 200-bilayer ($\boldsymbol{n}$ = 100) films of the e-LBL structures were also prepared on glass slides pre-coated with a water insoluble sacrificial layer of cellulose acetate (CA).[28] The e-LBL films showed very strong swelling in aqueous conditions which prevented us from using the previously described hydrofluoric acid (HF) etching of glass substrate for isolation of free-standing films.[3] Upon immersion of the dried films into the HF solution the films rapidly swell into strongly hydrated gel-like structures and lost their structural integrity. Assembly of the composites on CA allowed for simple and fast detachment of the films by dissolving the sacrificial layer with acetone in which the films showed excellent stability (Figure 60).

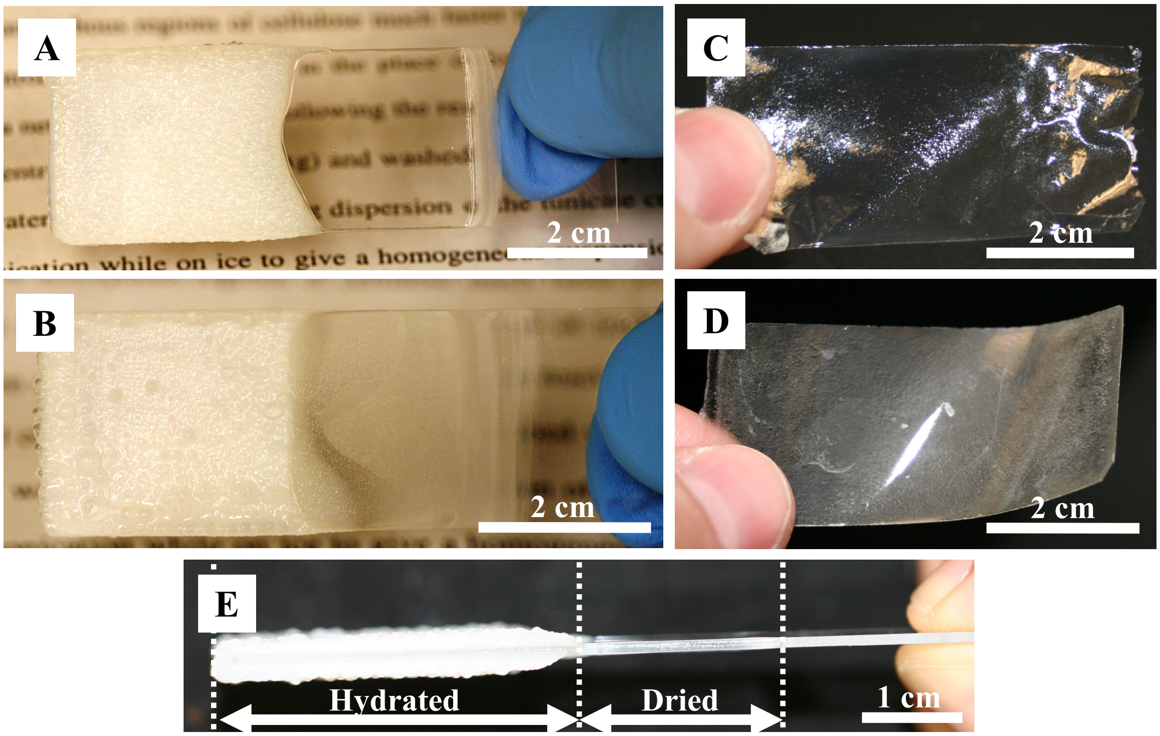

Figure 60. Photographs of exponentially grown films on microscope glass slides (A) $(PDDA/PAA)_{200}$ and (B) $(PDDA/MTM/PDDA/PAA)_{100}$ prepared with 30 sec depositions. The films are shown after 10 min immersion of ca. 1/2 of the film into water to show the different morphologies in dried and hydrated states. Note that the PDDA/PAA film shows complete optical transparency in the dried state. (D) and (E): photographs of free-standing films of $(PDDA/MTM/PDDA/PAA)_{100}$ and $(PDDA/PAA)_{200}$, respectively, prepared with 30 sec depositions and isolated using the sacrificial cellulose acetate layer. (E) Edge-on view of the PDDA/PAA film from (A) showing the dramatic changes occurring during swelling of the film. Slide's thickness is 1mm. The change in thickness of this film upon swelling is ca. 2500%!

Overall, the e-LBL films showed several interesting characteristics. Firstly, the dried PDDA/PAA films showed evolution of optical transparency. Initially, i.e. for less than 20 bilayers of deposition, the films were opaque in appearance due to high roughness and light scattering. With increasing number of layers, beyond 20 bilayers, the films became smooth and completely transparent as can be seen in Figures 60A and 60E. The films incorporating MTM were opaque regardless of the number of layers and showed a yellowish color indicating successful incorporation of the clay (Figures 60B and 60D). Another interesting aspect of the assembly was rapid swelling of the films in aqueous conditions. As can be seen in Figures 60A, 60B, and 60E, the films have swollen ca. 2500% in thickness in just 10 minutes of exposure to acidic water (pH ~2, adjusted with hydrochloric acid). This strong swelling can be explained by protonation of –COOH groups which decreases the charge density along PAA's backbone and thus loosens the strength of interaction with the permanently charged PDDA. The degree of swelling also appears to be pH-dependent since in our previous demonstration of reversible loading of NPs, swelling of the films at pH = 9 took ca. 7 hours.[29] This pH dependent swelling also means that during assembly, the films undergo continuous cycling through expansion and contraction of volume since the pH of MTM is ca. 9.5 and that of PDDA is only ca. 4.4.

Keeping these results in mind, one can quickly realize that the internal structure of the dried film incorporating MTM platelets should have appearance of a rather well mixed blend. This is in fact what we have observed for the PEI-e-LBL films incorporating MTM.[11] Contrary to those findings, characterization of the PDDA-e-LBL films' cross-sections with SEM showed most remarkable results (Figure 61). While the purely polymeric PDDA/PAA films displayed a homogeneous cross-section with vertical striations (Figure 61C), the PDDA/MTM/PDDA/PAA films revealed exceptionally well organized and stratified architecture with few-micrometers thick polymer layers alternated by thin MTM strata (Figures 61A and 61B). The vertical striations were also found in the MTM containing films, in each of the polymer layers, suggesting that it is characteristic to the PDDA/PAA films. This architecture is strikingly different from PDDA/MTM films presented in the past, which were found to have total thicknesses of only ~5 μm for 200 bilayers. To our knowledge, this is the first time this type of structure has been observed for any LBL films.

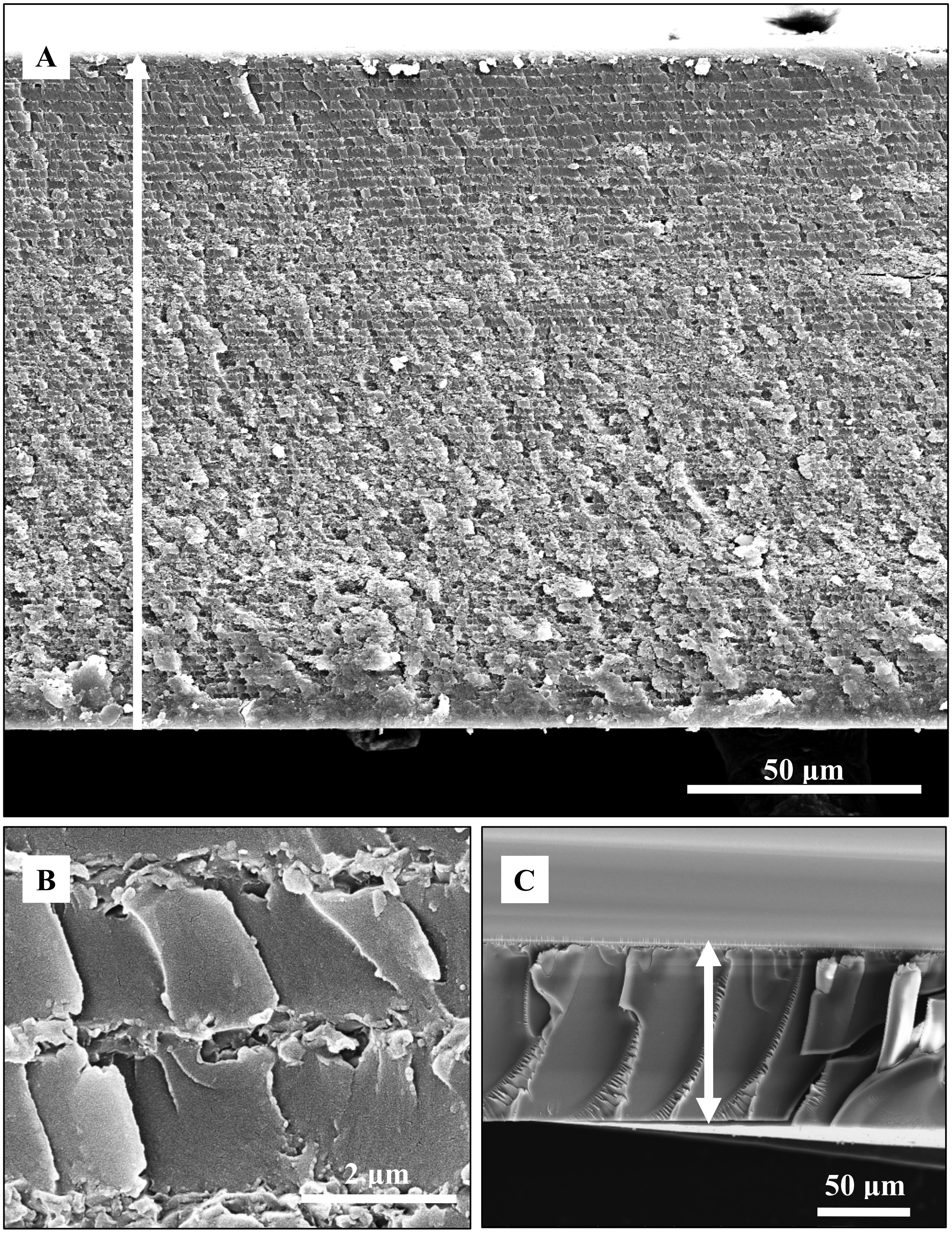

Figure 61. SEM images of cross-sections for free-standing films of: (A) $(PDDA/MTM/PDDA/PAA)_{100}$ with 10 min depositions; (B) magnified image of structure in (A); and (C) $(PDDA/PAA)_{100}$ with 5 min depositions. Arrows indicate span of the cross-section and the direction of film growth.

The question which quickly arises is how is this level of ordering possible in such a dynamic system? Further SEM characterization gave some clues to understanding the underlying mechanism. Counting the number of strata in this structure gave approximately 90 polymer- and 90 MTM-layers which is just 10 less than the total number of deposition cycles. Closer examination of 10- and 20-cycle films (Figure 62) showed that this difference comes from the fact that the strata do not become visible until more than 10 cycles of the film are deposited. As can be seen in Figure 62A the first 10 cycles showed a rather homogeneous structure with total thickness being comparable to the thickness of just one layer in a 100-cycle film. This is also directly related to the mechanism of exponential growth in e-LBL films composed of high molecular weight polymers. For e-LBL films, Porcel et al. have recently shown that for high molecular weight polymer pairs after initial exponential increase, the growth becomes linear with thick individual bilayers.[13] Evidence of this process can be especially seen in Figure 62B where the strata gradually increase in thickness until they reach a steady thickness of ~2 μm. Hence the number of strata is in fact equal to the number of deposited MTM layers. This suggests that during each deposition, MTM platelets remain localized in a thin layer while the polyelectrolytes diffuse around the platelets to form the polyelectrolyte complex atop of the adsorbed MTM sheets. This leads to the formation of the stratified structure.

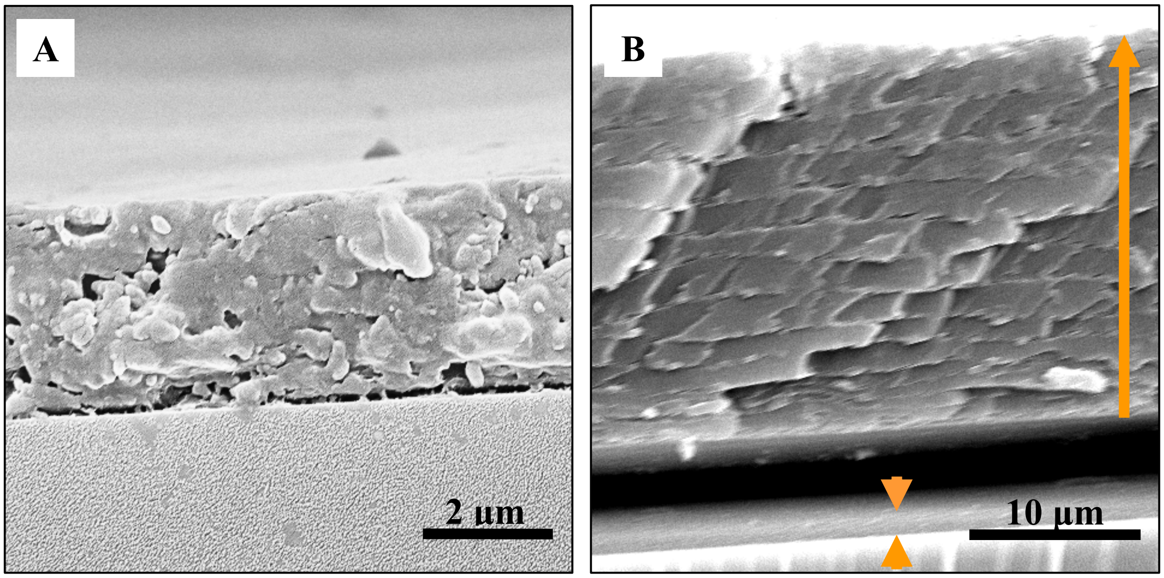

Figure 62. SEM images of cross-sections for e-LBL films atop of microscope glass slides: (A) (PDDA/MTM/PDDA/PAA)$_{10}$ and (B) (PDDA/MTM/PDDA/PAA)$_{20}$ prepared with 10 min depositions. Small arrows in (B) show that a small film is still attached to the surface of the glass slide. Large arrow indicates the direction of film growth.

Proof of the exponential process was also obtained from ellipsometric measurements of film growth on top of polished silicon surfaces (Figure 63).

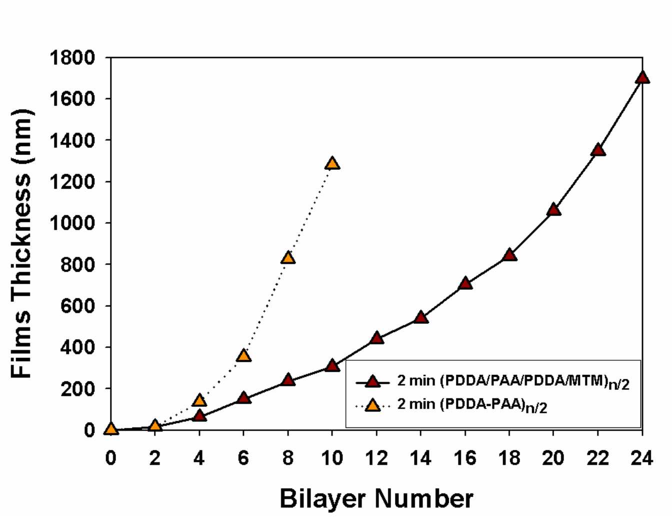

Figure 63. Comparison of l-LBL and e-LBL film-growth with and without MTM grown on a silicon wafer with thickness measured using ellipsometry. The deposition interval for e-LBL films was 2 min.

Similarly to the observations made for PEI-e-LBL films, both of the PDDA-e-LBL films: with and without MTM showed a clear upswing, especially when compared to the $(PDDA/MTM)_n$ reported previously.[3,11] Again, while exponential trend is unmistakable, it is less pronounced in film with MTM than for the $(PDDA/PAA)_n$. The ellipsometry results seem to show that exponential increase in films thicknesses with the increasing number of layers should continue indefinitely. However, the SEM images in Figures 61 and 62B show that strata thicknesses are rather constant after initial exponential increase. The later is in fact consistent with thickness measurements performed on the different sets of films using SEM and the observations made by Porcel et al..[13] (Figure 64) Being consistent with a diffusion-limited process, the curves show increasing steepness of the slope with increasing deposition time. This is also consistent with thicknesses of the polyelectrolyte complex layers found in the different films. For 30 sec depositions the thicknesses are only ca. 900 nm while for 10 min they are ca. 2.2 µm.

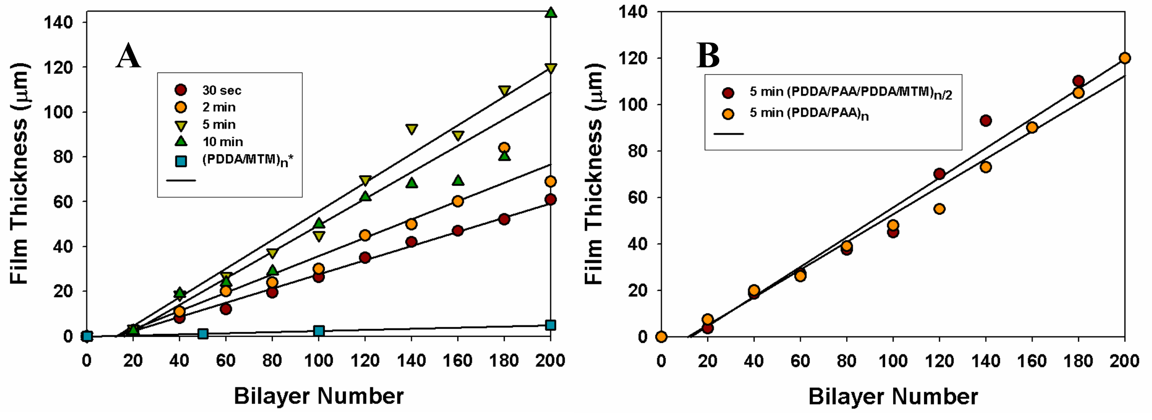

Figure 64. Compilation of thicknesses evolution of e-LBL and l-LBL films as a function of number of deposited layers and with different deposition intervals. (A) Comparison of thicknesses from SEM for $(PDDA/MTM/PDDA/PAA)_{\mathbf{n}}$ films with the specified deposition intervals prepared on microscope glass slides. The $(PDDA/MTM)_n$ regression is based on the values obtained by Tang et al..[3] (B) Comparison of $(PDDA/MTM/PDDA/PAA)_{\mathbf{n}}$ with and without MTM following 5 min depositions.

Previously, for PEI-e-LBL films, we showed that both PEI and PAA diffused through the film thickness, which if similarly occurring here, should have resulted in distorting of the internal structure. This is clearly not the case. Investigation of the diffusion mechanism using similar procedure to previous reports[46] showed very different results. Since PDDA could not be easily conjugated, PEI- and PAA-fluorescent dye conjugates were used instead. The polymers have been conjugated as described in previous section, with FITC and LYC fluorescent dyes, respectively, and their diffusion through the films was observed with confocal microscopy. In this experiment, we have immersed a glass slide coated with a 200-bilayer, e-LBL film of each structure into a dye-labeled polyelectrolyte for 30 min, and after rinsing and drying, we have imaged the cross-section of the film. (Figure 65) All of the films showed diffusion of the polycation (Figures 65A and 65C), which certainly confirms the e-LBL mechanism for MTM-containing multilayers. After the 30 min, the diffusion extended only through a portion of the film and between the two systems the depth of diffusion was nearly identical at ~28 and 30 μm. This is consistent with the molecular weight dependence of the diffusion and inability of the multilayer matrix to reach saturation of PDDA accumulation, which leads to the seemingly linearly growing e-LBL producing very thick films.[13]

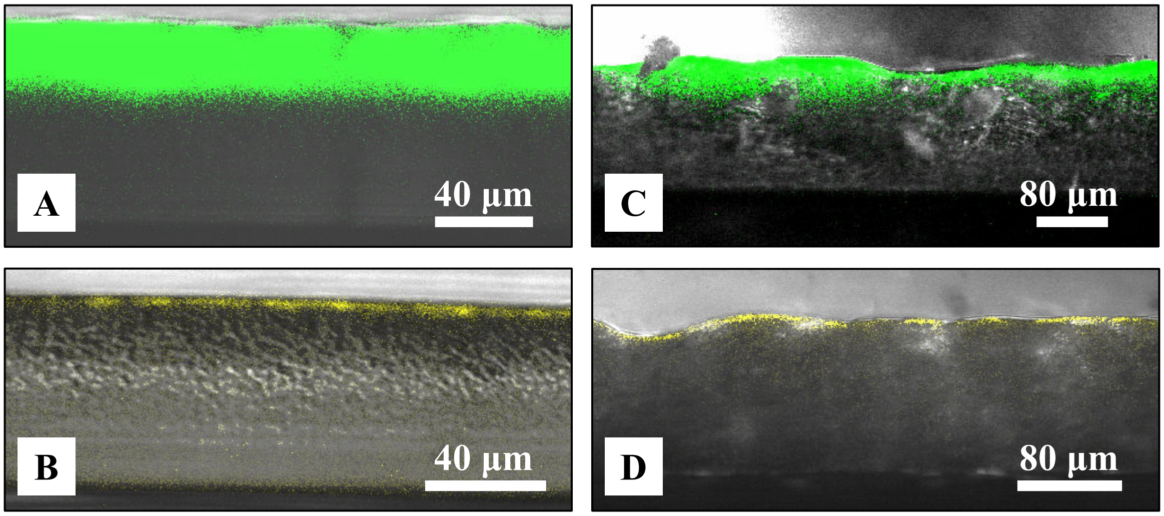

Figure 65. Laser scanning confocal microscopy characterization of dye-labeled polymer diffusion in the e-LBL systems. (A) and (B): $(PDDA/MTM/PDDA/PAA)_{100}$ with top layers of FITC-PEI and LYC-PAA, respectively. (C) and (D): $(PDDA/PAA)_{200}$ with top layers of FITC-PEI and LYC-PAA, respectively.

While PEI has clearly diffused through the films, after the 30 min the negatively charged PAA seems to be localized only in a very thin layer at the surface. (Figures 65C and 65D) This is very much reminiscent of the negatively charged MTM separation into distinct layers. Hence one can suggest that the unique organization of the PDDA-e-LBL films with MTM stems from the fact that negatively charged species will not diffuse into the film in PDDA-PAA structure. This suggests that organization of e-LBL films will be dependent on the choice of polymer pairs, and thus internal structure can have variety of interesting physico-chemical properties.

Last, we have investigated mechanical properties of the e-LBL films as they are of great interest for accelerating the preparation process of the ultra-strong nanocomposites. We have performed standard tensile tests as well as nanoindentation experiments. This allowed us to make a comparison with previous studies on PDDA/MTM and PEI-e-LBL with MTM.[3,11,15] Tensile tests gave remarkable results

(Figure 66 and Table 8). The e-LBL films showed strengths over 100 MPa, which is actually higher than the PDDA/MTM composite. This is remarkable since the e-LBL composites contain only ~3 wt.% of MTM or ~10 wt.% when normalized for the loss of weight in pure MTM, as was determined from the thermo-gravimetric analysis (Figure 67). Overall, ultimate tensile strength (σ_{UTS}) and Young's modulus, (E) of the composite increased by an order of magnitude in comparison to the pure PDDA, while the ultimate strain decreased 5-fold (Table 8). Also the toughness of the composite has increased by nearly 2-fold. In comparison to PDDA/MTM, σ_{UTS} is almost the same while E is 5 times smaller. The difference in E is directly related to the loading of the MTM. Since PDDA/MTM contains nearly ~70 wt.% of the stiff reinforcing filler, MTM, with homogeneous distribution, it is expected to have much greater stiffness when compared to a composite with only ~10 wt.% of the reinforcement.

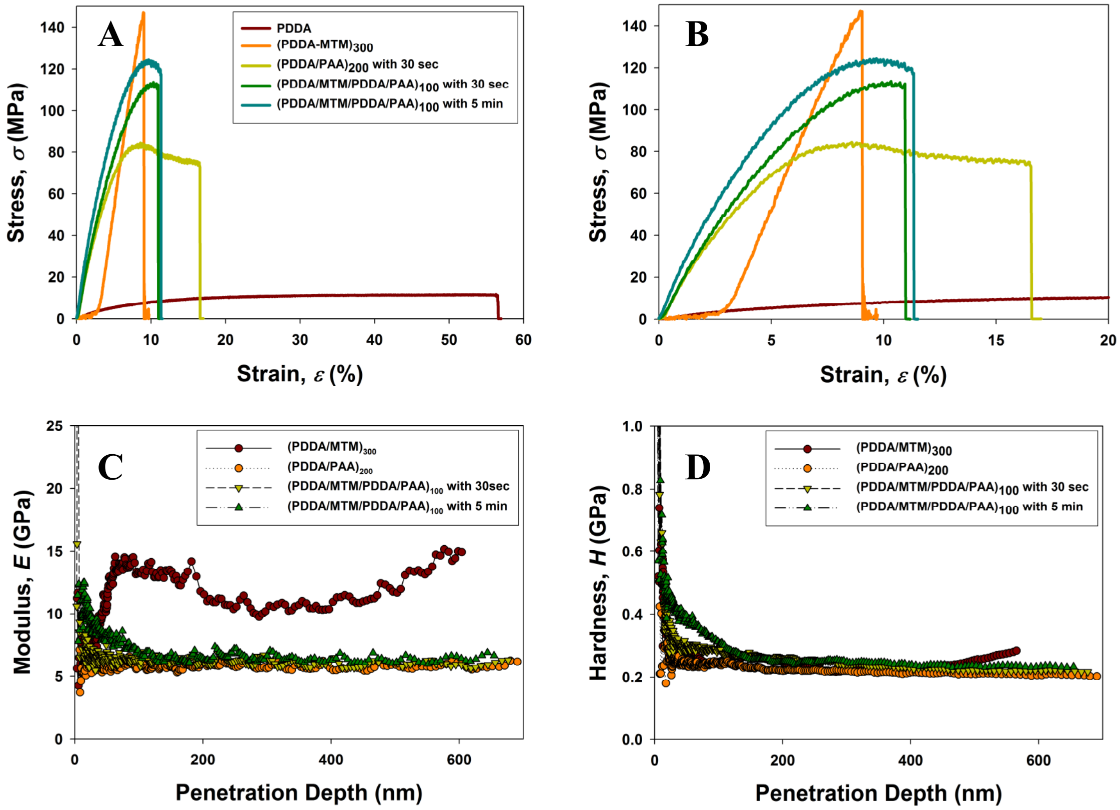

Figure 66. Representative results from tensile and nanoindentation tests for PDDA polymer, $(PDDA/MTM)_{300}$ with 5 min depositions, $(PDDA/PAA)_{200}$ with 30 sec depositions, $(PDDA/MTM/PDDA/PAA)_{100}$ with 30 sec depositions, and $(PDDA/MTM/PDDA/PAA)_{100}$ with 5 min depositions films. (A) and (B): Representative stress-strain curves. (C) Modulus as a function of penetration depth. (D) Hardness as a function of penetration depth. The nanoindentation results are from the "loading" (penetration as opposed to retraction of the tip) part of the experiment and the maximum load-to force was set at 2 mN, hence the different number of experimental points.

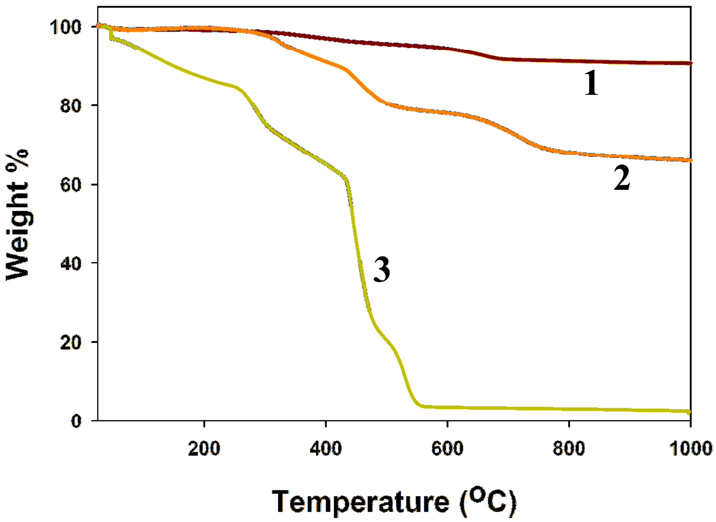

Figure 67. Thermo-gravimetric analysis results for: 1) pure MTM powder, 2) $(PDDA/MTM)_{300}$, and 3) $(PDDA/MTM/PDDA/PAA)_{100}$ with 30 sec deposition.

Table 8. Comparison of the mechanical properties for composites and pure polymers. Toughness values were obtained from integration of the area under the stress-strain curves.

Sample	Yield Strength, σ_Y (MPa)	Ultimate Tensile Strength, σ_{UTS} (MPa)	Young's Modulus, E (GPa)	Ultimate Tensile Strain, ε_{UTS} (%)	Toughness (MJ/m^3)
PDDA	-	12 ± 4	0.2 ± 0.03	48 ± 9	4.7 ± 2.0
PDDA-MTM	-	100 ± 10	11 ± 2	10 ± 2	~0.5
PDDA-PAA	76 ± 11	70 ± 8	1.7 ± 0.5	17 ± 1	10.1 ± 2.5
PDDA-PAA-MTM 30 sec	-	106 ± 7	1.9 ± 0.1	10 ± 2	7.2 ± 1.6
PDDA-PAA-MTM 5 min	-	120 ± 13	2.2 ± 0.4	11 ± 3	8.0 ± 2.9

Nanoindentation experiments also showed interesting results. Previously, Advincula et al demonstrated that the PDDA/MTM films posses modulus of $E = 9.5$ GPa, and hardness of $H = 0.46$ GPa.[15] In that study, the authors found that the hardness of $(PDDA/MTM)_{100}$ films was higher than the hardness of some of the high strength polymers, e.g. isotactic polypropylene ($H = 0.125$ GPa) and high density polyethylene ($H = 0.06$ GPa), and it was on par with a soft metal, copper, ($H = 0.46$ GPa).[15,27] Our results for PDDA/MTM films showed nearly identical values, with slightly lower hardness. (Table 9) Similarly to the tensile results, the e-LBL films showed lower modulus when compared to PDDA/MTM. On the other hand, the hardness of the e-LBL films was found to be nearly the same in spite of having much lower content of the very stiff MTM platelets. This trend is also different from the results obtained for PEI-e-LBL films which showed exceptional stiffness and hardness, much higher than the PDDA/MTM.

Table 9. Experimental results from comparison of the mechanical properties of (PDDA/MTM), (PDDA/PAA), and (PDDA/MTM/PDDA/PAA) LBL films using nanoindentation. *Data for (PDDA/MTM) are taken from Fan *et al.*.[15]

	Loading		Unloading	
Sample Type	Modulus, *E* (GPa)	Hardness, *H* (GPa)	Modulus, *E* (GPa)	Hardness, *H* (GPa)
PDDA/MTM*	9.5	0.46	-	-
PDDA/MTM	8.0 ± 2.9	0.28 ± 0.14	10.2 ± 2.2	0.22 ± 0.07
PDDA/PAA	6.0 ± 0.2	0.22 ± 0.01	5.7 ± 0.4	0.21 ± 0.02
PDDA-PAA-MTM 30 sec	6.5 ± 1.5	0.26 ± 0.10	6.2 ± 1.6	0.25 ± 0.11
PDDA-PAA-MTM 5 min	6.5 ± 0.7	0.25 ± 0.04	6.6 ± 0.5	0.25 ± 0.03

4. Conclusions

We presented here results from exponential LBL assembly of a hybrid organic/inorganic system which contrary to the expectations displayed remarkable structural organization. This observation suggests that e-LBL films are capable of forming unique structures which could not have been predicted from simple understanding of LBL assembly. The explanation for the stratification can come from strong adsorption of MTM on PDDA and inability of MTM to diffuse through the e-LBL structure, thus becoming localized to individual strata. The PDDA is still able to diffuse around the MTM platelets to form a polyelectrolyte layer with incoming PAA atop of the adsorbed MTM. The films also possess exceptional mechanical properties with σ_{UTS} reaching 130 MPa at a MTM loading of only ~10 wt.%. The mechanism(s) described here have great importance for acceleration of the manufacturing of layered composites with unique mechanical properties.

D. Highly Flexible Nanostructured Multilayered Thin Films from LBL Assembly of Oppositely Charged Polyurethanes

1. Introduction

As we have pointed out in the introduction to this chapter, the LBL films presented until today can be considered in general as rigid structures, while many applications, such as flexible electronics or biomedical coatings, would benefit from flexible and tough nanostructured coatings/free-standing membranes. In this section we focus on preparation of LBL composites using a new assembly component: water-soluble polyurethanes (PUs). PUs are well-known for their strength and toughness and they found broad applications in construction, transportation, household appliances, packaging, electronics, and implantable biomedical devices, to name a few. PUs have never been used in LBL assembly, and thus, represent an important new component of LBL technique with a variety of potential research venues.

Here, we demonstrate for the first time preparation of highly flexible nanostructured thin films from LBL assembly of oppositely charged PUs. Film buildup was characterized with UV-vis spectroscopy and ellipsometry, revealing uniform and steady growth. Composition of the film's surface was analyzed with x-ray photoelectron spectroscopy (XPS) and it revealed the two polymers to be present in a 7:1 ratio of the anionic-to-cationic PUs. Internal structure was characterized with scanning electron microscopy (SEM) and phase-contrast atomic force microscopy (AFM). SEM of cross-section revealed layered architecture while AFM showed cellular organization of the hard and soft domains on the surface of the LBL film. The cellular structure shows a striking contrast when compared to the chaotic organization in the blend of the two polymers prepared by mixing of the two in the same wt.% ratio. Further, we show preparation of free-standing films and the results from evaluation of their mechanical properties. The LBL films were found to be highly robust and flexible with ultimate strains reaching as high as 680 %. This result is more than 2 orders of magnitude greater than any LBL assemblies prepared thus far. The presented results open up a new research avenue into preparation of highly flexible and multifunctional nanostructured thin-films.

2. Experimental Procedure

With the exception of the materials and techniques listed here, all experiments were performed as described in Sections B2 and C2.

Materials and LBL Assembly

Aqueous dispersions of the cationic (Cat PU, ~35 wt.%, MW ≈ 92,000) and anionic (An PU, ~35 wt.%) polyurethanes were obtained from Hepce Chem Co., South Korea and used as received. Solutions used in the LBL assembly were 10x dilutions of the stock polymers, yielding approximately ~3.5 wt.% solutions. The LBL assembly was performed on microscope glass slides and silicon wafers either by hand for initial characterization or using a StratoSequence IV automated dipping robot, from nanoStrata

Inc. (Tallahassee, FL). The films were assembled using 2 min dips into the PUs solutions followed by 2 - 1min rinses with pure deionized water and a single, 1 min drying with compressed air. Free-standing films consisting of 300 bilayers were isolated by etching of the glass slides with 1% hydrofluoric acid. After thorough rinsing with pure water, the films were dried in an oven at 80 °C. Pure PUs films were prepared by dry-casting of the diluted solutions. Blended sample was prepared by mixing of the two components in the 7:1 wt.% ratio, dry casting, and hot-pressing to obtain a flat sample for AFM characterization.

Mechanical Properties Evaluation

The films were subjected to uniaxial tensile tests using a vertical tensile testing machine from Test Resources. Dog bone shaped test specimens were lightly airbrushed with a random, black speckle pattern before being cut with an elliptical punch to a gauge length of 13mm and a width of 2mm to 3mm. The specimens were pulled apart at a displacement rate of 80 μm/s and images of the center gage section were collected every 5 seconds, using a Nikon D2x camera equipped with a 300mm macro lens. The reactive tensile load on the specimen was measured using a 4.9 N load cell. The collected speckle images were analyzed using ImageJ software equipped with a MetaJ tracking macro. The X and Y coordinate data of two neighboring speckles as a function of specimen load, was then processed with a MATLAB script to produce Green-Lagrange strain data corresponding to each load state. The Green-Lagrange strain E_{11} in the direction of the axial force is defined as $E_{11} = \frac{1}{2}[(1+e_1)^2 - 1]$, where $e_1 = \frac{dx - dX}{dX}$, is the change in length per unit length of a line element that is parallel to the direction of axial stretching.[29] The force measurements from the load cell were divided by the measured initial thickness and initial width of the sample gage section to give engineering stress. This procedure results in a plot of engineering stress vs. e_1. Three to five samples were tested for each stack.

Film-Structure Characterization

SEM images were obtained with an FEI Nova Nanolab dual-beam FIB and scanning electron microscope operated at 15 kV beam voltage. Ellipsometry measurements were obtained using a BASE-160 Spectroscopic Ellipsometer produced by J. A. Woollam Co., Inc. The instrument was calibrated to the standard silicon wafer with a thin layer of silicon dioxide and the subsequent calculations were fitted using a Cauchy's model. AFM experiments were performed in tapping mode using NanoScope IIIa instrument from Veeco Instruments (Santa Barbara, CA). Differential Scanning Calorimetry (DSC) analysis was performed using a Perkin-Elmer DSC-7 (PerkinElmer, Wellesley, MA). A small amount (5 mg) of the sample was encapsulated in an aluminum pan and was first heated from 10 ºC to 300 ºC at a scan rate of 10 ºC/min. The sample was then cooled from 300 ºC to 10 ºC at the same rate. Data acquisition and processing was done with PerkinElmer Pyris software. X-Ray powder diffraction (XRD) patterns were collected on a Rigaku Miniflex (Rigaku, The Woodlands, TX). The diffractometer is equipped with a Cu X-ray tube (Cu Ka, l ¼ 1.54059 Å) with an operating voltage of 30 kV and current of 15 mA. Scans were performed continuously from 2° to 90° 2θ in increments of 5° per min.

Composition Analysis by XPS

XPS characterization was carried out using a Kratos Axis Ultra. A monochromated Al K alpha X-ray source was used to irradiate the sample using a power of 140 W (14 kV, 10 mA). Top surfaces of Cat PU and An PU were analyzed with survey scans performed using a pass energy of 160 eV, a step size of 1 eV, and a dwell time of 200 ms. Detailed scans were acquired with a pass energy of 20 eV, a step size of 0.1 eV, and a dwell time of 200 ms. A flood gun was used for charge compensation. All of the spectra acquired are referenced to the C 1s band at 285.0 eV, associated with the $-\underline{C}H_2$ species.

Survey scans of Cat PU, An PU, and the LBL films are shown in Figure 68A. Carbon, oxygen and nitrogen were detected in all samples, however, only a trace of N was detected in the Cat-PU sample. The Cat-PU sample had silicon impurities. The LBL film also had silicon and fluorine present. The integrated areas of the detailed spectra of C 1s, O 1s, and N 1s were used to calculated the atomic percentage of each element by using Wagner's sensitivity factors.[30] The atomic composition of the LBL film is close to that of the pure An PU film. This suggests the LBL film surface is predominately An PU. However, we shall consider the detailed spectra of C 1s, N 1s, and O 1s for further confirmation of this.

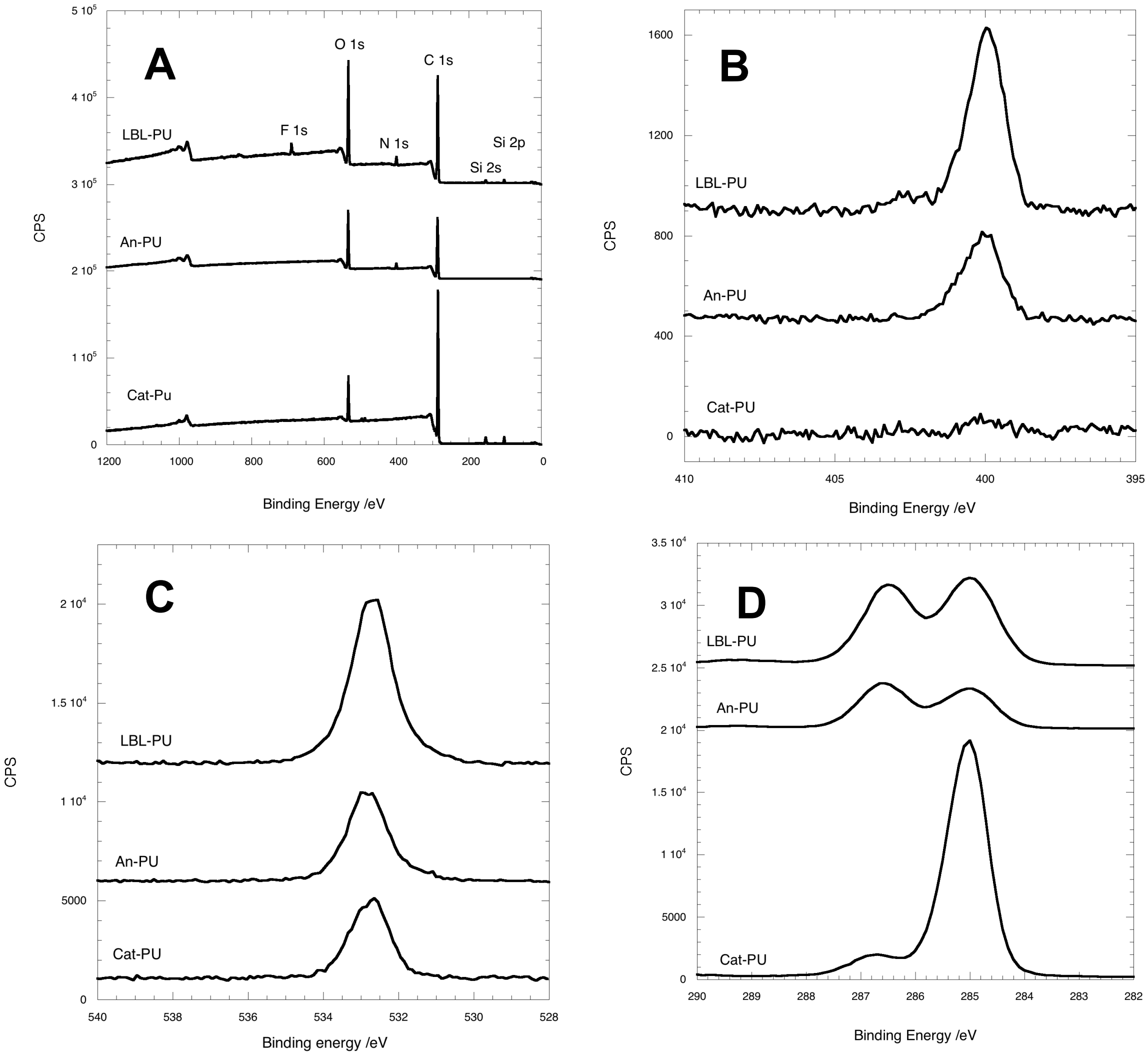

Figure 68. (A) XPS survey spectrum of Cat PU, An PU, and LBL films. The data have been vertically transposed for viewing purposes. (B) XPS spectra of the N 1s region. (C) XPS spectra of the O 1s region. (D) XPS spectra of the C 1s region.

Table 10. Atomic percentages of the main elements detected.

	C /atm. %	**O /atm. %**	**N /atm. %**
Cat PU	91.3	8.6	0.1
An PU	75.7	21.2	3.1
LBL Film	76.2	20.8	3

Figure 68B shows the N 1s spectra for Cat PU, An PU, and the LBL sample. The Cat PU has only a trace of nitrogen present. The LBL sample has N which indicates that the An PU component is present. Figure 68C shows the O 1s spectra for all three samples. The predominate source of the O 1s signal is from $-CH_2-\underline{O}-CH_2-$ species in all three samples. The C1s spectra are shown in Figure 68D. The Cat PU and An PU curves have different shapes, suggesting the composition of the carbon species is different. The An PU sample has a much higher fraction of $-\underline{C}H_2-O-CH_2$ species with respect to $-\underline{C}H_2-$ species. The LBL sample has a similar appearance to the An PU sample suggesting that more An PU monomers are present at the surface of the LBL sample. The ratio of $-\underline{C}H_2-$ to $-\underline{C}H_2-O-CH_2$ is larger for the LBL sample as compared to the An PU sample.

Figure 69 shows the curve fitting of the C1s of the LBL sample. The data are fitted to two synthetic curves representing An PU (red lines) and Cat PU (blue lines), to determine the fraction of An PU to Cat PU present in the LBL sample. Taking the area of the An PU and Cat PU components and normalizing them by the number of carbons in each monomer, respectively, can be used to determine the percentage of each monomers present at the surface of the film (see Table 11). Note XPS is surface sensitive and the composition may differ deeper into the film.

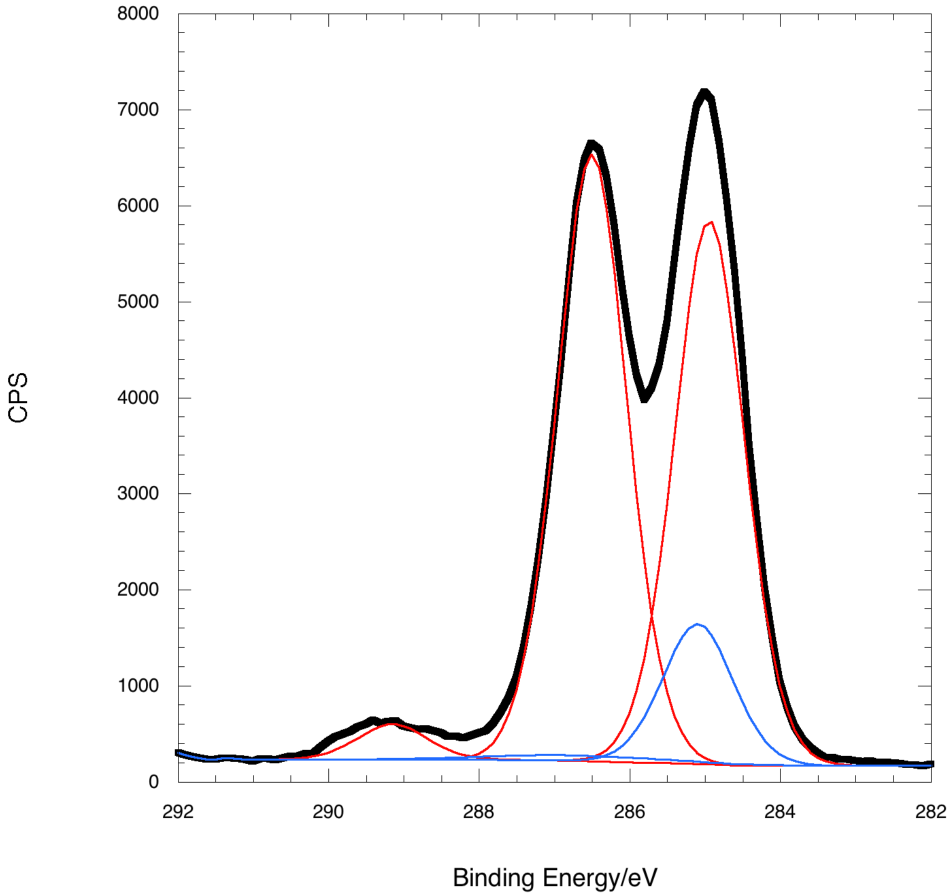

Figure 69. X-ray Photoelectron spectra of the C 1s region of the PU- LBL film fitted to the components of the An-PU film and Cat-PU film. The red lines represent the Cat-PU fit and the blue lines represent the An-PU fit.

Table 11. Compilation of compositional analysis results from XPS.

Component in the LBL C 1s spectra	Area /CPS.eV	Number of Carbons in monomer	Normalized area	Percentage of monomers present /%	MW /%
An PU	14598	371	39.3	85.4	88.6
Cat PU	1916	285	6.72	14.6	11.4

3. Results and Discussion

Polyurethanes represent a very large family of polymers with a common structural feature being the urethane linkers connecting its subunits. In this work we used two, commercially available PUs with chemical compositions shown in Figure 70. We note that the particular compositions are by no means the only possible choices; however, they satisfy two important parameters for LBL assembly: (1) they are soluble in aqueous conditions due to high density of hydrophilic groups and (2) they have charged units (Figure 70, red groups) in the form of a short tertiary ammonium side chain in the cationic PU and a carboxylic acid group in the anionic PU. Furthermore, we chose the particular structures because of fairly long "soft" segments (Figure 70, green groups), (-CH$_2$-CH$_2$-CH$_2$-CH$_2$-O-)$_{28}$ and (-C$_2$H$_4$-CH$_2$-O-)$_{51}$, for Cat and An PUs respectively, which impart these polymers with high ductility at the molecular and nanoscale levels.

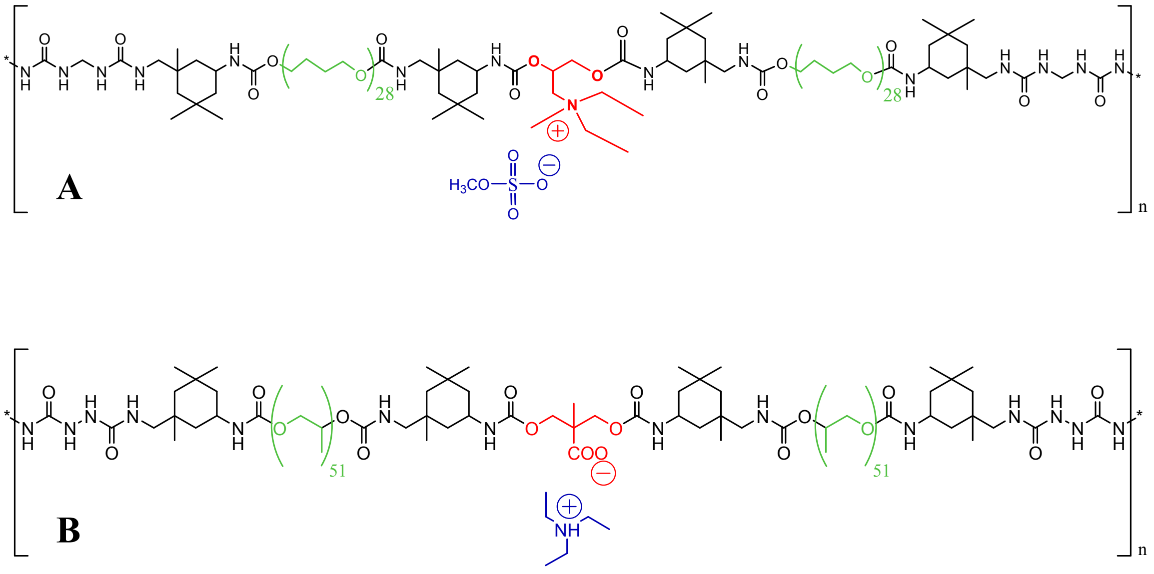

Figure 70. Chemical structures of: (A) cationic and (B) anionic polyurethanes. Charged groups are highlighted in red, counterions in blue, and soft segments in green colors.

The PUs multilayers were prepared using similar conditions to those used for MTM clay and CNRs multilayers presented in Chapters II and III. In a typical assembly, piranha cleaned substrates (microscope glass slides or silicon wafers) were first immersed into a ~3.5 wt.% solution of Cat PU for 2 min, rinsed with DI water, and dried with compressed air. In this stage Cat PU adsorbs onto the charged substrate via electrostatic and hydrogen bonds and under optimal conditions reverses surface charge to accommodate adsorption of a negative species. After adsorption of the polycation, the substrates were immersed into a ~3.5 wt.% solution of An PU for 2 min, and again rinsed with DI water, and dried with compressed air. Similarly to the polycation adsorption, the adsorbing polyanion reverses the surface charge to negative and returns the substrate to the original state. At this point the substrate is covered with a pair of cationic and anionic layers, which from this point forward will be referred to as bilayers. Reversal of the surface charge to the starting point allowed for adsorption of new bilayers, thus allowing incremental growth of the multilayers to a desired final thickness.

Film buildup was characterized with UV-Vis spectroscopy and ellipsometry. (Figure 71) Figure 71A shows compilation of spectra collected after successive adsorption of (Cat PU-An PU)$_1$ bilayers up to a total of 10 bilayers, denoted as (Cat PU-An PU)$_{10}$. Similarly to previous demonstrations of multilayer buildup, the assembly conditions described above showed uniform and regular growth. Plotting of absorbance vs. bilayers number for different wavelengths of light (Figure 71B) revealed steady and nearly linear growth with some evidence of an upswing when 10 bilayers were approached. Interestingly, ellipsometry showed complete linearity up to 20 bilayers with incremental growth of nearly ~10 nm per bilayers. (Figure 71C)

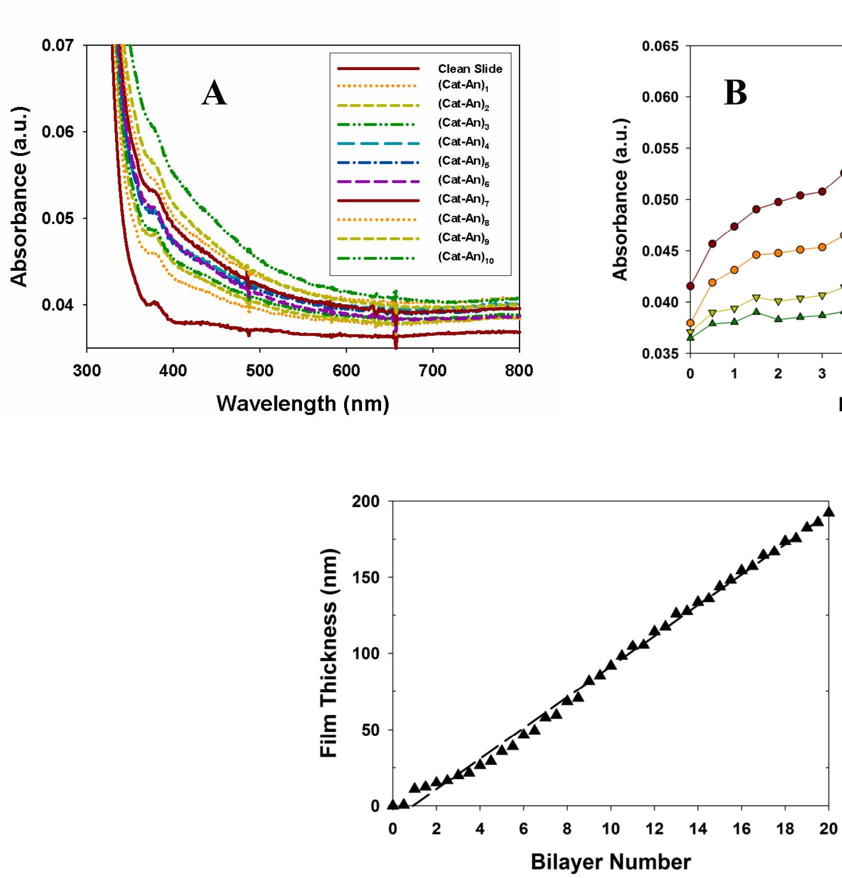

Figure 71. (A) Compilation of UV-Vis absorbance spectra for Cat PU-An PU assembly for the first 10 bilayers. (B) Absorbance vs. bilayer number regressions for Cat PU-An PU assembly from (A) showing uniform growth. (C) Ellipsometry results for Cat PU-An PU assembly on silicon substrate.

Having established successful growth of the multilayer, we proceeded with growing thick films on microscope glass slides using automatic dipping robots from nanoStrata (Tallahassee, FL). A set of 300-bilayer films was prepared and free-standing films were separated using the substrate etching with HF solution described in our previous publications.[3] (Figure 72A) Compared to the previous publications, we allowed the detached films to float in pure DI water to remove any excess of HF. The films were then lifted out from water using a rigid Teflon substrate.

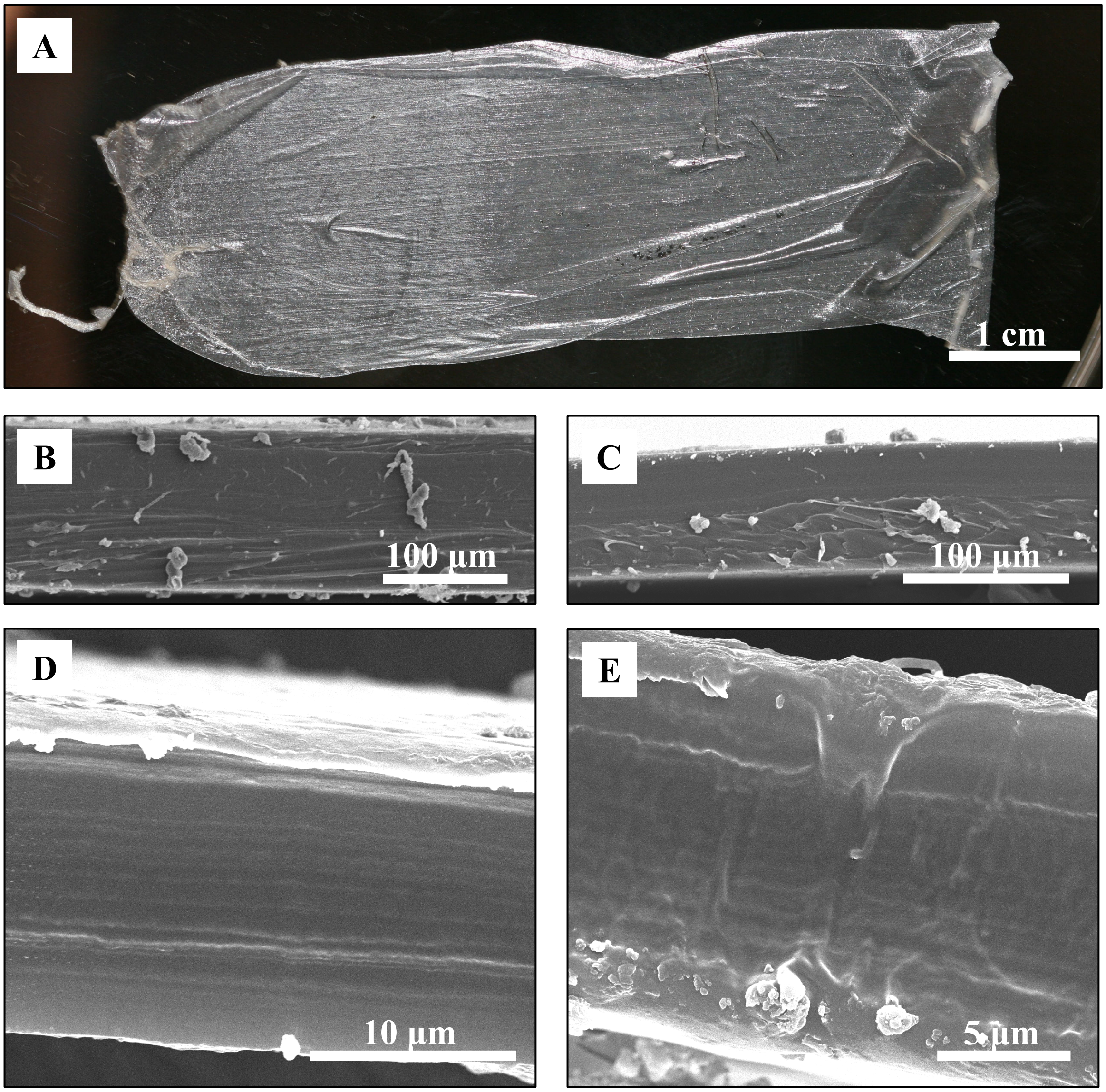

Figure 72. (A) Photograph of a free-standing, 300-bilayer Cat-An PUs LBL film. (B) SEM cross-section of pure cationic PU. (C) SEM cross-section of pure anionic PU. (D) and (E): Cross-sectional SEM images of the free-standing, 300-bilayer Cat-An PU LBL film showing regular stratification.

Upon removal from water, films supported on the Teflon were placed in a convection oven at 80 °C and allowed to dry. Using Teflon substrates allowed for easy detachment of free-standing films. The films were found to be thin, highly robust, and flexible. Careful handling was required as the films showed substantially lower stiffness when compared to the films incorporating nanoparticles.[2-4]

SEM characterization of the free-standing film revealed uniform cross-section however with much greater thickness then expected. Extrapolation of the data obtained from ellipsometry suggested that the thickness should not be more then ~3 μm for the 300-bilayer film, while the SEM revealed approximately 4x greater thickness of ~13 μm. This translates into an average of ~40 nm per bilayer. This could potentially be a result of incomplete rinsing of the films; however, a closer look at the SEM images revealed a well defined stratified structure throughout the entire thickness which was not observed in the pure polymers. (Figures 72B – E) An explanation may come from the fact that the charge density along the polymers' backbones is small and it is already well established that weakly charged polyelectrolytes can have nonlinear and even exponential growth leading to structures having thicknesses in excess of 100 μm for 200 bilayers.[11,14]

An important question that one needs to ask is how the molecular and nanoscale organization of the polymers is affected by nanostructuring via alternating layering of nanometer-thick strata in LBL. This is an especially important question because the exceptional ductility of the PUs is attributed to the ability of formation of "hard" (crystalline) and "soft" (amorphous) domains. In the case of our polymers, the hard domains contain charged groups which are primarily responsible for formation of electrostatic interactions (cross-links) between each other and may compromise the ability of the two polymers to form ductile and flexible material. To help answer this question we characterized chemical composition of the LBL film using XPS. (see Experimental Procedures) Note that because of close similarity between the two polymers, it would be difficult to accurately characterize composition of the LBL films using elemental analysis. The results revealed that surface of the film is composed in ~7:1 wt.% ratio of An PU : Cat PU. DSC characterization of the pure polymers and the LBL film (Figure 73A) showed that the characteristic transition peak of Cat PU present at ~300 °C was greatly suppressed when compared to the peak of An PU at ~375 °C. This suggested that the chemical composition of the film may in fact overall be 7:1 by weight. Characterization of the polymers and LBL film by wide angle x-ray scattering (WAXS) showed that the multilayer film in fact contains crystallites characteristic to both components. (Figures 73B and 73C) Comparison of a Cat PU-An PU polymer blend (prepared by simple mixing of the two in 7:1 ratio) and the LBL film showed very good overlap, suggesting that the conclusions drawn from DSC analysis may in fact be correct. (Figure 73D)

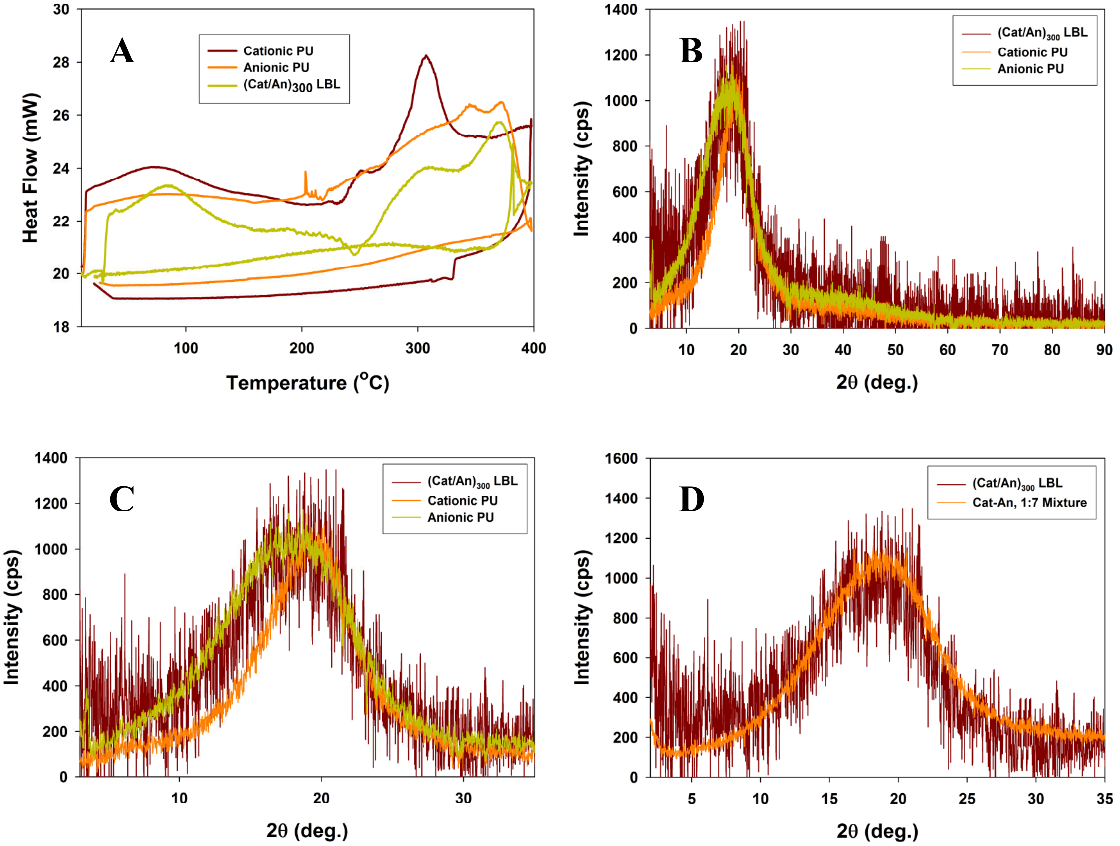

Figure 73. (A) Differential scanning calorimetry spectra comparison for pure polymers and LBL film. (B) – (D) Wide-angle x-ray scattering spectra comparison of pure polymers, LBL film, and a 7:1 blend of An PU : Cat PU. The spectra in DSC and WAXS are normalized to the same height due to large differences in the thickness of the samples. Because of small thickness of the LBL film, the spectrum shows lower signal-to-noise ratio when compared to pure polymers.

AFM characterization of top surface morphologies with phase contrast imaging mode showed dramatic differences between the different films, and especially between the LBL and the blend composites. (Figure 74) First, the two oppositely charged PUs showed very different morphologies: Cat PU (Figure 74A) showed a distinctly granular structure with hard domains clearly contrasting the soft regions while An PU showed very little contrast between the hard and soft domains. The hard domains in Cat PU have mainly oval shapes with widths up to ~150 nm and lengths as large as 2 μm (typical lengths are less than 1 μm). The LBL film also showed evidence of hard and soft domains as in the Cat PU (Figure 74C), but with very different morphology. The hard domains appear to form a cellular structure with hard domains having spherical shape and diameters up to ~150 nm. This morphology can be further contrasted with the structure of the blend, which shows clear phase separation between the two polymers and very different internal organization. Overall, evidence of domain formation was encouraging for the ultimate goal of this work, i.e. preparation of flexible multilayered films.

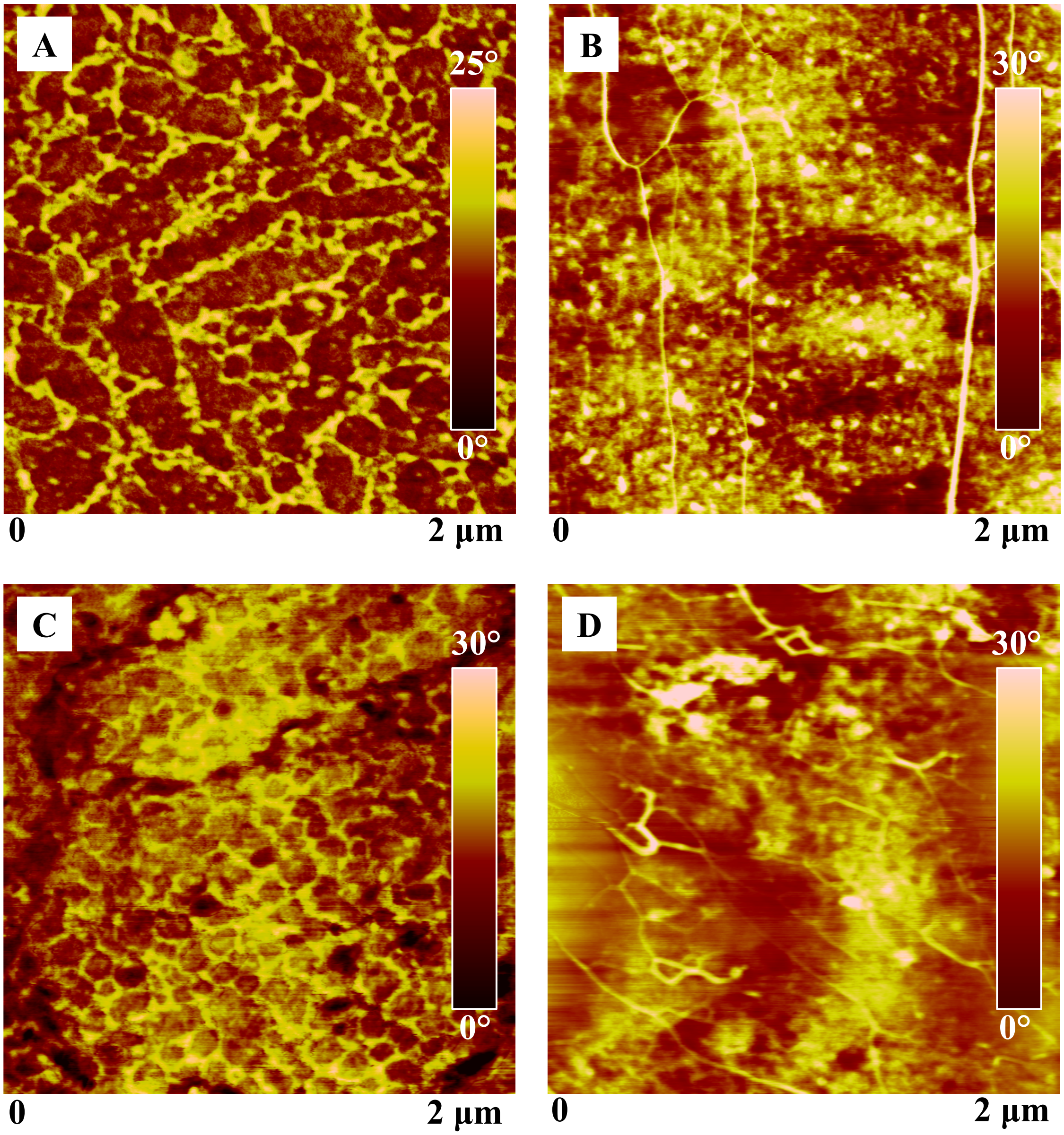

Figure 74. Phase-contrast atomic force microscopy (AFM) images of surface morphologies for: (A) Cat PU, (B) An PU, (C) Cat-An PU LBL film, and (D) a 7:1 An PU-Cat PU mixture. The images were obtained in tapping mode.

Evaluation of tensile mechanical properties of the films showed high level of elasticity with properties being intermediate between the two components. (Figure 75 and Table 12) The Cat PU showed yield strength of, σ_Y ~2 MPa, ultimate strength, σ_{UTS} ~30 MPa, modulus of, E ~26 MPa, and ultimate strain of, ε ~540 %. The An PU showed no evidence of yield strength, lower σ_{UTS} ~10 MPa and E ~2 MPa, however it showed much higher ε at ~1200 %. Comparing to the two, the LBL film showed improvement in σ_Y to ~3 MPa, but significant reduction of σ_{UTS} to ~6.5 MPa. The modulus and strain showed intermediate values between the two polymers: E ~15 MPa and ε ~630 %. The significant reduction in σ_{UTS} may be explained with fragility of the thin films to handling. While not visible with naked eye, very soft nature and small thicknesses of the films can be easily prone to defects from handling and the ultimate strength and strain can be reduced by premature failure. This can be especially seen from the significant variations in stress-strain responses of the films in Figure 75E.

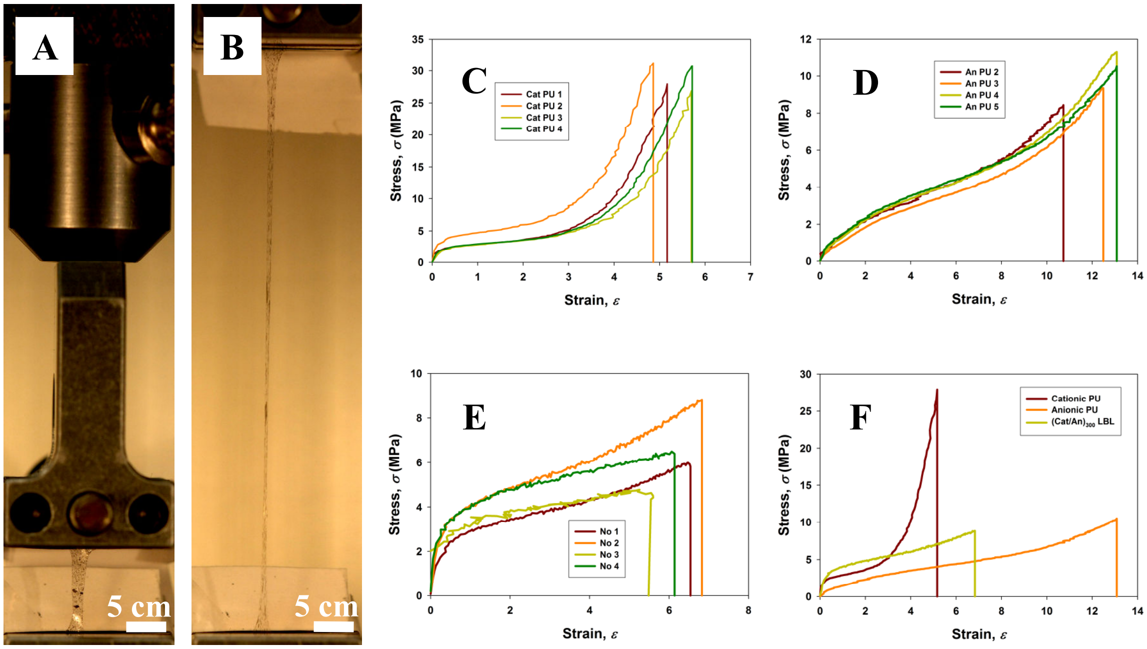

Figure 75. Mechanical properties of polyurethanes and LBL film. (A) Photograph of a dog-bone specimen of a 300-bilayer LBL sample prior to tensile test. (B) Photograph of the dog-bone specimen from (A) prior to rupture. Both images were taken at the same magnification and focal distance. The black dots on the surface of the specimens are paint marks which were used to accurately track the strain response. (C) Stress-strain responses for pure cationic PU. (D) Stress-strain responses for pure anionic PU. (E) Stress-strain responses for the 300-bilayer LBL film. (F) Comparison of cationic, anionic, and LBL films of polyurethanes.

Furthermore, the improvement in σ_Y can be attributed to the formation of electrostatic cross-links between the two polymers. The same cross-links can also be responsible for decreasing the ultimate strain to values closer to those of the Cat PU. Overall, these are excellent results given that all of the previously reported LBL films showed two orders of magnitude lower strains.[3,4,7,8,31,32] They open new opportunities for research and applications, especially when the assemblies will be combined with different nanomaterials, for preparation of mechanically responsive and flexible nanostructured thin films.

Table 12. Experimental results from comparison of the mechanical properties of cationic, anionic, and Cat-An PU LBL films.

Sample Type	Yield Strength, σ_Y (MPa)	Ultimate Tensile Strength, σ_{UTS} (MPa)	Young's Modulus, E (MPa)	Ultimate Tensile Strain, ε (%)	Toughness, (MJ/m^3)
Cationic PU	2.3 ± 0.7	29 ± 2	26 ± 15	540 ± 40	43 ± 4
Anionic PU	-	10 ± 1	2.4 ± 0.6	1220 ± 100	55 ± 9
Cat-An LBL	3.1 ± 0.4	6.5 ± 1.7	15 ± 6	630 ± 50	29 ± 8

4. Conclusions

In conclusion, we presented here the first preparation and characterization of highly flexible and free-standing LBL films. The films showed ultimate strains of several hundred percent, which is at least two orders of magnitude greater than all previous LBL assemblies. A new assembly component, i.e. charged polyurethanes, was instrumental to this demonstration and this work represents the first use of PUs in multilayered assemblies. Polyurethanes constitute a large family of polymers with wide range of compositions and when combined with the wide array of already available assembly components they represent a fundamentally novel material and open new research directions.

E. Hierarchically-Made, High-Toughness Macroscale Layer-by-Layer Assembled Laminates

1. Introduction

The layer-by-layer assembly (LBL) technique is currently one of the most widely utilized methods for the preparation of multifunctional, nanostructured thin films with applications ranging from nanocomposites,[2-4] drug delivery platforms,[21] superhydrophobic coatings,[33] and onto solid-state memory devices.[34] While quite beneficial in some areas of technology, for instance sensing, electronic materials, and transport phenomena, the typical nano- to microscale thickness of the LBL sheets and coatings limits its application in technologies where mechanical stresses exerted on the material are fairly high. This is an impeding factor, for instance, for production of the ultra-strong composites made by LBL of interest for a variety of industries.[2-4] Modified LBL processes that accelerate the composite accumulation process have been proposed, including spraying,[35] spin-coating,[36,37] and dewetting LBL[38]. However, all of these techniques have yet to show to have the ability to form macroscale structures. Another solution can be found in the "exponential" LBL (e-LBL), which we have discussed in Sections B and C.[14]

Here we demonstrate that (1) materials with macroscale thicknesses, suitable for different forms of manufacturing, can be produced by LBL technique and (2) that they exhibit novel mechanical (and other) properties. We also realized that in order to accomplish these tasks one will need to engineer these materials as hierarchically organized structures. Multiscale hierarchy is one of the fundamental principles in nature.[39] Compounding different levels of organization and functional engineering from nanoscale to macroscale is taken advantage of in production of materials with exceptional strength, stiffness, hardness, and toughnes.[39] Such materials are exemplified by seashell nacre,[40] teeth,[41] bones,[42] spider silk,[43] and squid beak[44], which are being studied as model systems for development of advanced, high-performance composites. The challenge in utilization of this principle and achieving similar mechanical and structural features in synthetic materials lays in difficulty of robustly traversing different length-scales and retaining the specific order at each level.[39] Consequently, the development of a new method that can show a fairly universal route to manufacturing of hierarchically structured materials is fundamentally important and here we give a first example of hierarchical structures derived from LBL films made by a simple lamination process. Along with simplicity of preparation, the resulting materials display high-toughness and ductility substantially exceeding the original polymeric materials.

2. Experimental Procedure

Materials, LBL assembly, and chemical composition characterization used in this section are the same as in previous sections, unless stated herein.

Materials, LBL Assembly, and Consolidation

Cationic polyurethane aqueous dispersion (PU, ~35 wt.%, MW ≈ 92,000) (Hepce Chem Co., South Korea) and poly(acrylic acid) (PAA, 35 wt.%, MW = 250,000, pH = 2.9) were used as-received by diluting to ~3.5 wt.% and 1 wt.% solutions, respectively, in deionized water. Fluorescein isothiocyanate isomer I (FITC) and tetramethyl rhodamine isothiocyanate (TRITC) fluorescent dyes were obtained from Sigma-Aldrich. PU/PAA multilayer films were prepared by conventional dipping LBL method using Midas II programmable slide stainers (EMD Chemicals. Inc.). In a typical assembly, 100-bilayer films of PU/PAA were prepared on microscope glass slides using 30 sec dips in each of the solutions and 1 min rinses with water between each dipping. Free-standing films were isolated by etching of the glass slides with 1% hydrofluoric acid. After thorough rinsing with pure water, the films were dried in an oven at 100 °C. Laminated samples were prepared by hot-pressing overlaid stacks of films at 100 °C and < 1 ton of pressure for at least 30 min, depending on stack thickness. Blended sample was prepared by mixing of the two components in the 9:1 wt.% ratio, dry casting, and hot-pressing using the same conditions. IR spectra were obtained using a Nicolet 6700 spectrometer utilizing the grazing angle accessory (Smart SAGA) at a grazing angle of 85º.

Compositional Characterization of e-LBL Films

a) Elemental Analysis

Carbon and nitrogen concentrations were found using a Perkin-Elmer 2400 Series II combustion analyzer. The results of the analysis are summarized in Table 13. Theoretical concentrations of the elements in pure polymers were determined from their chemical structures.

Table 13. Summary of elemental analysis for pure polymer and e-LBL samples. Reported values are in wt.%.

	PU		PAA		(PU/PAA)100		(PU/PAA)100, 40-film stack	
	C	N	C	N	C	N	C	N
Theoretical	63.24	3.88	50.00	0	-	-	-	-
Experimental	61.72	5.45	46.51	0.14	60.14	4.8	60.45	4.76

Using the results obtained for pure polymers, the wt.% of PU in the LBL samples was calculated at 88 – 92 wt.%. A median of the range was taken at ~90 wt.% PU and ~10 wt.% PAA.

b) XPS Analysis

The XPS spectra were collected on cast samples of PU and PAA, and on a cross-section of the ~4.1mm thick composite stack. Scan of the cross-section ensured correct interpretation of the data as the bulk chemistry, as opposed to the surface which could be rich in one of the components due to LBL deposition.

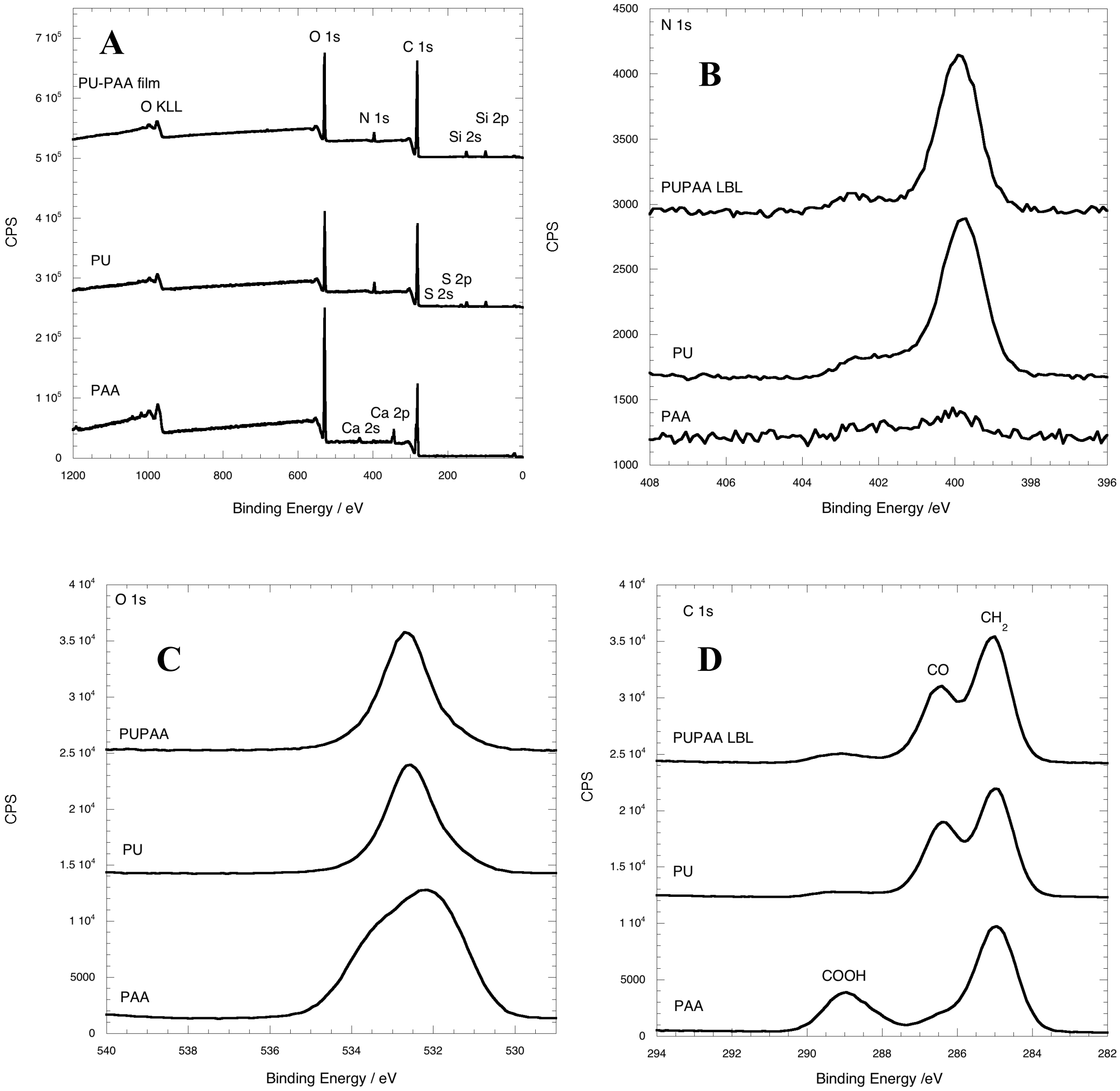

Figure 76. (A) XPS survey spectrum of PAA, PU and PU-PAA films. The data have been vertically transposed for viewing purposes. (B) XPS spectra of the N 1s region of PAA, PU, and the PU-PAA LBL film. (C) XPS spectra of the O 1s region of PAA, PU,

and the PU-PAA LBL film. (D) XPS spectra of the C 1s region of PAA, PU, and the PU-PAA LBL film.

Survey scans of PAA, PU and the LBL PU-PAA films are shown in Figure 76A. Carbon, oxygen and calcium were detected at the surface of the PAA. Calcium was an unexpected contaminates which was not present in the other two samples. Carbon oxygen and nitrogen along with some silicon impurities were present in both the pure PU sample and the LBL sample. In the case of the pure PU there were also peaks associated with sulfur, which is inductive of the presence of the PU counter ion; however, no evidence of sulfur was found in the PU-PAA LBL sample. It should be noted that the relative heights of the C:O:N are similar for the PU and PU-PAA samples suggesting that the composition of the LBL film is closer to that of pure PU than PAA.

The integrated areas of the detailed spectra of C 1s, O 1s, N 1s were used to calculated the atomic percentage of each element by using Wagner's sensitivity factors.[45] The composition of PAA and PU were found to be close to that expected. Interestingly, the composition of the PU-PAA film resembles the pure PU sample.

Table 14. Atomic Percentages of the main elements detected. Expected values are in brackets.

	C /atm. %	**O /atm. %**	**N /atm. %**
PAA	63.0 (60.0)	35.9 (40.0)	1.1 (0.0)
PU	74.2 (76.2)	21.4 (19.8)	4.4 (4.0)
PU-PAA LBL	76.5	18.9	4.6

Figure 76B shows the N 1s region in detail for the pure PAA and PU materials along with the PU-PAA LBL film. Although we were not expecting any nitrogen in the

PAA, we found a trace amount (quantified in Table 14). For the PU and PU-PAA samples, a shoulder is observed on the higher binding energy side of the main peak suggesting that that there more than one N species present in these samples.

The shape of the O 1s band of PAA differs from both the PU and the PU-PAA LBL film (Figure 76C). For PAA we expect a peak associated with the O=C-$\underline{O}$H and $\underline{O}$=C-OH species. However, these are not at a ratio of 1:1, which would suggest that there are more oxygen groups, perhaps due to impurities or contaminants. Not withstanding this, it is clear that the O 1s spectra of PU closely resemble the PU-PAA LBL film.

For certain polymers the C 1s region can be considered as like a finger print region since the binding energy of carbon is relatively sensitive to the chemical bond with other elements, and in particular, oxygen. We can identify the -$\underline{C}H_2$-, the –$\underline{C}$O-, the $\underline{C}$=O, and the $\underline{C}$OOH bands within the PU, PAA and PU/PAA LBL samples (Figure 76D). Assignments of each peak can be made. However, for the purposes of this work we shall use the shapes of the PAA and PU C1s spectrum to form synthetic curves in order to fit these to the LBL PU/PAA film to determine the relative quantities of PAA and PU in the PU-PAA LBL film. In doing this, the assumptions are that no new covalent bonds occur in the LBL process and that the change in local environment of the covalent bonds has minimal effect on their binding energies. Figure 77 shows the fit used to assess the relative quantities of PAA and PU in the LBL sample. In effect, the PAA and PU C1s spectrum were used to produce synthetic curves to fit to the LBL C1s region. The best fit is shown in Figure 77. By normalizing the sum of areas under the curves, by the total number of carbons in a PU monomer and a PAA monomer one can assess the percentage of PAA monomers to PU monomers to be 90% to 10%, respectively. The molecular weights of the PAA and PU monomers are 72.05 g/mol and 5412.33 g/mol, respectively, giving the ratio of PAA to PU in terms of molecular weight to be approximately 1:9. This result correlates well with the elemental analysis data.

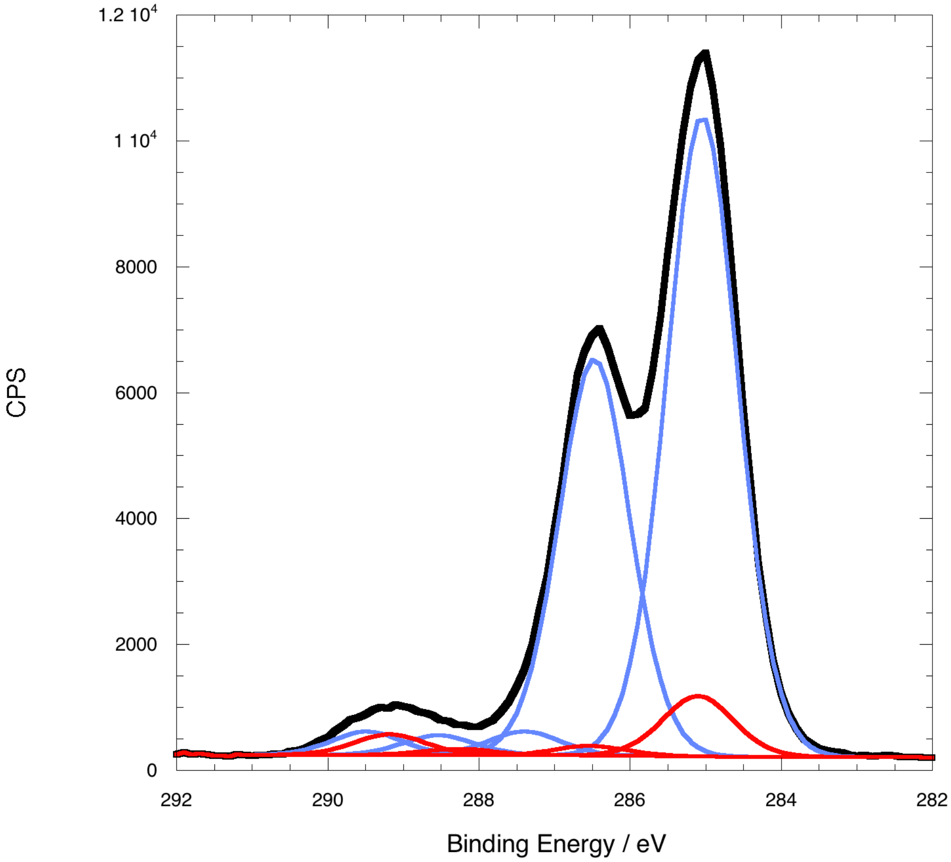

Figure 77. The C1s region of the PU-PAA sample. The black line represents the data collected. The blue lines are the curves used to fit the PU, and the red lines represent the curves used to fit the PAA. By fixing the relative ratios of each set of curves, a synthetic curve is produced for assessing the relative quantities of PAA and PU in the LBL sample.

3. Results and Discussion

Following the idea of hierarchical design we started with the molecular level of organization. One of the classes of materials well-known for their strength and toughness are polyurethanes (PU's), which found broad applications in construction, transportation, household appliances, packaging, electronics, and implantable biomedical devices, to name a few. PU’s have never been used in LBL assembly and in Section D of this chapter we showed the first preparation of LBL assemblies from oppositely charged PUs. For the purpose of this work we turned to the cationic PU presented in section D. (Figure 78A)

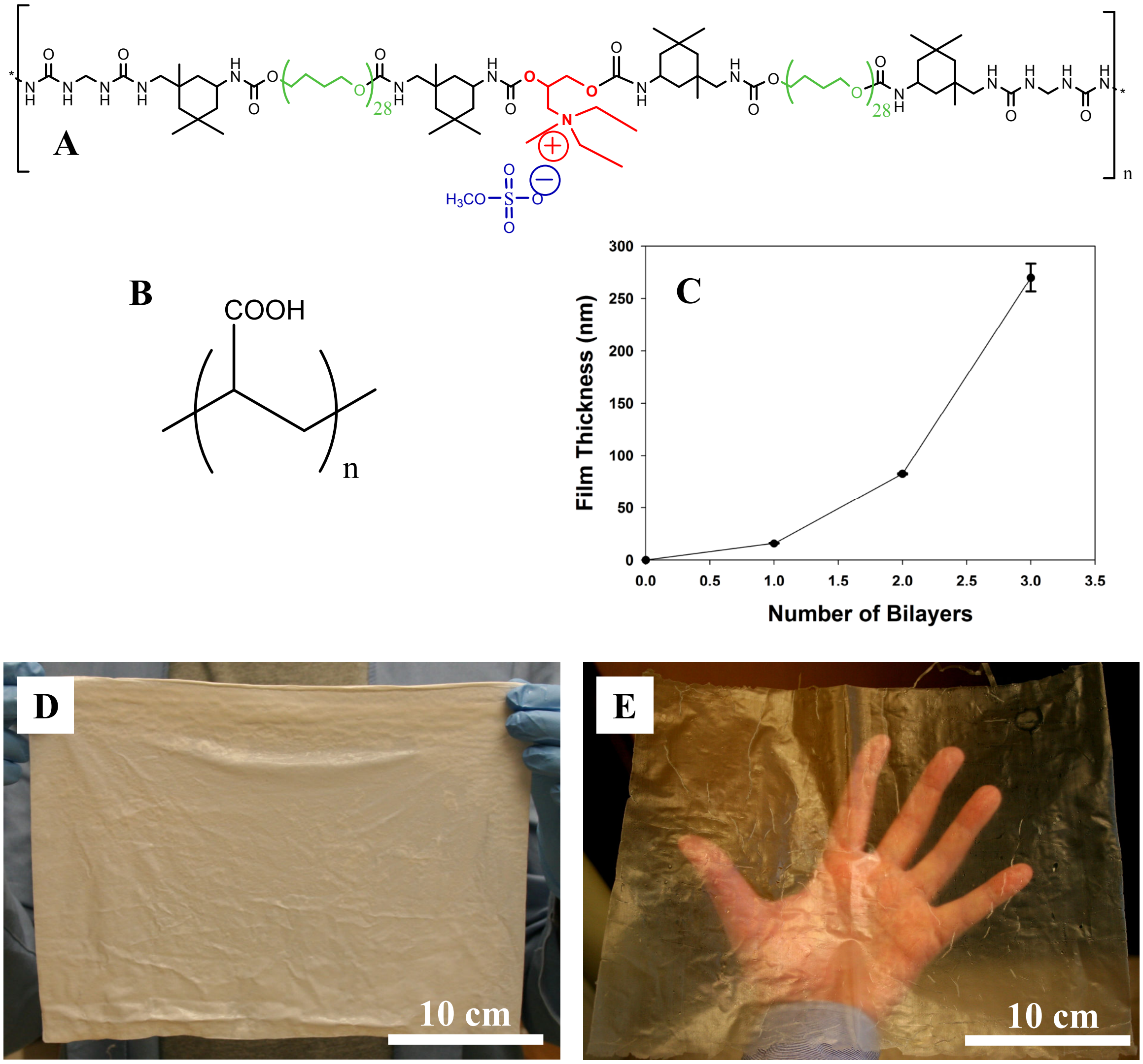

Figure 78. LBL assembly components, growth characterization, and free-standing LBL films. (A) Chemical structure of the cationic polyurethane copolymer. The cationic functional group of the polymer is highlighted in red, the counter-ion in blue, and the soft segments in green. (B) Chemical structure of poly(acrylic acid). (C) Ellipsometry results for film growth on top of polished silicon substrate showing rapid increase in thickness. Opaque appearance of the film prevented further measurements. Error bars for 1- and 2-bilayers are small and not visible in the graph due to difference in the magnitude of the values with the size of the y-axis. (D) Photograph of a 200-bilayer, hydrated PU/PAA

free-standing sheet grown on 12 in x 12 in glass substrate. (E) Photograph of a 100-bilayer, dried PU/PAA free-standing sheet grown on the same 12 in x 12 in glass substrate as in (C).

LBL assembly of this PU was carried out by sequentially dipping a glass microscope slide for only 30s intervals into aqueous solutions of negatively charged poly(acrylic acid) (PAA, 1 wt.%) and ~3.5 wt.% PU (Figures 78A and 78B) using an automated dipping robot. The pattern of the multilayer accumulation showed clear evidence of e-LBL growth: ellipsometry showed rapid exponential increase in the film thickness additional bilayers (Figure 78C). The film was strongly hydrated, which is typical for e-LBL, and had a cotton-like appearance. Its opaqueness in this swollen state prevented us from performing ellipsometry studies beyond few layers. Cross-sectional scanning electron microscopy (SEM) clearly indicated successful growth of PU and PAA films with the thickness of 10 ± 3 μm and 70 ± 10 μm for $(PU/PAA)_{18}$ and $(PU/PAA)_{100}$ respectively, where $(PU/PAA)_n$ represents the film obtained after *n* deposition cycles. Interestingly, although strongly swelling and hydrating, the films were easily separated from the substrate and handled (Figure 78D).[3] The free-standing films were found to be robust and strong allowing for easy scale-up to much larger substrates and film sizes. (Figures 78D and 78E)

Continuing with hierarchical design of the materials and entering the micron/macro scale, we have exploited the swelling characteristic of the e-LBL films to combine together individual sheets into a hierarchical, laminated composite according to the schematic in Figure 79. In this simple strategy, dried films are first allowed to swell in water to increase their flexibility and then they are overlaid on top of each other to achieve conformal overlap.

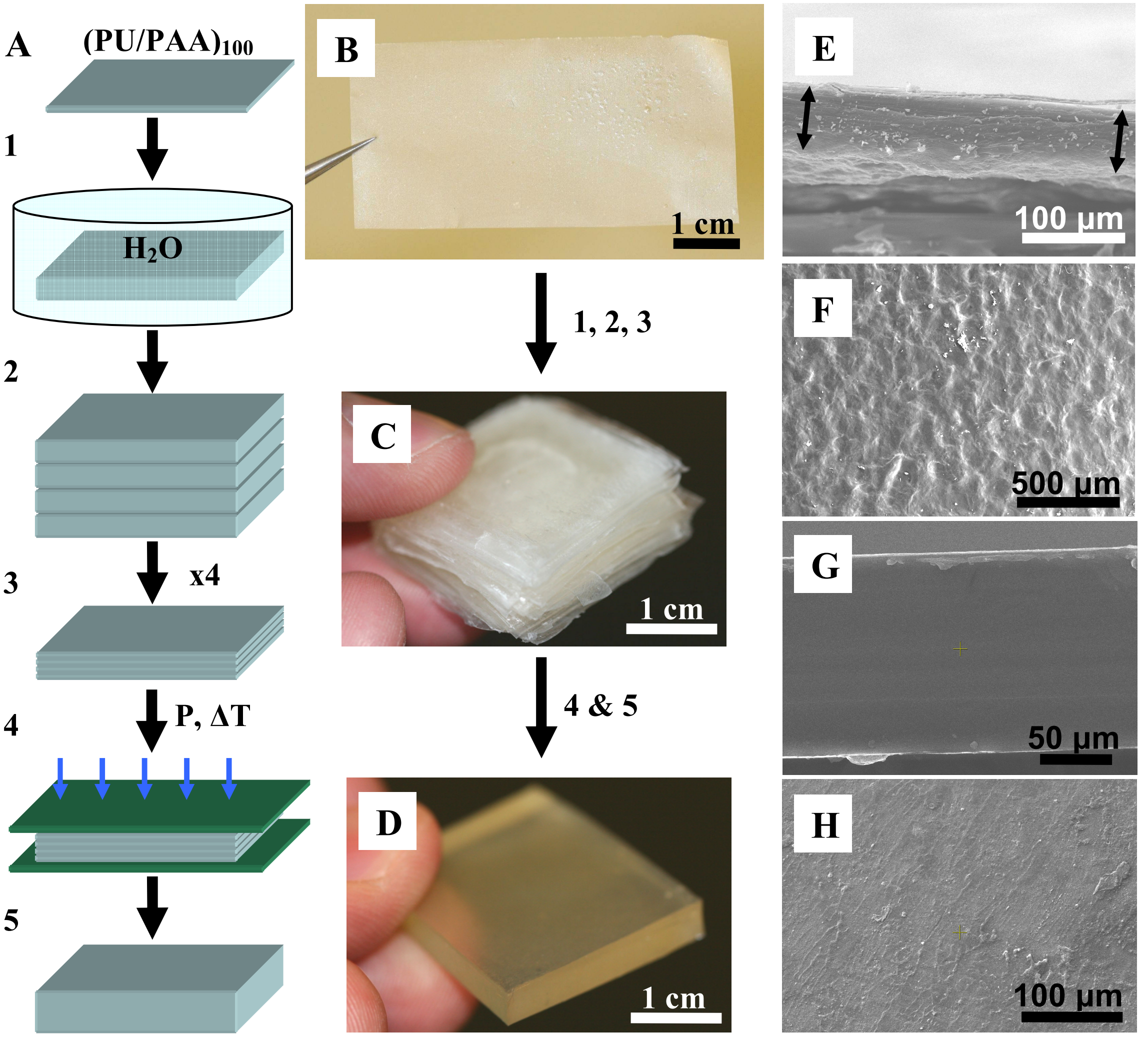

Figure 79. Schematic of consolidation of free-standing e-LBL films. (A) Experimental procedure for consolidation of free-standing PU/PAA films: (1) The films are allowed to swell in water for ~1h; (2) Any number of films are stacked together into a sandwich structure to achieve conformal overlap; (3) The stack is dried at 100 °C under vacuum to remove any bubbles; (4) The dried stack is hot-pressed at 110 °C and < 2 tons of pressure; (5) Final consolidated stack is removed from the press. (B) Photograph of a free-standing, 100-bilayer PU/PAA film before swelling. (C) Photograph of 100 – 100-bilayer, 1 in x 1 in, free-standing films combined into a stack after swelling and drying. (D) Photograph of a final hot-pressed stack from (C). The total thickness of this stack is ~4.1 mm and the total number of bilayers is 10,000. (E) SEM image of cross-section of a free-standing 100-bilayer PU/PAA film grown on microscope glass slide. Arrows indicate the span of the cross-section. (F) SEM image of the single 100-bilayer film in (E) revealing high surface roughness. (G) SEM image of cross-section of a consolidated sample composed of 5 x 100-bilayer PU/PAA films. The image shows complete coalescence of the interfaces between individual films. (H) SEM image of the top surface of the consolidated sample in (G).

The swollen and hydrated interfaces interdigitate between adjacent films and promote consolidation of the stack into a homogeneous structure. The stack is further dried in order to remove water, and the structure compacts. Once dried, the stack is finally compressed under mild pressure, <1 ton and at a temperature of 230 °F. The applied pressure is necessary in order to provide intimate contact between individual sheets. We found that temperatures in the range of 230 °F – 250 °F are optimal for successful consolidation. Below 230 °F there was no consolidation and films were easily pealed apart and above 250 °F the stacks showed signs of decomposition. Differential scanning calorimetry analyses revealed that this temperature range corresponds to a broad peak which can be attributed to the melting point of the LBL composite. (Figure 80)

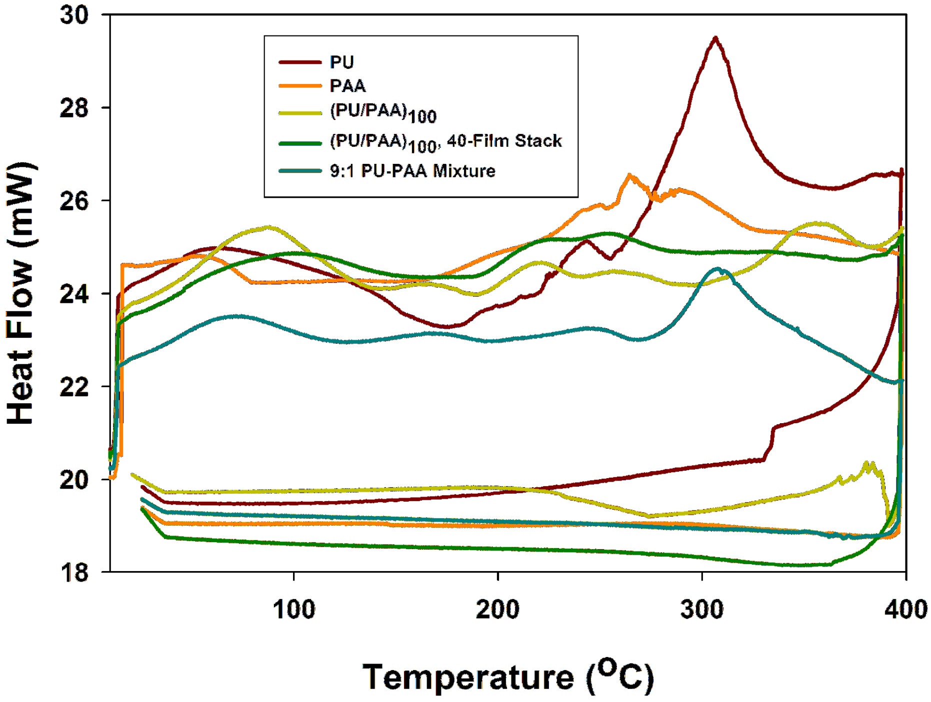

Figure 80. Differential scanning calorimetry analyses of: PU, PAA, $(PU/PAA)_{100}$, $(PU/PAA)_{100}$ - 40-film stack, and PU-PAA blend.

Successful consolidation resulted in a homogeneous and transparent material. SEM characterization of the individual and consolidated structures revealed that the origin of the opaque appearance in single films is due to large surface roughness. (Figures 79E and 79F) This roughness can be attributed to the non-uniform volume changes during drying of the swollen films as well as partial degradation of the films from shearing forces during rinsing. In comparison, the consolidated samples showed uniform and homogeneous cross-section and surface, indicating that the hot-pressing procedure removes defects originating from LBL assembly.

Investigation of mechanical properties gave some unexpected results. (Figure 81 and Table 15) Tensile mechanical properties of the base PU gave: yield strength, $\sigma_Y = 4.3 \pm 0.5$ MPa; ultimate strength, $\sigma_{UTS} = 30 \pm 3$ MPa; Young's modulus, $E = 55 \pm 5$ MPa; and ultimate strain, $\varepsilon = 420 \pm 30$ %. The available literature data for PAA give: $\sigma_{UTS} = \sim 4.5 - 12.3$ MPa and $\varepsilon = \sim 2 - 116$ %; and they correspond to the hydrated state due to the highly hydroscopic nature of the polymer.[46,47] Compared to the pure PU, in-plane tensile properties of single LBL films showed 3x increase in σ_Y to 12 MPa, no change in σ_{UTS}, and ~4x improvement in E ~230 MPa. The ultimate strain (ε), however, showed a reduction in nearly 50%, in comparison to PU, down to only ε ~250% and substantial improvement compared to PAA. This was an encouraging result, since none of the previously reported LBL films showed this level of ductility, thus establishing precedence for preparation of highly flexible multilayered films.[31]

Table 15. Summary of mechanical properties for PU, PAA, single e-LBL sheet, consolidated PU/PAA e-LBL structures, and a PU-PAA blend in 9:1 proportion by weight. [*]Mechanical properties for PAA are taken from Nam et al.[46] and Huang et al.[47].

Sample Type	Yield Strength, σ_Y (MPa)	Ultimate Tensile Strength, σ_{UTS} (MPa)	Young's Modulus, E (MPa)	Ultimate Tensile Strain, ε (%)	Toughness, (MJ/m^3)
PU	4.3 ± 0.5	30 ± 3	55 ± 5	424 ± 31	49 ± 6
PAA[*]	-	~4.5 – 12.3	-	~2 - 116	-
1 Film	12 ± 1	29 ± 8	228 ± 135	250 ± 32	48 ± 14
1 Film Hot-Pressed	15 ± 2	29 ± 7	126 ± 133	172 ± 55	39 ± 18
2-Film Stack	13 ± 0.5	54 ± 18	310 ± 45	366 ± 74	105 ± 40
3-Film Stack	13 ± 1	53 ± 5	333 ± 48	344 ± 46	92 ± 12
4-Film Stack	14 ± 0.5	61 ± 13	343 ± 123	362 ± 65	111 ± 32
5-Film Stack	**15 ± 1**	**86 ± 4**	**237 ± 19**	**361 ± 10**	**140 ± 2**
10-Film Stack	**14 ± 0.4**	**85 ± 3**	**325 ± 157**	**356 ± 10**	**132 ± 4**
9:1 PU/PAA Mixture	6.4 ± 0.3	39 ± 12	58 ± 6	353 ± 47	66 ± 23

Tensile tests on consolidated samples with hierarchical organization showed marked improvement of the modulus (E to ~340 MPa), and dramatic improvements in both the strength (σ_{UTS} ~85 MPa) and the strain (ε ~360 %) over the pure PU and even single LBL film. The toughness of the composite stacks composed of 5- and 10-sheets was nearly ~3x greater than that of the pure PU.

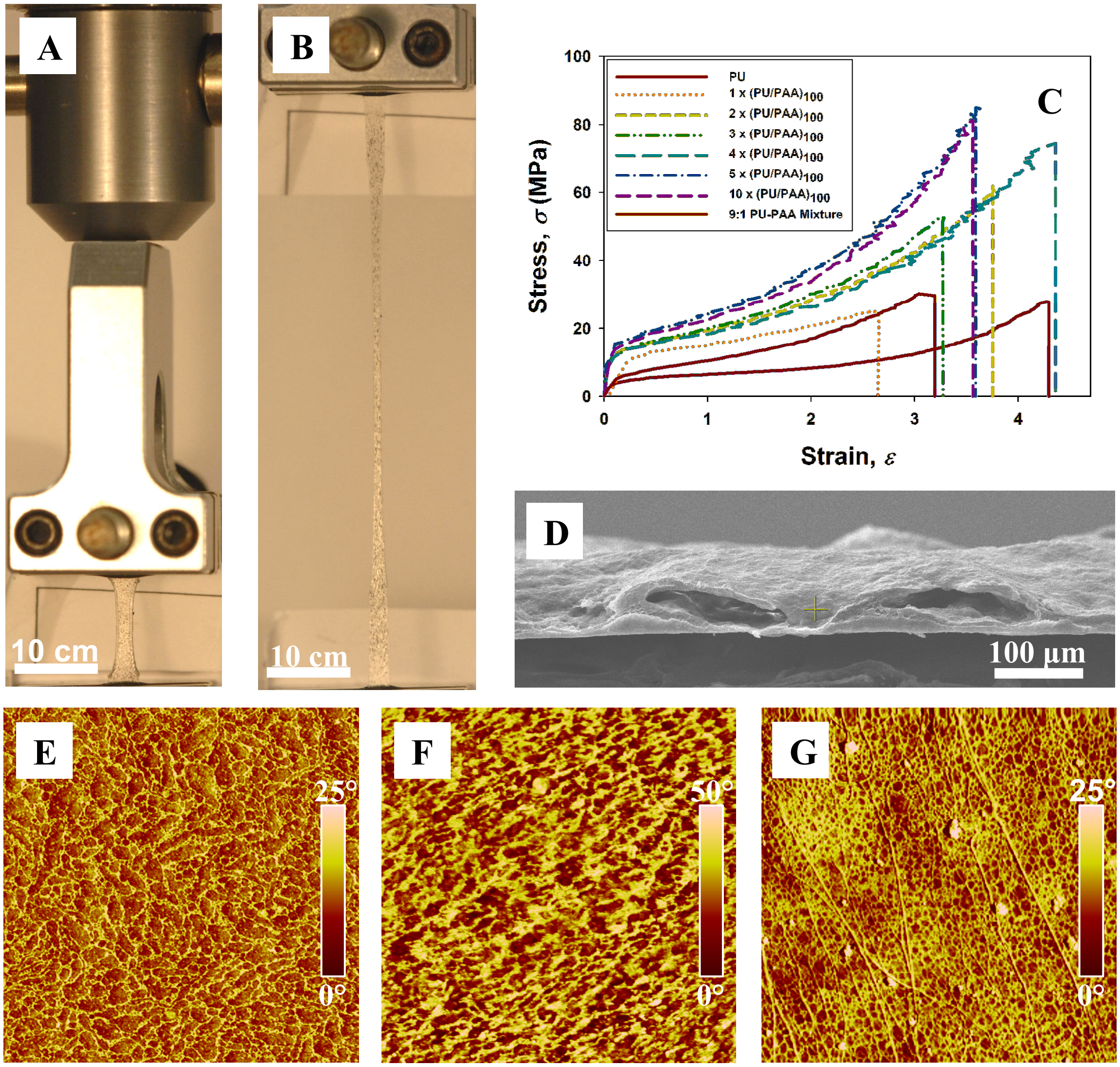

Figure 81. Mechanical properties of PU/PAA e-LBL composites. (A) Photograph of a dog-bone specimen of a 10-film consolidated sample prior to tensile test. (B) Photograph of the dog-bone specimen from (A) prior to rupture. Both images were taken at the same magnification and focal distance. The black dots on the surface of the specimens are paint marks which were used to accurately track the strain response. (C) Comparison of stress-strain responses for pure PU and consolidated samples composed of 1, 2, 3, 4, 5, and 10 films. (D) SEM image of the single, 100-bilayer film revealing cavities in the interior of the film. (E), (F), and (G), Phase-contrast atomic force microscopy (AFM) images of surface morphologies for: PU, 9:1 PU-PAA mixture, and a 5-sheet hot-pressed stack of e-LBL films, respectively. Each image represents a 5μm x 5μm area. Each sample was subjected to the same hot-pressing conditions.

Explanation of marked improvement of mechanical properties from pure materials, to LBL films, and then to consolidated structures lies at different levels of the hierarchical organization: molecular, nano-, and macro-scale. At the molecular scale, the chemical composition of the LBL films was found by elemental analysis and x-ray photoelectron scattering spectroscopy (XPS) to be ~90 wt.% PU and ~10 wt.% PAA. This large dominance of PU explains high ductility of the composite. Based on the molecular weights of the repeat units, the ratio of the charged groups between PU and PAA is actually 1:9, which suggests that they form a complicated electrostatic- and hydrogen-bonding network between each other in order to achieve electrostatic neutrality. The XPS analyses also revealed complete absence of sulfur (present in the sulfur-containing counterion, Figure 78A, blue color) in the LBL samples, which further suggests that the cationic groups directly interact with PAA via ionic and charge-dipole bonds. These cross-links, which are predominantly formed with the hard segments of the PU (Figure 78A, red and black groups) give rise to the improved mechanical properties without significantly perturbing the elastic soft domains. FTIR analysis further showed that hot-pressing of the films does not change the chemical signature of the material, i.e. by formation of new bonds from covalent cross-linking, thus further supporting the idea of ionic cross-linking reinforcement. (Figure 82) Our observation bears similarities with a recently presented work on selective reinforcement of hard domains in polyurethanes with clay nanosheets.[48]

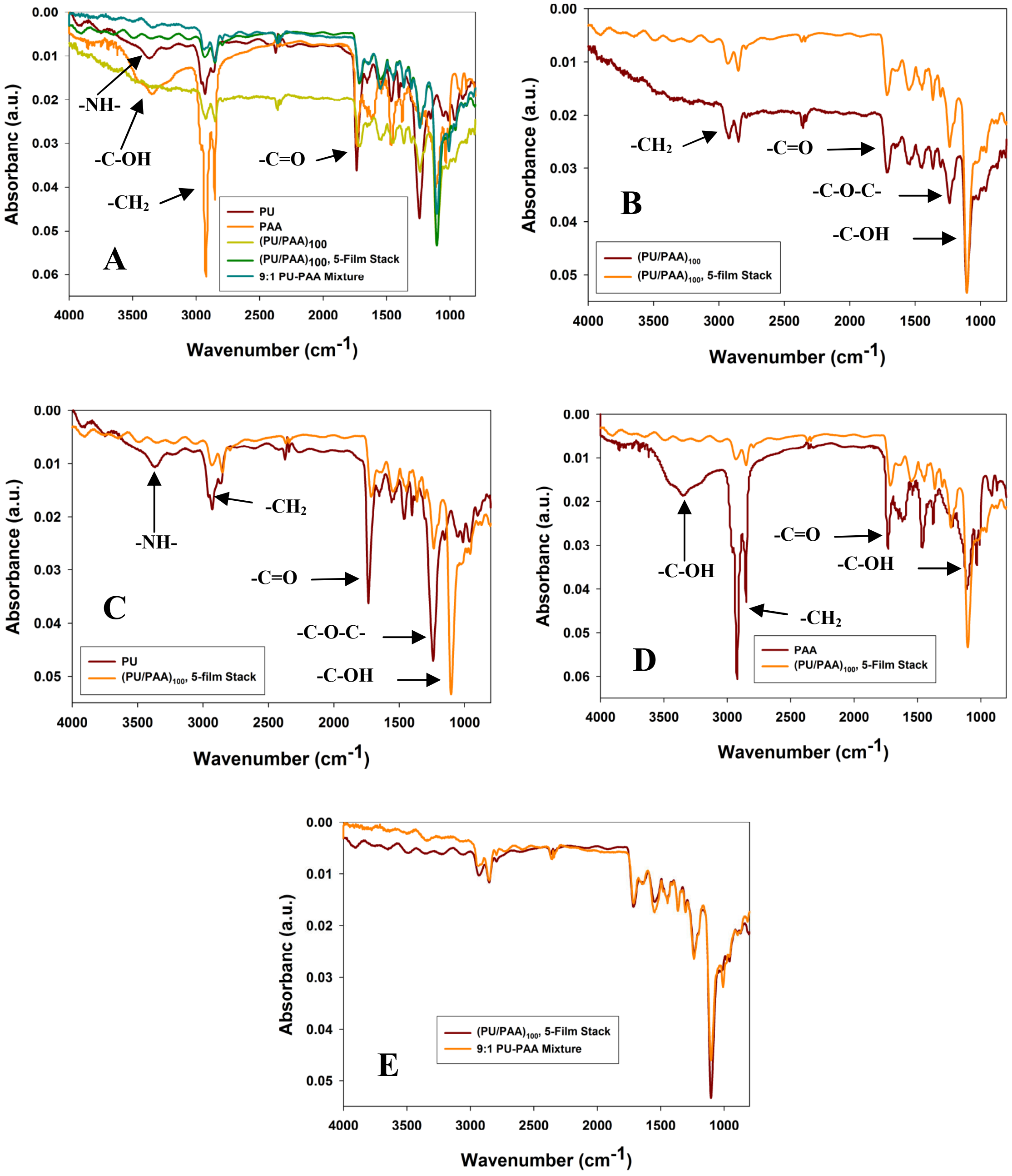

Figure 82. FTIR comparison of chemical composition and hot-pressing effect on chemical composition of PU/PAA e-LBL films. a, Comparison of all materials. b, Comparison of a single sheet and a 5-sheet stack. c, Comparison of PU and a 5-sheet stack. d, Comparison of PAA and a 5-sheet stack. e, Comparison of a 5-sheet stack and a 9:1 PU-PA mixture. Some peak assignment can be made as indicated in the images: (PU) -NH- peak at ~3370 cm^{-1}, alkyl double peak at ~2930 cm^{-1}, a -C=O- peak of urethane at ~ 1740 cm^{-1}, and a -C-O-C- peak at ~1240 cm^{-1}; (PAA) -OH peak at ~3320 cm^{-1} from hydrogen bonding and possible presence of water, alkyl double peak at ~2920 alkyl

double peak at ~2930 cm^{-1} and 2850 cm^{-1}, a -C=O- peak of carboxylic acid group at ~ 1740 cm^{-1}, and a -C-O- stretch at 1230 from -C-OH group.

Comparative characterization of a blend of the two polymers prepared by simple mixing showed slight improvement of E and σ_{UTS} over the bare PU, and similar reduction in ε when compared to e-LBL material. (Figure 81C and Table 15) The σ_Y and σ_{UTS} are however significantly lower than those of the e-LBL composite. This suggests that the nanostructuring imparted by LBL deposition process significantly alters morphology and crystalline structure of the composite. Atomic force microscopy (AFM) comparison of PU, PU-PAA blend, and PU/PAA e-LBL materials showed that they have dramatically different patterns and domain connectivity. (Figures 81E, 81F, and 81G) The nanoscale morphology in LBL films can be described as cellular network of soft (light) and hard (dark) molecular compositions with the presence of linear domains oriented parallel to the dipping direction. The approximate size of domains in the blend is 80 - 300 nm while the cellular network domains in LBL films have approximate diameter of 150 nm with the elongated domains having width of 30-50 nm and length as long as 5 microns and above. The difference in hardness contrast is also much greater in mixed film than in the LBL film suggesting that the multilayer is significantly more uniform. The pattern of domains in the LBL films has also some similarities with that of pure PU. The size of cells is substantially larger in PU and there are no linear features.

At the macro-scale, one additional mechanism plays a crucial role: elimination of defects in the lamination process. The defects in free-standing LBL films can be seen in the non-uniform thickness in Figures 79E and 79F, and in apparent cavities in the cross-section (Figures 81D). They likely originate from shearing forces during rinsing stage of the film preparation, and in the dried material they lead to premature rupture and thus decreased strain and strength of the individual film. Consolidation of the films gradually removes the defects with increasing thickness of the stack by: (a) compressing the cavities into continuous, solid material, (b) partial melting of the material and healing of the defects and, (c) cooperative sealing of the surface defects by adjacent films. This can be especially seen from the comparison of 1- to 5-film structures, in which the ultimate strain and stress gradually increase and asymptote to ε ~360 % and σ_{UTS} ~85 MPa. (Figure 81C and Table 15)

Lamination and the hierarchical design of material not only impart exceptional mechanical properties but also offer opportunities for incorporation of unique properties in the resulting structures. To demonstrate this, we prepared films with addition of FITC and TRITC fluorescent dyes. (Figure 83A) The dye-labeled films were further consolidated in different sequences and characterized using laser-scanning confocal microscopy. Alternate stacking of green- and red-fluorescent films revealed that in spite of partial surface melting the films do retain their individuality (Figure 83B). This property can be used to manufacture multifunctional materials with a variety of applications because the films can equally well incorporate other molecules or nanomaterials besides the fluorescent dyes by incorporation into deposition sequence.[11] Here, however, we want to show how this property can be useful for the study of mechanical properties.

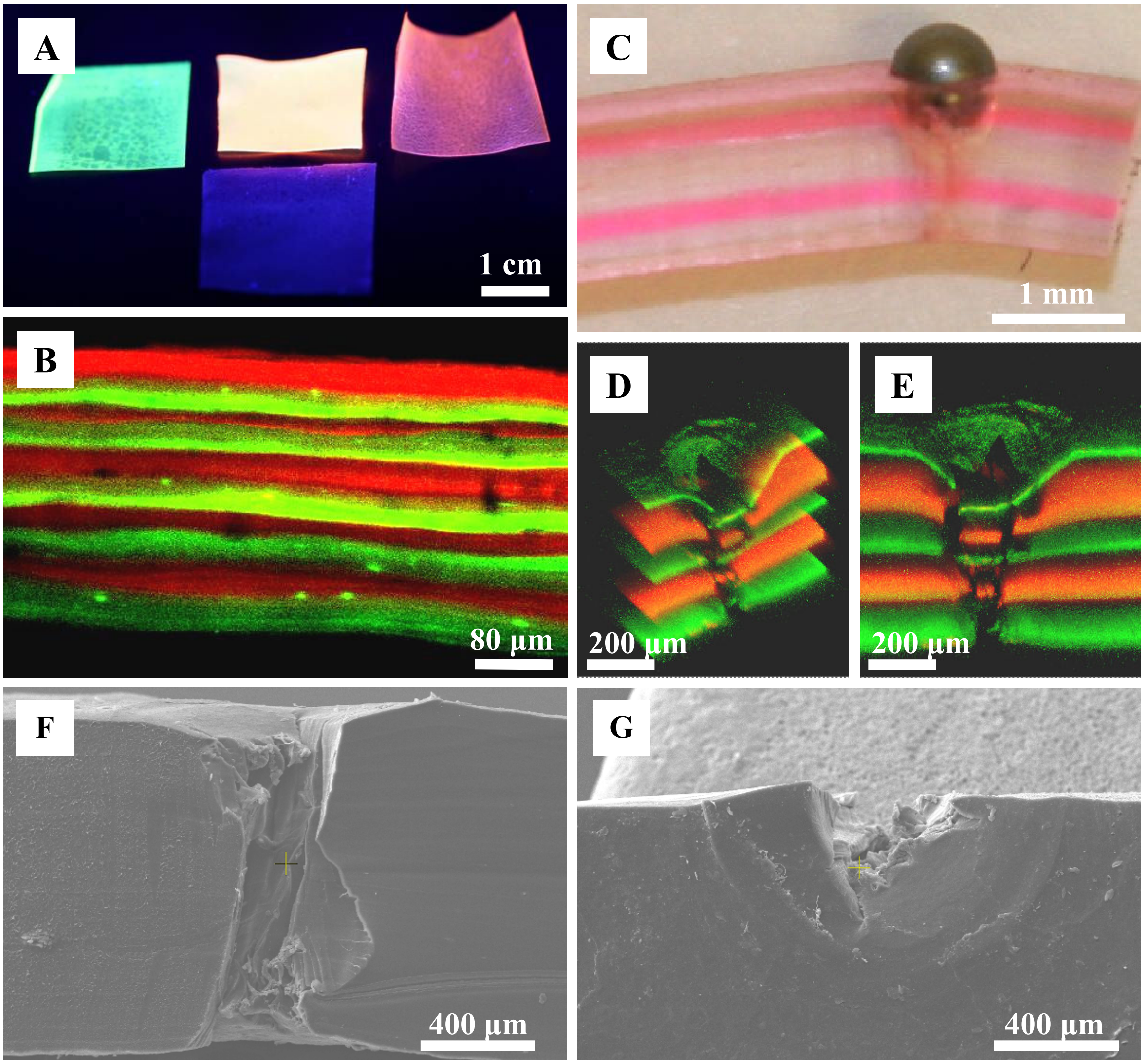

Figure 83. Demonstration of multifunctional potential of the consolidated e-LBL structures. (A) Photograph of fluorescent-dye-labeled, 100-bilayer PU/PAA e-LBL films, and a consolidated stack under UV light (365 nm) illumination. Top row: left: FITC-labeled 100-bilayer film, center: consolidated stack composed of 10, 100-bilayer dye-labeled films, and right: TRITC-labeled 100-bilayer film. Bottom: plain 100-bilayer film. The composite was prepared by alternate stacking of the dye-labeled films into a $(FITC/TRITC)_5$ structure. (B) Laser-scanning confocal microscopy image of cross-section of the dye-labeled 10-film alternating stack from (A). (C) A photograph of cross-section of a consolidated stack composed of alternating layers of FITC- and TRITC-labeled 100-bilayer films separated at every point by 3, not-labeled 100-bilayer films. For demonstration purposes a steel ball has been pressed into the film using a hydraulic press. The TRITC-labeled films are clearly visible as red bands. (D) and (E): Confocal microscopy 3D images of cross-section around the damage caused by the steel ball in (C). (F) Cross-section SEM image of the damaged area from steel ball in (C). (G) Top-down SEM image of the damage caused by the steel ball.

A ~1.2 mm thick sample in which the labeled films have been separated by 3 plain films was impaled with a small steel ball and the resulting damage was imaged using the confocal microscopy (Figure 83C). The ability of confocal microscopy to generate images at different focal lengths allows the user to generate 3D fluorescence images. Using this feature, we were able to generate 3D images of the resulting damage. (Figures 83D and 83E) Applying this technique in this context allowed us to visualize the structural deformations at different depths of the material, which would not be possible using optical or electron microscopes. (Figures 83F and 83G) The confocal microscopy imaging offers a noninvasive damage detection method with excellent spatial resolution (~1μm) when compared to other widely utilized techniques. Of the different methods available, e.g. electrical conductivity, optical fiber detection, or ultrasonic evaluation, only high resolution x-ray computed tomography (CT) has capability of approaching similar resolution.[49]

4. Conclusions

In conclusion we showed here the first preparation of exponential LBL films from polyurethanes having great toughness and flexibility. We further introduced a new concept in the LBL assembly, i.e. hierarchical structuring of the composite by consolidation of individual sheets. The hierarchical structures show further improvement in the mechanical properties when compared to individual films and pure polymers, with ultimate strength and toughness showing nearly three times improvement. Finally, we showed an application of the composite stack to damage detection as an example of potential new research directions for the hierarchically structured LBL composites.

Reference List

1. Decher, G. Fuzzy nanoassemblies: toward layered polymeric multicomposites. *Science (Washington, D. C.)* **1997,** *277* (5330), 1232-1237.

2. Mamedov, A. A.; Kotov, N. A.; Prato, M.; Guldi, D. M.; Wicksted, J. P.; Hirsch, A. Molecular design of strong single-wall carbon nanotube/polyelectrolyte multilayer composites. *Nature Materials* **2002,** *1* (3), 190-194.

3. Tang, Z.; Kotov, N. A.; Magonov, S.; Ozturk, B. Nanostructured artificial nacre. *Nature Materials* **2003,** *2* (6), 413-418.

4. Podsiadlo, P.; Kaushik, A. K.; Arruda, E. M.; Waas, A. M.; Shim, B. S.; Xu, J.; Nandivada, H.; Pumplin, B. G.; Lahann, J.; Ramamoorthy, A.; Kotov, N. A. Ultrastrong and Stiff Layered Polymer Nanocomposites. *Science (Washington, DC, United States)* **2007,** *318* (5847), 80-83.

5. Podsiadlo, P.; Paternel, S.; Rouillard, J. M.; Zhang, Z.; Lee, J.; Lee, J. W.; Gulari, E.; Kotov, N. A. Layer-by-Layer Assembly of Nacre-like Nanostructured Composites with Antimicrobial Properties. *Langmuir* **2005,** *21* (25), 11915-11921.

6. Podsiadlo, P.; Choi, S. Y.; Shim, B.; Lee, J.; Cuddihy, M.; Kotov, N. A. Molecularly Engineered Nanocomposites: Layer-by-Layer Assembly of Cellulose Nanocrystals. *Biomacromolecules* **2005,** *6* (6), 2914-2918.

7. Podsiadlo, P.; Liu, Z.; Paterson, D.; Messersmith, P. B.; Kotov, N. A. Fusion of seashell nacre and marine bioadhesive analogs: high-strength nanocomposite by layer-by-layer assembly of clay and L-3,4-dihydroxyphenylalanine polymer. *Advanced Materials (Weinheim, Germany)* **2007,** *19* (7), 949-955.

8. Podsiadlo, P.; Tang, Z.; Shim, B. S.; Kotov, N. A. Counterintuitive Effect of Molecular Strength and Role of Molecular Rigidity on Mechanical Properties of Layer-by-Layer Assembled Nanocomposites. *Nano Letters* **2007,** *7* (5), 1224-1231.

9. Podsiadlo, P.; Sui, L.; Elkasabi, Y.; Burgardt, P.; Lee, J.; Miryala, A.; Kusumaatmaja, W.; Carman, M. R.; Shtein, M.; Kieffer, J.; Lahann, J.; Kotov, N. A. Layer-by-Layer Assembled Films of Cellulose Nanowires with Antireflective Properties. *Langmuir* **2007,** *23* (15), 7901-7906.

10. Shim, B. S.; Tang, Z.; Morabito, M. P.; Agarwal, A.; Hong, H.; Kotov, N. A. Integration of Conductivity, Transparency, and Mechanical Strength into Highly Homogeneous Layer-by-Layer Composites of Single-Walled Carbon Nanotubes for Optoelectronics. *Chemistry of Materials* **2007,** *19* (23), 5467-5474.

11. Podsiadlo, P.; Michel, M.; Lee, J.; Verploegen, E.; Kam, N. W. S.; Ball, V.; Lee, J.; Qi, Y.; Hart, A. J.; Hammond, P. T.; Kotov, N. A. Exponential Growth of LBL Films with Incorporated Inorganic Sheets. *Nano Letters* **2008,** *8* (6), 1762-1770.

12. Kotov, N. A.; Magonov, S.; Tropsha, E. Layer-by-layer self-assembly of aluminosilicate-polyelectrolyte composites: mechanism of deposition, crack resistance, and perspectives for novel membrane materials. *Chemistry of Materials* **1998,** *10* (3), 886-895.

13. Porcel, C.; Lavalle, P.; Decher, G.; Senger, B.; Voegel, J. C.; Schaaf, P. Influence of the Polyelectrolyte Molecular Weight on Exponentially Growing Multilayer Films in the Linear Regime. *Langmuir* **2007,** *23* (4), 1898-1904.

14. Picart, C.; Mutterer, J.; Richert, L.; Luo, Y.; Prestwich, G. D.; Schaaf, P.; Voegel, J. C.; Lavalle, P. Molecular basis for the explanation of the exponential growth of polyelectrolyte multilayers. *Proceedings of the National Academy of Sciences of the United States of America* **2002,** *99* (20), 12531-12535.

15. Fan, X.; Park, M. K.; Xia, C.; Advincula, R. Surface structural characterization and mechanical testing by nanoindentation measurements of hybrid polymer/clay nanostructured multilayer films. *Journal of Materials Research* **2002,** *17* (7), 1622-1633.

16. Hermanson, G. T.; Editor. *Bioconjugate Techniques;* 1995.

17. Yoo, P. J.; Nam, K. T.; Qi, J.; Lee, S. K.; Park, J.; Belcher, A. M.; Hammond, P. T. Spontaneous assembly of viruses on multilayered polymer surfaces. *Nature Materials* **2006,** *5* (3), 234-240.

18. Ji, J.; Fu, J.; Shen, J. Fabrication of a superhydrophobic surface from the amplified exponential growth of a multilayer. *Advanced Materials (Weinheim, Germany)* **2006,** *18* (11), 1441-1444.

19. Elbert, D. L.; Herbert, C. B.; Hubbell, J. A. Thin Polymer Layers Formed by Polyelectrolyte Multilayer Techniques on Biological Surfaces. *Langmuir* **1999,** *15* (16), 5355-5362.

20. Tang, Z.; Wang, Y.; Kotov, N. A. Semiconductor Nanoparticles on Solid Substrates: Film Structure, Intermolecular Interactions, and Polyelectrolyte Effects. *Langmuir* **2002,** *18* (18), 7035-7040.

21. Wood, K. C.; Chuang, H. F.; Batten, R. D.; Lynn, D. M.; Hammond, P. T. Controlling interlayer diffusion to achieve sustained, multiagent delivery from layer-by-layer thin films. *Proceedings of the National Academy of Sciences of the United States of America* **2006,** *103* (27), 10207-10212.

22. Sun, B.; Jewell, C. M.; Fredin, N. J.; Lynn, D. M. Assembly of Multilayered Films Using Well-Defined, End-Labeled Poly(acrylic acid): Influence of Molecular Weight on Exponential Growth in a Synthetic Weak Polyelectrolyte System. *Langmuir* **2007,** *23* (16), 8452-8459.

23. Brown, G.; Editor. *The X-ray Identification and Crystal Structures of Clay Minerals;* 1961.

24. Roe, R. *Methods of X-Ray and Neutron Scattering in Polymer Science;* 2000.

25. Finnigan, B.; Jack, K.; Campbell, K.; Halley, P.; Truss, R.; Casey, P.; Cookson, D.; King, S.; Martin, D. Segmented Polyurethane Nanocomposites: Impact of Controlled Particle Size Nanofillers on the Morphological Response to Uniaxial Deformation. *Macromolecules* **2005,** *38* (17), 7386-7396.

26. Lutkenhaus, J. L.; Olivetti, E. A.; Verploegen, E. A.; Cord, B. M.; Sadoway, D. R.; Hammond, P. T. Anisotropic Structure and Transport in Self-Assembled Layered Polymer-Clay Nanocomposites. *Langmuir* **2007,** *23* (16), 8515-8521.

27. Gracias, D. H.; Somorjai, G. A. Continuum Force Microscopy Study of the Elastic Modulus, Hardness and Friction of Polyethylene and Polypropylene Surfaces. *Macromolecules* **1998,** *31* (4), 1269-1276.

28. Mamedov, A. A.; Kotov, N. A. Free-Standing Layer-by-Layer Assembled Films of Magnetite Nanoparticles. *Langmuir* **2000,** *16* (13), 5530-5533.

29. Srivastava, S.; Ball, V.; Podsiadlo, P.; Lee, J.; Ho, P.; Kotov, N. A. Reversible Loading and Unloading of Nanoparticles in \"Exponentially\" Growing Polyelectrolyte LBL Films. *Journal of the American Chemical Society* **2008,** *130* (12), 3748-3749.

30. Briggs, D.; Seah, M. P. *Practical Surface Analysis, Pt. 1;* 1990.

31. Gao, C.; Leporatti, S.; Moya, S.; Donath, E.; Moehwald, H. Stability and Mechanical Properties of Polyelectrolyte Capsules Obtained by Stepwise Assembly of Poly(styrenesulfonate sodium salt) and Poly(diallyldimethyl ammonium) Chloride onto Melamine Resin Particles. *Langmuir* **2001,** *17* (11), 3491-3495.

32. Mertz, D.; Hemmerle, J.; Mutterer, J.; Ollivier, S.; Voegel, J. C.; Schaaf, P.; Lavalle, P. Mechanically Responding Nanovalves Based on Polyelectrolyte Multilayers. *Nano Letters* **2007,** *7* (3), 657-662.

33. Zhai, L.; Cebeci, F. C.; Cohen, R. E.; Rubner, M. F. Stable Superhydrophobic Coatings from Polyelectrolyte Multilayers. *Nano Letters* **2004,** *4* (7), 1349-1353.

34. Lee, J. S.; Cho, J.; Lee, C.; Kim, I.; Park, J.; Kim, Y. M.; Shin, H.; Lee, J.; Caruso, F. Layer-by-layer assembled charge-trap memory devices with adjustable electronic properties. *Nature Nanotechnology* **2007,** *2* (12), 790-795.

35. Izquierdo, A.; Ono, S. S.; Voegel, J. C.; Schaaf, P.; Decher, G. Dipping versus Spraying: Exploring the Deposition Conditions for Speeding Up Layer-by-Layer Assembly. *Langmuir* **2005,** *21* (16), 7558-7567.

36. Cho, J.; Char, K.; Hong, J. D.; Lee, K. B. Fabrication of highly ordered multilayer films using a spin self-assembly method. *Advanced Materials (Weinheim, Germany)* **2001,** *13* (14), 1076-1078.

37. Chiarelli, P. A.; Johal, M. S.; Casson, J. L.; Roberts, J. B.; Robinson, J. M.; Wang, H. L. Controlled fabrication of polyelectrolyte multilayer thin films using spin-assembly. *Advanced Materials (Weinheim, Germany)* **2001,** *13* (15), 1167-1171.

38. Shim, B. S.; Podsiadlo, P.; Lilly, D. G.; Agarwal, A.; Lee, J.; Tang, Z.; Ho, S.; Ingle, P.; Paterson, D.; Lu, W.; Kotov, N. A. Nanostructured Thin Films Made by Dewetting Method of Layer-By-Layer Assembly. *Nano Letters* **2007,** *7* (11), 3266-3273.

39. Gao, H.; Ji, B.; Jager, I. L.; Arzt, E.; Fratzl, P. Materials become insensitive to flaws at nanoscale: Lessons from nature. *Proceedings of the National Academy of Sciences of the United States of America* **2003,** *100* (10), 5597-5600.

40. Kamat, S.; Su, X.; Ballarin, R.; Heuer, A. H. Structural basis for the fracture toughness of the shell of the conch Strombus gigas. *Nature (London)* **2000,** *405* (6790), 1036-1040.

41. Tesch, W.; Eidelman, N.; Roschger, P.; Goldenberg, F.; Klaushofer, K.; Fratzl, P. Graded microstructure and mechanical properties of human crown dentin. *Calcified Tissue International* **2001,** *69* (3), 147-157.

42. Rho, J. Y.; Kuhn-Spearing, L.; Zioupos, P. Mechanical properties and the hierarchical structure of bone. *Med Eng Phys* **1998,** *20* (2), 92-102.

43. van Beek, J. D.; Hess, S.; Vollrath, F.; Meier, B. H. The molecular structure of spider dragline silk: Folding and orientation of the protein backbone. *Proceedings of the National Academy of Sciences of the United States of America* **2002,** *99* (16), 10266-10271.

44. Miserez, A.; Schneberk, T.; Sun, C.; Zok, F. W.; Waite, J. H. The Transition from Stiff to Compliant Materials in Squid Beaks. *Science (Washington, DC, United States)* **2008,** *319* (5871), 1816-1819.

45. Briggs, D.; Seah, M. P. *Practical Surface Analysis, Pt. 1;* 1990.

46. Nam, S. Y.; Lee, Y. M. Pervaporation and properties of chitosan-poly(acrylic acid) complex membranes. *Journal of Membrane Science* **1997,** *135* (2), 161-171.

47. Huang, Y.; Lu, J.; Xiao, C. Thermal and mechanical properties of cationic guar gum/poly(acrylic acid) hydrogel membranes. *Polymer Degradation and Stability* **2007,** *92* (6), 1072-1081.

48. Liff, S. M.; Kumar, N.; McKinley, G. H. High-performance elastomeric nanocomposites via solvent-exchange processing. *Nature Materials* **2007,** *6* (1), 76-83.

49. Masters, J. E.; Editor. *Damage Detection in Composite Materials. (Papers Presented at the International Symposium on Damage Detection and Quality Assurance in Composite Materials, San Antonio, Texas, 13-14 Nov., 1990.) [In: ASTM Spec. Tech. Publ., 1992; STP 1128];* 1992.

Chapter V

Conclusions and Future Research Directions

The research, presented in this work, has shown that layer-by-layer (LBL) assembly provides an extremely versatile method for the preparation of thin films. The structure of the growing LBL stack and its physical and chemical properties are tunable and customizable through the choice of materials, assembly conditions, dipping order, and post-assembly processing. This method can be easily applied to a wide range of organic and inorganic materials, which gives the possibility of preparing composite films with wide spectra of possible applications.

In summary, the versatility of the LBL method for preparation of thin films of nanocolloids with unique structural organization and mechanical properties was demonstrated. Emphasis was placed on LBL assembly of two natural nanomaterials: nanosheets of montmorillonite clay and nanocrystals of cellulose. We used the LBL method as a model system to study the mechanics of NCs with high volume fractions of NPs and we showed ability of the LBL assembly method to effectively harness the exceptional mechanical properties of NPs. We further showed that the thin-film fabrication method can be extended to preparation of macro-scale composites via hierarchical structuring.

The results presented here are only a tip of the iceberg in terms of potential research directions. The results achieved with clay, while exceptional and suitable for thin-film applications and coatings, require scaling to macroscale structures. This would require development of rapid deposition methods. Potential directions would be spin-coating or printing technologies involving micro- and nano-fluidics. Spin-coating offers not only increased speed of deposition but also a different method for controlling organization of the nanomaterials owing to the centrifugal forces. Possible developments would be gradient distribution of nanomaterials for biomedical applications or alignment of axial colloids, with the latter being important for electronics and mechanics of composites. Most likely, the molecular and nanoscale organization of polymer layers would also be affected by the centrifugal and shear forces, e.g. organization of the polyurethanes or the process of exponential LBL assembly. Similarly, the hierarchical structuring presented in the last chapter could be expanded to preparation of laminated composites, allowing for greater diversity in terms of structural organization.

Another direction would be extension of the results obtained for the clay to other nanomaterials, e.g. CNTs, graphene and graphite sheets, silica nanoparticles, or other synthetic nanomaterials for preparation of high-performance nanocomposites. Theoretical and experimental results show that CNTs are the strongest known materials on Earth, and if similar results were obtained to those for clay, the LBL nanosheets would yield nanocomposites with incredible mechanical properties, by far surpassing the currently available composite materials. Along this line of thought, we have only studied one type and one size distribution of clay. It would be interesting to study the effect of platelet size on the properties of the nanocomposites. Further modification of clay surfaces to improve cross-linking density and effectiveness of interactions with the polymer matrix would potentially improve the mechanical properties even further. Similarly, improving exfoliation of the clay particles would further improve mechanical and optical properties.

In connection to the cellulose nanocrystals results, thus far we have only shown feasibility of LBL assembly and preliminary results on mechanical properties of the assemblies. The nanocrystals present a unique reinforcing nanomaterial having natural and renewable origins as well as unique surface chemistry, rich in hydroxyl groups which unlike inorganic nanosheets, are amenable to chemical modification and cross-linking. Extension of the understanding gained with clay to the nanocrystals has a potential to generate even stronger nanocomposites in perspective. The assemblies from nanocrystals also showed interesting optical properties which should be explored further, including their liquid crystal properties.

The results presented with the exponential LBL assembly of hybrid organic/inorganic structures have opened a new research avenue. Incorporation of other nanomaterials besides clay will surely lead to even more interesting structures, *in situ* self-assembly of the nanomaterials, and variety of applications. The currently understood mechanism of assembly, while plausible, still does not explain some of the observations, e.g. diffusion of just one component in some cases. Understanding of the process will require computational tools and presents another research direction. The gel-like structures of the swollen films are already being explored for biomedical applications. Similarly, the research can be further extended to novel separation membranes or reaction centers.

Finally, the results with polyurethanes open yet another research direction into highly flexible multilayered membranes. Further combination with the well explored polyelectrolytes, e.g. PDDA or PSS, incorporation of different types of nanocolloids, and utilization of the viscoelastic properties of the polymers for mechanically and reversibly controlling properties of the films will surely lead to many novel applications.

In the end, these are just a few thoughts and ideas which come to mind. The tremendous diversity of available pool of nanocolloids and the versatility of LBL technique to combine multiple components into user-defined architectures hold unlimited possibilities for materials design and research for many more years to come.